UNIVERSITÀ
DEGLI STUDI DI BARI
ALDO MORO

UNIVERSITÀ DEGLI STUDI DI BARI ALDO MORO

DIPARTIMENTO INTERUNIVERSITARIO DI FISICA
Dottorato di Ricerca in Fisica - XXXII CICLO - SSD FIS/02

PHASE BEHAVIOR AND TOPOLOGICAL DEFECTS OF ACTIVE BROWNIAN PARTICLES IN TWO DIMENSIONS

Dottorando:
Dott. Pasquale Digregorio

Supervisore:
Chiar.mo Prof.
Giuseppe Gonnella

Coordinatore:
Chiar.mo Prof.
Giuseppe Iaselli

Esame finale 2020

Contents

Chapter 1

Activity and ordering in two-dimensional systems

This first Chapter serves as a rather detailed introduction to the thesis. Two main fundamental topics constitute almost the entire theoretical background of this work and thus need to be introduced, in order to address our purposes with accuracy.

The first one of the two, is the so-called *Active Matter*, which refers to a wide field in the area of soft-condensed matter that, although considered as an independent topic at most from about twenty years, already includes a relevant amount of works and widely agreed understandings, being on the other hand much fast evolving. The main reason of the high and intensively growing interest in active matter, comes from the fact that it is mainly devoted to build a theoretical framework for systems of agents which can sustain tasks by themselves. Being more specific and trying already to get closer to our targets, though probably ruling out someone of the facets of this field, active constituents are those which are able to exploit internal energy sources to maintain their own motion. Needless to say, such ability is primary of living agents, whose widely unexplored and most diverse behaviors are continuously stimulating research in this field.

The second argument we have been largely deal with is the theory of ordering for materials in two spatial dimensions. Mostly developed in the seventies as a fundamental theory in statistical mechanics, it accounts for the profound relations between phase transitions and dimensionality, and it reveals relevant differences between melting of 2D systems and the much better known, because closer to our everyday-life experience, 3D ones.

We will thus shortly present both active matter and 2D melting in the next two Sections and then we will address the main points of our work and the overall structure of the thesis.

1.1 Active systems

For the motion of active constituents to be self-sustained, a supply of energy is needed at the level of each single one of them. Thinking to alive constituents, such internal energy comes from nutrients, which, being "processed" from the organism, allow it to fulfil all the "living" works, included motion. Besides living systems, a lot of active matter synthetic realizations exist to date. Among them, the most well-known strategy to realize autonomous propulsion at the microscale is to make use of the so-called *Janus colloids*. They are artificial (usually spherical) colloids that, due to a different chemical treatment of the two hemispheres, are able to produce solute concentration or temperature gradients and thus to swim via *self-phoretic* mechanisms (see for instance [Spe19, Kap13, BDLL$^+$16, MP17, PP18]).

Systems composed of many of such active objects are inherently out of thermal equilibrium. From the two examples given above, it is easy to understand that self-driven motion breaks detailed balance, which is a key ingredient for the equilibrium behavior. For this reason, even the steady states of active systems are allowed to violate equilibrium statistical mechanics, and can thus show a great variety of collective behaviors. This is not unexpected for living systems, which are well-known to undergo numerous collective phenomena, such as flocking, swarming, accumulation, *etc*. We shall see that similar large-scale collective motions also arise for very simple toy-models of active matter, which we are very interested in for the aims of this work.

Because of the large appeal towards active matter, many attempts have been carried out to find suitable theoretical frameworks for understanding the physics of such rich phenomenology. Though a unified theory is not currently available, many accurate results have been achieved. We are not willing to review the several theoretical ideas and approaches, especially since some very detailed and exhaustive analysis are already available, for example in Refs. [MJR$^+$13, Cat12, SWW$^+$19].

Nevertheless, we will present both in this introductory Chapter and throughout the thesis, some of the fundamental models for active systems, which will help us to describe and justify many of the features we have been dealt with during our work.

1.1.1 Relevant models for active dynamics

We start this short survey of theoretical modeling, with one of the first that came out, due to Tamás Vicsek, whose appearance probably coincides with

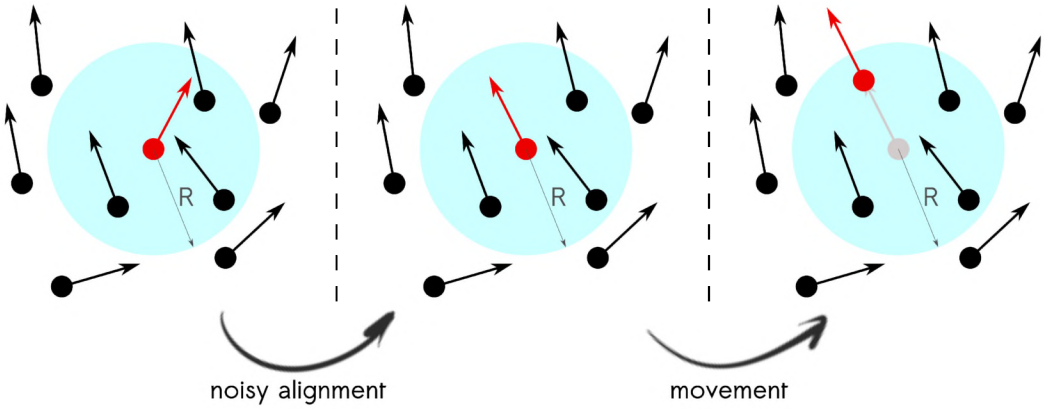

Figure 1.1: Schematic view of the dynamics of the Vicsek's model: local alignment interaction with noise, and ballistic movement.

the beginning of the huge spreading of the studies in active matter. The main success of the pioneering work of Vicsek was to recognize that collective behaviors, namely large-scale flocking of point-like non interacting objects, is intimately related to self-driven motion.

Vicsek's model and collective alignment

The Vicsek model [VCBJ+95], describes the motion of point-like particles with alignment interaction and fixed speed immersed in an inert background. The direction of motion of each one of these "moving arrows" changes according to a local rule that requires arrows to align with their neighbors at each time.

The velocity $\mathbf{v}_i$ (of fixed magnitude v_0) of a particle can be identified by the angle θ_i between $\mathbf{v}_i$ and an arbitrary reference direction. Particles evolve and they reorient time by time according to the following alignment to the neighbors:

$$\mathbf{v}_i(t+1) = v_0 \frac{\langle \mathbf{v}_j(t) \rangle_R}{|\langle \mathbf{v}_j(t) \rangle_R|} + \eta_i \,, \tag{1.1}$$

where the average is taken over a set of neighbors within a radius R around the particle i. The stochastic process η accounts for errors in alignments, and it is a zero mean Gaussian white noise with a given variance. The scheme described by Eq. (1.1) is sketched in figure 1.1.
The trajectory of each particle is easily reconstructed by means of the updated velocities:

$$\mathbf{x}_i(t+1) = \mathbf{x}_i(t) + \mathbf{v}_i(t+1) \tag{1.2}$$

As interestingly found in [VCBJ+95], taking as order parameter the normalized average velocity

$$\varphi = \frac{1}{Nv_0} \left| \sum_{i=1}^{N} \mathbf{v}_i \right|, \tag{1.3}$$

this very simple model undergoes a phase transition from a disordered to an ordered phase with decreasing noise strength or increasing density.
The ordered phase of the Vicsek model very closely resembles the one observed in a flock, with all the birds coherently moving along a common direction [*] . Even more interestingly, from this very short treatment is should be already clear that collective attitudes does not need a long-range sensing, but they arise from simple local interactions.

A theory for flocking in the continuum

A continuum effective theory for the flocking model of Vicsek *et al.* was proposed in 1995 by Toner and Tu [TT95]. Within their famous works, they formulated a hydrodynamic model, able to catch the relevant features of flocking, using a so-called "top-down" approach, relied only on the symmetries of the system. We want to sketch here such approach, referring to a very pedagogical set of lectures by John Toner [Ton18].

Summarizing some requirements related to the Vicsek prescriptions (see previous Subsection), this continuum model aims to describes a large flock of arrows in d spatial dimensions, which try to align to their closer neighbors, though making some random error.
The only symmetries of this model are rotational and translational invariance. Translational invariance means that the physics of flock does not change under rigid displacements in space, while rotational invariance means that the flock has no *a priori* preferences on its directions of motion. This immediately suggests that, to account for long-range alignment and thus coherent direction of the whole flock, rotational symmetry should be spontaneously broken for some given values of the control parameters. On the other hand, translational invariance does not need to be broken in the context of the Vicsek phase transition.

Contrary to general hydrodynamic Navier-Stokes-like description, this model is not invariant under general Galilean transformation, specifically under arbitrary boosts. The lack of Galilean invariance is justified for the

[*] See for instance the beautiful movie at `https://www.youtube.com/watch?v=0j9L70Fh9PM`, from numerical simulation of Eqs. (1.1) and (1.2), with a manifest swarming behavior.

scope of the models, because flocks always move in a resistive medium, which represents a special Galilean reference frame, and its physics, as well as the physics of the Vicsek model, would change moving to a different frame.

In addiction to symmetries, one point to be noted here is that there is no momentum conservation in the Vicsek's model, and thus no momentum conservation is required for its description in the continuum. Since, as in Eqs. (1.1) and (1.2), we are dealing only with the variables of the system, thus disregarding the medium, we have to allow the total momentum to vary. This is the reason why such models are generally called *dry* models. On the other hand, also much advanced *wet* theories exist for active matter, see for instance [ASR02, SR02, Sim03, HRRS04, Ram10], but we will not mentioned them within this overview.
The only conserved quantity for the present model is the total number of particles, which means that the density field ρ must agree a continuity equation of the form

$$\frac{\partial \rho}{\partial t} + \boldsymbol{\nabla} \cdot (\rho \mathbf{v}) = 0 \,. \tag{1.4}$$

Rotational invariance implies that $\partial_t \mathbf{v}$ must equals a sum of vectors. In the following we will explore all the possibilities allowed by such constraint, to build the more general equation for $\mathbf{v}$.

The first obvious possibility is a term of the form

$$(\partial_t \mathbf{v})_1 = U(|\mathbf{v}|, \rho)\mathbf{v} \,. \tag{1.5}$$

with U a function of density and velocity. This term closely resembles the usual friction term. However, this generalization allows positive values for U, which do not correspond to friction, but accounts instead for self-propulsion. A bird in the flock is accounted, by means of this term, to be able to sustain its velocity. A natural choice for U is related to spontaneous rotational symmetry breaking, which rules the disorder-to-order transition. Given that the term can be derived for a "potential" according to

$$U\,\mathbf{v} = -\partial V(\mathbf{v})/\partial \mathbf{v} \,, \tag{1.6}$$

the notable choice for V of the form

$$V(\mathbf{v}) = -\frac{1}{2}\alpha(\rho)|\mathbf{v}|^2 + \frac{1}{4}\beta(\rho)|\mathbf{v}|^4 \,, \tag{1.7}$$

makes the velocity evolve, for a suitable choice of the parameters α and β, towards a ring of identical minima at $|\mathbf{v}| = v_0$, namely the self-propulsion velocity.

Other terms allowed from symmetries are the ones in the form

$$(\partial_t v_i) \propto v_l \partial_j v_k \,. \tag{1.8}$$

It is easy to show that, all the possible consistent choices for contraction of the indices in the above form, leads to the following three different terms:

$$(\partial_t \mathbf{v})_2 = -\lambda_1 \mathbf{v}\cdot\boldsymbol{\nabla}\mathbf{v} - \lambda_2 \mathbf{v}(\boldsymbol{\nabla}\cdot\mathbf{v}) - \lambda_3 \boldsymbol{\nabla}(|\mathbf{v}|^2) \,. \tag{1.9}$$

If we include also combinations of one gradient, $\mathbf{v}$, and the density ρ, a third set of terms arises. Some of them can be absorbed in the three before, allowing the λs to depend on $(|\mathbf{v}|, \rho)$, while two new pressure-like terms must be explicitly added:

$$(\partial_t \mathbf{v})_3 = -\boldsymbol{\nabla} P(|\mathbf{v}|, \rho) - \mathbf{v}(\mathbf{v}\cdot\boldsymbol{\nabla}) P_2(|\mathbf{v}|, \rho) \,. \tag{1.10}$$

Finally, it turns out from *a posteriori* considerations, that also terms with two gradients have to be included. The most general one of this kind must have the form

$$(\partial_t v_i) \propto [v_p v_n \dots v_s v_u] \partial_j \partial_k v_l \,, \tag{1.11}$$

and suitable contractions of the indices brings to three other terms

$$(\partial_t \mathbf{v})_4 = D_T \nabla^2 \mathbf{v} + D_B \boldsymbol{\nabla}(\boldsymbol{\nabla}\cdot\mathbf{v}) + D_2 (\mathbf{v}\cdot\boldsymbol{\nabla})^2 \mathbf{v} \,, \tag{1.12}$$

where, again, the coefficient are functions of both velocity and density.

Taking all the terms in (1.5),(1.9),(1.10),(1.12) together, we have obtained the most general hydrodynamic equation consistent with the symmetries of the model

$$\begin{aligned} &\partial_t \mathbf{v} + \lambda_1 \mathbf{v}\cdot\boldsymbol{\nabla}\mathbf{v} + \lambda_2 \mathbf{v}(\boldsymbol{\nabla}\cdot\mathbf{v}) + \lambda_3 \boldsymbol{\nabla}(|\mathbf{v}|^2) = \\ &U(|\mathbf{v}|, \rho)\mathbf{v} - \boldsymbol{\nabla} P - \mathbf{v}(\mathbf{v}\cdot\boldsymbol{\nabla}) P_2 + D_T \nabla^2 \mathbf{v} + D_B \boldsymbol{\nabla}(\boldsymbol{\nabla}\cdot\mathbf{v}) + D_2 (\mathbf{v}\cdot\boldsymbol{\nabla})^2 \mathbf{v} + \mathbf{f} \,, \end{aligned} \tag{1.13}$$

where we only added the Gaussian white noise $\mathbf{f}$.

We are not going to proceed further in describing the method for solving Eq. (1.13) and (1.4), because it would go beyond the scope of our presentation. We just care to underline that, although technically complicated, this approach is a truly powerful one, because, as mentioned before, the form of the equation does not depend on the microscopic details of system. At the expense of transparency, the same form can be retained to deal with Vicsek-like models, also with changing its microscopic behavior. Adding inter-particle attractive or repulsive potential, modifying the rule of selecting neighbors, introducing memory effects, *etc*, would easily be accounted at the hydrodynamic level of Eq. (1.4) by only changing the coefficients.

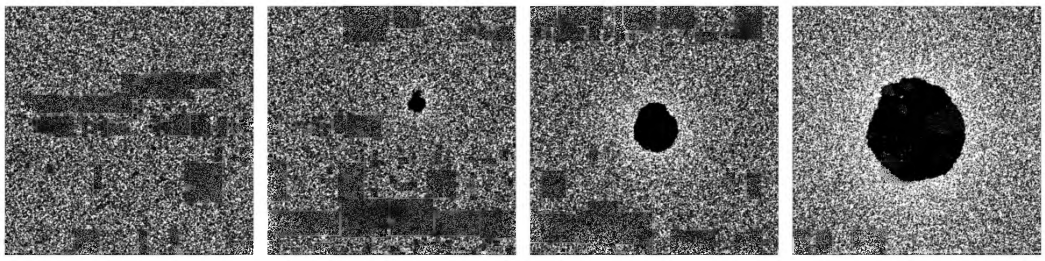

Figure 1.2: Coarsening dynamics with MIPS for AB disks without alignment. See the equations of motion 1.19. Single disks are printed as black points. Once the instability is triggered within the homogeneous phase, particles begin to accumulate and the system segregate into a dense cluster and a gaseous phase.

Other than for its importance in the development of active matter, we have included the Toner-Tu model in this presentation, for reasons that we will explain in the next Section, which deal with order-disorder transition accounted. It is of fundamental theoretical importance for the focus of our analysis.

Kinetic theories and Motility-Induced Phase Separation

Together with large-scale alignment found above, another quite surprising a broadly investigated collective behavior in active matter is a clustering phenomenon in absence on either attractive interactions or alignment, but only driven by activity, thus called *Motility-Induced Phase Separation* (MIPS). This phase separation was first found by Cates and co-workers [TC08] for a system of self-propelled run-and-tumble particles, then observed in many others systems of motile objects [FM12, RHB13, CT13, BLS13], and thus became one of the fingerprints on active matter.

The reason why MIPS is ubiquitous in active system has to do with the mechanisms that triggers the phase separation. Cates *et al.* already addressed it from the beginning in [TC08], and they demonstrated that such mechanism is driven solely by the motility of the particles and is it thus really robust against either inter-particle interactions changing or every kind of alignment rule.

This mechanism is so-called *self-trapping* and it is easily derivable, as in [CT13, GMST15, MM15], from explicitly coarse-graining microscopic run-and-tumble (RT) dynamics, basing on a general coarse-graining technique developed in [Sch93].

Self-propelled RT particles mimic the dynamics of several species of motile bacteria, which explore the space around them with moving straight for almost constant distances ('runs') and instantaneously changing direc-

tion between two runs with time-rate α ('tumbles').

Coarse-graining this model means considering as a global variable, the distribution $f(\mathbf{r}, \mathbf{u}, t)$ of active particles with position $\mathbf{r}$, swimming in the direction $\mathbf{u}$, with speed v, at a given time t. The prescribed evolution of such distribution is the following Boltzmann-like kinetic equation:

$$\partial_t f(\mathbf{r}, \mathbf{u}, t) = -\boldsymbol{\nabla}_{\mathbf{r}} \cdot \Big[v\mathbf{u} f(\mathbf{r}, \mathbf{u}, t) \Big] - \frac{f(\mathbf{r}, \mathbf{u}, t)}{\tau} + \frac{\int \mathrm{d}^{d-1}\mathbf{u} f(\mathbf{r}, \mathbf{u}, t)}{\tau \Omega_d} , \tag{1.14}$$

where τ is the average time-distance between two consecutive tumbles, $\Omega_d = \int \mathrm{d}^{d-1}\mathbf{u}$ is total solid angle in a d-dimensional space.
The first term on the right-hand side accounts for the runs, while the second and third ones are collisional rates for tumbling out the direction $\mathbf{u}$ and into it, respectively.

Applying a Chapman-Enskog-like gradient expansion to Eq. (1.14), it can be shown that, up to the second order in the derivatives:

$$\partial_t \rho = \frac{\tau}{d} \boldsymbol{\nabla} \cdot \Big[v \boldsymbol{\nabla} (\rho v) \Big] , \tag{1.15}$$

with $\rho = \int \mathrm{d}^{d-1}\mathbf{u} f(\mathbf{r}, \mathbf{u}, t)$ is the hydrodynamic density of the swimmers.

The last equation encodes the self-trapping mechanism, since for the steady-state (with $\partial_t \rho = 0$) it predicts that $\rho \sim 1/v(\mathbf{r})$, which means that swimmers accumulate where they move slower. A sketch of the gradient expansion leading to Eq. (1.15) is given in Appendix A. It is easy to show that such outcome does not arise for a generalized passive Brownian motion with space-dependent diffusivity, because a similar coarse-graining leads to

$$\partial_t \rho = \boldsymbol{\nabla} \cdot \Big[D(\mathbf{r}) \boldsymbol{\nabla} \rho \Big] , \tag{1.16}$$

which returns a homogeneous steady-state concentration.

To explicitly see how the "weird" accumulation rule of active particles gives rise to phase phase separation, we have to make a further assumption about crowding-induced slowing-down of particles. Let us assume an exponential decay

$$v \sim \mathrm{e}^{\lambda \rho / 2} v_0 , \tag{1.17}$$

with λ left as a free parameter to account for different kinds of hindering mechanisms.
With this assumption, Eq. (1.15) becomes

$$\partial_t \rho = \boldsymbol{\nabla} \cdot \left[\frac{\tau v^2}{d} \left(1 - \frac{\lambda \rho}{2} \right) \boldsymbol{\nabla} \rho \right] \equiv \boldsymbol{\nabla} \cdot \Big[D_{\mathrm{eff}}(\rho) \, \boldsymbol{\nabla} \rho \Big] , \tag{1.18}$$

which is built as an extension of (1.16), but with an effective diffusivity that depends on density. Most importantly, for high enough ρ, D_{eff} becomes negative, signalling an instability in the density field, which leads to macroscopic phase separation between a low-density gaseous phase and highly packed clusters.

Hence, MIPS has been shown to be triggered by such positive feedback mechanism, totally driven by self-propulsion, according to which active particle accumulate where they go slower and they slow down due to crowding, resulting in a macroscopic condensation. This general phenomenon has been shown to hold for a large class of self-propelled particles, which also includes, importantly for our purposes, also the so-called *Active Brownian* (AB) *Particles* models, first proposed by Fily & Marchetti [FM12].

We introduce the simple AB model for spherical particles in two dimensions, in order to present another important result coming from a kinetic approach, that we will also use in the following Chapters to find important features related to activity.
The AB particles model is a mesoscopic particle-based model. It considers a collection of interacting Brownian objects, thus coupled with the surrounding medium through stochastic effective interactions. The microscopic mechanisms for self-driven motion are not manifestly treated in ABP models, and only an effective self-propulsion is taken, which results in a directional persistency in the motion. Being ABP model the only one adopted in our work, we just introduce it for the proposes of this discussion and will describe it in many details for the two type of particles considered: isotropic disks will be extensively characterized in Chapter 3, while rigid dimers, named *dumbbells* will be presented in Chapter 5.

A system of N interacting circular ABPs of diameter σ, without alignment, on a surface S satisfy the following equations of motion:

$$\dot{\mathbf{r}}_i = -\frac{1}{\gamma}\boldsymbol{\nabla} U(\{\mathbf{r}_i\}) + v_{\text{p}}\hat{\boldsymbol{\nu}}_i + \sqrt{2D}\,\boldsymbol{\eta}_i^{\text{T}}\,, \qquad \dot{\theta}_i = \sqrt{2D_{\text{r}}}\,\eta_i^{\text{R}}\,, \tag{1.19}$$

where $\{\mathbf{r}_i,\theta_i\}$ are the positions and the self-propulsion directions of the particles, γ the friction coefficient, U the inter-particle potential, v_{p} the magnitude of self-propulsion, $\hat{\boldsymbol{\nu}}_i = (\cos\theta_i, \sin\theta_i)$ the self-propulsion direction and η_i zero mean and unit variance Gaussian white independent noises. Fluctuation-dissipation relation holds true in the passive limit as $D = k_B T/\gamma$, and $D_{\text{r}} = 3D/\sigma^2$.

Once we have described the self-trapping mechanism triggering MIPS, we want to outline some of its basic features. Most importantly, we want

to catch its dependence on the global parameters of the model. This fundamental analysis can be carried out by means of another kinetic approach. Redner *et al.* introduced such technique based on a balancing between the inward flux of particles from the gaseous phase to the dense cluster and the outward flux of particles leaving the aggregate [RHB13, RBH13]. The two relevant parameters of the model are the surface fraction $\phi = N\pi\sigma^2/4S$ and the Péclet number $\mathrm{Pe} = v_\mathrm{p}\sigma/D$ (we will explain much more in depth the meaning of such non-dimensional parameter, later in Chapter 3).

The model deals with one large close-packed cluster coexisting with a dilute gas, assumed to be homogeneous and isotropic. Since the equation for self-propulsion direction is autonomous, particle are free to diffuse in the angular variable, regardless they are in the dense or in loose phase. Particles in the interior of the cluster are strongly caged, while the ones on the surface are able to leave the aggregate, towards the gaseous phase.

We want first of all to compute the condensation rate. Assuming a flat boundary between the two phases, the flux of gaseous particles in the direction $\hat{\boldsymbol{\nu}}$, across a plane parallel to the boundary, is $\frac{1}{2\pi}\rho_g v_\mathrm{p}(\hat{\boldsymbol{\nu}}\cdot\hat{\boldsymbol{n}})$, being ρ_g the homogeneous number density in the gas and $\hat{\boldsymbol{n}}$ the normal versor to the surface, oriented towards the exterior of the aggregate. Assuming further that each particle hitting the cluster is trapped, a simple integration over angles of the product $(\hat{\boldsymbol{\nu}}\cdot\hat{\boldsymbol{n}})$ gives the condensation rate

$$k_\mathrm{in} = \frac{\rho_g v_\mathrm{p}}{\pi} \,. \tag{1.20}$$

For a particle to escape from the cluster, the effective propulsion force along the outward normal has to exceed a maximum pulling force F_max (*e.g.* attraction between particles or hindering due to packing inside the cluster), which depends on the details of the model, and thus we let as a fitting parameter. We can easily recast balancing between the two forces, into a minimum escape angle $\alpha = \pi - \cos^{-1}\!\left(F_\mathrm{max}/\gamma v_\mathrm{p}\right)$.
Evaporation rate is found by solving the diffusion equation for the variable θ, with absorbing boundaries:

$$\frac{\partial P(\theta,t)}{\partial t} = D_\mathrm{r}\frac{\partial^2 P(\theta,t)}{\partial\theta^2} \,, \qquad P(\pm\alpha,t) = 0 \,, \tag{1.21}$$

for some initial probability distribution functions $P(\theta,0)$. A general solution for this class of boundary problems, is given in term of the following expansion (see the textbook of Redner [Red01] for a general treatment):

$$P(\theta,t) = \sum_{q=1}^{\infty} A_q \cos\!\left(\frac{q\pi\theta}{2\alpha}\right)\mathrm{e}^{-D_\mathrm{r}\frac{q^2\pi^2}{4\alpha^2}t} \,. \tag{1.22}$$

The flux of particles escaping from the cluster is thus given by

$$k_{\text{out}} = -\frac{1}{\sigma}\frac{\partial}{\partial t}\int_{-\alpha}^{\alpha} P(\theta, t)\mathrm{d}\theta|_{t=0} \,. \tag{1.23}$$

To infer the properties of the steady state, we can discard all the terms in the expansion (1.22), which are rapidly decaying in time, but the first. We can thus easily compute the integral in (1.23), given a normalization condition for P, obtaining

$$k_{\text{out}} = \frac{D_r \pi^2 \lambda}{4\sigma\alpha^2} \,, \tag{1.24}$$

with λ another fitting parameter, which accounts for effects not included in this simple description, such as non-flatness of the boundary, non-perfects close-packing of particles inside the cluster, *etc.*

A balance between the rates, $k_{\text{in}} = k_{\text{out}}$, easily allows to obtain a parametric function for the surface of cluster formation in the (Pe $-$ ϕ) space:

$$f = \frac{16\phi\alpha^2 \text{Pe} - 3\pi^4\lambda}{16\phi\alpha^2 \text{Pe} - 6\sqrt{3}\pi^3\phi\lambda} \,, \tag{1.25}$$

which agrees with the results from simulations, and also accounts for interesting feature, like re-entrant phase behavior in presence of attractive inter-particle interactions [RHB13, RBH13].

1.2 Ordered phases in 2D and recent challenges in out-of-equilibrium problems

Understanding the physics of melting has been one the most challenging problems for statistical mechanics. Phase transitions are commonly associated to the changing of macroscopic physical properties of matter, as a result of the variation of global parameters, such as temperature, pressure or density. Useful ways to distinguish between two phases with distinct thermodynamic behavior are often related to experiencing their response to external stresses. Many response functions, such as mechanical compressibility or shear modulus are usually greatly different for, say, high and low temperature phase. Generally, continuum elasticity theories account for the most relevant features of materials' stiffness and are able to catch the features of such responses.

Statistical mechanics provides powerful theoretical tools for recognizing thermodynamics phases, which are based on their symmetries in space. As a rule, the high temperature phase is always more symmetric than the low temperature one. In a fluid, for instance, the positions of the atoms are all equally likely, as a result of its well known disordered structure. In the language of symmetries, equal probabilities means that the fluid phase hold both continuous translational and rotational symmetry. On the other side, space periodicity in the solid phase breaks the continuous symmetries into discrete ones. From a thermodynamics point of view, the system can lower its free energy $F = E - TS$ either by introducing order, thus reducing its energy, or by establishing symmetries, increasing its entropy. The fluid can freeze into an ordered structure as soon as a loss of entropy S (that enters free energy F with a negative sign thereby leading to an increase of free energy) is overcompensated by the reduction of the internal energy E. Phase transitions are then statistically driven by the balancing between potential energy and thermal energy.

Theories aimed to universality, such as macroscopic elasticity, thermodynamics and symmetry-breaking-grounded approaches, do not account for microscopic mechanisms, reliable on the scale of the constituents of the system, which are inherently system-dependent. However, as we will see shortly in Section 1.2.2, such microscopic details are much important, and their analysis has provided in many cases the right way for a profound understanding of general relevant phenomena, like superfluid transition, topological ordering transition, Coulomb gas description.

1.2.1 Absence of 'true' order in 2D and the Mermin-Wagner theorem

Among all the thermodynamics elements affecting the phase transitions outlined above, we neglected the spatial dimensionality of the system. Pioneering arguments by Peierls [Pei] and Landau [Lan37a, Lan37b] demonstrated that, indeed, phase transitions strongly depend on that. Particularly, they argued that one- or two-dimensional systems can not crystallize into long-ranged (LR) periodic structure at non-zero temperature. Since we are interested in studying phase transitions in 2D systems, in this Section we will review the main points of these arguments, and some of the general results that came out after that, in order to collect the most important features of melting in two dimensions.

As a representative simple model of crystals, Peierls considered an array of atoms in d spatial dimensions with harmonic interactions between

nearest neighbors (this classical harmonic approximation is a very common one [AM76]). He proved that such system can not sustain crystal periodic structure over long distances under thermal fluctuations in $d \leqslant 2$.

Given that at zero temperature atoms are frozen in on the sites $\mathbf{R}_i$ of a periodic lattice, the density of the sample is

$$\rho(\mathbf{r}) = \sum_i \delta(\mathbf{r} - \mathbf{R}_i) \, . \tag{1.26}$$

Low-temperature thermal fluctuations displace the atoms from their frozen position, of small amounts $\mathbf{u}_i$. Instantaneous position of the i-th atom becomes

$$\mathbf{r}_i = \mathbf{R}_i + \mathbf{u}_i \, , \tag{1.27}$$

so that the overall stability of the crystalline structure is governed by the mean-square displacement $\langle [\mathbf{u}(\mathbf{r}) - \mathbf{u}(\mathbf{r}')]^2 \rangle$.

It is easy to show that within the harmonic approximation, the total potential energy is

$$\begin{aligned} U^{(\mathrm{harm})} &\propto \sum_{\mathbf{k}} \tilde{u}^*_{\beta,\mathbf{k}} \, \chi_{\alpha\beta\mu\nu} \, k_\mu \, k_\nu \, \tilde{u}_{\alpha,\mathbf{k}} \\ &\equiv \sum_{\mathbf{k}} \tilde{u}^*_{\beta,\mathbf{k}} \, \lambda_{\alpha\beta}(\mathbf{k}) \tilde{u}_{\alpha,\mathbf{k}} \, , \end{aligned} \tag{1.28}$$

where $\tilde{\mathbf{u}}_\mathbf{k}$ are the Fourier components of the displacement. The greek indices α,β,μ,ν run over the cartesian coordinates.
From canonical Gaussian probability density, a direct computation leads to the mean square fluctuations

$$\langle u_{\alpha,\mathbf{k}} u^*_{\beta,\mathbf{k}} \rangle = k_B T \, \lambda^{-1}_{\alpha\beta}(\mathbf{k}) \, , \tag{1.29}$$

where $\lambda^{-1}_{\alpha\beta}(\mathbf{k})$ are the components of the tensor inverse to $\lambda_{\alpha\beta}$.
Summing over long wavelengths, the mean square value of the displacement field is obtained:

$$\langle |\mathbf{u}|^2 \rangle \propto k_B T \int \frac{A_{\alpha\alpha}(\hat{\mathbf{k}})}{k^2} \, \mathrm{d}^d\mathbf{k} \, , \tag{1.30}$$

where the k^2 dependence of $\boldsymbol{\lambda}$ has been extracted again, with $\lambda^{-1}_{\alpha\beta}(\mathbf{k}) \equiv A_{\alpha\beta}(\hat{\mathbf{k}})/k^2$. The behavior of long wavelengths fluctuations can be inferred from the above integral. It linearly diverges in $d = 1$ and it diverges logarithmically in $d = 2$, meaning that fluctuations diverge at large distances for

$d \leqslant 2$. The integral is instead finite for $d \geqslant 3$, where thus small-temperature fluctuations are not able to destroy the crystal long-range periodicity.

Following the idea of Peierls, Mermin provided a general proof for absence of positional LR order in $d \leqslant 2$, for systems with arbitrary short-range interactions $\Phi(\mathbf{r})$ [Mer68]. The proof was based on the following criterion for crystallization. Being $\tilde{\rho}_{\mathbf{k}}$ the Fourier components of the density $\rho(\mathbf{r})$,

$$\begin{aligned} \tilde{\rho}_{\mathbf{k}} &= 0 \qquad \text{for } \mathbf{k} \text{ not a reciprocal lattice vector,} \\ \tilde{\rho}_{\mathbf{k}} &\neq 0 \qquad \text{for at least one non-zero reciprocal lattice vector,} \end{aligned} \tag{1.31}$$

in the thermodynamic limit.
Mermin demonstrated that the condition above can not be fulfilled in $d \leqslant 2$, because for all $\mathbf{k}$, $\tilde{\rho}_{\mathbf{k}}$ is always bounded from above by a quantity that vanishes in the thermodynamic limit.
The above result was further generalized for generic ordering transitions, with the so-called *Mermin-Wagner theorem* (MW), which states that continuous symmetries can not be spontaneously broken in $d \leqslant 2$ for system with short-range interactions, thus preventing standard phase transition for such systems at low dimensionality, according to the general considerations on symmetries given above.

Such strong theoretical constraint for phase transitions in 2D needed however to be combined with the earlier numerical simulations of particle systems in two dimensions. Indeed, the first numerical attempts in studying the structural behavior of large systems and their phase transitions was already available even before the MW theorem came out. For instance, Alder & Wainwright [AW62] performed one the first (thus probably the most famous) large-scale numerical experiment, with about 10^3 hard disks, making use of the novel Monte Carlo methods with Metropolis algorithm. Calculating the pressure of the system from collisions between atoms, they found a first-order phase transition with a co-existence region and a non-monotonic equation of state.

Because of the MW theorem, the equilibrium or version of Vicsek's algorithm described above, in which the orientation of the pointers is updated according to the rule (1.1), but they do not actually move, can never develop a true long-range ordered state in which all the $\mathbf{v}_i$'s point, on average, in the same direction, since such a state breaks a continuous symmetry, namely rotation invariance.
Yet the moving flock evidently has no difficulty in doing so. As Vicsek's simulation shows, even two-dimensional flocks with rotationally invariant dynamics, short-ranged interactions, and noise—i.e., seemingly all of

the ingredients of the Mermin-Wagner theorem—do move with a nonzero macroscopic velocity, which requires breaking rotation invariance, in apparent violation of the theorem.
Actually, Vicsek's model has a fundamental additional ingredient: the self-sustained motion. Vicsek's moving pointers do not truly violate MW theorem because they are self-propelled from non-thermal sources [TT95]. Though, it is of crucial relevance to understand how this happens in more details. We present in Appendix B an interesting argument towards this purpose, taken from [Ton18]. This particular ability of active systems of overcoming MW theorem to establish long-range order even in 2D is certainly one of the central theoretical grounds for our work, which indeed deals with ordered phases for self-propelled particles.

1.2.2 Basic notions of KTHNY theory of melting

Alongside its argument that forbids standard crystallization in 2D materials, Mermin also proposed a possibility for ordering in 2D, which is allowed within its results. He actually observed for the first time the bond-orientational order can be a true-long-ranged one, even in $d \leqslant 2$. If $\mathbf{a}_1$ is one of the two base vectors of the crystal lattice, bond-directional order is controlled by the quantity

$$\langle [\mathbf{r}(\mathbf{R} + \mathbf{a}_1) - \mathbf{r}(\mathbf{R})] \cdot [\mathbf{r}(\mathbf{R}' + \mathbf{a}_1) - \mathbf{r}(\mathbf{R}')] \rangle \,. \tag{1.32}$$

At zero temperature it would be equal to a_1^2, for all length scales.
At finite temperature, fluctuations are not able in general to destroy such correlation, which thus could remain finite over large distances, with $|\mathbf{R} - \mathbf{R}'| \to \infty$.

Halperin & Nelson exploited this idea to build their theory of melting in 2D particle systems [HN78, Nel78, NH79]. The details of such theory will be presented with much accuracy in Chapter 2, because they are profoundly useful for our purposes. We only outline here the basic concepts, to shortly introduce the review to this argument.
The fundamental basis of melting in 2D concerns noting that, even if a true-long-ranged order is absent in 2D arrays of atoms, for low enough temperature they are still able to resist to shear stress in the same way as true solids do. Such ability comes from the weak logarithmic divergence of fluctuations in 2D, as obtained from Eq. 1.30, that leads to an algebraic decay of position correlation functions. Systems with algebraically decaying correlation functions are called *quasi-long-range* (QLR) ordered. 1D systems does not maintain the same behavior, since long wavelength fluctuations grow linearly with the system size.

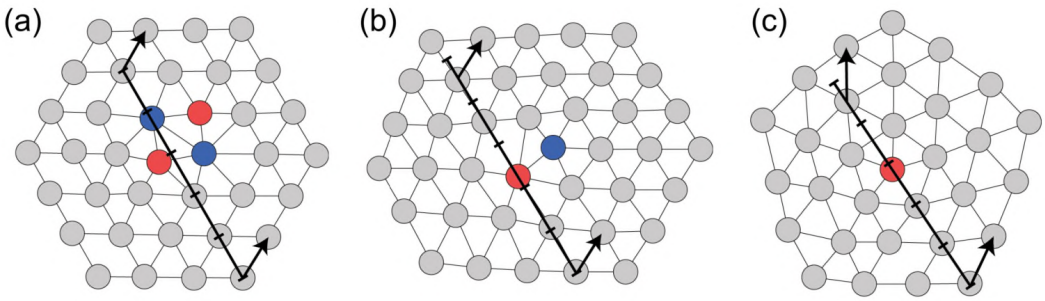

Figure 1.3: Schematic summary of melting transition in a 2D particle system, as predicted by Halperin & Nelson. Temperature increases from left to right. (a) Dislocation pairs in the low-temperature phase do not interfere with QLR translational order and LR bond-orientational order (see that both the two periodicities are preserved over short distances around the defect core). (b) Free dislocations destroy translational periodicity, but the orientational one is retained. (c) The presence of free disclinations is not compatible with any kind of order, thus their appearance drives the system into the isotropic liquid phase. Figure adapted from [TAA+18].

Relying on this properties and following the insightfully results of Berezinskii, Kosterlitz and Thouless on melting in 2D planar spin models, Halperin and Nelson argued that melting of QLR ordered phases can proceed through a mechanism of unbinding of topological defects. According to their theory, the low-temperature phase with QLR translational ordered can host dislocation pairs. Such pairs dissociate at given non-zero temperature breaking translational order. It easy reasonably easy to make this picture evident from a simple energetic argument. Within the continuum elasticity framework, it can be be shown that the energy of a free dislocation in a 2D triangular lattice sample of area A (see for instance [Fri64] or [Nab67]) is

$$E = \frac{K}{16\pi} \ln\left(\frac{A}{a^2}\right), \tag{1.33}$$

with K proportional to the translational stiffness and a^2 the linear size of the dislocation core. Since there are approximately A/a^2 possible locations for the dislocation, its entropy scales as

$$S = k_B \ln\left(\frac{A}{a^2}\right). \tag{1.34}$$

with the sample's size. Thus, at low temperature free dislocation are not allowed for energetic reasons. Increasing the temperature leads to negative Helmholtz free energy, corresponding to proliferation of free dislocations at the critical point

$$k_B T_c = \frac{K}{16\pi}. \tag{1.35}$$

At higher temperature, elastic stiffness drops to zero and the solid lose its ability to rigidly respond to shear stresses. Accordingly to the Mermin hypothesis, this phase with short-range translational order, is still able to sustain bond-orientational QLR order. Halperin & Nelson called this phase *hexatic* and proved that it melts with a second phase transition mediated by the unbinding of dislocations into free disclinations. This resulting two-step melting is summarized in Fig. 1.3.
We will repeat in Chapter 2 some of the concepts mentioned here for clarity. However, we will treat with many more details the relation between topological defects, ordering and the mechanical properties of the sample, in order to make a full review of this fundamental theory of melting.

1.3 Summary of the work and structure of the manuscript

This manuscript concerns the characterization of the phase diagram of two different models of ABP in two spatial dimensions: the self-propelled (SP) disks model and the self-propelled dumbbells model. During the last three years we have been characterized the complete phase transition diagram of these two models, which evolve out of thermal equilibrium, in the (Pe – ϕ) parameter space. We have been performed large-scale Molecular Dynamics simulation to study significant features of these two models and to compare them as two different, though both paradigmatic, examples of motile particles.
We have been found few remarkable differences between the two phase diagrams, concerning the nature of MIPS and the way the melting scenario and the equilibrium stable phases are affected by the presence of activity. For disks a two-stage melting passive scenario with a first order phase transition between liquid and hexatic and a BKT transition between hexatic a solid is maintained up to small values of activity. All the three pure phases survive as stable phases up to very high activities. Moreover, the existence of an "active hexatic" phase and an "active solid" one plays a crucial role in recognizing the nature of the coexisting phases in MIPS.

- We will present the ABP model for disks in Chapter 3 and we will outline some of the fundamental properties of such model, in and out of thermal equilibrium. We will describe the numerical method used for the MD simulations. Referring to relevant works on phase equilibrium in active systems, we will present our understandings on the complete phase behavior of the model, which, furthermore,

reveals a strong relation between ordering and activity-driven phase separation.

The presence of separate hexatic and solid phase for AB disks suggested us to proceed further in studying the similarity of our system with its passive counterpart, with a careful characterization of out-of equilibrium transitions in terms of the population of topological defects and their large-scale behavior.

- In Chapter 4, we will present our results from such analysis. First, we will introduce the methodology that we use for pinpointing the defects from the output configurations of simulations, and how we characterize the nature of the defects. Then, we will compare the behavior of defects with the phase transition, finding remarkable confirmation of an underlying KTHN scenario and interesting novelties about the role of extended defects like grain boundaries in the melting.

For dumbbells we observe a macroscopic coexistence between hexatically ordered regions and disordered ones over a finite interval of packing fractions, for all activities. In the passive limit, this interval remains finite, as with the disks, but, differently from them, we do not find discontinuous behavior upon increasing activity from the passive limit.

- In Chapter 5, we will present our model of AB dumbbells, with many of its interesting features. We will then report the procedure used to draw up the full phase diagram for AB dumbbells. Together with the phase diagram, we will characterize in many details the macroscopic dynamics of the dense aggregates of dumbbells, with respect to the strength of the self-propulsion.

Chapter 2

The KTHNY theory of melting transitions in two dimensions

In this chapter the classical theory of melting in two spatial dimensions is going to be reviewed, trying to recap the rise of the original problem and its historical development as well as its modern revival. In fact, as it will be discussed in the last two sections of this chapter, there has been a recent breakthrough in the understanding of phase transition in 2D, mainly coming from the application of new numerical and experimental approaches to it, which has shed new interest in this old problem and that has definitely been the starting point of this PhD project, together with the aim of recasting the original questions about ordering in 2D for systems out of thermal equilibrium.

2.1 Dislocation-mediated melting in 2D

This Section is named after the famous paper by Nelson and Halperin, which traces the full theoretical understanding of the melting scenario for two-dimensional crystals [NH79], that is known as KTHNY scenario, after the scientists Kosterlitz, Thouless, Halperin, Nelson and Young who gave all the crucial contributions to the building of this theory. The main deduction which brought to the formulation of the theory was that in two dimensional systems phase transitions are driven by a process of unbinding of topological defects. The point that made this idea so important for the statistical physics community at the time is that the same defects-driven transition was found to be present in a huge class of systems of different nature which share some general properties such as: living in a two dimensional space; being characterized by an order parameter that in the disor-

dered phase has a continuous symmetry; possessing the right periodicity in order to allow for topological singularities to be excited from the ordered phase. Among others, systems which fulfill these few requirements and thus undergo the same defects-mediated phase transition are, beside 2D solids which are going to be described in all the details throughout this chapter, also planar rotor models in 2D such as the two-dimensional *XY model*, the *Coulomb gas model* or the *superfluid* ^{4}He *film*.

As already discussed in Chapter 1, different theoretical arguments raised by Mermin and Wagner [MW66, Mer68] in 1966-68 and, even before, by Peierls and Landau [Pei, Lan37a, Lan37b] had been pointed out that no spontaneously-broken symmetry mechanism can happen for systems with short-range interactions and continuous symmetries in spatial dimensions less than three, and thus no long-range ordered phase can exist for such systems at any, even small, non-zero temperature. Very shortly after these strong arguments against the existence of ordering phase transitions for such class of models, some numerical experiments had shown that, indeed, ordered phases do exist for, e.g., a system of hard spheres in two dimensions [AW62] or 2D planar rotors [SK66]. This gap between theory and experiments had remained answered for years, until Berezinskii [Ber71, Ber72] and, independently, Kosterlitz and Thouless [KT73, Kos74] formulated their theory of vortices-unbinding-mediated phase transition for 2D planar rotor and of dislocation-unbinding-mediated melting for 2D crystals.

They argued that for all the kinds of systems mentioned above there is a phase transition between a so-called *quasi-long-range* ordered (QLRO) phase (see in the Chapter 1 all the properties of this kind of order that is typical of systems in $d = 2$) and a disordered phase, that is driven by the excitation of singularities of the order parameter. Regarding 2D crystals, KT stated that the excitation of isolated dislocations is responsible for driving the system from a low-temperature crystal with quasi-long ranged translational order to a high-temperature isotropic liquid.

After the insights of KT, Halperin and Nelson and Young [Nel78, HN78, NH79, You79] realized that dislocation unbinding at a temperature $T = T_m$ does not melt the 2D crystal into an isotropic liquid. For $T > T_m$, although the system loses translational order as correctly established by KT, a QLRO orientational order survives. Due to the six-fold symmetry of this residual orientational order, this anisotropic fluid phase is called *hexatic*. At $T_i > T_m$ another phase transition of KT type with unbinding of topological *disclinations* drives the hexatic phase to melt into a true isotropic liquid with no positional and no orientational order. In Fig. 2.1 a summary schematic picture of Halperin-Nelson result is shown, which includes a

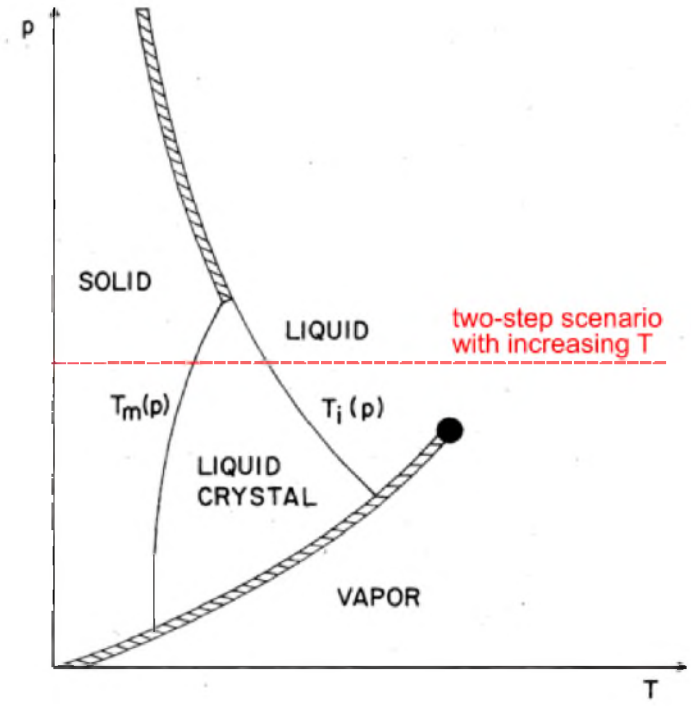

Figure 2.1: Sketch of the emergence of a liquid-crystal (hexatic) phase in the Halperin-Nelson picture of phase transition, in the pressure-temperature phase diagram. Solid-hexatic melting at T_m and hexatic-liquid one at T_i are shown as continuous KT transitions, while hatched lines indicate first-order transitions. The red dashed line indicates the possible two-step melting scenario, as described in the text. Figure adapted from [NH79].

possible two-step melting scenario, as described above.

Within this Section the theory of double-step melting is going to be presented with many details. The description will start with a short introduction to the classical elasticity theory for 2D systems, useful to describe the presence of different kind of defects throughout the system. Then the two transitions will be described using the renormalization group analysis devised by HN, and all the relevant properties of the thermodynamic phases involved will be inferred.

2.1.1 Elastic theory and dislocations in 2D systems

Some basic concepts of classical elasticity theory will be shortly presented here with the aim to introduce the theoretical background useful for the understanding of the BKTHNY picture for the phase transition scenario in 2D crystals. All the notions presented are much more extensively and

detailed reviewed in [LLKP86, CC95].

Since the purpose of this preamble is just to introduce the useful things for the Halperin-Nelson theory of melting, only 2D hexagonal crystal is going to be considered. Such hexagonal crystal is constituted of atoms placed in the positions $\mathbf{r}_i = \mathbf{R}_i + \mathbf{u}_i$, where $\mathbf{R}_i = n_{1i}\mathbf{a}_1 + n_{2i}\mathbf{a}_2$, with n_{1i} and n_{2i} are integers and $\mathbf{a}_1$, $\mathbf{a}_2$ are the two vectors of the triangular lattice base, while $\mathbf{u}$ is the displacement vector field that takes into account the thermal fluctuations of the position of the atoms from the underlying lattice. In the context of classical elasticity theory, the 2D hexagonal lattice is known to be fully characterized by only two independent elastic constant, λ and μ that are called *Lamé coefficients*. The elastic free energy density is

$$f_{el} = \frac{\lambda}{2} u_{ii} u_{jj} + \mu u_{ij} u_{ij} \,, \tag{2.1}$$

where $u_{ij} = (\partial_i u_j + \partial_j u_i)/2$ is the symmetric part of the so-called *strain tensor* derived as usual from the displacement field $\mathbf{u}$. Explicit relation between Lamé coefficients and the physical behavior of the body is obtained by decomposing the strain tensor u_{ij} into a scalar $\delta_{ij} u_{kk}/2$ and a symmetric traceless tensor $u_{ij} - \delta_{ij} u_{kk}/2$, so that Eq. (2.1) becomes

$$f_{el} = \frac{B}{2} u_{ii}^2 + \mu \Big(u_{ij} + \frac{1}{2} \delta_{ij} u_{kk} \Big)^2 \,, \tag{2.2}$$

with $B = \lambda + \mu$. It is easy to show that the first term in this recast equation represents the contribution to the free elastic energy due to pure area changes only, while the second term quantifies the free elastic energy related to deformations with constant area. Thus, B and μ are called respectively *bulk modulus* and *shear modulus*.

Another quantity that will be shown to be crucial in the treatment of our problem is the so-called *Young's modulus* and it will be denoted as K. This quantity is defined as the coupling between an uniaxial tension and the strain along the same direction. Defining the *stress tensor* as usual by

$$\sigma_{ij} = \frac{\partial f_{el}}{\partial u_{ij}} = B u_{kk} \delta_{ij} + 2\mu \Big(u_{ij} - \frac{1}{2} \delta_{ij} u_{kk} \Big) \,, \tag{2.3}$$

and inverting the relation as follows

$$u_{ij} = \frac{1}{4B} \sigma_{kk} \delta_{ij} + \frac{1}{2\mu} \Big(\sigma_{ij} - \frac{1}{2} \delta_{ij} \sigma_{kk} \Big) \,, \tag{2.4}$$

the strain that results from applying a force f_y along the y-direction is

$$\begin{aligned} u_{xx} &= \left(\frac{1}{4B} - \frac{1}{4\mu}\right) T \\ u_{yy} &= \left(\frac{1}{4B} + \frac{1}{4\mu}\right) T \\ u_{xy} &= 0\,, \quad u_{yx} = 0\,, \end{aligned} \tag{2.5}$$

being T the force per unit length so as $f_y = Tdl$, and thus $\sigma_{ij} = T\delta_{iy}\delta_{jy}$. From these relations, given by the definition above that $T = Ku_{yy}$, is easy to obtain the form of the Young's modulus

$$K = \left(\frac{1}{4B} + \frac{1}{4\mu}\right)^{-1} = \frac{4\mu\,(\lambda + \mu)}{\lambda + 2\mu}\,. \tag{2.6}$$

Dislocations in the 2D hexagonal lattice

According to the classical theory of defects in crystals, a dislocation is, as suggested by its name, a topological defect that arises, restricting the description to lattices in two dimensions, from the sliding of two lattice lines between each other, or rather from the insertion of half lattice lines into the perfect underlying lattice. To be more specific, because of the six-fold lattice symmetry of planar triangular lattice, the only case of interest for this analysis, an isolated dislocation is the topological effect of inserting two half lattice lines as shown in Fig. 2.2.

The configuration that results from this procedure can not be brought back to the initial perfect lattice by any continuous deformation, due to topological reasons. The only way to restore the perfect original periodic structure is to cut the crystal and then relax back the positions of its sites along the cut. This procedure, called *Volterra cut* [CC95], is shown in Fig. 2.2: cutting the crystal along the thick hatched line and then rigidly displacing the lattice on one side of the cut by the vector **b**, so as to let the sites pairs A and A′, B and B′, C and C′, *etc.* to become next neighbors again, the perfect triangular array is restored. The vector **b** is called *Burgers vector* and it represents the topological charge of the dislocation. A way to define the Burgers vector directly from the distorted lattice is also shown in Fig. 2.2: a path along the lattice bonds that would be a close circuit in the perfect lattice fails to close if it circles a dislocation; the missing amount for the path to be closed is the Burgers vector.

Beginning to build up the HN theory, it is crucial to outline the description of dislocations in terms of the elasticity theory. The definition of the

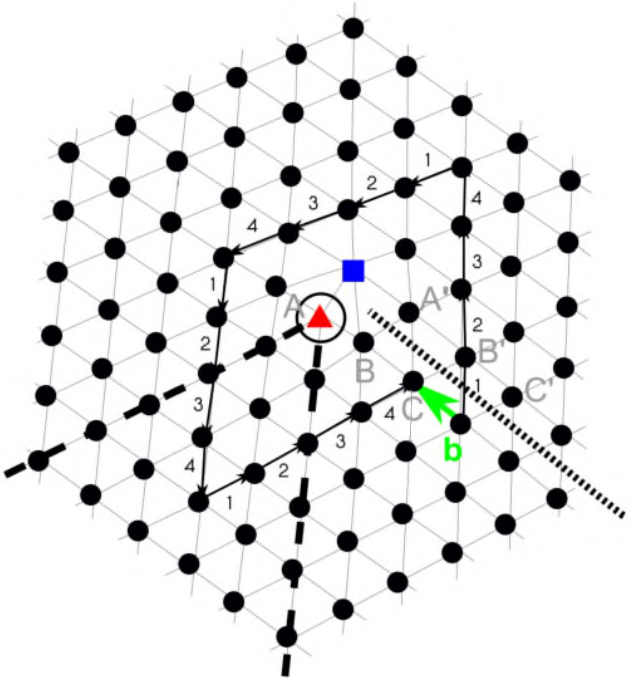

Figure 2.2: Single dislocation in on a triangular lattice. Black circles are the six-fold lattice sites. Dislocation correspond to the 5-fold (red triangle) and 7-fold (blue square) pair. The two inserted lines are shown with thick dashed lines; they both end into the 5-fold site. Black hatched line is the Volterra cut (see text) needed to relax the system back to a perfect lattice. The green vector is the Burgers vector, which is the vector needed to close the contour around the defect, shown with the small numbered arrows. Figure adapted from [vGKM14].

dislocation charge by means of the Burgers vector is easily translated in the language of crystals' deformations as

$$\oint \mathrm{d}\mathbf{u} = a_0 \mathbf{b}(\mathbf{r}), \tag{2.7}$$

where a_0 is the lattice spacing and $\mathbf{b}$ is the dimensionless Burgers vector associated to a dislocation at $\mathbf{r}$. Given that in equilibrium the internal forces $f_i = \partial_i \sigma_{ij}$ on a area element must be zero, from Eq. (2.3), equilibrium condition for the displacement field reads

$$\lambda \frac{\partial u_{kk}}{\partial x_i} + 2\mu \frac{\partial u_{ij}}{\partial x_j} = 0 \quad i = x, y. \tag{2.8}$$

It can be shown that a solution for (2.8) compatible with the constraint (2.7) for a dislocation in the origin with Burgers vector $\mathbf{b} = b\hat{x}$ is the

following:

$$\begin{aligned} u_x &= \frac{ba_0}{2\pi}\left(\phi + \frac{K}{8\mu}\sin 2\phi\right) \\ u_y &= -\frac{ba_0}{2\pi}\left(\frac{\mu}{\lambda+2\mu}\ln r + \frac{K}{8\mu}\cos 2\phi\right) \end{aligned} \tag{2.9}$$

being (r, ϕ) the cylindrical coordinates. Calculating the stress tensor from Eq. (2.3), the elastic energy is given by

$$E_{el} = \frac{1}{2}\int \mathrm{d}^2\mathbf{r}\sigma_{ij}u_{ij}\,, \tag{2.10}$$

and thus the total energy associated to a single dislocation is

$$E = E_{el} + E_c = \frac{a_0^2 b^2 K}{8\pi}\ln\frac{R}{a} + E_c\,, \tag{2.11}$$

where from the integral in (2.10), the contribution E_c of the defect core of size a is finite and it has been set apart, and R is the size of the sample. The total energy of a single dislocation is thus divergent with the size of the system.

The same calculation with two constraints of the type in (2.7) for two dislocations $\mathbf{b}$ and $-\mathbf{b}$ of the same core size a and $\mathbf{d}$ apart from each other, gives

$$E = \frac{a_0^2 b^2 K}{4\pi}\ln\frac{d}{a} - \frac{a_0^2 K}{4\pi}\frac{(\mathbf{b}\cdot\mathbf{d})^2}{d^2} + 2E_c\,. \tag{2.12}$$

This result is the first notable one with respect to the melting theory, because it shows that the energy of a configuration of two dislocations with opposite charges does not have a logarithmic divergence as for the single defect case. This means that the a dislocation pair can be thermally excited at finite temperature. Moreover, Eq. (2.12) also points out that, after having created a dislocation pairs, a further energy supply (that grows logarithmically with the distance) can move the two dislocations away from each other eventually also leading, in the limit of $d \gg a$, to a configuration with two isolated dislocations. The same arguments can be applied to the general case of a arbitrarly complicated group of more than two dislocations with zero total Burgers vector $\sum \mathbf{b}_i = 0$. The mechanism (with no energy divergences) of dislocation unbinding is sketched in Fig. 2.3 where it is shown on the left how, with continuous displacements, a dislocation pair is excited and, again by means of a continuous deformation of the lattice, the two defects dissociate.

The results summarized in this subsection are the basis of the argument built by Halperin and Nelson, that will be discussed below.

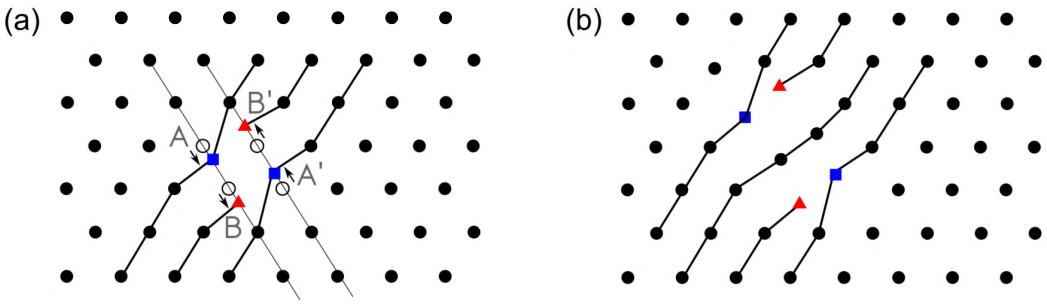

Figure 2.3: A sketch of the mechanism, described in the text, of formation of a dislocation pair from a perfect lattice with continuous displacements of the atoms. 6-fold particles are shown in black, red triangles are 5-fold and blue squares are 7-fold. Figure adapted from [vGKM14].

2.1.2 Renormalization group analysis of the dislocation-unbinding process

Before starting to go through the details of Halperin-Nelson theory, it is useful to show that the central idea of melting in 2D can be actually grasped by looking again at the details of Eq. (2.12), that has been discussed qualitatively before. Neglecting for the moment the second angular term, a logarithmic attraction between two dislocations of opposite Burgers vector results:

$$\beta v(r) = \frac{\beta K a_0^2}{4\pi} \ln \frac{r}{a}, \tag{2.13}$$

where, again, K is the Young's modulus, a_0 the lattice spacing, a the size of the dislocations' core and r their distance. Remembering from the previous section that the Halperin-Nelson transition is driven by unbinding of dislocations, a first estimation of the melting temperature comes from requiring that the average separation between dislocation pairs diverges. From

$$\langle r^2 \rangle = \frac{\int \mathrm{d}^2\mathbf{r} r^2 e^{-\beta v(r)}}{\int \mathrm{d}^2\mathbf{r} e^{-\beta v(r)}} = \frac{8\pi - \beta K a_0^2}{16\pi - \beta K a_0^2} a^2, \tag{2.14}$$

one obtains that

$$\lim_{T \to T_m^-} \frac{K(T) a_0^2}{k_B T} = 16\pi. \tag{2.15}$$

Although this results will be formally derived later, Eq. (2.15) introduces the idea of Halperin-Nelson renormalization group approach, as will be reviewed in this Section. As the temperature approaches T_m , the crystal is soft enough, and $K(T)/T$ is small enough, to allow the dislocations to unbind and the system to melt. However, since the Young's modulus $K(T)$,

as well as all the elastic constants, are affected by both the temperature and the presence of the defects itself, recursive relations that iteratively renormalize the elastic constants are needed to extract the true behavior of the system.

Thus, the first step to implement the renormalization group procedure is to separate the thermal contributions from the singular ones, due to the presence of the defects in the elastic description of the crystal. According to this plan, the strain tensor can be separated into

$$u_{ij}(\mathbf{r}) = \phi_{ij}(\mathbf{r}) + u_{ij}^{sing}(\mathbf{r}) \,, \tag{2.16}$$

where, as said, $\phi_{ij}(\mathbf{r})$ is a smoothly varying part to the strain due only to thermal effects, while $u_{ij}^{\text{sing}}(\mathbf{r})$ is the contribution to the strain that comes from the presence of the singularities that correspond to topological defects. Accordingly, the full Hamiltonian of the system is written as

$$H = H_0 + H_D \,. \tag{2.17}$$

The purpose of this calculation is to renormalize the elastic constants $\lambda \to \lambda_R$ and $\mu \to \mu_R$, so as to replace the Hamiltonian $H_0(\lambda, \mu) + H_D$ with a renormalized Hamiltonian $H_0(\lambda_R, \mu_R)$ where the effect of the defects is absorbed into the elastic constants.

Therefore, it is needed to calculate the singular part of the strain tensor and, accordingly, the full Hamiltonian in (2.17). Following the treatment in [LLKP86], it can be shown that

$$u_{ij}^{(sing)} = \left(\frac{1}{2\mu} \epsilon_{ik}\epsilon_{jl} \frac{\partial^2}{\partial r_k \partial r_l} - \frac{\lambda}{4\mu(\lambda+\mu)} \delta_{ij} \nabla^2 \right) a_0 \int \mathrm{d}^2\mathbf{r}' \; b_m(\mathbf{r}') G_m(\mathbf{r}, \mathbf{r}') \,, \tag{2.18}$$

where ϵ_{ij} are the elements of the antisymmetric matrix

$$\boldsymbol{\epsilon} = \begin{bmatrix} 0 & 1 \\ -1 & 0 \end{bmatrix}, \tag{2.19}$$

while $G_m(\mathbf{r}, \mathbf{r}')$ is called *Green's function* because it allows to determine the displacement produced in the medium by a local stress concentrated at $\mathbf{r}'$. It is thus needed in this context to calculate the singular contribution to the strain from the stress produced by all the defects in the system. For $|\mathbf{r} - \mathbf{r}'| \gg a_0$, it takes the form

$$G_m(\mathbf{r}, \mathbf{r}') \simeq G_m(\mathbf{r} - \mathbf{r}') = -\left(\frac{K}{4\pi}\right) \epsilon_{mn}(r_n - r_n') \left[\ln\left(\frac{|\mathbf{r} - \mathbf{r}'|}{a} \right) + C \right], \tag{2.20}$$

with C a positive constant that depends on the lattice structure. Since, from (2.1), the Hamiltonian for the defects-free system has the form

$$H = \frac{1}{2}\int \mathrm{d}^2\mathbf{r}\left(\lambda u_{ii}^2 + 2\mu u_{ij}u_{ij}\right), \tag{2.21}$$

inserting the decomposition (2.16) into it and making use of the form (2.18) for u_{ij}^{sing}, the full Hamiltonian results

$$\begin{aligned} H =& \frac{1}{2}\int \mathrm{d}^2\mathbf{r}\left(\lambda\phi_{ii}^2 + 2\mu\phi_{ij}\phi_{ij}\right) \\ &- \frac{a_0^2 K}{8\pi}\sum_{\alpha\neq\alpha'}\left[\mathbf{b}(\mathbf{r}_\alpha)\cdot\mathbf{b}(\mathbf{r}_{\alpha'})\ln\frac{R_{\alpha,\alpha'}}{a} - \frac{[\mathbf{b}(\mathbf{r}_\alpha)\cdot\mathbf{R}_{\alpha,\alpha'}][\mathbf{b}(\mathbf{r}_{\alpha'})\cdot\mathbf{R}_{\alpha,\alpha'}]}{R_{\alpha,\alpha'}^2}\right] \\ &+ E_c\sum_\alpha |\mathbf{b}(\mathbf{r}_\alpha)|^2 , \end{aligned} \tag{2.22}$$

where the greek indices α, α' run over the defects and $\mathbf{R}_{\alpha,\alpha'} = \mathbf{r}_\alpha - \mathbf{r}_{\alpha'}$. The last term, with $E_c = (C+1)K/8\pi$, accounts for the core energy of the defects. For this results the condition of zero global Burgers vector is needed

$$\sum_\alpha \mathbf{b}_\alpha = 0 , \tag{2.23}$$

which of course derives from the physical assumption that neutral pairs unbinding can produce isolated dislocations.

The role of the defects in altering the elastic constants can be extracted by considering the general form for the Hooke's law of Eq. (2.4)

$$u_{ij} = K_{R,ijkl}^{-1}\,\sigma_{ij} , \tag{2.24}$$

where $K_{R,ijkl}^{-1}$ is the inverse renormalized *elastic tensor* (bacause now also defects are present in the system). The bare elastic tensor is

$$K_{ijkl} = \mu(\delta_{ik}\delta_{jl} + \delta_{il}\delta_{jk}) + \lambda\delta_{ij}\delta_{kl} , \tag{2.25}$$

and its inverse is

$$K_{ijkl}^{-1} = \frac{1}{4\mu}(\delta_{ik}\delta_{jl} + \delta_{il}\delta_{jk}) - \frac{\lambda}{4\mu(\mu+\lambda)}\delta_{ij}\delta_{kl} . \tag{2.26}$$

The inverse renormalized elastic tensor can be expressed in terms of a correlation function of the strain tensor at the boundary of the sample

$$K_{R,ijkl}^{-1} = \frac{\langle U_{ij}U_{kl}\rangle}{\Omega} , \tag{2.27}$$

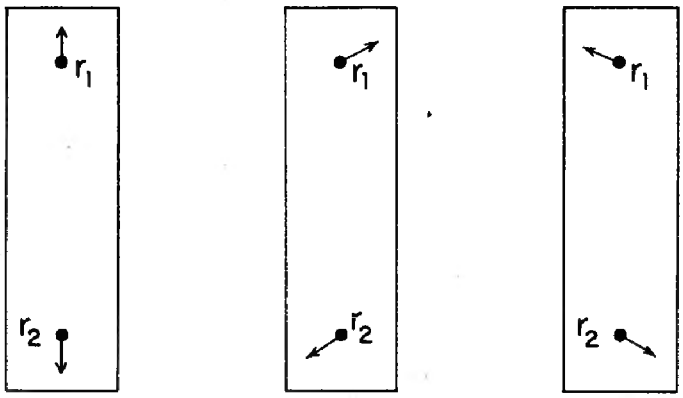

Figure 2.4: All the possibile configuration of dislocation pairs with total zoer Burgers for a triangular lattice. Figure adapted from [NH79]

with U_{ij} defined operatively as

$$U_{ij} = -\frac{1}{2}\oint_P \mathrm{d}l\,(u_i\hat{n}_j + u_j\hat{n}_i)\,, \tag{2.28}$$

where P is the boundary of the sample and $\hat{\mathbf{n}}$ is a unit vector normal to the boundary that points outwards from the sample. Using the decomposition (2.16), though it is not possible to use Green's theorem to write

$$U_{ij} = \int \mathrm{d}\mathbf{r}\, u_{ij}(\mathbf{r})\,, \tag{2.29}$$

because the singular part of the strain is indeed singular near the defects, it is not hard to see that

$$U_{ij} = \int \mathrm{d}\mathbf{r}\phi_{ij}(\mathbf{r}) + U_{ij}^{(sing)}\,, \tag{2.30}$$

with

$$U_{ij}^{(sing)} = \frac{1}{2}\sum_\alpha \left[b_i(\mathbf{r}_\alpha)\epsilon_{jk}r_{\alpha,k} + b_j(\mathbf{r}_\alpha)\epsilon_{ik}r_{\alpha,k}\right], \tag{2.31}$$

and thus

$$K^{-1}_{R,ijkl} = K^{-1}_{ijkl} + \frac{\langle U_{ij}^{(sing)}U_{kl}^{(sing)}\rangle}{\Omega}. \tag{2.32}$$

Since, as already clarified, dislocations appear in pairs with opposite Burgers vectors and that only three different pair configurations are compatible with the triangular lattice considered, as shown in Fig. 2.4, it is easy

obtained, being the Hamiltonian the one in (2.22),

$$K^{-1}_{R,ijkl} = K^{-1}_{ijkl} + \frac{1}{4}y^2 \sum_{p=1}^{3} \left(b_{p,i}\epsilon_{jm} + b_{p,j}\epsilon_{im}\right)\left(b_{p,k}\epsilon_{ln} + b_{p,l}\epsilon_{kn}\right) \times \int_{R>a} \frac{\mathrm{d}^2\mathbf{R}}{a^2}\,\frac{R_m R_n}{a^2}\,A_p \left(\frac{R}{a}\right)^{-\beta K a_0^2/4\pi}, \tag{2.33}$$

with

$$\begin{aligned} \mathbf{b}_1 &= \begin{bmatrix} 0 \\ 1 \end{bmatrix}, \quad \mathbf{b}_2 = \begin{bmatrix} \sqrt{3}/2 \\ 1/2 \end{bmatrix}, \quad \mathbf{b}_3 = \begin{bmatrix} -\sqrt{3}/2 \\ 1/2 \end{bmatrix}; \\ A_1 &= e^{(\beta K a_0^2/4\pi)\cos^2\theta}, \\ A_2 &= e^{(\beta K a_0^2/4\pi)\cos^2(\theta - 2\pi/3)}, \\ A_1 &= e^{(\beta K a_0^2/4\pi)\cos^2(\theta + 2\pi/3)}, \end{aligned} \tag{2.34}$$

where $\mathbf{R}$ is the vector between the two paired dislocations, θ is the angle between this vector and the Burgers vector of the pair, and where the so-called *dislocation fugacity* y is defined as

$$y = e^{-\beta E_c}\,. \tag{2.35}$$

Eq. (2.33) is correct up to $O(y^3)$ because only interactions between single dislocations within a pair have been taken into account.

As seen in (2.15), it is useful to build Halperin-Nelson recursive relations for the renormalized Young's modulus K_R, or actually for its inverse

$$K_R^{-1} \equiv K^{-1}_{R,xxxx} = K^{-1}_{R,yyyy}\,. \tag{2.36}$$

Assuming that $K^{-1}_{R,ijkl}$ has the isotropic form (2.26), but with renormalized Lamé coefficients λ_R and μ_R, is easy to obtain:

$$\begin{aligned} K_R^{-1} &= \frac{1}{4}\left[\frac{1}{\mu_R} + \frac{1}{(\mu_R + \lambda_R)}\right] \\ &= K^{-1} + \frac{3}{4}\pi y^2 \left(\frac{1}{2\pi}\int_0^{2\pi} \mathrm{d}\theta\, e^{(\beta K a_0^2/4\pi)\cos^2\theta}\right)\int_a^\infty \frac{\mathrm{d}R}{a}\left(\frac{R}{a}\right)^{3-\beta K a_0^2/4\pi} \\ &\quad + \frac{3}{2}\pi y^2 \left(\frac{1}{2\pi}\int_0^{2\pi} \mathrm{d}\theta\, \sin^2\theta\, e^{(\beta K a_0^2/4\pi)\cos^2\theta}\right)\int_a^\infty \frac{\mathrm{d}R}{a}\left(\frac{R}{a}\right)^{3-\beta K a_0^2/4\pi}. \end{aligned} \tag{2.37}$$

As expected, the integrals diverge as $\beta K a_0^2$ approaches 16π. These divergences are recursively isolated by breaking the integral as

$$\int_a^\infty \to \int_a^{ae^{\delta l}} + \int_{ae^{\delta l}}^\infty \tag{2.38}$$

with δl small.
Absorbing the large R integral into the renormalized elastic constants and rescaling the cutoff parameter as

$$ae^{\delta l} \to a\,, \tag{2.39}$$

the same form of Eq. (2.37) is obtained for a rescaled inverse Young's modulus $(K')^{-1}$ if the rescaling factors are instead absorbed into a redefinition of the fugacity y.
Applying this procedure, the following coupled recursive relations result:

$$\begin{aligned}
\frac{\mathrm{d}K^{-1}(l)}{\mathrm{d}l} &= \frac{3}{2}\pi y^2(l)\, e^{\beta K a_0^2/8\pi}\, I_0\!\left(\frac{K(l)}{8\pi}\right) \\
&\quad - \frac{3}{4}\pi y^2(l)\, e^{\beta K a_0^2/8\pi}\, I_1\!\left(\frac{K(l)}{8\pi}\right) + O(y^3), \\
\frac{\mathrm{d}y(l)}{\mathrm{d}l} &= \left(2 + \frac{K(l)}{8\pi}\right) y(l) \\
&\quad + 2\pi y^2(l)\, e^{\beta K a_0^2/16\pi}\, I_0\!\left(\frac{K(l)}{8\pi}\right) + O(y^3),
\end{aligned} \tag{2.40}$$

where I_0 and I_1 are modified Bessel functions.
The two previous renormalization-group equations represent a powerful tool devised by Halperin and Nelson (applying the general idea of Kosterlitz, Thouless and Berezinskii) to treat the problem of the dislocation-unbinding mechanism in a two-dimensional elastic material and derive its phase transition behavior.
Since they have been derived assuming the invariance of the elastic tensor, the renormalized elastic constants can be evaluated using:

$$\begin{aligned}
\mu_R(\mu, \lambda, y) &= \mu_R(\mu(l), \lambda(l), y(l))\,, \\
\lambda_R(\mu, \lambda, y) &= \lambda_R(\mu(l), \lambda(l), y(l))\,, \\
K_R(K, y) &= K_R(K(l), y(l))\,.
\end{aligned} \tag{2.41}$$

Figure 2.5 shows schematically the renormalization-group flows of the two coupled variables (K, y). Above a certain temperature T_m, the fugacity increases as l increases. Both $y(l)$ and $K^{-1}(l)$ flow to ∞, indicating that the dislocations unbind and the crystal is melted.
Below the melting temperature T_m, the fugacity y_R flows to zero and thus the Young's modulus K_R, as well as the elastic constants μ and λ, converges to a finite values, as one would expect for the elastic constants in the solid phase. Between these two regions, on the separatrix that determines the

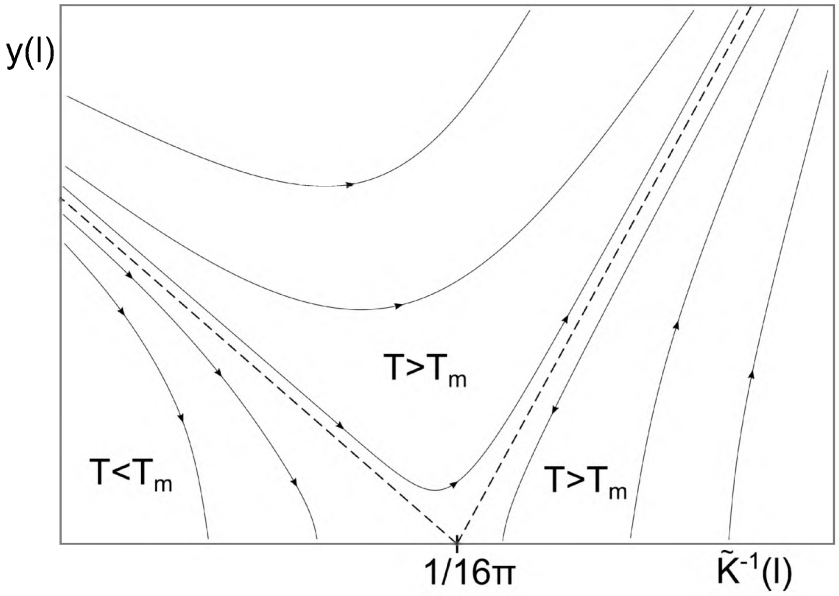

Figure 2.5: Sketch of the renormalization group flow for the inverse Young's modulus $\beta a_0^2 K$ and the fugacity, from Eqs. (2.40). The arrows denote the flow direction for increasing l. Below T_m the fugacity converges to zero and the Young's modulus to a finite value. Above T_m they both diverge. The elastic modulus takes its critical value on the separatix between the two regions, shown with a dashed line.

melting temperature, K_R approaches the universal behavior

$$\lim_{T \to T_m} \beta a_0^2 K_R = 16\pi, \tag{2.42}$$

that confirms the result in (2.15).

Many others interesting results about this melting can be derived from Eqs. (2.40) (they are reviewed in [NH79]), such as fundamental scaling behaviors of the elastic constant in the vicinity of the critical point or the correlation length for the dislocations' distortion field. But only one of them, that is of considerable interest for the arguments of this thesis, is going to be reviewed here: the behavior of the translational correlation function across the melting transition.

As observed in Chapter 1, the quantity that catches the positional order in periodic crystals is the so-called *Debye-Waller correlation function*, defined, given $\rho_{\mathbf{G}}(\mathbf{R}) = e^{i\mathbf{G}\cdot[\mathbf{R}+\mathbf{u}(\mathbf{R})]}$ with $\mathbf{G}$ a reciprocal lattice vector, by

$$\begin{aligned} C_{\mathbf{G}}(\mathbf{R}) &= \langle \rho_{\mathbf{G}}(\mathbf{R}) \rho^{\star}_{\mathbf{G}}(\mathbf{0}) \rangle = \langle e^{i\mathbf{G}\cdot[\mathbf{u}(\mathbf{R})-\mathbf{u}(\mathbf{0})]} \rangle \\ &\simeq \exp\left\{ -\frac{1}{2}\, q_i q_j \, \langle [u_i(\mathbf{R}) - u_i(\mathbf{0})][u_j(\mathbf{R}) - u_j(\mathbf{0})] \rangle \right\}, \end{aligned} \tag{2.43}$$

where a cumulant expansion is used for the last equality, that is correct to $O(y^2)$. Since below T_m the average is over the free form of the Hamiltonian (with all the couplings renormalized) that is quadratic in $u_i(\mathbf{q})$, it is easy to see that

$$\frac{q^2}{\Omega}\langle u_i(\mathbf{q})u_j(-\mathbf{q})\rangle = k_B T\left(\frac{1}{\mu_R}\delta_{ij} - \frac{\mu_R+\lambda_R}{\mu_R(2\mu_R+\lambda_R)}\frac{q_i q_j}{q^2}\right). \tag{2.44}$$

This allows to evaluate

$$\langle [u_i(\mathbf{R})-u_i(\mathbf{0})][u_j(\mathbf{R})-u_j(\mathbf{0})]\rangle = \delta_{ij}\frac{k_B T}{4\pi}\left(\frac{1}{\lambda_R+2\mu_R}+\frac{1}{\mu_R}\right)\ln\left(|\mathbf{R}|\Lambda\right), \tag{2.45}$$

and thus

$$C_{\mathrm{G}}(\mathbf{R}) \sim |\mathbf{R}|^{-\eta_{\mathrm{G}}}, \tag{2.46}$$

with

$$\eta_{\mathrm{G}} = \frac{k_B T}{4\pi}\left(\frac{1}{\lambda_R+2\mu_R}+\frac{1}{\mu_R}\right)G^2. \tag{2.47}$$

A perturbation analysis of Eqs. (2.40) close to the critical point, where $K^{-1}(l) \simeq (\beta_m a_0^2/16\pi)[1+x(l)]$, shows that as the temperature approaches T_m from below, the Young's modulus, as well as the other elastic moduli $\mu(l)$ and $\lambda(l)$, vanish as one would expect from a material that does not respond as a solid to external elastic stress anymore, but that behaves like a fluid. In the next Section will be shown that 2D periodic materials, above the melting temperature T_m, are not pure isotropic fluids, but they preserve instead a six-fold anisotropy typical of a liquid-crystal.

2.2 Hexatic phase and HN theory of melting in two stages

Besides calculations for building a consistent theory of the dislocation unbinding, Halperin and Nelson introduced a true novelty in the context of melting transitions for 2D systems. They proved that, although dislocation unbinding destroys translational order, above T_m a residual quasi-long-range order survives for the reciprocal orientations of the lattice bonds.
As already said in Chapter 1, this result complemented a general intuition by Mermin [Mer68] who had already settled that, within the context of simple two-dimensional harmonic crystals, the correlation between orientations

$$\langle [\mathbf{u}(\mathbf{R}+\mathbf{a}_i)-\mathbf{u}(\mathbf{R})]\cdot[\mathbf{u}(\mathbf{R}'+\mathbf{a}_i)-\mathbf{u}(\mathbf{R}')]\rangle, \tag{2.48}$$

with $\mathbf{a}_i$ the lattice base vectors, does not decay in the 2D solid phase as $|\mathbf{R}-\mathbf{R}'| \to \infty$.

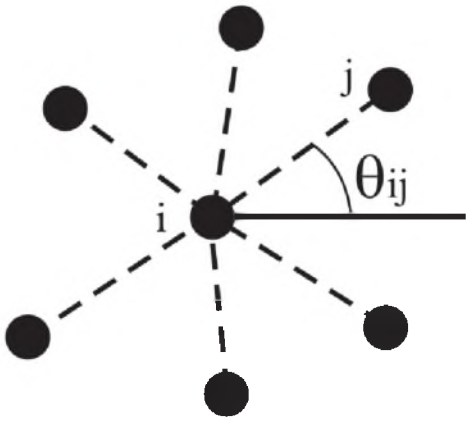

Figure 2.6: Illustration of the variables involved in the defeinition of local hexatic order parameter, as in Eq. (2.49). To compute $\psi_{6,i}$, associated to the i-th particles, only the directions θ_{ij} between the particles and its neighbors have to be take into account, not the particles' positions.

2.2.1 The hexatic phase

Halperin and Nelson [HN78, NH79] justified this result by studying the properties of the appropriate orientational order parameter that takes into account the six-fold symmetry of the solid phase

$$\psi_6(\mathbf{R}_k) = \frac{1}{N_k} \sum_j e^{i(6\theta_{kj})} , \tag{2.49}$$

where k labels the particles, N_k is the number of neighbors of particle k, and θ_{kj} is the orientation of the bond between particles k and its j-th neighbor with respect to some reference direction. A schematic representation of the quantities involved in the definitions of this so-called *hexatic order parameter* is given in Fig. 2.6.

It can be explicitly shown that, below T_m, the solid possesses a true long-range orientational order, observing that in the continuum limit $\theta(\mathbf{r})$ is related to the displacement field $\mathbf{u}(\mathbf{r})$ by

$$\theta(\mathbf{r}) = \frac{1}{2}\epsilon_{ij}\partial_i u_j(\mathbf{r}) . \tag{2.50}$$

Thus is easy to find, making use of the renormalized Hamiltonian $H_0(\lambda_R, \mu_R)$ obtained before, that

$$\langle \psi(\mathbf{r})\psi(\mathbf{0})\rangle \simeq \exp\Big[-36\left(\langle\theta^2(\mathbf{0})\rangle - \langle\theta(\mathbf{r})\theta(\mathbf{0})\rangle\right)\Big] \tag{2.51}$$

does decay to a nonvanishing temperature-dependent constant as $|\mathbf{r}| \to \infty$.

The guess that, as said, dislocation unbinding drives the system to an anisotropic liquid-crystal phase with a residual QLR orientational order would mean that above T_m the Hamiltonian would take the form

$$H_A = \frac{1}{2} K_A(T) \int |\nabla \theta(\mathbf{r})|^2 \, \mathrm{d}^2\mathbf{r} \,, \tag{2.52}$$

with finite so-called *Frank constant* $K_A(T)$ defined, as usual, by

$$\frac{k_B T}{K_A} = \tilde{K}_A^{-1} = \lim_{q \to 0} \frac{q^2}{\Omega} \langle \theta(\mathbf{q}) \theta(-\mathbf{q}) \rangle \,. \tag{2.53}$$

This is typical of anisotropic media and it is used to describe the elastic response of the orientational degrees of freedom. Although in a generic liquid crystal is a tensor of rank two, for a six-fold symmetric two-dimensional system is a single scalar constant.

Using a *Debye-Huckel theory* for dealing with the behavior of the system above the melting temperature, where a population of bonded and free dislocations exists in the material, it is possible to check that K_A acquires a finite non-vanishing value. Thus, being the hypothesis (2.52) a correct description of the elastic rotational thermodynamics of the particle-particle segments throughout the sample, one can conclude that at T_m 2D quasi-solids melt into a so-called *hexatic phase*.

Moreover, from (2.52) is now straightforward to calculate the hexatic correlation function

$$\langle \psi_6(\mathbf{r}) \psi_6(\mathbf{0}) \rangle \sim r^{-\eta_6(T)} \,, \tag{2.54}$$

with

$$\eta_6(T) = \frac{18 k_B T}{\pi K_A(T)} \,. \tag{2.55}$$

Because of this algebraic decay of the orientational correlation function, the hexatic phase is characterized by a QLR orientational order.
Deriving from (2.53) and (2.50) the expression of K_A in terms of the elastic constants of the solid phase, and applying the renormalization-group procedure returns:

$$\tilde{K}_A = \mathrm{e}^{2l} \tilde{K}_A(\tilde{\mu}(l), \tilde{\lambda}(l), y(l)) \,. \tag{2.56}$$

Note that the K_A is not required to be invariant under the renormalization-group transformations and actually it is not. However, Eq. (2.56) tells that below T_m the Frank constant diverges, as one would expect for a true long-ranged orientationally ordered phase and, accordingly, η_6 in (2.54) goes to zero.

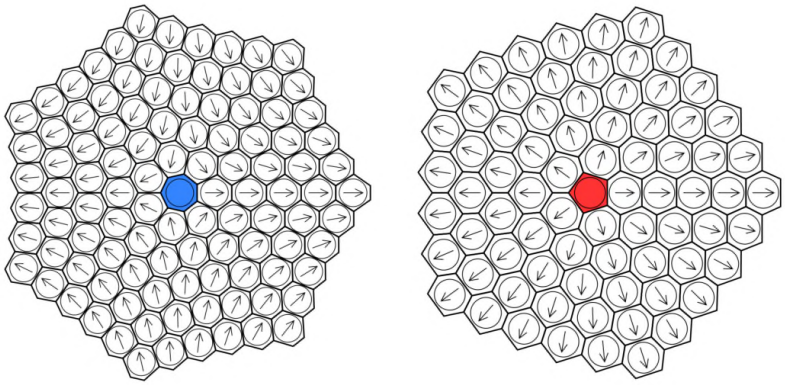

Figure 2.7: The two disclinations of lowest energy for a 2D triangular lattice. The defect on the left has charge $+\pi/3$, and it can be identified with a single 7-fold miscoordinated particles, while the defects on the rigth is a $-\pi/3$ disclination with a 5-fold particle. FIgure adapted from [Ber11].

2.2.2 Disclination-unbinding solid-liquid transition

Further increasing the temperature above T_m, another phase transition finally takes the hexatic phase into a pure isotropic liquid phase. This transition, as established by Halperin and Nelson [NH79], is driven by the unbinding of isolated dislocations, which are free to be excited in the hexatic phase, into another class of topological defects, called *disclinations*. As their name bring to mind, disclinations in 2D solids arise from twisting (instead of sliding as for dislocations, see in Sec. 2.1.1) the two sides of a Volterra cut relative to each other. For a triangular array of lattice sites, two different disclinations can be built with this protocol by a rotation of either $+\pi/3$ (positive disclination) or $-\pi/3$ (negative disclination). This definition reads as the following constraint on the orientational field:

$$\oint_C \mathrm{d}\theta = \frac{\pi}{3} s, \tag{2.57}$$

with s integer and C a closed path around the defect. As shown in Fig. 2.7, where both the two resulting configurations are sketched, the twisting procedure leaves a miscoordinated atom at the defect core with, respectively, 7 and 5 next neighbors.

As also suggested by the picture, although it would be hopeless to thermally excite a single disclination because this would mean to apply the Volterra cut described before, is instead possible for two disclinations of opposite charge to arise from the dissociation of an isolated 5-7 dislocation. Indeed, according to the Halperin-Nelson theory, at a temperature $T_i > T_m$

dislocations unbinding into free disclinations mediates the melting of the hexatic phase into the isotropic liquid, thus destroying the residual QLR orientational order.

In order to apply the same theoretical approach for dealing with this other unbinding process, the angle variable $\theta(\mathbf{r})$ is decomposed into a smoothly varying part $\phi(\mathbf{r})$ and a singular part due to the presence of a collection of free disclinations. The Hamiltonian (2.52) becomes

$$\begin{aligned} H_A = & \frac{1}{2} K_A \int \mathrm{d}^2\mathbf{r} \left(\nabla\phi\right)^2 \\ & - \frac{K_A}{2\pi}\left(\frac{\pi}{3}\right)^2 \frac{1}{2} \sum_{\alpha\neq\alpha'} s_\alpha s_{\alpha'} \ln \frac{R_{\alpha,\alpha'}}{a_s} \\ & + E_s \sum_\alpha s_\alpha^2 \,, \end{aligned} \tag{2.58}$$

where α runs over the defects, s_α is the integer charge of the defects, E_c is the defect core energy and a is the core size. Again, as for the derivation of dislocation Hamiltonian (2.22), the disclination population has global null charge, which reads $\sum_\alpha s_\alpha = 0$.

As immediately noted by Halperin and Nelson, the disclination problem (2.58) is exactly mapped onto the planar rotor problem mentioned before, that was already solved by Kosterlitz-Thouless-Young and where the phase transition is driven by unbinding of spin vortices *.

For this reason, without carrying on the perturbative analysis of the rotor problem [Kos74] (which follows the same approach as the one outlined before for the dislocation mediated melting), is possible to borrow only the main results from it.

As the temperature approaches the melting temperature T_i from below the renormalized Frank constant takes the universal value

$$\lim_{T\to T_i^-} K_A(T) = \frac{72 k_B T}{\pi} \,. \tag{2.60}$$

*Note that the KT Hamiltonian of the XY model in two dimensions that accounts for the presence of spin vortices is [KT73]

$$\begin{aligned} H = & \frac{1}{2} K(T) \int \mathrm{d}^2\mathbf{r} \left(\nabla\chi(\mathbf{r})\right)^2 \\ & - \pi K(T) \int_{|\mathbf{R}-\mathbf{R}'|>a} \mathrm{d}^2\mathbf{R}\mathrm{d}^2\mathbf{R}'\, n(\mathbf{R})\, n(\mathbf{R}') \ln \frac{|\mathbf{R}-\mathbf{R}'|}{a} - E_v \int \mathrm{d}^2\mathbf{R}\, n^2(\mathbf{R}) \,, \end{aligned} \tag{2.59}$$

with χ the smoothly varying part of the spin field, K the spin-stiffness, n the charge of the vortex and E_v its core energy.

It discontinuously vanishes above T_i and remains zero into the liquid phase.
At the critical point the hexatic correlation (2.54) decays with a universal exponent

$$\eta_6(T_i) = \frac{1}{4}. \tag{2.61}$$

Above T_i the same hexatic correlation function decays exponentially with a correlation length that diverges as $T \to T_i^+$.

Thus, concluding, within the KTHNY theory of melting, there are two continuous symmetries that are broken to discrete ones at two different temperature: translational symmetry is broken at T_m and orientational symmetry at T_i. Each of the transitions is associated with a specific modulus of stiffness. The reduced Young's modulus $\beta a_0^2 K$ jumps from zero to 16π at T_m (see Eq. (2.42)), which is in agreement with our experience that a crystal can resist to shear stress. The same applies to the transition from the liquid to the hexatic phase: the Frank constant defined in Eq. (2.53) jumps from zero to $72/\pi$ at T_i, thus reflecting the fact that the hexatic phase, but not the liquid can resist rotational stress.

2.3 Experimental and numerical works on KTHNY theory

After having presented in many details the theoretical efforts devoted, mainly during the 70's, to the understanding of the physics of melting in 2D, in this section a glimpse will be get to the huge amount of experimental and numerical works that from decades try to compare evidences from real systems to the main results of the theory, supporting or contradicting its predictions.

This review does not pretend to include all the works in this wide field, but it only aims to present some of the crucial attempts to measure the quantities involved in the BKTHNY theory from experiment or simulations. This is needed as a prelude to the main part of this thesis, which is itself a numerical work on melting in two dimensions. For this reason experiments and simulations will be presented all together in the present Section trying to cover most of the methods used over the years.

The first category of experiments that is worth to be mentioned is the one in which systems are constituted of colloidal particles interacting with a screened Coulomb potential. Rather than other experiments such as on liquid crystals, micron-sized colloidal systems have many experimental

advantages. Most importantly, colloidal particles, though they are big enough to be directly observable by means of video microscopy, at the same time they are still small enough to perform thermally driven Brownian motion and can thus be considered as a statistical ensemble in thermal equilibrium. Since the typical diffusing time of such systems is of the order of few seconds, not only the length but also the time scale for thermal equilibration are in an easily observable regime. The use of digital image processing techniques allows to extract the trajectories of the particles and, as for a standard molecular dynamics numerical simulation, to analyze them on all relevant time and length scales.

Murray and Van Winkle [MVW87] performed one of the first of these experiments using charged spherical polystyrene-sulfonated micro-spheres of $\sim 0.3\mu$m in an aqueous suspension. Confinement to two dimensions is realized by squeezing the suspension between two nearly parallel glass plates providing the colloids to move in two dimensions. A narrow wedge geometry of the glass plates along one horizontal direction is realized in the experiment by tilting the upper plate by a small ($\sim 4 \times 10^{-4}$rad) angle. The thickness of the fluid layer thus increases along the same direction and, due to the interaction between the colloids and the glass plates, a density gradient of the particles is observed in equilibrium with low density in the thinner region. Because of this, different types of crystal symmetries were found in the arrangement of the colloids along the density gradient.

Thanks to this experiment, the authors were the first who identified the hexatic phase in colloidal systems by measuring both structure factors and the distance dependence of the orientational, see Eq. (2.54), and translational, Eq. (2.43), correlation functions. They found that, in accordance with the KTHN theory, the orientational correlation length and the translational one diverge at two different values of density and that the intermediate phase has a structure compatible with a pure hexatic phase. However, although Murray *et al.* clearly observe a two-stage KTHNY-melting from a correlation length analysis, they failed to find paired dislocations in the solid phase or free dislocations in the hexatic phase. Instead, they observed in the fluid phase islands of six-fold coordinated particles surrounded by a network of grain-boundaries of fourfold, five-fold and seven-fold coordinated particles. Inside the hexatic phase, these grain boundaries did not disappear, but neighboring grains began to orient with respect to each other.

A similarly contradictory result has been obtained by Tang *et al.* [TAMO89] with an experiment of melting of spherical colloids of the same kind of the ones used in [MVW87]. In order to avoid a possible influence of the inherent particle density gradient, a flat cell geometry was used. Two disk-

shaped glass plates with different diameters were glued concentrically on top of each other, so that the smaller one would act like a stamp when pressed against a third plate. The space between the first and third glass plate was sealed used as a reservoir for the $\sim 1\mu$m sized spheres.
These authors were unable to observe any unbinding of isolated dislocation into disclinations, but they identified a grain-boundary-induced melting [†] mechanism with spontaneous cluster formation of dislocations and dislocation pairs and even the formation of interconnected liquid-like islands. And, still, they clearly derived correlation lengths and power-law exponents in good agreement with the KTHNY theory.

A different experimental approach was carried out by Marcus and Rice [MR96, MR97] who set up a colloidal system with essentially hard core repulsion combined with a short range square attractive part. Particles of a diameter 0.93μm were suspended in aqueous solution in order to eliminate sedimentation. The spacing between the walls of a flat thin glass cell was found to be optimal at $\sim 1.2\mu$m thereby avoiding both immobilization and out-of-plane motion. The quantity to be varied in different measurements was the particle density.

A large number of Voronoi constructions (see Section 3.3 for the definition of the Voronoi cells) of colloid configurations, that allows to determine the coordination number of each colloid, are presented and discussed in the paper of Marcus and Rice and summarized in Fig. 2.8. Bound dislocation pairs occur as clusters of two five-fold and two seven-fold particles. Unbound free dislocations made up of individual tightly bound five-fold and seven-fold sites are clearly observable. Marcus and Rice analyzed whole sequences of these configurations and found that dislocations and clusters of dislocation defects appear and disappear on the time scale of successive video frames, and that their absolute locations are temporally uncorrelated. It is the presence of a small steady-state concentration of unbound dislocations (stemming from a dissociation of these short-lived bound dislocations) that causes the slow algebraic decay of the bond-orientational order in the hexatic phase. Such Voronoi constructions of configurations were also taken by Marcus and Rice to demonstrate that there exist states with coexistence between the hexatic and the fluid phase, and between the solid and the hexatic phase. This result, which would imply that the liquid-hexatic and hexatic-solid transition are first-order, are interpreted by the authors as system-dependent characters.

As clearly emerges from the two examples illustrated above, the analysis of direct images of colloidal configurations does not always lead to

[†] A small review of grain-boundary-induce melting theories is given later in Chapter 4.

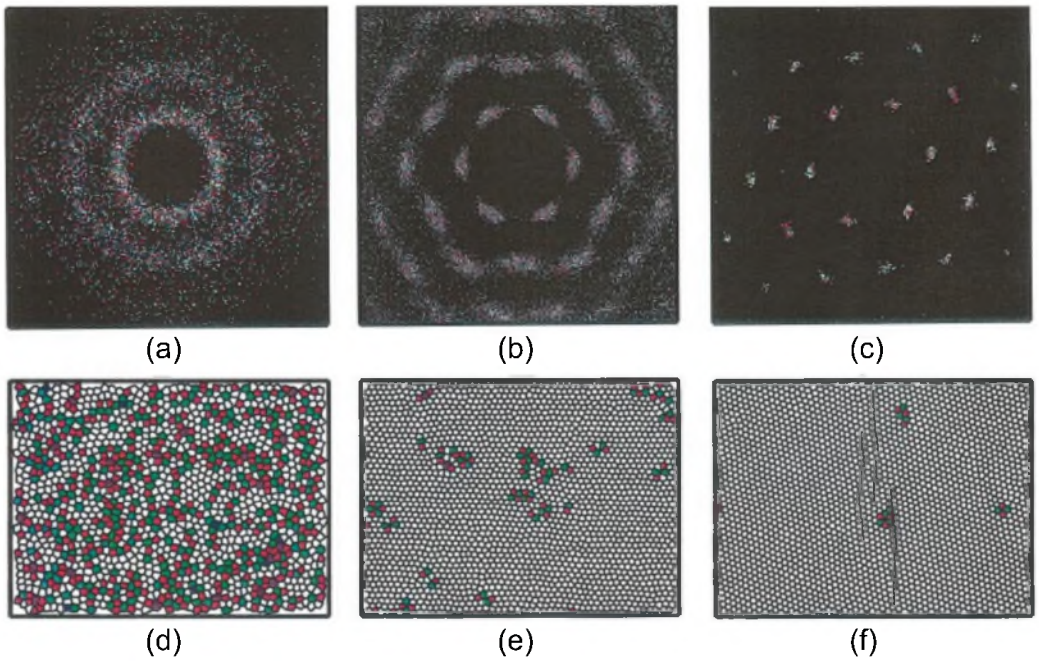

Figure 2.8: In the first row, the static structure factor $S(\mathbf{q}) = N^{-1}\sum_{i,j} e^{i\mathbf{q}\cdot(\mathbf{r}_i-\mathbf{r}_j)}$, for an experimental system of colloidal particles in the liquid phase (a), in the hexatic phase (b) and in the solid (c). In the second row, Voronoi constructions of one representative snapshot for the three phases, with all the defects highlighted: 7-fold particles are shown in green, 5-fold particles are shown in red, 4-fold particles in blue, 8-fold ones in purple. Figure adapted from [MR96].

unambiguous results about the nature of melting transitions in 2D. Even though the direct knowledge of the instantaneous positions of the particles is enough to extract with acceptable accuracy the structural behavior of the system and thus to infer the two-step melting scenario with an intermediate hexatic phase, the defects unbinding processes, as described by Halperin and Nelson [NH79], are not so easily observed.

Dislocations and disclinations behaving as expected from the KTHNY theory were actually first observed for a colloidal model system of paramagnetic particles with the setup described in Refs. [ZLM99, ZM00, KMvG07, ZMAM97, vGKZM04].
Spherical colloids of diameter $d \sim 4.5\mu$m are confined by gravity to a water/air interface formed by a water drop suspended by surface tension in a top sealed cylindrical hole of 8mm diameter of a glass plate; see a sketch of the configuration of the setup for example in [KMvG07]. A magnetic field $\mathbf{H}$ is applied perpendicular to the interface inducing a magnetic moment $\mathbf{M} = \chi\mathbf{H}$ (with χ the magnetic susceptibility) in each particle. This lead to

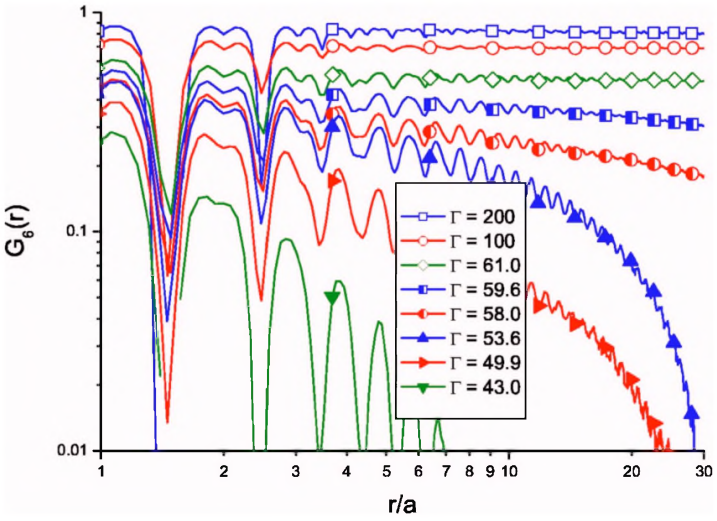

Figure 2.9: Orientational correlation function $g_6(r)$ as a function of the inverse temperature in a log-log plot. From top to bottom: three curves for the crystalline phase showing the long-range orientational order ($\lim_{r\to\infty} g_6(r) \neq 0$), two curves showing the quasi-long-range order of the hexatic phase ($g_6(r) \sim t^{-\eta_6(\Gamma)}$), and three curves showing the short-range order typical of the isotropic liquid ($g_6(r) \sim \mathrm{e}^{r/\xi_6(\Gamma)}$). Figure adapted from [KMvG07].

a pure repulsive dipole-dipole pair-interaction given by

$$U^H(r) = \frac{\mu_0(\chi H)^2}{8\pi}\frac{1}{r^3}. \tag{2.62}$$

The dimensionless interaction strength $\Gamma = \langle U^H\rangle/k_BT$ can be interpreted as an inverse temperature and can be controlled by means of the intensity of the applied magnetic field H.

Hexatic phase was undoubtedly observed from direct image detection in these kind of experiment, as evidenced for example in the behavior of hexatic correlation function - see Eq. (2.54) - in [KMvG07] and shown in Fig. 2.9. Hexatic correlation is short-ranged in the isotropic liquid, it decays algebraically in the intermediate anisotropic hexatic phase and it approaches a constant value in the solid phase, where the orientational order is a true-long-range one. The oscillations reflect the shell structure of neighboring particles and are due to the fact that colloids with large deviations from their typical equilibrium distance are poorly correlated in their bond orientation. Also, the statistical weight of the maxima and minima is very different. Whereas the histogram of particles with distances near the maxima increases linearly with r, the corresponding histogram for the first minima shows a different dependence and it is significantly smaller. Many particle pair distances contribute to the maxima, but only

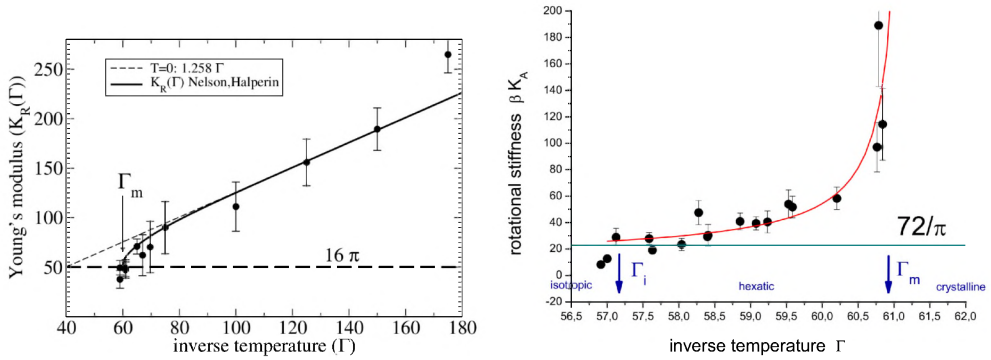

(a) (b)

Figure 2.10: (a) Young's modulus as a function of the inverse temperature. The solid curve is $K_R(\Gamma)$, renormalized according to HN prescription (see Eq. (2.37)), while the dashed curve is based on the $T = 0$ prediction (see the details in [vGKZM04]). (b) The Frank's constant as a function of the inverse temperature Γ becomes $72/\pi$ at T_i. At T_m it diverges, indicating that the perfect orientational symmetry of the crystalline phase is approached. Figure adapted from [KMvG07].

a few to the minima. At large distances, these differences are washed out and the oscillations fade away.

The true novelty introduced in the analysis of Keim *et al.* is that the unbinding of defects has been proven to be responsible for the melting process, as predict by HN, by observing the behavior of the elastic constants of the system. As explained in the previous Section, the dislocation unbinding temperature T_m can be related to the temperature-dependent Young's modulus through Eq. (2.42). Similarly, the disclination unbinding temperature is related to a jump in the Frank constant through Eq. (2.60). The success of this idea will be shown next and it is based on the following reasons. Eqs. (2.42) and (2.60) are, though quite simple, also strongly universal, because they apply in the same form to all the 2D systems. Moreover, since these are macroscopic criteria, no details of the pair-potential need to be known, but only the temperature-dependence of the Young's modulus and the Frank constant.

Keim *et al.* [vGKZM04] described a method to determine the elastic dispersion relation of a two dimensional colloidal system. These relations quantify the elastic behavior of the crystal in q-space. Analyzing the low-q behavior of the longitudinal and transversal bands one can extract the Lamé coefficients λ and μ which can then be used to determine the Young's modulus K. This allows to measure this modulus as a function of temperature and to compare it to the function $K_R(T)$ obtained from the

Halperin-Nelson recursion relations (2.40).

Fig. 2.10-(a) shows the results of the comparison between measured elastic Young's modulus from the experiment, and the behavior predicted by HN theory. Experimental data are significantly compatible with the theoretical prediction and both of the curve approach the universal value $K_R = 16\pi$ at the measured melting temperature T_m.

Frank constant can be also easily extracted from video-microscopy experimental data by measuring the exponent η_6 from the decay behavior of the hexatic correlation function (2.54) and then using the the relation in (2.55) [KMvG07]. In Fig. 2.10-(b) is shown the result of such analysis which again confirms the defects unbinding theory according to which $\beta_i K_A(T_i) = 72/\pi$.
From both Figs. 2.10-(a),(b) is also evident that both the Young's modulus and the Frank constant jump to zero discontinuously above the temperature T_m and T_i, respectively, and that K_A goes to infinity as $T \to T_m$ from above.

Two more works will be presented here, one numerical and one experimental, from the last few years which deal both with a system of hard disks in two dimensions. These two works are of considerable importance in the field of 2D melting, because they are agreeingly accepted to be a *solution* of the problem of establishing the exact scenario of melting of repulsively interacting particles in two dimensions.

The first of these two works is the one by Krauth *et al.* [BK11] who carried out a set of numerical simulations of a huge number of hard disks, that allows them to establish with a certainly good precision that the melting scenario agrees generally with the two-step KTHNY theory and, further, the location of the two meltings and the nature of them.

Equilibration of up to 10^6 disks has been attained by Krauth *et al.* in a reasonable computational time by means of a optimized *event-chain* Monte Carlo algorithm whose basic idea is the following. As depict in Fig. 2.11, a move of the Monte Carlo (MC) starts by sampling an initial disk k and an angle θ. Displacing the disk k straight along the direction θ, it will somewhere collide with another disk, say k'. Once this happens k stops moving and k' begins to be displaced in the same direction as before. These "chained" displacements are repeated until they add up to a total length l, that is therefore the only tunable parameter of the algorithm. The optimal dimensionless total length has been shown to be $l \sim \sqrt{N}$, with N the total number of the disks [BKW09]. Therefore this even-chain MC allows to displace $\sim \sqrt{N}$ disks in a single move, thus with no rejections, which means that the global displacement scales with the length of the side of the

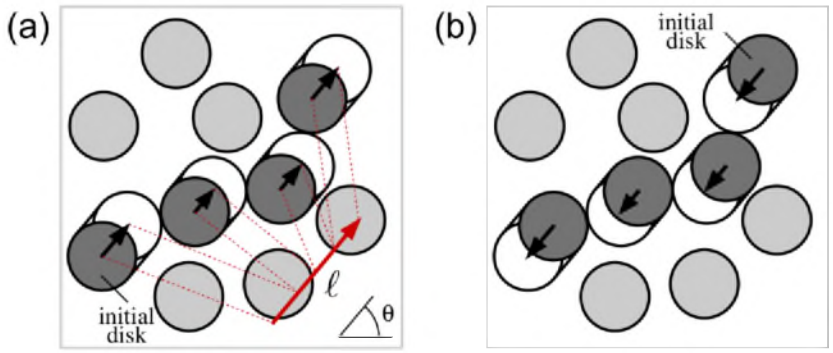

Figure 2.11: A move of the event-chain algorithm from a configuration A (a) to a configuration B (b). See text for details. Disks are displaced individually in the same direction until they collide with another disk or the total length l is used up (red arrow). (b) Event-chain move from the configuration B with the angle $\theta + \pi$ starting with the last displaced disk of the move shown in (a). The algorithm is reversible. Figure adapted from [BKW09].

simulation box, providing the equilibration to be very fast.

Since the interactions between hard disks are true steric interactions, the temperature plays no role for this system and the only relevant variable is the surface fraction ϕ, which measures the area occupied by the disks with respect to the total available surface. Krauth and collaborators strongly established the location of both solid-hexatic and hexatic-liquid transition by means of the analysis of the structure of the system at different fixed values of the packing fraction. Moreover, measuring the thermodynamic pressure, they also found distinct evidences that the hexatic-liquid is a first order phase transition marked, in the constant density statistical ensamble, by a finite co-existence region. More details about this results and the methods used will be given in Chapter 3, because many of the tools they used are adopted within our work, and thus it is thought useful to describe them extensively while presenting our analysis.

These results have been perfectly reproduced in the experiments realized by Thorneywork *et al.* [TAAD17], which deals with hard spheres in two dimensions. As shown in Fig. 2.12, the authors observed a tilted monolayer of colloidal hard spheres to establish the phase behavior of such system. The experiment is prepared by allowing 2.79μm diameter melamine formalydehyde spheres in a water/ethanol mixture to sediment at the base of a glass sample cell and extracting the position of each colloids by means of a video-microscopy apparatus. The values α of the tilt angle are chosen such that the gravitational height $h_{g\|}$ parallel to the base of the cell is large, resulting in an area fraction gradient $\phi(z)$ as a function of the height z (see Fig. 2.12-(b)). This also means that the gravitational height

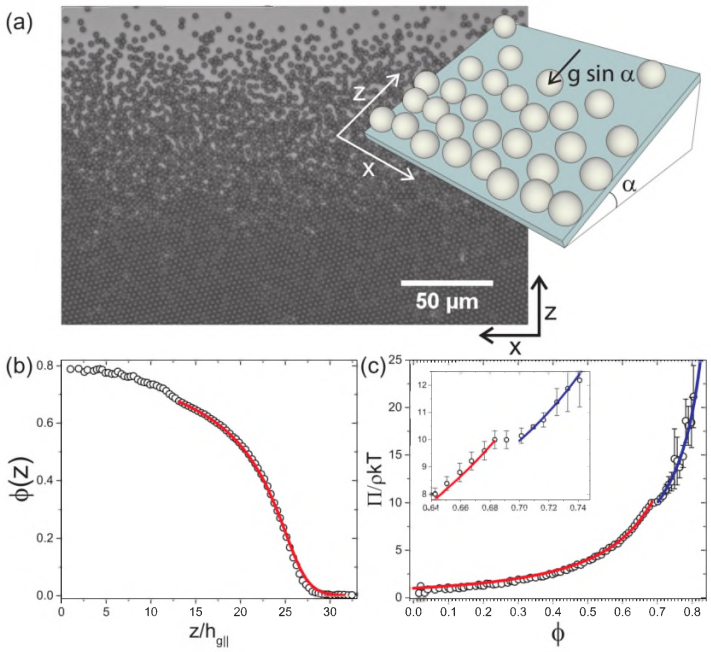

Figure 2.12: (a) A typical experimental image of the system in sedimentation-diffusion equilibrium for a tilt angle α (see the inset). (b) The density profile, $\phi(z)$, as a function of the height, z, rescaled by the in-plane gravitational height, $h_{g\|}$ (see the text for the details). (c) The equation of state $\Pi/\rho k_B T$. The inset shows an expanded view of the behaviour of the equation of state in the region of the discontinuity. Figure adapted from [TAAD17].

$h_{g\perp}$ perpendicular to the base of the cell is small enough to ensure the 2D nature of the system at all area fractions.

The equation of state of the system is

$$\frac{\Pi}{\rho k_B T} = \frac{1}{h_{g\|}} \frac{1}{\phi(z)} \int_z^\infty \phi(z')\, dz', \tag{2.63}$$

with ρ the number density. Fig. 2.12-(c) shows that the EOS has a discontinuous behavior at the liquid-hexatic transition, which undoubtedly signals the first-order nature of the transition, as found by Krauth *et al.*.
As already said, this fundamental and almost accepted result of a first-order liquid-hexatic transition, represents one of the points that our work moved from. As will be explained in Chapter 3, our aim was to push the analysis used in these last two works presented here, to system out of thermal equilibrium.

Chapter 3

Melting scenario for self-propelled disks in 2D

Within the present Chapter we review molecular dynamics numerical analysis carried out on a system of self-propelled (SP) disks in two spatial dimensions. SP agents are able to consume energy from their environment by means of internal mechanisms, in order to move in a medium. Because the energy that they use for their propulsion is not of thermal nature, systems composed by many of these agents evolve out of equilibrium accordingly to the general framework of an *active system*. Many aspects of SP dynamics and collective behaviors of active systems are described in the introduction of this thesis (see Chapter 1).
Although the general ideas that compose the recent active matter theory continue to be used for treating an increasingly number of theoretical models and to describe a huge variety of real systems with their fascinating collective behaviors, many of the fundamental physical properties emerging with activity are still actively debated and they still don't meet any strongly accepted theoretical background. This is one of the main reasons that pushed us to begin to pose some fundamental questions for a very simple, though paradigmatic, active matter model, that will be presented here. Actually, the whole work of this thesis has been dealing with two models which both capture most of the key features of active systems and are both very simple and paradigmatic realizations of them: the Active Brownian (AB) disks model and the Active Brownian Dumbbells model.
This chapter is devoted to introduce all the physical quantities of interest and to report all the results found for SP disks. The work on dumbbells will be presented later in Chapter 5.

The main point which we aimed to address is to build a complete phase diagram of these two models, and thus to study all the stationary

phases and the phase transitions that occur with respect to variations of the relevant control parameters, exploring the whole accessible parameters' space. Such aim is twofold. First of all, although some indications towards crystalline order in dense assemblies of SP particles exist (see for instance [BSL12]), a complete discussion about the phase transition scenario is absent in the literature, even for the simplest AB disks model. Moreover, such complete analysis has been gave us the opportunity to further clarify the interplay between ordering phase transition and motility-induced phase separation. In fact, it has been recently suggested that MIPS shares many fundamental properties with equilibrium phase separation, at least at the mean field level (see for instance [CT15]). Even if, as we will show in Section 3.1.2, this viewpoint has allowed to explore some very general characters of MIPS, no one had examined such non-equilibrium phase separation on the ground of a complete phase diagram of the model.

The central idea of this work is that, regardless to the SP out-of-equilibrium dynamics of the model, most of the fundamental structural properties, the underlying spatial symmetries and thus the nature of the stationary states of a system of interacting active disks are the same as the ones of its passive counterpart. Therefore, the BKTHNY theory of melting presented in Chapter 2 is expected to be the main reference theory for interpreting our results and from which borrow the key physical ideas, the analytical approach and most of the tools and quantities of interest. As for a HN theory, we thus propose for the first time to interpret the structural changes in a system of SP particles as defects mediated phase transitions. In particular, we are much interested in exploring the structural arrangement of the particles within the dense phase in MIPS, thus studyng both translational and bond-orientational order of such phase.

It must be said that, since self-propulsion mechanisms are able to drive our system far away from thermal equilibrium, Halperin-Nelson scenario does not straight apply to the case. As widely reviewed in Chapter 2, such theory accounts for the elastic properties of a two dimensional medium to be affected by the presence of topological defects, in a way that eventually drives melting of the whole sample. Since the equilibrium elasticity theory is certainly violated by SP particles, the melting point and the critical behavior can not be predicted in our case. Moreover, as already shown elsewhere for different purposes [TT95], active systems can violate the Mermin-Wagner theorem, and are able to overcome its prescriptions (see Chapter 1, and Appendix B) to eventually form true ordered crystals even in two dimensions. This is undoubtedly possible because, while long wavelength thermal fluctuations are responsible of destroying 2D crystal periodicity, in an active dense suspension particles' positions fluctuate

around their periodic sites due to non-thermal sources. Thus, true long-range order can be eventually sustained at non-zero temperature of the bath for a suitable configuration of the fluctuation field. It is worth noting that this is the underlying physical reason why active matter systems can show a great abundance of collective behaviors with highly ordered structures over large scales, that would be forbidden in equilibrium.

For all these evidences, BKTHNY theory does not give us quantitative *a priori* indications to figure out either the presence of a melting point, or its location and its nature for the active system. However, as said, in order to interpret the results obtained from large-scale molecular dynamics simulations, we made a wide use of many of the elements of that theory which are believed to hold beyond thermal equilibrium. A list of them is given below:

- in a quasi-long-range (QLR) translationally ordered system the correlation length diverges, but the Debye-Waller correlation function $C_{\mathbf{q}_0}(r) = \langle e^{i\mathbf{q}_0\cdot(\mathbf{r}_i-\mathbf{r}_j)}\rangle$ decays as a power law as $r \to \infty$ and the system size grows indefinitely (see Eq. 2.43);
- QLR orientational order is associated to configurations where the hexatic correlation function $g_6(r) = \langle \psi_6(\mathbf{r}_i)\psi_6(\mathbf{r}_j)\rangle$ decays as a power law (see Eq. 2.54);
- if true-long-range ordered is established, the respective correlation function should approach a non-zero constant as $r \to \infty$ in the limit of infinite system size;
- the topological nature of both the solid-hexatic and the hexatic-liquid transition should be preserved. Thus free dislocations should appear only once the solid is melted into the hexatic, whereas free disclinations should be excited across the hexatic-liquid melting.

Besides, one important property of the SP disks model allowed us to obtain valuable results about the nature of the transitions, that is the possibility to define a consistent equation of state (EOS) even for our model. This important result is going to be discussed within this Chapter, along with all the results coming from using it within our context.

3.1 A minimal model of self-propelled disks

The model used to describe our system of SP disk is the simplest realization of Active Brownian Particles (ABP), which are isotropic particles that move

in two spatial dimensions according to a Langevin dynamics, but also swim along one axis that itself diffuses. Hence, considering N of these particles of diameter σ_d in a box of area $V = L^2$, the equations of motion for the $3N$ degrees of freedom are the following:

$$\begin{aligned} \gamma \dot{\mathbf{r}}_i &= F_{\mathrm{act}} \mathbf{n}_i - \boldsymbol{\nabla}_i \sum_{j(\neq i)} U(r_{ij}) + \boldsymbol{\xi}_i \,, \\ \dot{\theta}_i &= \sqrt{2D_\theta}\eta_i \,, \end{aligned} \tag{3.1}$$

where θ_i is the angular variable defining the direction of the self-propulsion $F_{\mathrm{act}}\mathbf{n}_i$ as $\mathbf{n}_i(t) = \big(\cos\theta_i(t), \sin\theta_i(t)\big)$. The strength of the self-propulsion is the constant F_{act} and is related to the swim velocity modulus $v_0 = F_{\mathrm{act}}/\gamma$ in the dilute limit.
As in the usual Langevin framework, $\boldsymbol{\xi}$ is a white zero-mean Gaussian noise of strength proportional the temperature of a passive reservoir

$$\langle \boldsymbol{\xi}_i(t)\boldsymbol{\xi}_j(t')\rangle = 2\gamma k_B T\, \mathbf{1}\, \delta_{ij}\delta(t-t') \,. \tag{3.2}$$

According to Green-Kubo relation, the temperature is related to the diffusion coefficient in the passive dilute limit through

$$D_0 = \frac{1}{2}\int_0^\infty \langle \dot{\mathbf{r}}(t)\cdot\dot{\mathbf{r}}(0)\rangle \,\mathrm{d}t = \frac{k_B T}{\gamma} \,. \tag{3.3}$$

The η_is are other N zero-mean and unit strength Gaussian white noises which instead settle the diffusion dynamics of swim directions. The angular diffusion coefficient D_θ is set to be related to the temperature of the bath through $D_\theta = 3k_BT/\gamma\sigma_d^2$, assuming thus that rotational diffusion is of a thermal origin. It is quite easy to see that the last assumption for D_θ would come out from Stokes flow in the solvent and stick boundary conditions on the particles surface.

The inter-particle interactions are mediated by the purely repulsive short-range potential $U(r_{ij})$ which depends only on the distance $r_{ij} = |\mathbf{r}_i - \mathbf{r}_j|$ between the interacting particles. In order to avoid the disks to overlap much, aiming to simulate particles that quite closely resemble hard-disks with only excluded volume interactions, U has been chosen to have the following *Mie* shape [Mie03]:

$$U(r) = \begin{cases} 4\varepsilon\left[\left(\frac{\sigma}{r}\right)^{64} - \left(\frac{\sigma}{r}\right)^{32}\right] + \varepsilon & \text{if } r < r_{min} \\ 0 \qquad \text{elsewhere} \end{cases} \tag{3.4}$$

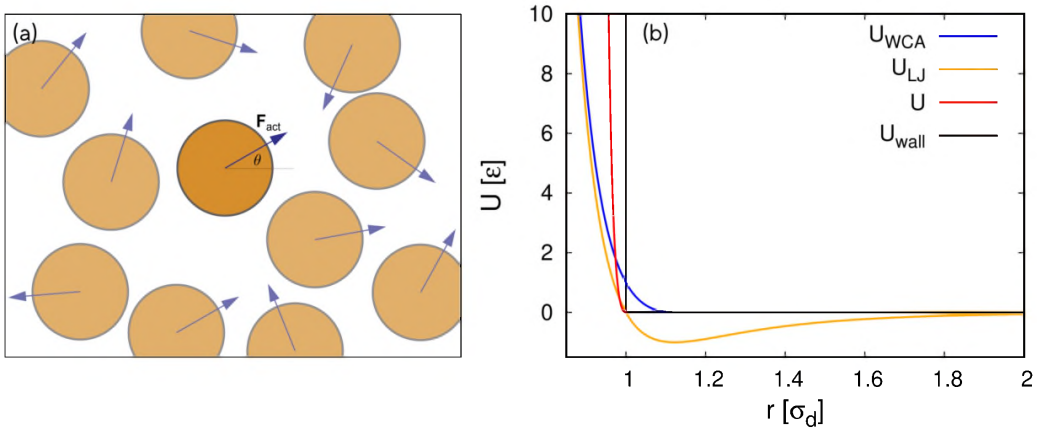

Figure 3.1: (a) - Detail of a SP disks system. Blue arrows are the directions of self-propulsion for each disk. They form an angle θ with the reference x-axis. (b) - A set of standard inter-particle potential. Yellow line is the usual Lennard-Jones potential, with both a repulsive core and an attractive tail. The WCA potential (blue line) is realized by just cutting the attractive part of the LJ one a shifting the minimum to zero. A modified Mie-potential is represented with a red line and is a generalization of the WCA (see Eq. (3.4)). Black line is a discontinuous hard wall.

where $-\varepsilon$ is the depth of the minimum $U(r_{min})$ below zero, and $\sigma = (1/2)^{1/32}$ has been tuned to have $r_{min} = \sigma_d$, so as particles begin to interact as soon as they overlap. The reason of having considered this stiff interactions will be clear soon in this Chapter and it is mostly due to have the hard-disk system as a reference in the equilibrium case, because the results found before for such model are complete and quite conclusive. See Fig. 3.1 (b) to get an idea of how much close to the hard-disks limit the interaction is.

3.1.1 Single particle limit and persistent motion

This model of SP disks encodes one important property of living systems, which is *persistency* in the movement (see for instance [WL00]). A persistent random walk is a theoretical stochastic motion that mimic the behavior of a body who has the tendency to keep moving into the same direction with a constant velocity, before changing its direction. It can be realized by a random walker with time-correlated velocity over a time that is thus called *persistence time*.
To check how a persistence motion arises for the present case, the mean square displacement has to be evaluated from (3.1) in the dilute limit. Since velocity depends on the direction of self-propulsion, this demands

to calculate the time-correlation

$$\begin{aligned}\langle \mathbf{n}(t)\cdot\mathbf{n}(t_0)\rangle &= \langle \cos\theta(t)\cos\theta(t_0)\rangle + \langle \sin\theta(t)\sin\theta(t_0)\rangle \\ &= \langle \cos\Big[\theta(t)-\theta(t_0)\Big]\rangle\,,\end{aligned} \tag{3.5}$$

where t_0 is the initial time for the measurements. The particles' label are omitted in this single-particle calculation.
Recasting the equation for $\theta(t)$ as

$$\mathrm{d}\theta(t) = \sqrt{2D_\theta}\,\mathrm{d}W(t)\,, \tag{3.6}$$

with $W(t)$ a Wiener process of unit amplitude, it becomes clear that $\theta(t)$ is itself a Wiener process of amplitude D_θ. This means that the process $(\theta(t)-\theta(t_0))$ is characterized by Gaussian law with zero mean and variance $D_\theta(t-t_0)$. This allows to easily evaluate the mean in (3.5) by only using the properties of Gaussian integrals and thereby to obtain

$$\langle \mathbf{n}(t)\cdot\mathbf{n}(t_0)\rangle = \mathrm{e}^{-D_\theta(t-t_0)}\,. \tag{3.7}$$

The mean square displacement comes straightforwardly from the equation of motion as follows:

$$\begin{aligned}\langle\Big(\mathbf{r}(t)-\mathbf{r}(t_0)\Big)^2\rangle &= \int_{t_0}^{t}\mathrm{d}t'\int_{t_0}^{t}\mathrm{d}t''\,\langle\dot{\mathbf{r}}(t')\cdot\dot{\mathbf{r}}(t'')\rangle \\ &= \frac{4k_BT}{\gamma}(t-t_0)+\left(\frac{F_{\mathrm{act}}}{\gamma}\right)^2\int_{t_0}^{t}\mathrm{d}t'\int_{t_0}^{t}\mathrm{d}t''\,\mathrm{e}^{-D_\theta(t'+t''-2\min(t',t''))} \\ &= \frac{4k_BT}{\gamma}(t-t_0)+2\left(\frac{F_{\mathrm{act}}}{\gamma}\right)^2\frac{1}{D_\theta^2}\Big[D_\theta(t-t_0)+\mathrm{e}^{-D_\theta(t-t_0)}-1\Big]\,.\end{aligned} \tag{3.8}$$

The persistence time emerges from this results as the time $\tau_P = 1/D_\theta$ which separates the two following dynamical regimes. For $(t-t_0)\ll\tau$, expanding the exponential up the second order, a ballistic regime emerges with persistent velocity $v_0 = F_{\mathrm{act}}/\gamma$, while for long time the motion is diffusive with diffusion constant

$$D_{\mathrm{eff}} = D_0 + \frac{v_0^2}{2D_\theta}\,, \tag{3.9}$$

which depends on self-propulsion strength.

3.1.2 Finite density and Motility-induced phase separation

Although the zero density limit treated in the previous section allows to catch many fundamental properties of self-driven motion, we will deal from now on with systems of finite density.
Needless to say, the properties of the system strongly depend on the density of particles, because at finite density short-range repulsive interactions become to come into play for the evolution of each SP particle, and they will affect the dynamics of the whole system the more as density increases. The non-dimensional parameter to account for that is the global surface fraction

$$\phi = \frac{\pi\sigma_d^2}{4V}\,, \tag{3.10}$$

where V is the total surface available to the system.
A second global parameter is needed to account for self-propulsion. The so called *Péclet number* is commonly used for such purpose. It expresses the ratio between the work done by self-propulsion along the relevant length scale of the system and the thermal energy. Since the only *a priori* length scale for our system is the diameter σ_d of the particles, we define the Péclet number as

$$\mathrm{Pe} = \frac{F_{\mathrm{act}}\sigma_d}{k_B T}\,. \tag{3.11}$$

We will use large-scale MD simulations to analyze the phase behavior of SP disks in many details, using the constant density and constant Péclet number ensamble and thus carefully exploring interesting regions of the (ϕ-Pe) parameters' space. We will describe within the next Section the numerical method used and we will point out some relevant detail about the values of the global parameters in the range of interest. Before this, we outline in this Section some relevant features for finite density systems of SP objects.

The most important of such features is the motility-induced phase separation (MIPS), which is an aggregation without attraction driven by activity, and plays a central role in our work. We already shown in Chapter 1 some of the most fundamental characters of MIPS, dealing with kinetic approaches to the problem. The instability the triggers MIPS is a positive feedback between accumulation in the low-speed regions and slowing-down due to crowding. Because of this feedback, SP particles, regardless of their shape and the repulsive interaction, like to accumulate about denser regions, eventually driving phase separation. As a prelude to Section 3.4, we review now some relevant analytical results for phase separation that

emerge from explicit coarse-graining microscopic models of SP particles, referring to [SSW+15, SSC+18b, SSC+18a].

These works have been demonstrated that fundamental aspects of phase equilibrium of MIPS can be inferred from a generalized thermodynamic treatment, provided that the SP particles agree with some general microscopic features. Such approach descends from writing a generalized Cahn-Hilliard equation for the local density ρ of out-of-equilibrium SP particles, in the form

$$\begin{aligned} \dot{\rho} &= \boldsymbol{\nabla} \cdot (M \boldsymbol{\nabla} g[\rho]) \,, \\ g[\rho] &= g_0(\rho) + \lambda(\rho)(\boldsymbol{\nabla}\rho)^2 - \kappa(\rho)\nabla^2\rho \,, \end{aligned} \tag{3.12}$$

which can be obtained as a coarse-grained dynamics for many relevant models of SP-particles [SSC+18a]. In the equilibrium counterpart of the Cahn-Hilliard dynamics, which is gained from (3.12) in the limit of $2\lambda+\kappa' = 0$ (the prime being the derivative with respect to ρ), $g[\rho]$ is the derivative of a free-energy functional

$$g = \frac{\delta \mathcal{F}}{\delta \rho} = \frac{\delta}{\delta \rho}\left\{ \int \mathrm{d}\mathbf{r}\left(f(\rho) + \frac{\kappa(\rho)}{2}(\boldsymbol{\nabla}\rho)^2 \right) \right\} . \tag{3.13}$$

This ensures that equilibrium co-existing densities are the ones which minimize the free energy (under the constraint of constant average density) and thus the ones extracted from the common tangent construction on the bulk free energy density $f(\rho)$ (see for instance [Bra94]). The same two co-existing densities fulfill the following equal-area Maxwell construction

$$\int_{v_g}^{v_l} \left[P(v) - \bar{P} \right] v = 0 \,, \tag{3.14}$$

with v the inverse density and $\bar{P}$ the equilibrium bulk pressure, being the pressure defined as $P(\rho) = \rho f'(\rho) - f(\rho)$. The two methods are sketched in Fig. 3.2

For the out-of-equilibrium generalization (3.12), nothing guarantees that a free-energy functional exist to govern the thermodynamic behavior. Although a zero-current condition for the steady state leads to the equality of chemical potential in the two phases, there is not a common tangent construction which provides the co-existing densities [WTS+, SSC+18b]. However, it is still possible to write g as the functional derivative of a generalized free energy $\mathcal{G}$, with respect to a new variable R defined through the relation

$$\kappa R'' = -(2\lambda + \kappa')R' \,. \tag{3.15}$$

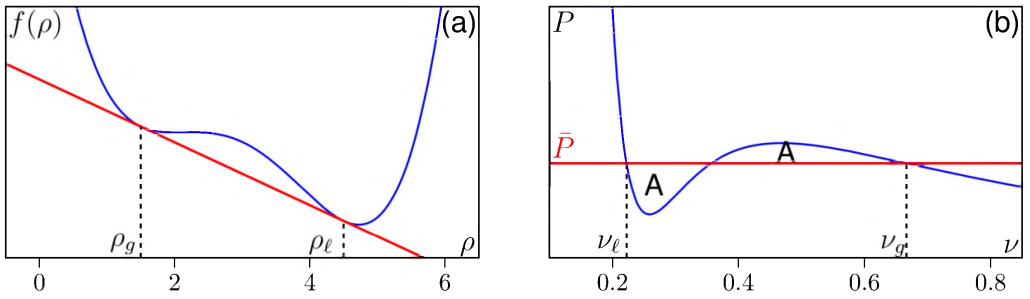

Figure 3.2: A sketch of the two thermodynamics constructions for computing the co-existing densities. (a) Common tangent construction on the free energy density $f(\rho)$. Referring to the equilibrium limit of Eq. (3.12), the free energy density is defined through the equality $f'(\rho) = g_0(\rho)$. (b) Maxwell equal-area construction on the pressure. Figure adapted from [SSC+18a].

In this way Eq. (3.12) assumes the equilibrium-like form

$$\dot{\rho} = \boldsymbol{\nabla} \cdot \left(M[\rho] \, \boldsymbol{\nabla} \frac{\delta \mathcal{G}}{\delta R} \right), \tag{3.16}$$

with

$$\mathcal{G} = \int \mathrm{d}\mathbf{r} \left[\phi(R) + \frac{\kappa}{2R'} (\boldsymbol{\nabla} R)^2 \right], \qquad \frac{\mathrm{d}\phi}{\mathrm{d}R} \equiv g_0 \tag{3.17}$$

Following this route, although dealing with a non-conserved parameter R and generalized thermodynamic functional $\mathcal{G}$ which could have no physical meaning, allows to recover a common tangent construction for the generalized free energy density ϕ. It results into reasonable co-existing densities, as shown for instance in [SSW+15, SSC+18a].

Moreover, this procedure leads to a natural definition of a generalized bulk pressure from

$$P = R \frac{\mathrm{d}\phi}{\mathrm{d}R} - \phi \, . \tag{3.18}$$

In general, it does not correspond to mechanical pressure. Although, for Active Brownian isotropic particles, it can be shown that such generalized definition of pressure surprisingly agrees with a generalized mechanical pressure, coming from an explicit construction of a microscopic stress tensor. We will shown such construction later in Section 3.4.2, because such property will crucially help us with our analysis of the phase diagram of SP disks and with building a relation between phase transition and MIPS.

3.2 Numerical integration of the Langevin equations of motion with self-propulsion

To integrate Eq. (3.1) and numerically generate the trajectories of all the N disks in the system we made large use of the software LAMMPS [lam]. This allowed us to easily simulate systems with a large number of particles, up to $\sim 10^6$ disks, by making use of the built-in algorithms for parallel calculus.
The integration algorithm implemented in LAMMPS for Brownian dynamics is the one devised in [SS78], which solves the underdamped version of our equations of motion up to the forth order in the size of the integration timestep.
The following discussion will thus deal with an Ornstein-Uhlenbeck like treatment of self-propelled motion of interacting particles, staring with the underlying deterministic dynamics and then adding, in a step-by-step way, the friction force first, the stochastic force, and next self-propulsion.

The deterministic Newton equations read

$$m_i \ddot{\mathbf{r}}_i(t) = -\boldsymbol{\nabla}_i U(\{\mathbf{r}_i\}) \,, \tag{3.19}$$

with m_i the masses of the particles.
Given the timestep Δ, forward and backward Taylor expansions up to the forth order give

$$\begin{aligned} \mathbf{r}_i(t+\Delta) &= \mathbf{r}_i(t) + \Delta\ \dot{\mathbf{r}}_i(t) + \frac{1}{2}\Delta^2\ \ddot{\mathbf{r}}_i(t) + \frac{1}{6}\Delta^3 \dddot{\mathbf{r}}_i(t) + O(\Delta^4) \,, \\ \mathbf{r}_i(t-\Delta) &= \mathbf{r}_i(t) - \Delta\ \dot{\mathbf{r}}_i(t) + \frac{1}{2}\Delta^2\ \ddot{\mathbf{r}}_i(t) - \frac{1}{6}\Delta^3 \dddot{\mathbf{r}}_i(t) + O(\Delta^4) \,. \end{aligned} \tag{3.20}$$

Adding the two expansions, it results

$$\mathbf{r}_i(t+\Delta) = 2\mathbf{r}_i(t) - \mathbf{r}_i(t-\Delta) + \Delta^2\ \ddot{\mathbf{r}}_i(t) + O(\Delta^4) \,. \tag{3.21}$$

Note that for the knowledge of $\mathbf{r}_i(t+\Delta)$, the positions $\mathbf{r}_i$ have to be known both at the timesteps t and $t-\Delta$. It is quite easy to calculate $\mathbf{r}_i(t-\Delta)$ from Eqs. (3.19) and (3.20). After having established the integration scheme for the bare positions, and moving forward to the damped deterministic equations

$$m_i \ddot{\mathbf{r}}_i(t) = -\boldsymbol{\nabla}_i U(\{\mathbf{r}_i\}) - \gamma \dot{\mathbf{r}}_i \,, \tag{3.22}$$

it is easy to see how, using the auxiliary variable $\mathbf{y}_i(t) = \mathrm{e}^{\gamma t/2m_i}\mathbf{r}_i(t)$, they can be easily brought back to the original friction-free form of Eq. (3.19)

$$\ddot{\mathbf{y}}_i = \left(\frac{\gamma}{2m_i}\right)^2 \mathbf{y}_i - \frac{\mathrm{e}^{\gamma t/2}}{m_i}\boldsymbol{\nabla}_i U(\{\mathbf{r}_i\}) \,, \tag{3.23}$$

which thus can be integrated using Eq. (3.21). The integration scheme for the true positions is therefore

$$\begin{aligned}\mathbf{r}_i(t+\Delta) = \mathbf{r}_i(t) + \Big[\mathbf{r}_i(t) - \mathbf{r}_i(t-\Delta)\Big]\, \mathrm{e}^{-(\gamma/m_i)\Delta} \\ - \frac{\Delta^2}{m_i}\mathrm{e}^{-(\gamma/2m_i)\Delta}\boldsymbol{\nabla} U(\{\mathbf{r}_i\}) + O(\Delta^4)\,.\end{aligned} \tag{3.24}$$

Adding the stochastic force accounting for the underdamped coupling with a thermal bath at temperature T, results in the following equations of motion

$$m_i\ddot{\mathbf{r}}_i(t) = -\boldsymbol{\nabla}_i U(\{\mathbf{r}_i\}) - \gamma\dot{\mathbf{r}}_i + \boldsymbol{\eta}_i(t)\,, \tag{3.25}$$

where, η_i^α with α running over the cartesian coordinates, are Gaussian-distributed zero-mean noises with amplitude

$$\langle \eta_i^\alpha(t)\, \eta_j^\beta(t')\rangle = 2\gamma k_B T \delta_{ij}\delta^{\alpha\beta}\delta(t-t')\,. \tag{3.26}$$

For this discrete-time Gaussian distributed Markov process, the times t_k separating two pulses are exponentially distributed according to

$$p(t_k) = \frac{1}{\tau}\mathrm{e}^{-t_k/\tau}\,, \tag{3.27}$$

with τ the average time separation between two pulses. The probability p that a pulse acts within the integration timestep Δ is thus $p \simeq \Delta/\tau$.
An ansatz for the process $\boldsymbol{\eta}$ which verifies these properties is the following

$$\eta_i^\alpha = A\sum_k \delta(t-t_k)\, \Gamma_i^\alpha(t_k)\, \Theta(p - a_{ik}^\alpha)\,, \tag{3.28}$$

where k labels the timesteps, $\Gamma_i^\alpha(t_k)$ are Gaussian distributed random numbers, and a_{ik}^α are random number uniformly distributed in the interval $(0,1)$. To recover the desired thermal behavior for the noise in (3.25), long-time correlations have to be extracted, given the form (3.28). Using the properties of the Gaussian random numbers, one gets

$$\begin{aligned}\langle \eta_i^\alpha(t)\, \eta_j^\beta(t+\tau)\rangle &= \lim_{S\to\infty}\int_0^S \mathrm{d}t\, A^2 \sum_{k,k'}\delta(t-t_k)\delta(t-t_{k'}+\tau) \\ &\qquad \langle \Gamma_i^\alpha(t_k)\, \Gamma_j^\beta(t_{k'})\, \Theta(p-a_{ik}^\alpha)\, \Theta(p-a_{jk'}^\beta)\rangle \\ &= \lim_{S\to\infty}\frac{A^2}{S}\int_0^S \mathrm{d}t \sum_k \delta(t-t_k)\delta(t-t_k+\tau)\, p\, \delta^{\alpha\beta}\delta_{ij} \\ &= \lim_{N\to\infty}\frac{A^2}{N\Delta}\, p\, N\delta^{\alpha\beta}\,\delta_{ij}\delta(\tau)\,.\end{aligned} \tag{3.29}$$

Comparing this result with the expected correlation for the noise, it is immediate to obtain

$$A = \sqrt{\frac{2\gamma k_B T \Delta}{p}} \,. \tag{3.30}$$

Considering the variation of the velocity over an small enough time interval $\epsilon \to 0^+$ due to the noise, from Eq. (3.25), it results that

$$\delta \dot{r}_i^\alpha(t) = \sqrt{\frac{2\gamma k_B T}{m_i^2 p}} \Delta \; \Gamma_i^\alpha(t) \; \Theta(p - a_i^\alpha) \,. \tag{3.31}$$

Velocity varies also due to friction according to $\dot{r}_i^\alpha(t+\delta t) = \dot{r}_i^\alpha(t) \mathrm{e}^{-(\gamma/m_i)\delta t}$. This, integrating the whole variation of the position along one timestep, gives

$$\delta r_i^\alpha(t+\Delta) = \delta \dot{r}_i^\alpha(t) \; \Delta \; \mathrm{e}^{-(\gamma/2m_i)\Delta} \,. \tag{3.32}$$

Adding this variation to the total variation (3.24), the full integration scheme is obtained

$$\begin{aligned} \mathbf{r}_i(t+\Delta) = \mathbf{r}_i(t) + \Big[\mathbf{r}_i(t) - \mathbf{r}_i(t-\Delta)\Big] \, \mathrm{e}^{-(\gamma/m_i)\Delta} \\ - \frac{\Delta^2}{m_i} \, \mathrm{e}^{-(\gamma/2m_i)\Delta} \left[\nabla U(\{\mathbf{r}_i\}) + \sqrt{\frac{2\gamma k_B T}{m_i^2 p \Delta}} \, \boldsymbol{\Gamma}_i(t) \; \Theta(p - \mathbf{a}_i)\right] . \end{aligned} \tag{3.33}$$

Finally, in order to complete the integration of the active dynamics, we have added the self-propulsion forces of the form $\mathbf{F}_{\mathrm{act,i}}(t) = F_{\mathrm{act}} \mathbf{n}_i(t)$ to the sum of all the forces computed with the previous algorithm for the passive case. Given the equation (3.1) for the directions $\mathbf{n}_i$, since the processes of the increments $\Delta\theta_i$ are Wiener processes of amplitude $2D_\theta$, it is easy to compute the values of the angles $\theta_i(t)$ at any given time by taking at the time $t = 0$ the initial θ_i^0s at random and then calculating

$$\theta_i(t) = \theta_i^0 + \Delta\theta_i(t) \,, \tag{3.34}$$

with the $\Delta\theta_i(t)$s sampled from a Gaussian distribution with zero mean and variance $2D_\theta t$.

It must be said that, whereas the integration scheme described above and used for all the simulations is a forth-order algorithm for the underdamped equations of motion, where thus the dynamic variables are the particles' positions, we instead adopted for the theoretical treatment of the problem an overdamped Langevin equation, as in (3.1). However, for the

entire portion of parameters' space explored, we ensured the dynamics to evolve in a strong viscous regime, being hence safe in disregarding all the inertial effects. To be quantitative, a Reynolds number can be defined for our system of active particles, taking into account the balancing between self-propulsion strength and friction, as follows:

$$\mathrm{Re}^{\mathrm{act}} = \frac{\rho L v_0}{\gamma} = \frac{m F_{\mathrm{act}}}{\gamma^2 \sigma_d}, \tag{3.35}$$

being ρ the density, L the characteristic length of the system which is the diameter σ_d of the disks, v_0 the self propulsion velocity as defined in (3.9), and m the mass of the particles. Then, taking care keeping $\mathrm{Re}^{\mathrm{act}}$ low, both inertia-to-friction (ruled by m/γ) and activity-to-friction ratios would be small enough for all our purposes.

The numerical stability of the integration procedure is instead strongly limited by the ratio between both temperature and self-propulsion force over the pair interaction strength. Particularly for our stiff core interactions, if any of the two leads to some excessive overlaps between two particles within one integration timestep, the potential energy would readily diverge. Both these two instability sources are carefully avoided by choosing a small enough timestep, depending to the temperature and the activity used.

Given that we used the mass m of the particles, their diameter σ_d and the energy scale ε of the potential as reference units, all the other quantities are expressed in terms on one combination of these three. Since for all the simulations (except where otherwise indicated) we kept the temperature constant at $k_B T = 0.05$ (in units of ε), and we pushed self-propulsion force to a maximum value of 10 (in units of ε/σ_d), a safe choice of the integration time, considering the issues above, is $\Delta t = 0.001$. Even with this small value of the step, which considerably raises the computational efforts needed, thanks to the powerful performance optimization of LAMMPS, we managed to thinly span the whole interesting range of global parameters simulating systems of up to 10^6 particles.

3.3 A two-step melting scenario for SPPs

After having outlined the key properties of the AB disks model and described with many details the numerical procedure used, we now start handling the results obtained. Within this Section all the tools that we used for the analysis of the configurations as well as the way of representing

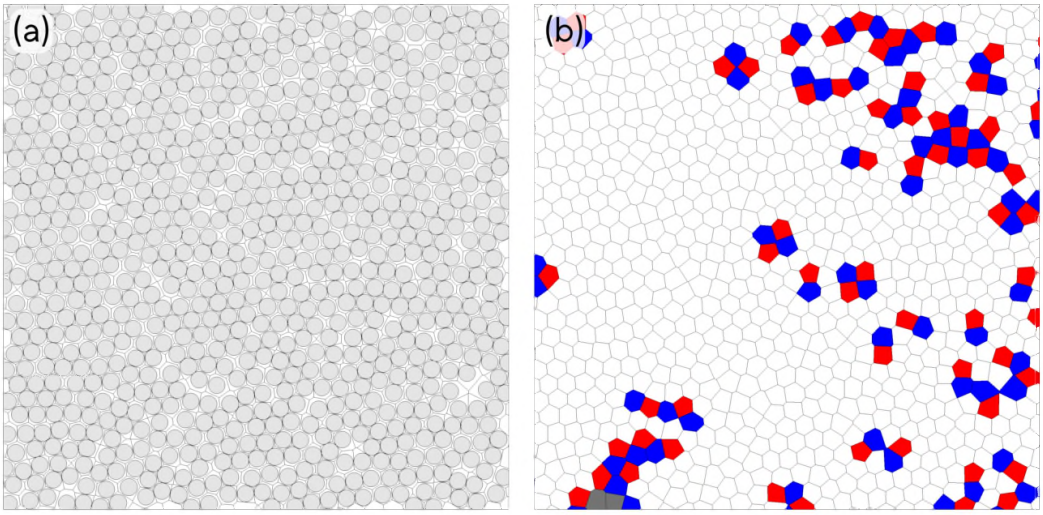

Figure 3.3: (a) - Voronoi tessellation for an arrangement of disks. Each disk has its Voronoi region, that delimits the portion of space around it of the points that are closer to it than to any other. (b) - The Voronoi construction defines colloids' neighborhood. Taking the i-th disk and its cell, we choose as its neighbors all other disks whose cell have one side in common with the i-th cell. Cells are colored according to the coordination number of the disks: disks with five neighbors belong to cells with five sides and are colored in red, in blue the cells with seven neighbors and in gray all the other cases.

all the physical quantities of interest will be explained first. Then, moving on examining the liquid-hexatic-solid phase transition scenario, some of the regions of the full phase diagram will be mapped out considering structural measurements over many configurations of disks from constant density and constant Péclet number simulations. Finally, the phase diagram will be then complete in Section 3.5, adding information about the nature of the phase transition found, and considering motility-induced phase separation as well.

First-neighbors identification with Voronoi tessellation

A first need when dealing with analysis of structure in solids, is to establish a next-neighbors network for particles. Especially to deal with local positional and orientational order, that is actually the case for our purposes, the way to settle next-neighbors pairs is of crucial importance. See in this regards, how significant is this to define the local hexatic parameter defined in (2.49), that of course will determine the existence of an hexatic phase, as predicted for the equilibrium system within the HN theory of melting.

The so-called *Voronoi tessellation* is a method to unambiguously carry

out this task. It associates a portion of the available space to each particle, comprising all the points that are closer to the particle than to any other one. Fig. 3.3 shows a Voronoi tessellation of the space for a generic configuration of disks, which thus allows, once the whole available surface is partitioned, to define two particles to be neighbors if they share one side of their polygonal cells. As also shown in Fig. 3.3, this procedure provides the coordination number of each particle. As we will see later, this will be of great importance for identifying topological defects throughout the sample, which, as established with the HN theory, play a fundamental role in the melting because their formation/annihilation is responsible of driving phase transitions.

From Voronoi diagram we can also easily extract a local surface fraction measure. In fact, since every bead has its Voronoi region, the local value of the surface fraction at the position $\mathbf{p}_i$ of a particle is given by the ratio between the surface of the particle S_i and the surface $S_i^{(\mathrm{cell})}$ of the cell:

$$\phi(\mathbf{p}_i) = \frac{\pi(\sigma_d/2)^2}{S_i^{(\mathrm{beads})}} \,. \tag{3.36}$$

In Fig. 3.4 is shown an example for this procedure. Although very easy, this estimation of the local density of the system has an extreme local nature, and then it results in a strongly fluctuating density profile. When the estimation of the density is made through this method, a successive coarse-graining procedure has to be performed, in order to suppress the larger fluctuations and recover a smoother density profile.

Local hexatic parameter

After having assigned the Voronoi tessellation to one configuration of disks, we are thus able to compute the local bond-orientational order (2.49), which, as explained before, provides a quantitative measure of the local orientational six-fold periodicity of the system.

From (2.49), one can immediately recognize that

$$\psi_{6,i} = \sum_{j \,\in\, \mathrm{nn(i)}}^{N_i} \mathrm{e}^{6\mathrm{i}\theta_{ij}} \tag{3.37}$$

is a complex parameter and can therefore be identified with its absolute value $|\psi_{6,i}|$ and its phase $\arg(\psi_{6,i})$. If neighbors of the particle i are arranged on a perfect triangular lattice, $\psi_{6,i}$ gains of course its maximum unit modulus and its phase rotates by 2π as the lattice is rigidly rotated by an angle

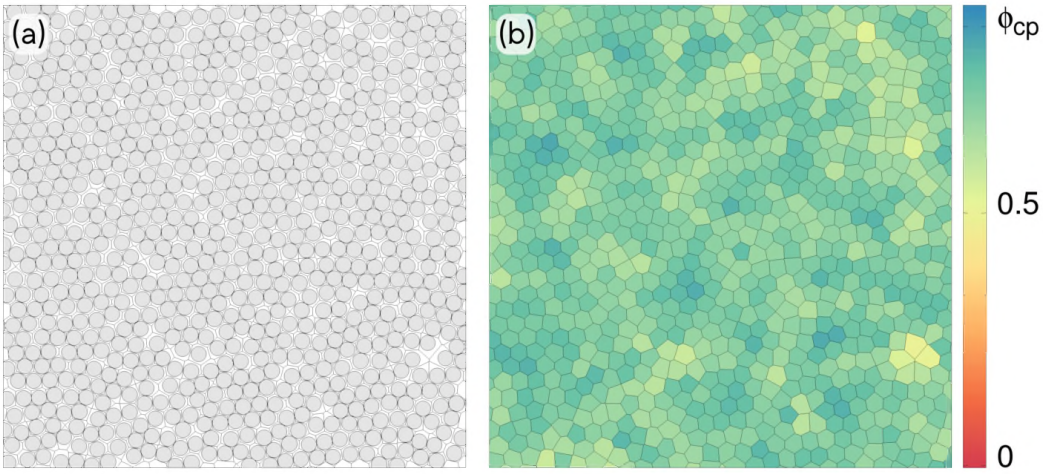

Figure 3.4: (a) - Voronoi tessellation. (b) - The local values of the surface fraction, as defined in the text, are plotted using the color gradient shown on the right. ϕ_{cp} in the color axis is the close-packing fraction for hard disks ($\phi_{cp} \approx$).

of $\pi/3$. Obviously, this property comes from the $\pi/3$-periodicity for an hexagon under rotation on the plane. However, $\psi_{6,i}$ is equal to one, even for a translational disordered arrangement, provided that orientations of the bonds are periodically arranged. Referring to Fig. 3.5 (a), this means that hexatic order would not change if neighbors particles moved along the dashed lines.
For a non-periodic arrangement of nearest neighbors $|\psi_{6,i}| \leqslant 1$, and the orientation in the complex plane does not generally have a simple relation with the orientation of the bonds. Although the hexatic parameter would need a two-components representation, as the one shown in Fig. 3.5, a useful color view of $\psi_{6,i}$ is obtained by the projection of $(\mathrm{Re}\,\psi_{6,i}, \mathrm{Im}\,\psi_{6,i})$ onto the direction $\hat{\Psi}_6$ of the sample-averaged $\arg\left(\sum_i \psi_{6,i}/N\right)$. So, in Fig. 3.5 (d) red particles have local hexatic of modulus one and direction along the average direction $\arg(\hat{\Psi}_6)$, while blue particles have local hexatic of modulus one and direction perpendicular to the average hexatic. Green particles are either particles of zero $|\psi_{6,i}|$ or they have non-zero $|\psi_{6,i}|$ and direction $\pi/4$ away from the average hexatic. We will discuss this ambiguity time by time whenever it will be necessary.

Orientational order and the hexatic phase

Starting from all the well-established results for passive hard-disks [BK11], we have carefully examined how activity affects the phase behavior of our 2D systems of isotropic particles. To achieve this target, we performed

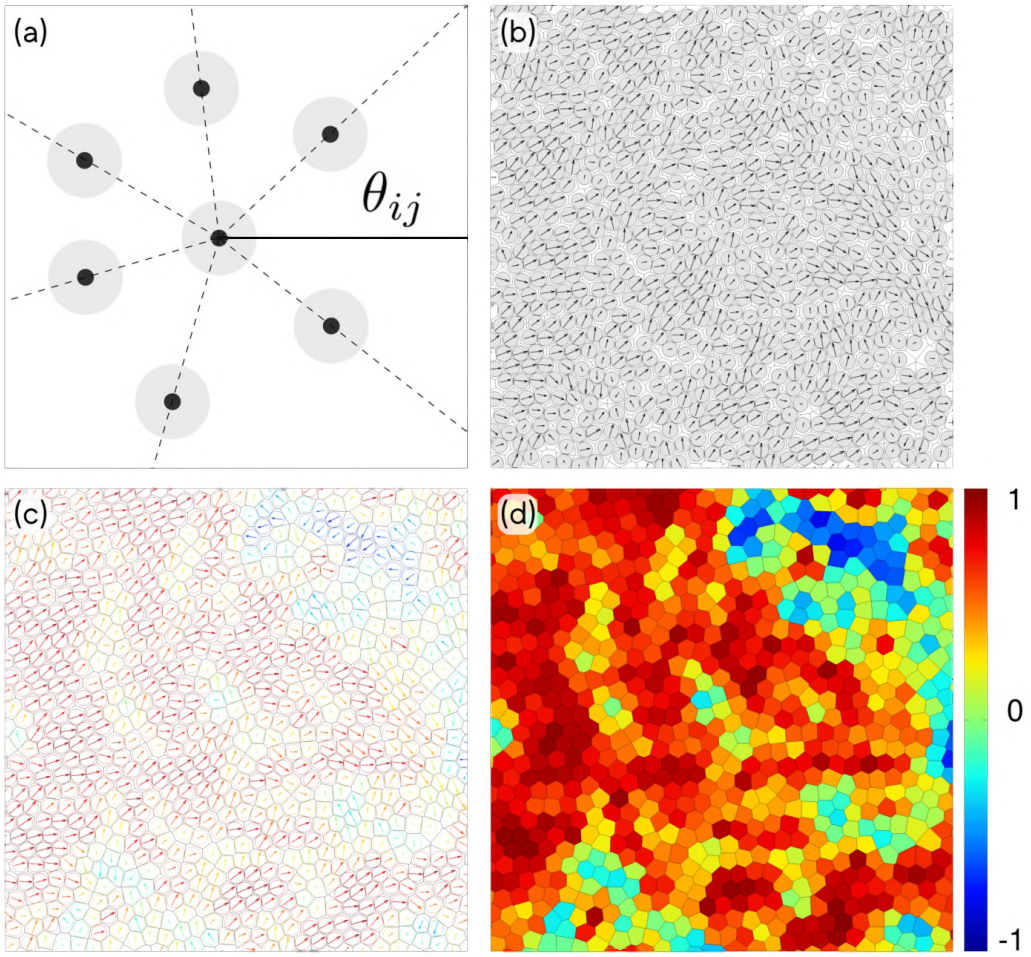

Figure 3.5: (a) - Local six-fold orientational order concerns the directions of the bonds between pairs. (b) - The value of the local hexatic parameter is computed locally. It is a complex number by definition, so the arrows are in their complex plane, with the real axis along the horizontal and the imaginary axis along the vertical. (c) - A color code is chosen, which represents the projection of the local hexatic parameter onto the sample orientation. (d) - Colors are assigned to the corresponding Voronoi cells. This is what we actually plot wherever a local hexatic map is shown. This procedure is inspired from [BK11].

simulations at fixed packing fraction and activity, exploring the (ϕ, Pe) space from the dilute regime to close packing ($\phi_{\mathrm{cp}} \approx 0.91$) and for $\mathrm{Pe} \gtrsim 0$ to $\mathrm{Pe} = 200$.

Knowing that liquid-hexatic transition is present in the passive case, as a first focus, we thus wanted to tell whether it still exists with activity. As we mentioned in the introduction to this Chapter, there are no theoretical predictions ensuring that for high enough values of the packing fraction a hexatic order would establish. However, some previous numerical in-

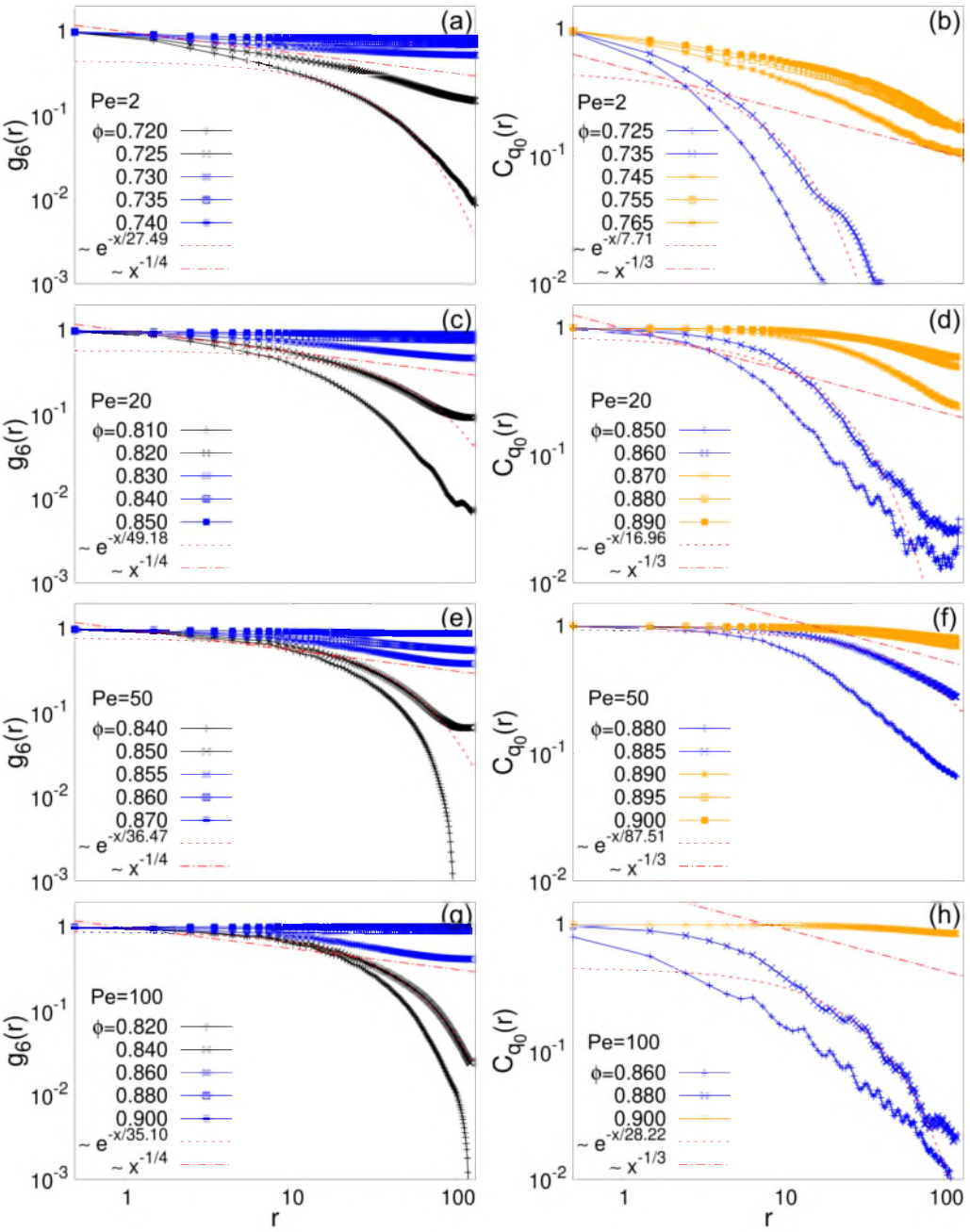

Figure 3.6: Hexatic correlation functions (see Eq. (3.38)) and positional correlation functions (see Eq. (3.39)) side by side for Pe= 2, 20, 50, 100. Global packing fraction values are given in the key. We used black curves for points in the liquid, blue curves in the hexatic phase, and orange curves in the solid.

vestigation of dense arrangements of active particles already suggested that pushing the packing fraction of the system toward the close-packing limit would force the system to reach a highly order structure (see for example [BSL12]). Therefore, even without any underlying theory, but having in mind the two-step Krauth scenario, we aimed to check whether the bond-orientational symmetry of the isotropic active liquid could break, driving the system into a anisotropic hexatic phase.

Thus, according to the description of the hexatic phase reported in Section 2.2.1, we put to the test whether the hexatic correlation function

$$g_6(r = |\mathbf{r}_j - \mathbf{r}_k|) = \frac{\langle \psi_6(\mathbf{r}_j)\psi_6(\mathbf{r}_k)\rangle}{\langle \psi_6^2(\mathbf{r}_j)\rangle} \tag{3.38}$$

are allowed to decay algebraically, which implies a diverging hexatic correlation length and thus hexatic QLRO.

The results of such analysis are given in the first column of Fig. 3.6 for Pe $= 2, 20, 50, 100$. This picture unambiguously demonstrates that, for the entire range of activity explored, the system undergoes a liquid-hexatic phase transition at a given value of the global surface fraction ϕ_i. Regardless the strength of activity, increasing the density of the system drives the settling of a QLR six-fold bond-orientational order with algebraic correlation functions. We also highlighted in the plots the critical exponent $r^{-1/4}$ (see Eq. (2.61)) of the equilibrium HN theory, and we observe that it quite agrees with our location of the melting from simple observations of the decaying of the correlation functions. It is worth saying that no *a priori* expectations exist for the critical value of the exponent and that thus the red dashed curves in Fig. 3.6 are only considered as a reference. However, they certainly suggest that our liquid-hexatic transition quite resembles the one predicted by Halperin and Nelson.
Furthermore, from Fig. 3.6 is also evident that the liquid-hexatic transition area surface fraction ϕ_i moves towards higher values as activity is increased from zero.

Positional order and the solid phase

Further increasing the packing fraction above the liquid-hexatic transition we move forward, asking whether the second step of a HN-like scenario would take place, *i.e.* if the hexatic phase would crystallize at $\phi_m > \phi_i$ into a 2D solid with QLR translational order and true LR orientational order.

This would be compatible with saturation of $g_6(r)$ (see Eq. (3.38)) to large scales above ϕ_m because hexatic order is true-long-ranged in the

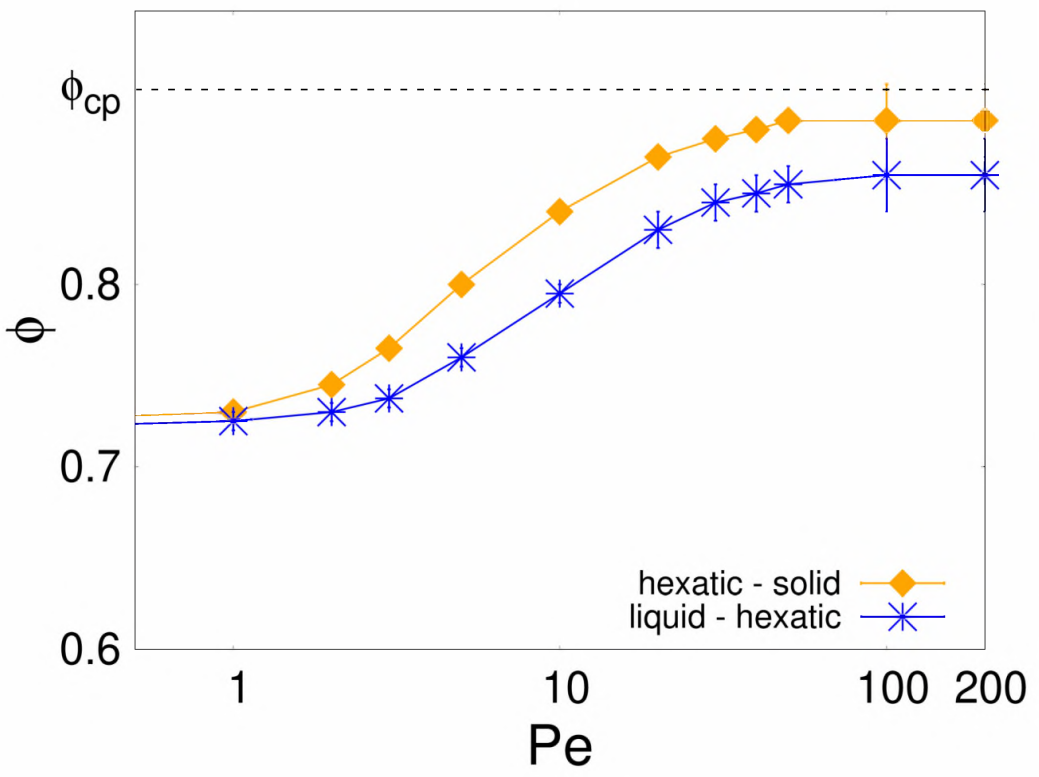

Figure 3.7: Solid-hexatic melting (orange points) and hexatic-liquid melting (blue points) are given for all the values of activity considered in the (Pe − ϕ) space.

solid. However, since, as we said, hexatic correlation functions decay as power laws even below ϕ_m, is quite hopeless to locate the point where they cease decaying, unless for very large system size which is very beyond any numerical capability. Much better is to look at the positional order, which instead would establishes above ϕ_m as QLR order. In the second column of Fig. 3.6, positional correlation functions

$$C_{\mathbf{q}_0}(r) = \langle e^{i\mathbf{q}_0\cdot(\mathbf{r}_i-\mathbf{r}_j)}\rangle \tag{3.39}$$

are shown for the same values of Pe as before, which allow us to access the translational periodicity of the sample and, according to HN picture, algebraically decay in the solid (see Eq.(2.46)).

As well as for the hexatic, regardless the strength of self-propulsion, the system crystallizes. The phase transition is signalled in Fig. 3.6 with changing the color of the curves from blue to orange across the the hexatic-solid transition.

From these two observations, we conclude that self-propulsion doesn't

affect the overall melting scenario for the hard-disks system. It is very interesting to see that both the hexatic and the solid exist as pure phases for all the values of Pe explored. Together with the liquid-hexatic transition, also the this second step to the solid is continuously pushed towards higher packing fraction with increasing the self-propulsion strength.

This is clear from Fig. 3.7, where we see both the two values ϕ_i and ϕ_m monotonically moving to denser regions as activity increases. This behavior has an intuitive, but still not characterized so far, interpretation. An increasing activity, and consequentially greater persistency in the motion, is able to melt an ordered structure. This results is quite in agreement with all the conclusions about effective temperature in active systems [LMC08, LMC11a, LMC11b], which all demonstrate how the greater is the activity that drives the system out of equilibrium, the higher is the effective temperature extracted from the amount of violation of fluctuation-dissipation theorems. We also shown that, in the same way, self-propulsion allows the particles to move persistently, which results in an augmented diffusion coefficient at long times, with respect to passive brownian diffusion.

We can not exclude, as a matter of principle, that at very high values of packing fractions above ϕ_m or activity beyond the range considered, true positional order will appear. Although this is strongly forbidden by the Mermin-Wagner theorem at equilibrium, there is not a counterpart of such theorem in the non-equilibrium realm that rules out this possibility. This had been firmly pointed out in very early studies on active systems [TT95] to justify findings on very large-scale collective behaviors, such as global alignments and swarming. Even if we are not able to check such hypothesis within our investigations because this would require an accurate knowledge of the very long-range behavior of positional correlation function, we are convinced that is fair enough to state that we did not find any evidences of that, not event for packing fraction really close to maximum packing allowed for our system. We always observe indeed a small decaying of translational correlation functions, in accordance with absence of true LR positional order.

3.4 The nature of the hexatic-liquid melting

Starting from the information included in Fig. 3.7 about bond-orientational and translational order of our system, we can move now to examine the nature of the two phase transitions involved, based on the evidences for hard-disks without propulsion.

3.4.1 First order hexatic-liquid melting for passive disks

In Chapter 2, besides an extended review of the HN theory for melting in two dimensions, we have been presented a selection of works which have been aiming to put to the test such theory into a wide range of 2D systems. In view of its accuracy and the experimental confirmations in [TAAD17], the analysis performed by the Krauth's group is to date trusted to have brought a nearly conclusive understanding of the nature of the phase transition scenario for a large class of systems living in two spatial dimensions, which includes systems with short-range repulsive pairwise interactions. Due to its simplicity, the hard-disks model is a paradigmatic representative of this class. In summary, these results support the HN scenario of a double-step transition and predict a first-order nature for the hexatic-liquid melting.

The main point that allowed to confirm the discontinuous behavior for hexatic-liquid transition was the analysis of the equation of state (EOS) by means of the measurement of the thermodynamic pressure. The non-monotonic behavior of the EOS is indeed one of the key features of a discontinuous phase transition, as well explained in the famous paper by Mayer and Wood [MW65]. Non-monotonicity of the pressure, resulting in a loop-shaped EOS across the phase transition, is strongly related for finite-size experiments to the presence of interfaces between the two pure phases, which are allowed to coexist at a first-order phase transition. The two branches of the Mayer-Wood loop are thermodynamically stable, but they disappear in the limit of infinite size, as surface effects become negligible.

Actually, it is known that the presence of a Mayer-Wood loop in the equation of state is observed in systems showing a first-order transition as well as systems with a continuous transition. However, the behavior of the loop in the two cases is different with increasing system size. Since first-order phase transitions show stable co-existence between the two pure phases, the loop across the coexistence region arises from the interface free energy F. In two dimensions, the interface free energy per disk $\Delta f = \Delta F/N$ scales as $f \propto N^{-1/2}$ with the system size. Thus, although the loop disappears in the thermodynamic limit, the EOS remains non-monotonic and it collapses to the co-existence pressure given by the *Maxwell construction*. In contrast, for a continuous transition f decays faster because it only arises from bulk contributions, meaning that $f \propto N^{-1}$. This leads to a thermodynamically unstable loop and therefore the equation of state to become monotonic for large enough system size.

As shown in Fig. 3.8 (a), thanks to the finite-size behavior of the equation of state, Krauth *et al.* [BK11] had been able to recognize the first-order nature

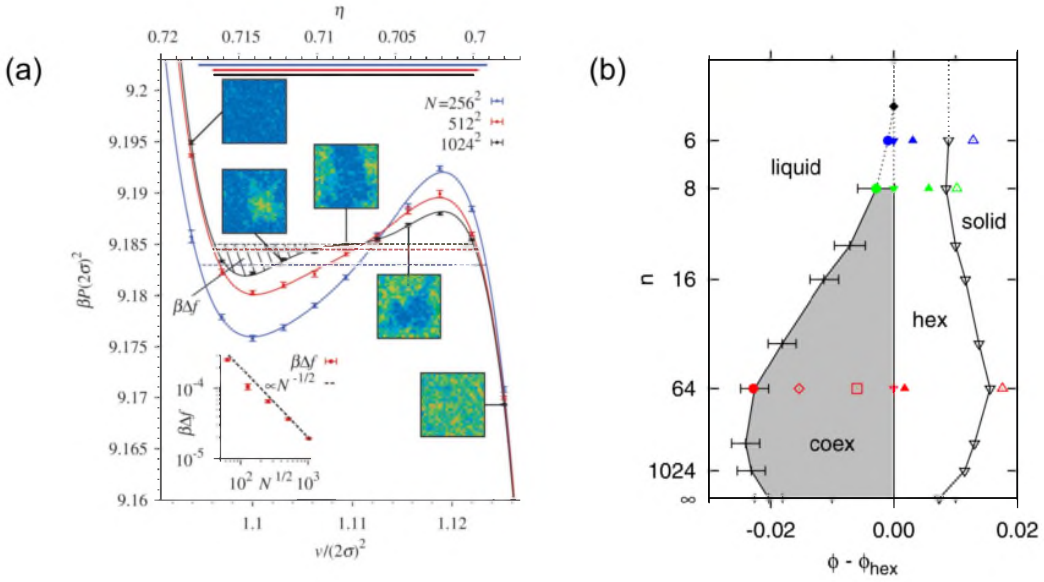

Figure 3.8: (a) Equilibrium equation of state for hard disks. The pressure is plotted vs volume per particle ($v = V/N$) (lower scale) and density η (upper scale). In the coexistence region, the strong system-size dependence stems from the interface free energy. The Maxwell constructions (horizontal lines) suppress the interface effects for each N. The interface free energy per disk $\beta\Delta f$ (hatched area) scales as $1/\sqrt{N}$ (see inset). Figure adapted from [BK11]. (b) Phase behavior of r^{-n} soft disks for $n \geqslant 6$. Phase diagram as a function of density ϕ relative to the density ϕ_{hex} of the pure hexatic at coexistence. The non-monotonic liquid-hexatic coexistence interval vanishes around $n = 6$. Figure adapted from [KK15].

of the hexatic-liquid transition verifying the $\propto \sqrt{N}$ scaling of the interface free energy per disk by means of large scale Monte Carlo simulations.

Besides, Kapfer and Krauth [KK15] had been also demonstrated that first-order liquid-hexatic transition is not a universal results for melting of passive disks, but it strongly depends on the shape of the inter-particle interactions. They have been investigated this dependence, systematically studying, by computer simulations, the KTHNY scenario for a wide range of repulsive power-law and Yukawa potentials. Fig. 3.8 (b) shows a graphical summary of their work, with liquid-hexatic coexistence region spreading and shrinking, upon varying the exponent in the power-law repulsive pair interaction core.

This result is quite important for our purposes because it shows that, though the NH two-step melting is a robust scenario for a wide range of system of disks with short-range interactions, the nature of liquid-hexatic transition is instead strongly system-dependent and much sensitive to the microscopic details of the inter-particle interaction. We aim thus to extend

such analysis taking into account the activity, as another parameter along which to consider universality in the nature of liquid-hexatic and hexatic-solid phase transitions.

3.4.2 Pressure of a SP disks system

The analysis of the local order parameters shown in Section 3.3 allowed us to establish, within the underlying HN picture, whether the active system is in the solid phase, in the hexatic, or in the isotropic liquid. However, the mere study of long-distance order of the system does not provide information about the nature of the phase transitions between the phases. Although one would be tempted to say that, since the global scenario for the whole range of activity explored agrees with the HN prescriptions, the phase transitions would also meet those predictions and thus they would be of a HN type, this is not of course the case. Indeed, as seen above, even for the simple hard-disk model at equilibrium, the hexatic-liquid transition is of first-order, and we thus have asked ourselves whether this is also the case within our context.

We have been able to answer this question, because it recently came out that a well defined equation of state exists also for self-propelled isotropic particles. We will outline how this generalized equation of state can be built up and why it can be defined only for isotropic SP particles. Finally, we will summarize some of the recent properties of active disks that was extracted from the EOS.

Takatori *et al.* [TYB14] argued that self-propulsion could be responsible of an extra term in the equation of state of an active system. They accordingly called it *swim pressure*, and they studied some of its consequence as a extra-pressure. The full strategy to obtain a formulation of the pressure for ABPs appeared for the first time in [WWG15]. They proved that, starting from the equation of motion of N self-propelled disks, a *virial-like* EOS can be constructed, that is well-defined in the sense that Irving and Kirkwood prescribed [IK50]. This means that the stress tensor extracted from the microscopic equation of motion satisfies the right conservation laws into the corresponding coarse-grained description.

We start outlining this procedure, which is well reviewed in [Pet17], writing again the Langevin equation of motion, being $\mathbf{n}_i = (\cos\theta_i, \sin\theta_i)$ the self-propulsion direction,

$$\dot{\mathbf{r}}_i(t) = v_0\mathbf{n}_i(t) + \frac{1}{\gamma}\mathbf{F}_i(t) + \frac{1}{\gamma}\boldsymbol{\xi}_i(t), \quad \dot{\theta}_i(t) = \sqrt{2D_\theta}\,\eta_i(t)\,, \tag{3.40}$$

where $\mathbf{F}_i$ is now the total force acting on the i-th particle and, again

$$\begin{aligned} &\langle \boldsymbol{\xi}_i \rangle = 0 \,, \quad \langle \boldsymbol{\xi}_i(t)\, \boldsymbol{\xi}_j(t') \rangle = 2\gamma^2 D_0\, \mathbf{1}\, \delta_{ij}\delta(t-t') \,; \\ &\langle \eta_i \rangle = 0, \quad \langle \eta_i(t)\, \eta_j(t') \rangle = \delta(t-t') \,, \end{aligned} \tag{3.41}$$

with $D_0 = k_B T/\gamma$ the translational diffusion coefficient in the dilute passive limit already evaluated before, and, we remind, $v_0 = F_{\mathrm{act}}/\gamma$.

Multiplying the equation for of motion by $\mathbf{r}_i$ and taking the average over different realizations of the stochastic process, the following equation is obtained:

$$\langle \dot{\mathbf{r}}_i(t) \cdot \mathbf{r}_i(t) \rangle = v_0 \langle \mathbf{n}_i(t) \cdot \mathbf{r}_i(t) \rangle + \frac{1}{\gamma} \langle \boldsymbol{\xi}_i(t) \cdot \mathbf{r}_i(t) \rangle + \frac{1}{\gamma} \langle \mathbf{F}_i(t) \cdot \mathbf{r}_i(t) \rangle \,. \tag{3.42}$$

The pressure is defined from the virial of the forces exerted by the walls on the confined system as follows:

$$P = -\frac{1}{2V} \sum_i^N \langle \mathbf{F}_i^{\mathrm{wall}} \cdot \mathbf{r}_i \rangle \,, \tag{3.43}$$

with V the volume inside the walls. This definition makes use of the assumption that the pressure is homogeneous throughout the system, though it is not always true for systems out of thermal equilibrium. However, Winkler *et al.* [WWG15] demonstrated that this requirement is not necessary for system of isotropic particles interacting over a short range with walls and if walls have some simple geometry, like the squared one that we used for our simulations.

Then, taking $\mathbf{F}_i = \mathbf{F}_i^{\mathrm{int}} + \mathbf{F}_i^{\mathrm{wall}}$ in (3.42) and using (3.43), the pressure reads

$$2PV = -\gamma \sum_i \langle \dot{\mathbf{r}}_i \cdot \mathbf{r}_i \rangle + \gamma v_0 \sum_i \langle \mathbf{n}_i \cdot \mathbf{r}_i \rangle + \sum_i \langle \boldsymbol{\xi}_i \cdot \mathbf{r}_i \rangle + \sum_i \langle \mathbf{F}_i^{\mathrm{int}} \cdot \mathbf{r}_i \rangle \,. \tag{3.44}$$

In a confined motion, the term

$$\sum_i \langle \dot{\mathbf{r}}_i(t) \cdot \mathbf{r}_i(t) \rangle = \frac{1}{2} \frac{\mathrm{d}}{\mathrm{d}t} \sum_i \langle \mathbf{r}_i^2(t) \rangle \propto D \tag{3.45}$$

vanishes. Moreover, using the formal solution to the equation of motion

$$\mathbf{r}_i(t) = \mathbf{r}(-\infty) + \int_{-\infty}^{t} \mathrm{d}t' \left(v_0 \mathbf{n}_i(t') + \frac{1}{\gamma} \boldsymbol{\xi}_i(t') \right) . \tag{3.46}$$

it is easy to see, given that the two noises $\boldsymbol{\xi}$ and η are not correlated, that

$$\langle \boldsymbol{\xi}_i(t) \cdot \mathbf{r}_i(t) \rangle = 2k_B T \,. \tag{3.47}$$

Thus, the pressure becomes

$$P = \frac{Nk_BT}{V} + \frac{\gamma v_0}{2V}\sum_i \langle \mathbf{n}_i \cdot \mathbf{r}_i \rangle + \frac{1}{4V}\sum_{ij} \langle \mathbf{F}_{ij} \cdot \mathbf{r}_{ij} \rangle \,, \tag{3.48}$$

which only depends on bulk properties of the system and that can thereby be used as an equation of state. The first term is the ideal gas contribution P_0, the third is the virial term P^{int} that accounts for interactions between particles as the system departs from the ideal gas behavior, while the second term P^{swim} is the active term that we mentioned before as *swim pressure*.
In the dilute regime, this swim pressure can be easily evaluated by using a result for the correlations of self-propulsion direction given at the beginning of this Chapter (see Eq. (3.7)) and the solution (3.46):

$$\langle \mathbf{n}_i(t) \cdot \mathbf{r}_i(t) \rangle = v_0 \int_{-\infty}^{t} \mathrm{d}t' \, \langle \mathbf{n}_i(t) \cdot \mathbf{n}_i(t') \rangle = v_0 \int_{-\infty}^{t} \mathrm{d}t' \, \mathrm{e}^{-D_\theta (t-t')} = \frac{v_0}{D_\theta} \,. \tag{3.49}$$

Thus the whole pressure in the dilute active regime becomes

$$P_0^{\text{act}} = P_0 + P_0^{\text{swim}} = \rho k_B T + \frac{\gamma \rho v_0^2}{2D_\theta} = \rho k_B T_{\text{eff}} \,. \tag{3.50}$$

The dilute active gas thus resembles an ideal gas with a effective temperature

$$T_{\text{eff}} = T\left(1 + \frac{v_0^2}{2D_0 D_\theta}\right), \tag{3.51}$$

that of course depends on the activity.

The definition of the pressure has been thus extended to confined system of SP Brownian particles. We nevertheless would need a method to compute a pressure for a system with periodic boundary conditions. This had been achieved in [WWG15], from a calculation devised for the same purpose in a passive equilibrium system [WMY92].

Eq. (3.42) for periodic systems after summing over particles reads

$$\frac{1}{2}\sum_i \frac{\mathrm{d}}{\mathrm{d}t}\langle \mathbf{r}_i^2(t) \rangle = \frac{2Nk_BT}{\gamma} + v_0 \sum_i \langle \mathbf{n}_i(t) \cdot \mathbf{r}_i(t) \rangle + \frac{1}{2\gamma}\sum_{ij}\sum_{\mathbf{k}} \langle \mathbf{F}_{ij}^{\mathbf{k}}(t) \cdot \mathbf{r}_{ij}(t) \rangle \,, \tag{3.52}$$

where no walls exist now, but the i-th particle in the primary box interacts with both all the other particles in the same box and with all the periodic images in the repeated boxes, labeled with $\mathbf{k} \in \mathbb{Z}$.

Since the motion is not limited anymore, the left-hand side term does not vanish, but it gives a contribution proportional to the diffusion coefficient D. Subtracting to both the two sides the term

$$\frac{1}{2}\sum_{ij}\sum_{\mathbf{k}}\langle \mathbf{F}_{ij}^{\mathbf{k}}\cdot\mathbf{R}_{\mathbf{k}}\rangle\,, \tag{3.53}$$

with $\mathbf{R}_{\mathbf{k}}$ indicating the position of the periodic box $\mathbf{k}$ with respect to the primary one, two equal quantities arise:

$$\begin{aligned} P_i &= \frac{Nk_BT}{V} + \frac{\gamma v_0}{2V}\sum_i\langle \mathbf{n}_i\cdot\mathbf{r}_i\rangle + \frac{1}{4V}\sum_{ij}\sum_{\mathbf{k}}\langle \mathbf{F}_{ij}^{\mathbf{k}}\cdot(\mathbf{r}_i-\mathbf{r}_j-\mathbf{R}_{\mathbf{k}})\rangle\,,\\ P_e &= \frac{ND\gamma}{V} - \frac{1}{4V}\sum_{ij}\sum_{\mathbf{k}}\langle \mathbf{F}_{ij}^{\mathbf{k}}\cdot\mathbf{R}_{\mathbf{k}}\rangle\,. \end{aligned} \tag{3.54}$$

According to the derivation for the confined system, both these two terms correspond to a pressure. The first term is the usual virial pressure along with the swim contribution, while P_e is the external pressure. It accounts for interactions between particles in the primary box and the ones outside, as well as for the diffusion of the particles. The diffusion term is the one that brings the dependence on the activity into the external pressure. Both the two forms of the pressure can be used for molecular dynamics simulations with periodic boundary conditions, even if P_i is the most convenient because it only includes interaction within the primary box.

3.4.3 The role of the swim pressure for ABPs

The behavior of the EOS for active particles had been studied in recent years, trying to infer out-of-equilibrium properties of these system, above all to characterize MIPS. Indeed, as seen before, although driven by the activity, MIPS quite resemble a spinodal de-mixing, that happens in equilibrium across first-order phase transition could find a consistent description by means of the properties of the equation of state.

Among others, Levis *et al.* [LCP17] observed very closely the behavior of the EOS derived in (3.54) with a large set of numerical simulations. As shown in Fig. 3.9, the authors outlined the two binodal branches for the phase separation by measuring coexisting densities and the probability for a particle to be in the clusters. Furthermore, they found from the equation of state that a spinodal-like branch exists in the low-density region of the co-existence region, below which no separation takes place due to high energy barrier for nucleation of clusters.

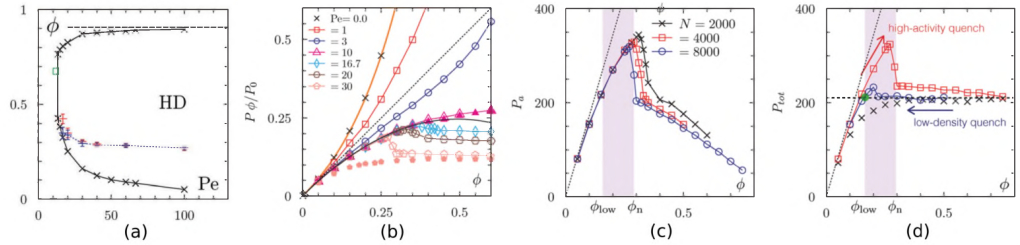

Figure 3.9: Figures adapted from [LCP17]. (a) - (Pe $-\phi$) phase diagram of AB hard-disks. Black symbols show the coexisting densities ϕ_{low} and ϕ_{high} defining the binodals. Red points indicate the onset of MIPS (see text for the details). Blue points correspond to the location of the pressure drop. The horizontal dotted line indicates the closest packing of hard disks. (b) - Total pressure times ϕ normalized by the ideal gas pressure, for different values of Pe given in the key, in systems with PBC (line-open symbols) and in systems with confining walls (in filled symbols). The continuous (orange) line corresponds to the analytical equation of state for hard disks; the dotted one is the ideal gas limit. (c) - Active pressure for systems of AB hard-disks with PBC of different size for Pe= 30. (d) - Hysteresis in the EOS of AB-hard-disks for Pe= 30: the red points are obtained by quenching the system with PBC from an homogeneous state; the blue points were obtained by quenching the system with PBC from a phase separated state. Black points show the equation of state in the confined system.

The location of spinodal has been established by observing an abrupt drop in the pressure, as increasing the density of the system from the gaseous phase at constant activity. This behavior has been justified by the drop in the swim pressure for particles trapped in a cluster. Indeed, it is easy to see, reminding that the swim term in (3.54) depends on the correlation $\langle \mathbf{n}_i(t) \cdot \mathbf{r}_i(t) \rangle$ and using the stationarity of correlations in the steady-state regime, where measures are supposed to be done, that

$$\langle \mathbf{n}_i(t) \cdot \mathbf{r}_i(t) \rangle = \int_{-\infty}^{t} \mathrm{d}t' \, \langle \mathbf{n}_i(t) \cdot \dot{\mathbf{r}}_i(t) \rangle = \int_{0}^{\infty} \mathrm{d}t' \, \langle \mathbf{n}_i(t') \cdot \dot{\mathbf{r}}_i(0) \rangle \, . \tag{3.55}$$

Being $\dot{\mathbf{r}}_i(0)$ and $\mathbf{n}_i(t')$ correlated because they are both correlated with $\mathbf{n}_i(0)$, we get

$$\langle \mathbf{n}_i(t') \cdot \dot{\mathbf{r}}_i(0) \rangle = \langle \dot{\mathbf{r}}_i \cdot \mathbf{n}_i \rangle \, \mathrm{e}^{-D_\theta t'} = v_i \, \mathrm{e}^{-D_\theta t'} \, , \tag{3.56}$$

where the time invariance of correlations has been used again and v_i is the projection of the velocity along the self-propulsion direction. Solving the integral in (3.55) and summing over the particles gives

$$P^{\text{swim}} = \frac{N\gamma}{2V \, D_\theta} \, v_0 \, v(\phi) \, , \tag{3.57}$$

with $v(\phi)$ the average velocity along the self-propulsion direction. As said, it diminishes as soon as a number of particles are caged into an aggregate.

In Fig. 3.9 is shown how the pressure drops for values of the density well above the spinodal and then reaches a constant values within the MIPS. This constant values has been observed to be very close to the value of the coexisting pressure. This behavior mimics the mechanism of *Maxwell construction* for van der Waals loop, which of course does not work out of thermal equilibrium.
Levis *et al.* also verified a hysteresis behavior across the metastable region between the binodal and the spinodal and they also accordingly found that the loop disappear for simulations with walls, because walls work as nucleation sites for clustering, preventing a metastable region to exist.

3.4.4 First-order to continuous liquid-hexatic transition

As stated before, we have been able to establish the nature of both the two transitions of Fig. 3.7, all along the Pe-axis of our phase diagram with the help of the pressure defined in (3.54) [DLS+18]. We show in this subsection all the fine details of such analysis, carefully describing the four plots shown in Fig. 3.10.

We first reproduced, as a reference starting point, the double-loop structure of the equation of state for passive disks, by computing the standard virial pressure at Pe= 0. The grey curve in Fig. 3.10 (a) refers to this case. It quite good overlaps with the EOS computed by Krauth *et al.* (see Fig. 3.8) and it is supplemented by showing the analytical behavior for its liquid branch, constructed with a perturbative method in the local density reported in [KR06] and the related references.

Fig. 3.10 (a) also shows three cases where the virial pressure, together with the swim contribution, is computed for Pe= $1, 2, 3$. As quite evident from the figure, as we turned on activity and moved slightly from the passive limit, the shape of the EOS changes smoothly, retained the double-loop shape. It can be shown that the relevant contribution to the non-monotonicity comes from P^{int} in Eq. (3.54), that is the same for passive systems, while P^{swim} smoothly increases from zero. A zoom over the loop area in the Pe = 1 clearly shows such statement . Comparing the EOS with the analysis of correlation functions, for all of the four cases described in Figure 3.10, we find the loop region across ϕ_i, meaning that the right-hand branch of the EOS, immediately next to the loop, belongs to the hexatic phase.
Therefore, this allowed to claim that up to Pe$\sim$ 3 the liquid-hexatic transition is a first-order phase transition that thus would show, as for the passive case, liquid-hexatic co-existence, responsible for the non-monotonicity of

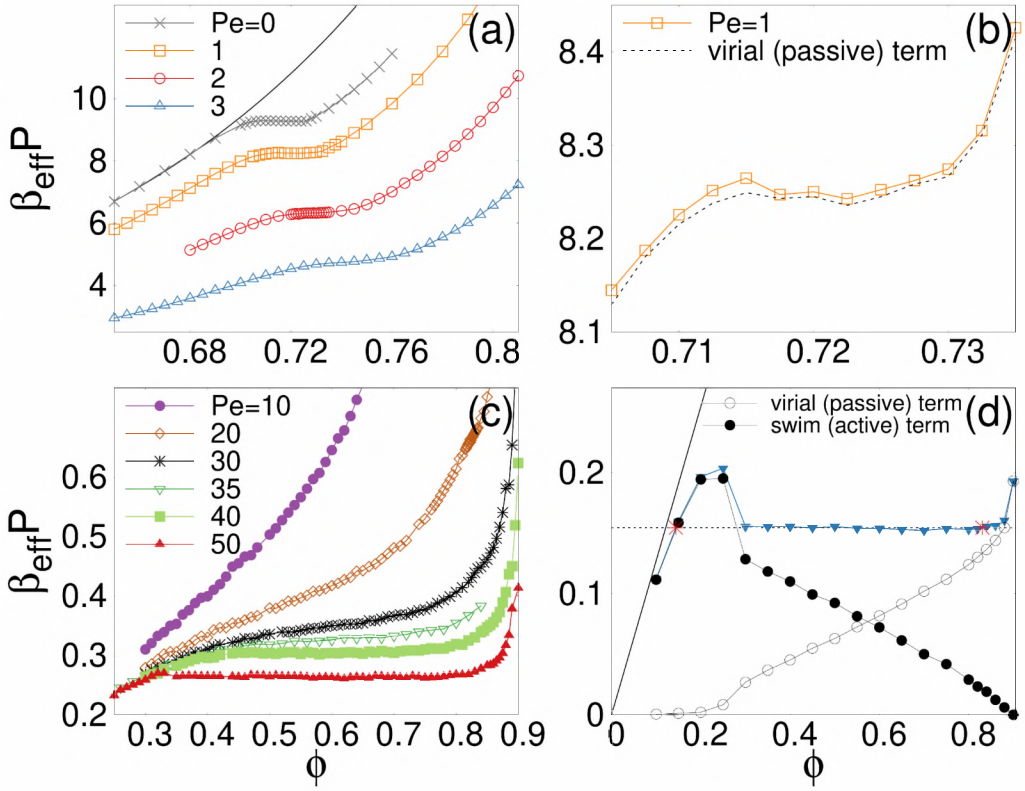

Figure 3.10: Equation of state for self-propelled disks. The effective temperature β_{eff} is the one defined in (3.51). (a) Numerical data for low Pe and analytical form for passive hard disks (continuous line) [KR06]. (b) Details around the liquid-hexatic coexistence region for Pe= 1. (c) Data for intermediate Pe. (d) Swim P^{swim} and interaction P^{int} contributions to P in Eq. (3.54) from the gas to the solid at Pe= 100. The ideal gas law is shown with a continuous line. Figure adapted from [DLS⁺18]

the EOS. We will see later how this hypothesis is confirmed by the analysis of both local density and local hexatic parameter. Although the equal-area Maxwell construction, that allows to directly extract the binodal, cannot be readily applied for Pe > 0, we use it by extension of the passive disks analysis, as a first identification of the co-existence region.

Increasing Pe above Pe= 3 (Fig. 3.10 (c)), we did not find evidence of co-existence until the high-Pe regime where MIPS is attained. Representative curves for Pe= $10, 20, 30$ in this region are shown, which are strictly increasing functions of the density. Increasing activity further, for Pe $\gtrsim 35$ the $P(\phi)$ curves become flat in between two densities. As described before, at very high Pe, the pressure drops abruptly at the vicinity of MIPS as a consequence of the existence of a metastability region with a very large nucleation barrier. We thus inferred that liquid-hexatic transition becomes

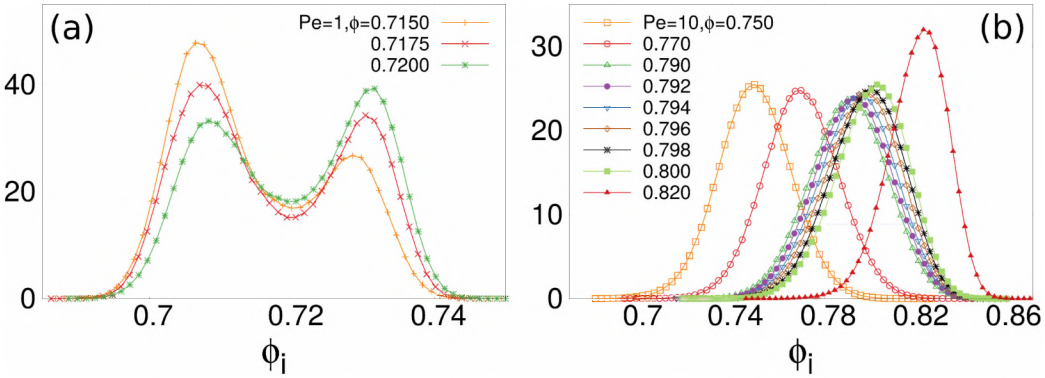

Figure 3.11: Density PDFs across the liquid-hexatic coexistence region for Pe= 1 (a) and the liquid-hexatic transition for Pe= 10 (b). Values of the global packing fraction for each curve are provided in the two keys. The coarse-graining parameter R was chosen to be $R = 20$ in (a) and $R = 5$ in (b). For Pe= 1 there is liquid-hexatic coexistence in between $\phi \sim 0.7125$ and $\phi \sim 0.7275$. For Pe= 10 (no coexistence) the critical densities $\phi_i \sim 0.795$.

continuous for Pe $\gtrsim$ 3. However, as soon as activity is high enough to promote MIPS, the transition nature is hindered by the presence of contribution to the pressure from macroscopic phase separation. Indeed, in contrast to previous considerations for the loop shape at low Pes, the flatness of EOS in the MIPS region is entirely driven by P^{swim}, as shown in Fig. 3.10 (d). We obtain the limits of MIPS with an extrapolation of the flat part of $P(\phi)$ across the pressure jump (or spinodal), as illustrated in Fig.3.10 (d) for Pe = 100.

The elements understood for both EOS and correlations functions clearly depict the overall behavior of the phase diagram in the (Pe $-$ ϕ) parameters' space. We studied the probability density distributions of both local density and local hexatic to attain confirmations of that.

The procedure to compute density pdfs is described above in Section 3.3 and it avails of a coarse-graining of the very local values. We proved the stability of all the results against the choice of the coarse-graining radius in the range $[5\sigma_d, 20\sigma_d]$. The final choice that we made case to case depends on the length-scale of the details that we desired to show.

It is interesting to see how the results coming from density pdfs are in very good agreement with all that we said so far.
In the low Pe limit (see Fig. 3.11 (a)), we see that the three curves displayed, corresponding to global densities varying over the very narrow interval [0.715 : 0.72], are bimodal. The weight under the two peaks slowly transfers from the one at low ϕ to the one at high ϕ for increasing global packing fraction. No double-peak structure is found beyond Pe= 3 and before the critical point for MIPS is reached. Fig. 3.11 (b), where data for Pe= 10

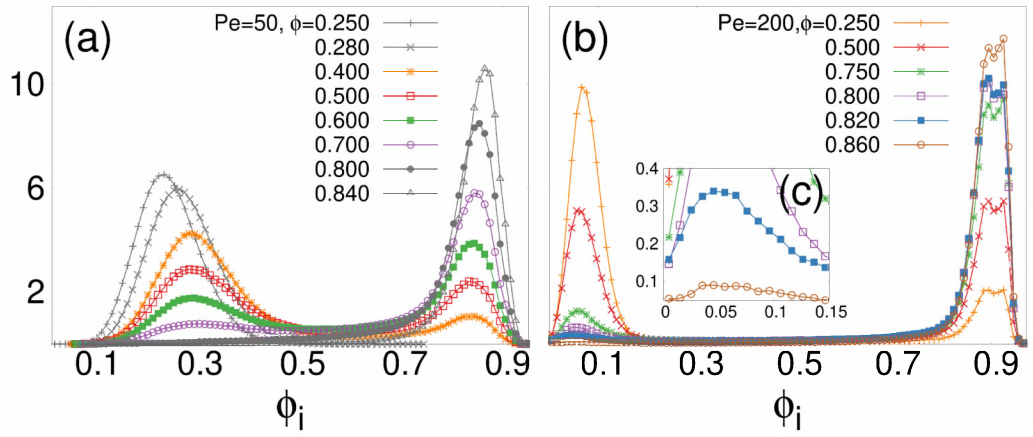

Figure 3.12: Density PDFs across the MIPS region for Pe= 50 (a) and Pe= 200 (b). Curves with a single mode are shown in grey (uniform phase), while bimodal curves are shown with colors (phase coexistence). Values of the global packing fraction for each curve are provided in the two keys and the coarse-graining parameter $R = 5$ was used in both panels. As a references, for Pe= 50 we observed MIPS for $0.310 < \phi < 0.800$. For Pe= 200, MIPS was found for $0.100 < \phi < 0.900$.

are plotted, demonstrates that for all ϕ the curves are single-peaked and their average displaces towards higher values with increasing the packing fraction. This proves that there is no co-existence for this Pe and, in fact, for a rather wide range of Pe values before MIPS.

For Pe= 50, in Fig. 3.12 (a) single-peaked curves are shown in grey, either at low or high values of packing fraction. In color the bimodal curves that show a similar transport of weight from low to high local densities upon increasing ϕ. Similar features characterize the data at Pe= 200 depicted in Fig. 3.12 (b). The insert (c), zooms over the low local density values showing that systems at average packing fraction $\phi = 0.820$ and $\phi = 0.860$ are in the coexistence region as well.

From the location of the two peaks in the local density pdfs and the shape of the equation of state we infer the binodal for MIPS in the range of activity with Pe $\gtrsim$ 35. We find that activity-driven co-existence region enlarges over the surface fraction coordinate as activity strength is increased. For activity slightly above the critical value Pe $\sim$ 35, we observe phase separation within the range of surface fraction $\phi \in [0.550, 0.700]$, approximately. For Pe = 50, as shown in Fig. 3.12 (a), we have MIPS over the interval $\phi \in [0.310, 0.800]$, and for Pe = 200 we observe a strong segregation of a very dilute gas of less than 1% surface fraction and a quite close packed dense phase of more that 90% surface fraction.

Interestingly, the spreading of the binodal range with increasing activ-

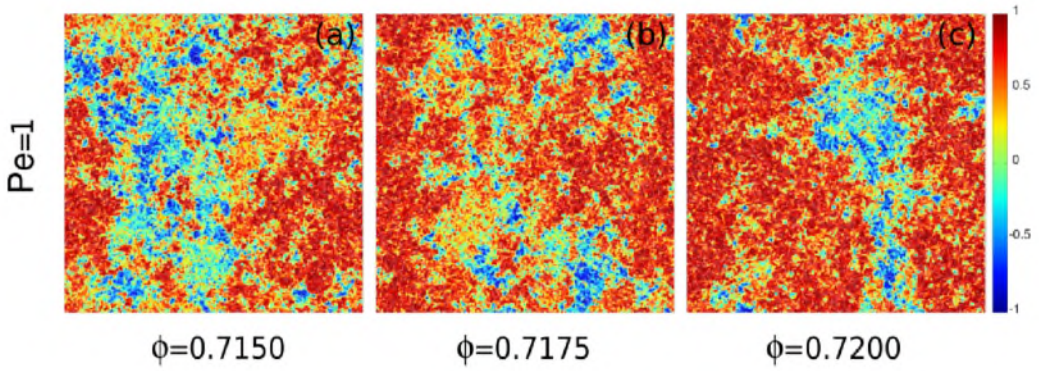

Figure 3.13: Maps of the local hexatic order parameter $\psi_{6,i}$, in the stationary regime for Pe= 1 across the co-existence region at $\phi = 0.715$ (a), $\phi = 0.7175$ (b) and $\phi = 0.72$ (c). We recall that for Pe= 1 we have liquid-hexatic co-existence in between $\phi \sim 0.7125$ and $\phi \sim 0.7275$, as measured by the pressure, followed by the hexatic-solid transition at $\phi_m \sim 0.730$.

ity, seems to be independent on the location of the two structural liquid-to-hexatic and hexatic-to-liquid transitions found above. Such behavior results in a non-trivial nature of the co-existing phases in MIPS, which changes with activity. For Pe = 50, we have that the high-density branch of the binodal is well beyond the liquid-hexatic transition (blue points in Fig. 3.7). This means that the high-density phase for MIPS at Pe = 50 does not have hexatic order and thus it is a dense liquid phase. On the other hand, at Pe = 200, the high-density binodal moves above the hexatic-solid transition (orange points in Fig. 3.7), suggesting that dense clusters in high-Pe MIPS have translational QLR order.

We will go back to this point in the next Section, as soon as we will present the complete phase diagram. However, it is interesting to see how the picture emerged so far is in a strong agreement with the behavior of local hexatic parameter, as defined in Eq. (2.49). We discuss below the feature of $\psi_{6,i}$, using the color representation described in Section 3.3, and we show in the pictures the same cases as the ones considered before, in order to present the correlations between local hexatic and local density. We remind that, according to the colors scheme used, uniformly colored regions are hexatically ordered along a direction $\arg(\Psi_6^{\rm loc})$ with respect to the average hexatic direction. For red regions $\arg(\Psi_6^{\rm loc}) \sim \langle \arg(\Psi_6^{\rm loc}) \rangle$, while for blue regions $\arg(\Psi_6^{\rm loc}) \sim \langle \arg(\Psi_6^{\rm loc}) \rangle \pm \pi/2$. All the configurations shown are taken in the stationary regime.

In the low Pe case displayed in Fig. 3.13, the three panels span the coexistence region of the phase diagram. We see large, non compact regions with red color that correspond to the same local hexatic order that are

surrounded in a rather disordered way by regions with no hexatic order at the short scale. These features are very similar to the ones seen in the passive disk models with sufficiently hard repulsive potential studied by Krauth and collaborators [BK11].

In Fig. 3.14 we display maps at Pe= 10, an activity for which we do not see co-existence. To start with, the color map in panel (a) looks different from the ones shown in the three panels in Fig. 3.13, with no large red zone in this configuration, that corresponds to a low local packing fraction everywhere ($\phi = 0.5$) and that we interpret as an active liquid one. The intermediate panel (b), obtained for $\phi = 0.820$, displays an almost uniform, relatively light, red pattern and it lies in the active hexatic phase. Finally, a much darker uniform red state is shown in the last panel (c), in which $\phi = 0.860$, and the system is an active solid, as confirmed by the analysis of the positional correlation functions.

The case Pe= 50 is above the critical Pe value for which MIPS occurs. Typical color maps of the local hexatic order parameter are shown in Fig. 3.15 for global densities that lie well within the MIPS region (a), above MIPS and below liquid-hexatic transition (b), and in the active hexatic (c). We remind that for Pe= 50 we observe MIPS in between $\phi \sim 0.310$ and $\phi \sim 0.800$ and $\phi_i \sim 0.855$.

At Pe= 200 (see Fig. 3.16), MIPS generates the de-mixing of the system into a very low-density ($\phi_{\text{low}} \sim 0.07$) and a rather high-density ($\phi_{\text{high}} \sim 0.9$) phase with, on top, local hexatic order of different kinds. This is illustrated in the snapshots in panels (a) and (b) by the dense regions of particles sharing the same color, in co-existence with very low density

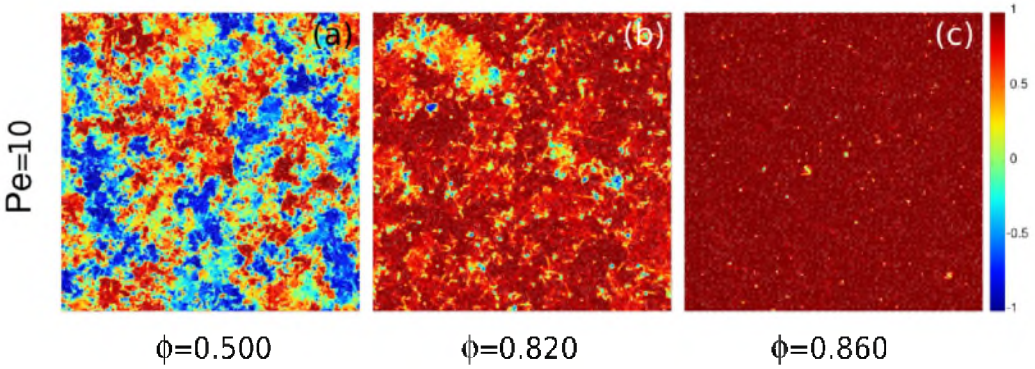

Figure 3.14: Maps of the local hexatic order parameter $\psi_{6,i}$, in the stationary regime for Pe= 10 at $\phi = 0.500$ (in the active liquid phase) (a), $\phi = 0.820$ (in the active hexatic phase) (b) and $\phi = 0.860$ (in the active solid phase) (c). Note that at this Pe the critical densities $\phi_i \sim 0.795$ and $\phi_m \sim 0.840$ were obtained from the analysis of the orientational and positional correlation functions.

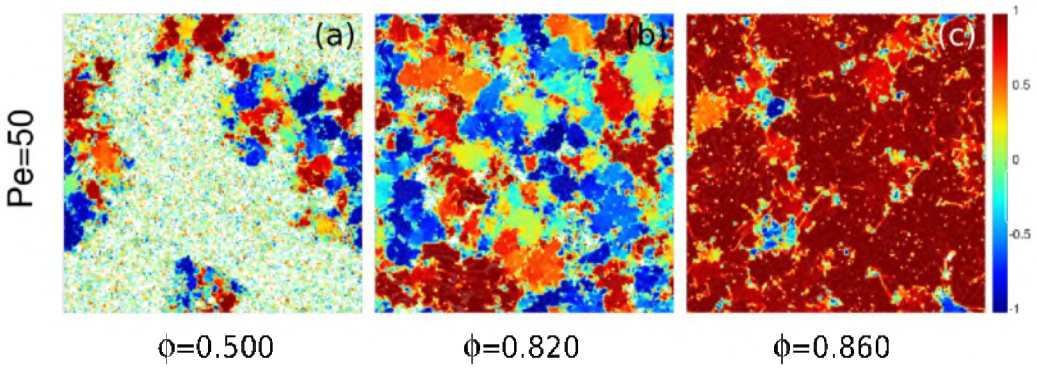

Figure 3.15: Maps of the local hexatic order parameter $\psi_{6,i}$, in the stationary regime for Pe= 50 at $\phi = 0.500$ (in the MIPS coexistence region) (a), $\phi = 0.820$ (in the dense active liquid phase) (b) and $\phi = 0.860$ (in the active hexatic phase) (c). For this value of Pe we observed MIPS for $0.310 < \phi < 0.800$, and we measured $\phi_i \sim 0.855$ and $\phi_m \sim 0.890$.

regions. As largely reported in the MIPS literature [FM12], the dense phase induced by activity is subjected to anomalously large density fluctuations: it continuously breaks and reforms, giving rise to the observed distribution of orientationally ordered patches of finite size, instead of a single uniform one.

3.5 The full phase diagram of SP disks

Summarizing, we established the full phase diagram of 2D ABP, with active liquid, hexatic and solid phases, as well as co-existence and MIPS. The nature of the non-equilibrium liquid-hexatic phase transition was established by the characteristic shape of the pressure curves and the pdfs of local densities, together with the visual inspection of configuration snapshots, and hexatic correlation functions. They evidence co-existence between liquid and hexatic order below Pe$\sim$ 3 in a narrow interval of packing fractions and a continuous transition for higher activity. They also allow us to catch the nature of co-existing phases in MIPS.

First, we proved that the overall scenario of 2D melting of passive disks is maintained for small enough Pe. This is a notable results within the studies of systems of SP particles, because it gives strong indications about the robustness of HN theory of melting against out-of-equilibrium perturbations. Activity acts indeed as a small perturbation on the passive case that, however, destabilizes passive order. This is shown by the fact that, increasing Pe, both the liquid-hexatic and hexatic-solid transitions shift to higher densities and the liquid-hexatic coexistence region shrinks

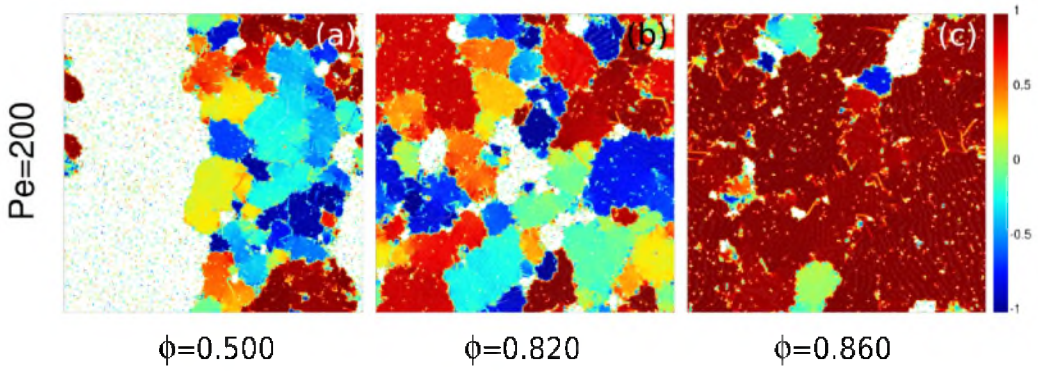

Figure 3.16: Stationary-state snapshots showing the local hexatic order parameter $\psi_{6,i}$ for Pe= 200 within the MIPS coexistence region at different packing fractions: $\phi = 0.500$ (a), $\phi = 0.820$ (b) and $\phi = 0.860$ (c). At Pe= 200, and for high enough density, activity induces phase separation into a low density gas and a high density solid phase. Note, as a reference, that for this Pe we observed MIPS for $0.100 < \phi < 0.900$, and we measured $\phi_i \sim 0.860$ and $\phi_m \sim 0.890$ from the change from exponential to algebraic decay of the hexatic and positional correlation functions, respectively.

and eventually disappears. Such behavior can be due to the effective softness introduced by activity, quantified by the ratio between the active and potential forces $\Gamma = \varepsilon/(\sigma F_{\mathrm{act}})$, since particle softness plays a similar role in equilibrium 2D melting [KK15]. The liquid-hexatic transition allows for co-existence, and the hexatic order in this region tends to remain the same in the steady state and occupies a finite portion of the full system.

At high Pe, the MIPS region opens up independently of the hexatic and solid transition lines and prevails the emergence of hexatic and solid order. In the largest part of the MIPS phase, many patches with finite size and different hexatic order coexist at any moment. However, the large activity makes these patterns regularly rearrange *via* breaking and recombination, very differently from what happens at low Pe. Although particle mobility strongly enhances fluctuations, we have been able to infer the structure of the co-existing phases by means of orientational and translational correlation functions. For low activity within the MIPS binodal up to Pe $\sim$ 60 (see for instance the case at Pe = 50 treated above) a loose gaseous phase and a dense liquid co-exist. For higher activity, around Pe = 100, the dense phase shows an underlying hexatic order, while, at even stronger activity, above Pe = 200, the gas co-exists with a highly packed 2D solid.
This last characterization of MIPS is a true novelty in the field of active matter, and it represents a further step forward in the understanding of such universal non-equilibrium phase separation.

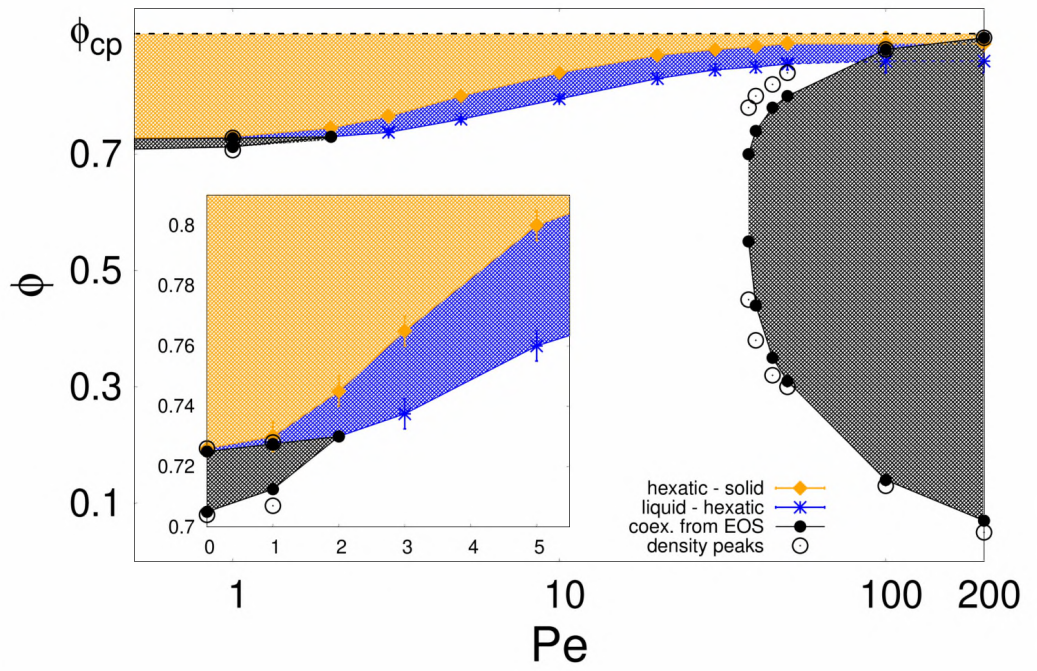

Figure 3.17: Pe$-\phi$ phase diagram of ABP. In the inset, a zoom over the low Pe - high ϕ regime highlights the connection with 2D melting. In the black area there is coexistence, in the blue hexatic order and the orange one is an active solid phase. The black filled (open) points were obtained from pressure (density) measurements; the blue stars from the hexatic order and the orange symbols from the spatial correlations decay. Although narrow, the blue area persists for Pe$\rightarrow$ 0 and broadens as Pe increases. Picture published in [DLS+18].

In Chapter 4, we will start from this phase diagram and go beyond the bare observation of the structure of the phase with activity, trying to understand the mechanism that mediate the phase transitions. Since our AB disks show, in a wide range of activity, a HN-like melting scenario, we aim to keep going into this new evidence, with studying how topological defects are involved in the two melting transitions.

3.6 Finite size analysis

We complete this Chapter describing the methods we used for a finite-size analysis of the critical behavior of our system and showing results which confirm the scenario observed both for the passive and the active case.
As shown before, regarding the behavior of the equation of state, finite-size effects are of large importance upon studying the nature of the phase

transitions, because they allow to access the infinite-size behavior of the relevant quantities from measures on finite systems, which are the only ones we can get from numerical simulations. Moreover, even the scaling of suitable variables with the size of the system provides by itself important information about the behavior of the system in the vicinity of the phase transition. Actually, as explained in [WMB95], this is the case also for our purposes, because with a finite-size analysis we are able to locate with more precision the liquid-hexatic transition and confirm the scenario presented this far. Both extrapolating the infinite-size values of global variables and observing the scaling of such quantities with different sizes give us access to the true large-scale behavior of the system.

The relevant variable for liquid-hexatic phase transition is of course the hexatic order parameter, that, we remind, is

$$\Psi_6 = \left| \frac{1}{N} \sum_{i}^{N} \psi_{6,i} \right| . \tag{3.58}$$

We also remind that, according the HN theory at equilibrium, Ψ_6 is expected to have the following behavior with increasing the packing fraction of the system in the thermodynamic limit: it should be zero in the isotropic liquid; remain equal to zero in the hexatic phase because the bond-orientational order is QLR in the hexatic; it should discontinuously jump to some finite value smaller than one at the hexatic-solid transition and then reach the unit as the packing fraction approaches the close-packing limit. Note that the same large-scale scenario would occur even with a first-order liquid-hexatic phase transition. Therefore, the finite-size analysis of Ψ_6 does not give any chance to distinguish the two cases.

We can however apply these knowledge for inferring some results from finite-size scaling of the hexatic order parameter, which are really useful to our purposes.

As shown in Fig. 3.18, Ψ_6 has non a non trivial scaling with the system size within the MIPS region for Pe = 50. Specifically, we note that at fixed values of the packing fraction, the global hexatic parameter diminishes with increasing system size. Both the curves in the main plot (Fig. 3.18 (a)) and the scaling behavior in the inset (b) are thus compatible with vanishing hexatic order inside the MIPS region. Such behavior confirms the results obtained before from the hexatic correlation functions, which drove as to claim that for intermediate Pe values, the system segregates because of activity into a gaseous phase and a dense liquid.

We move now to the second moment of bond-orientational order pa-

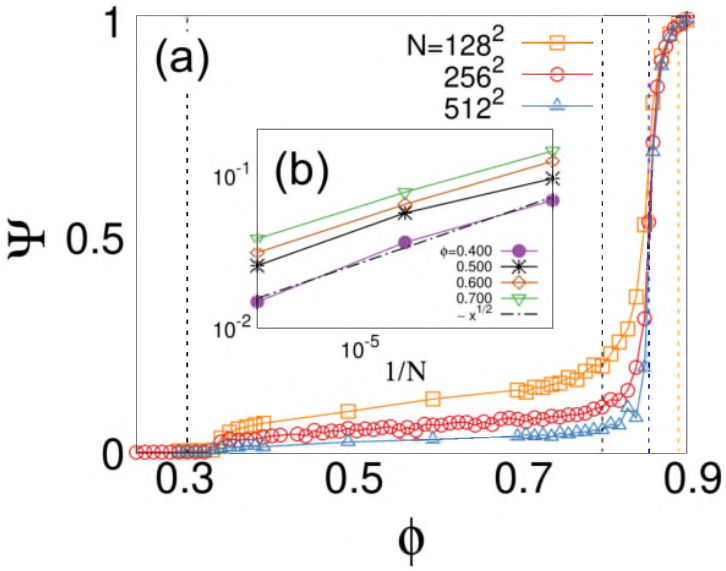

Figure 3.18: (a) Scaling of the global hexatic order parameter, defined in Eq. (3.58) for Pe = 50. Vertical dashed lines delimit the different phases. The two black curves are the lower and upper limits of the MIPS region, blue line is the liquid-hexatic transition, and the orange line is the hexatic-solid one (see the phase diagram in Fig. 3.17). (b) In the inset the scaling of global hexatic parameter is shown at fixed surface fraction.

rameter, which is the susceptibility

$$\chi_L = L^d \left(\langle \Psi_6^2 \rangle_L - \langle \Psi_6 \rangle_L^2 \right), \tag{3.59}$$

where the subscript L indicates the linear size of the system where averages are taken, and d the space dimensionality.
Hexatic fluctuations sharply increase as the transition is approached from the liquid. The behavior of the susceptibility in the vicinity of the transition would actually allow us to tell whether the transition is a HN continuous transition or a first-order one. If the transition is discontinuous, with coexistence between the values ϕ_l and ϕ_h of packing fraction, fluctuations don't diverge approaching ϕ_l from below, but they remain finite, though very large, and go to infinity as $\phi \to \phi_h$. According to the HN theory, on the other hand, since it predicts that the hexatic correlation length

$$\xi \sim \exp\left\{(\phi_i - \phi)^{-1/2}\right\}, \quad \phi \to \phi_i^- \tag{3.60}$$

diverges at the critical point, hexatic susceptibility diverges as well with the same behavior

$$\chi(\phi) \sim \exp\left\{(\phi_i - \phi)^{-1/2}\right\}, \quad \phi \to \phi_i^- \tag{3.61}$$

approaching the critical point from the liquid. However, although the two behaviors would be in principle distinguishable, we remind that liquid-hexatic co-existence in the low-Pe region of the phase diagram is a very narrow interval of packing fractions. Thus, trying to address a solution would demand at least one order of computing time more than the one we used for the previous analysis. We therefore decided to abandon the idea to recognize first-order from finite-size computation.

However, we are still able to use a fourth-order cumulant, as defined in [WMB95], to explore further finite-size features and thus to extract other useful information for our system. This reduced cumulant is

$$U_L = 1 - \frac{\langle \psi^4 \rangle_L}{3\langle \psi^2 \rangle_L^2} \,. \tag{3.62}$$

In principle, the behavior of U_L would allow to identify a genuine HN picture from a mixed scenario, as the one we observed. Indeed, away from criticality the cumulant would assume in general different finite-size values, depending on the system size. The more the system is far from the HN critical point, the more the values of the cumulant for different L will separate between each other. Though, since according to the HN theory the system is scale-free within the whole hexatic phase, the cumulant should collapse into a single curve along the entire range of parameters inside the hexatic. This would not be the case within the co-existence region for a first-order liquid-hexatic transition. Nevertheless, we should be able to catch such difference within a very tiny region in the parameter's space. Hence, as for the susceptibility, the resolution of points at our disposal from simulations in not high enough, thus making this analysis beyond our possibilities.

Although resigning to use finite-size analysis for unveil the nature of the liquid-hexatic transition, we use the Binder cumulant to gain confirmation about the phase diagram and to reach very high precision in the determination of the transition point. See from Fig. 3.19 that, while in the low-density liquid the cumulant assumes well separated values for different sizes and spread with decreasing the density, all the curves overlap at $\phi = \phi_i$, as obtained from the analysis of the correlation functions (see above in this Chapter the values obtained) and tend to remain one on top of each other as the density of the system is increased in the hexatic phase. This happens both for Pe = 10 and Pe = 20, where we do not observe co-existence and then a continuous liquid-hexatic transition is expected. Overlapping of the Binder cumulant thus strongly agrees with the location of the critical points for liquid-hexatic phase transition and represents a

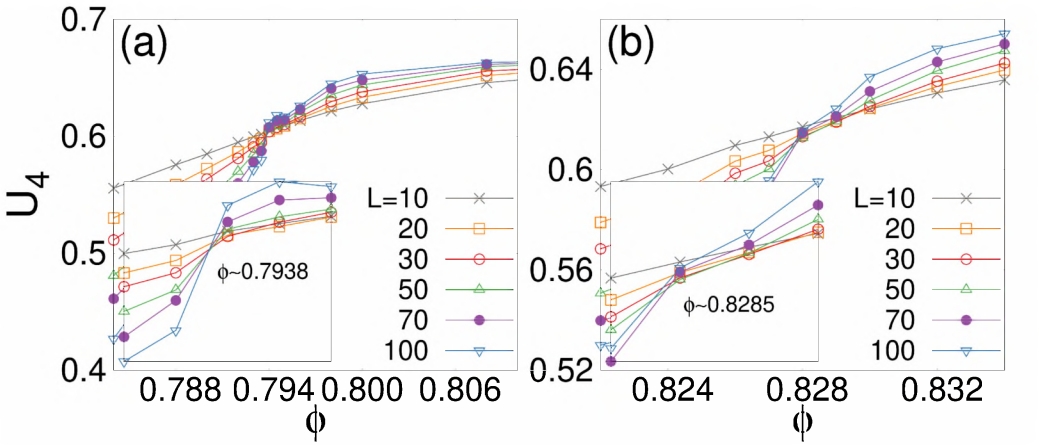

Figure 3.19: The Binder fourth-order cumulant of Eq. (3.62), for different system sizes, given in the keys, at (a) Pe = 10 and (b) Pe = 20. The two inset show respective enlargements of the region close to the transition point.

strong validation of the HN two-step transition scenario for Pe > 0, against different possible ones.

Chapter 4

Topological defects in two-dimensional melting of AB disks

In the short review of in Section 2.3, we found that the KTHNY picture seems to greatly interpret many of the outcomes from experiments and numerics on melting transitions in 2D systems of isotropic particles. Many of these most recent results show indeed that melting proceeds in two steps, from the solid phase to the anisotropic hexatic phase, and than to the disorder liquid. Analysis of large-scale ordering undoubtedly demonstrates, for a large variety of 2D systems with short-range interactions, that translational and bond-orientational QL-ranged symmetries break at two distinct values of the control parameter (the temperature for thermally-driven transitions and the surface fraction for non-thermal cases, like hard-disks). The behavior of both translational and rotational stresses has also been shown to behave accordingly, and the HN renormalization scheme to take very good into account the role of topological defects.

Though, some of the most recent results [BK11, TAAD17] have been provided strong evidences about first-order hexatic-liquid melting for repulsively interacting disks with sufficiently hard potentials. Interestingly, as shown in the previous Chapter, we confirm that such behavior is robust against pushing hard-disks system slightly out of thermal equilibrium. In Chapter 3, we demonstrate that weakly self-propelled disks, evolving according to equations of motion (3.1), show the same discontinuous liquid-hexatic phase transition and continuous hexatic-liquid one. We also show that, as soon as self-propulsion strength is increased enough, a continuous liquid-hexatic transition is restored, similarly to what happens with softening the hard-core repulsion for passive disks [KK15].

We are interested in characterizing more in depth the liquid-hexatic transition, whose nature subtly departs from the one predicted by KTHNY theory. Specifically, we want to closely examine the behavior of topological defects in our system, both with and without activity, to understand if some further defect-mediated mechanism, other than dislocation unbinding (see Chapter 2), is important for melting and if it can explain its discontinuous nature. In fact, as we will show later in Section 4.3, first-order phase transition are likely to be related to grain-boundaries proliferation, rather than to KTHNY-like unbinding mechanisms.

We will thus first describe below one existing similar attempt for passive hard-disks, which is based on MD simulations, in order to shown which kind of picture emerged so far in the realm of equilibrium systems. After that, we will show how such picture extends to AB disks according to our numerical results. Then, we will shortly review some of most relevant theories on defects-mediated phase transition, which, differently from the KTHNY one, involve the role of grain-boundaries and extended defects. Accordingly, we will show the results of our analysis on such large-scale defects with respect to the phase transitions.

4.1 Analysis of the role of topological defects in melting. Numerical results for passive isotropic particles

Dijkstra *et al.* have been carried out a numerical analysis on a system of hard spheres confined on quasi-2D layer by two hard walls [QGD14]. They have been used an Event-Driven Molecular Dynamics (EDMD) algorithm for simulation, according to which the system evolves via a time-ordered sequence of elastic collision events. Collisions are elastic ones, thus preserving both energy and momentum, and their dynamics is governed by Newton's equations of motion. The spheres move at a constant velocity between collisions, and the velocities of the respective particles are updated when a collision occurs. Periodic boundary conditions are used for the in-plane borders of the system.

One of the purposes of Dijkstra and collaborators was to investigate the effect of out-of-plane degrees of freedom on the melting scenario. For this reason, the spheres are allowed to fluctuates outside the 2D plane, by up to half of one diameter. Different heights have been put to the test for such analysis and the true 2D limit has been studied. They have been demonstrated that, regardless out-of-plane fluctuations, two-stage melting

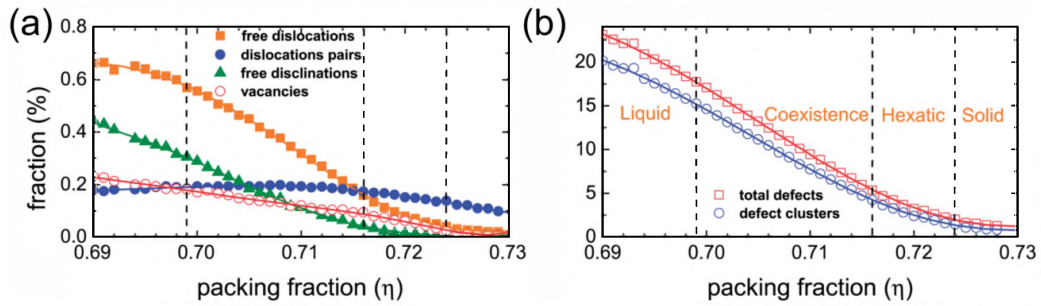

Figure 4.1: (a) Number fraction of free dislocations (squares), free disclinations (triangles), bound dislocation pairs (filled circles) and vacancies (open circles) versus the 2D packing fraction $\eta = \pi N\sigma^2/4A$, where σ is the diameter of the spheres and A is the in-plane area of the simulation box, for 2D hard-disk system ($H/\sigma = 1$, with H the height of the simulation box). Number fraction (in %) is defined as the number of respective defects divided by the total number of particles. (b) The total number of defects per particle (open squares) and the number of defects belonging to defect clusters per particle (open circles) versus η.

scenario is exhibited from hard-spheres, with continuous KTHNY solid-hexatic and first-order hexatic-liquid transition, thus in agreement with the results discussed above. Such statements come from the analysis of both translational and bond-orientational correlation functions, and from the measure of the pressure, similarly to what performed in [BK11] and to the procedure used in Chapter 3.

After having established the melting picture, the authors also have been performed a careful analysis of all the defects "species" and their relevance with respect to the melting for the case of the perfectly in-plane system. As shown in Fig. 4.1 (a), they distinguish the defects into free disclinations, free dislocations, dislocations pairs, vacancies and clusters.

We have already described dislocations and disclinations while reviewing the KTHNY theory in Chapter 2. Dislocation pairs are tightly bounded pairs of dislocations, while vacancies are defects constituted by one empty spot in the triangular array of spheres. Clusters of defects are defects' assemblies which do not fall into anyone of the four species listed before. We remind the first three of them are directly involved in the KTHNY melting mechanism: unbinding of dislocations pairs into free dislocations mediates the solid-hexatic transition, while unbinding of free dislocations into free disclinations drives the hexatic-liquid melting.

According to the measures of the fraction of all these species of defects, with respect to the total number of particles in the system, shown in Fig. 4.1 (a),(b), the KTHNY scenario is confirmed for the solid-hexatic transition, from the clear evidence of a proliferation of free dislocations across the

solid-hexatic melting. Most surprisingly, also the hexatic-liquid melting, although being a first-order, agrees with KTHNY picture, since free disclinations are highly excited within the co-existence region, where the liquid phase starts to invade the system. Neither vacancies, nor clusters appear to take fundamental roles in the melting.
However, as shown in Fig. 4.1 (b), clusters of defects are largely the most abundant species throughout the whole interval of packing fractions explored, creating thus strong questions about their marginal effect on the global behavior of the system.

The authors thus, while confirming the KTHNY nature of the solid-hexatic transition (also verifying the correct behavior of the elastic constants at the melting point), have been suggested that hexatic-liquid transition could be driven by a different mechanism, which involve extended defects and grain boundaries. We are interested in deepening such idea, given in this work as an bare qualitative evidence, using instead a quantitative approach. We will try in particular to explain the role of extended defect clusters into the melting scenario both for passive and active disks.

4.2 Point-defects for AB disks

Before starting to look at the behavior of the defect clusters, we give in this Section our analysis on point defects, that is inspired on the one performed by Dijkstra *et al.*, but it is extended to the case of SP disks, as a first complement to the phase diagram showed in the previous Chapter. Such analysis concerns counting of the defects and their classification, for passive disks and active ones at different values of the Péclet number.

4.2.1 Strategy for defects counting

In order to distinguish the different kinds of topological defects, we have built a numerical protocol inspired from a work by Pertsinidis & Ling [PL01], who devised a method to analyze different configurations of point defects for a two-dimensional array of colloidal particles.

The purpose of that work was to use video-microscopy to study the time-evolution of artificially created vacancies and explore the free energy landscape of local resettlement of particles around the empty site into a perfectly ordered 2D crystal. They prepared the perfect crystal as an $\sim 1\%$ volume aqueous suspension of 0.360μm diameter negatively charged polystyrene-sulfate monodisperse microspheres that crystallize due to strong electrostatic interactions. Particles were confined between

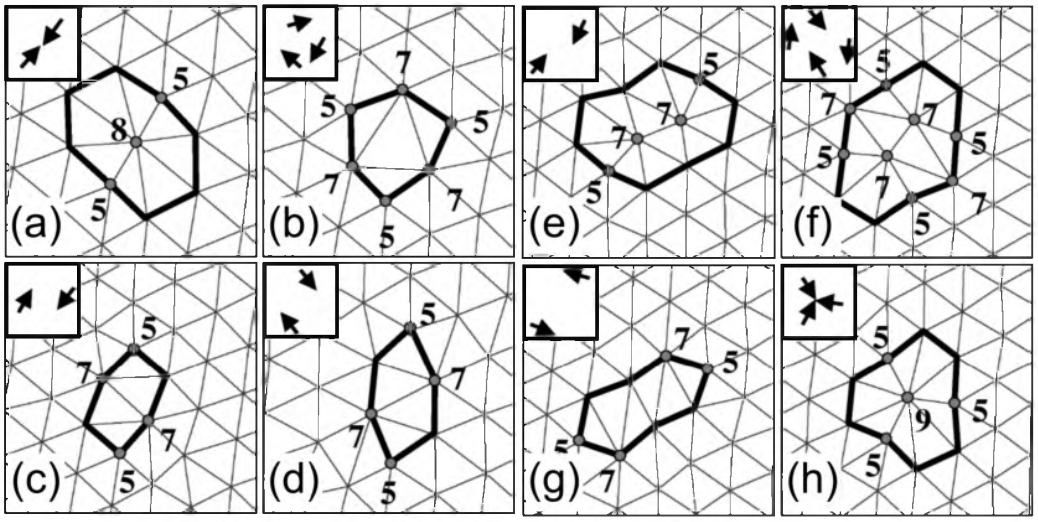

Figure 4.2: (a)-(d) Configurations of so-called *monovacancies*. Top left insets in every figure show configuration of the vectors ϵ_{ij} defined in the text. The grey dots show the arrangement of miscoordinated particles in the core of the defect. (e)-(h) Configurations of *divacancy*. Figure adapted from [PL01]

two silica substrates, able to strongly suppress out-of-plane motion. Point defects were created by dragging a particle away from its lattice point, leaving a vacant site behind, by means of optical tweezers. This provided a fast enough protocol, to overcome the restoring force from the crystal and to be able to drag the particle faster than the relaxation time of the lattice. The dynamics of such single, isolated point defects were thus studied in real time.

As shown in Fig. 4.2, vacancies evolve into different configurations of a number of tightly bonded miscoordinated particles, namely particles which do not have six neighbors, as in the perfect triangular lattice. We have already shown in Chapter 2 that, although point defects are rigorously defined from local lattice distortion, they can be related with deviations of coordination number of the particles in the defects' core. For example, one free disclinations of opposite charge correspond to 5–fold and 7–fold particles, while single dislocations correspond to pairs of 5-7–fold particles. Pertsinidis & Ling also observed that all the vacancy configurations strictly satisfy the two following topological constraints. (i) the mean coordination number of every pair, triplet, etc., is always equal to six, and (ii) the vectors ϵ_{ij} can be defined, which start from a particle i with coordination number $n_i < 6$ and terminating to a nearest neighbor j with $n_j > 6$. The number of vectors originating from i is $(6 - n_i)$ and the number of vectors terminating on j is $(n_j - 6)$. Then for every configuration, $\mathbf{S} = \sum_{\langle ij \rangle} \epsilon_{ij} \sim 0$.

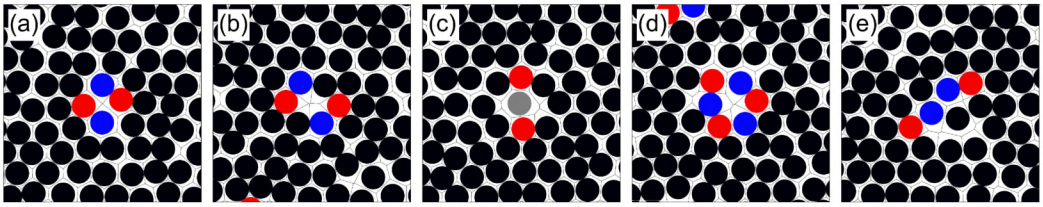

Figure 4.3: Some examples of vacancies found in our passive hard disks system, which agree with the description of Pertsinidis & Ling (see text for details). Black disks have 6 neighbors, red ones are 5–fold miscoordinated disks, blue ones are 7–fold, grey one have 8 neighbors. See that configuration in (a) remarkably correspond to the (c) of Fig. 4.2. In the same way (b) corresponds to (d), (c) to (a), (d) to (b) and (e) to (e).

They have also noted that these point defects are "topologically neutral" since they have zero total Burgers vector. For a single dislocation in a 2D triangular lattice, the Burgers vector is in a one-to-one correspondence with the vector $\boldsymbol{\epsilon}$ defined above. Specifically, the Burgers vector $\mathbf{b}$ connects the 5–fold coordinated particle with its first nearest neighbor, moving counterclockwise after the 7–fold neighbor. Thus, as long as $\mathbf{S} \sim 0$, the point defect satisfies $\sum \mathbf{b} \sim 0$.

Interestingly, we find very good accordance between our point defects and the description of Pertsinidis *et al.*, as shown in Fig. 4.3. Almost all the defects observed in our system can be easily mapped onto the picture described above. We thus accept the topological characterization used in [PL01] and built the numerical protocol accordingly, thus making the following classification:

- Free disclinations: one-particle defects.
- Free dislocations: two-particle defects of one 5–fold and one 7–fold particle, which thus have Burgers vector of modulus $b = |\boldsymbol{\epsilon}_{5\to7}| \sim a_0$ (a_0 being the lattice spacing).
- Vacancies of size n: any configuration of n miscoordinated nearest-neighbors particles with mean coordination number equal to six and $S < S_{\text{th}}$, where S_{th} is a threshold value (replacing zero) taken to be a half of the mean separation between particles. Nearest neighbors are chosen according to the Voronoi construction, described in Section 3.3
- A cluster of size n is any set of n nearest-neighbor miscoordinated particles with $S > S_{\text{th}}$

For point defects of small number of particles in the defect core, the procedure above determines a unique arrangement of the vectors $\boldsymbol{\epsilon}_{ij}$. As

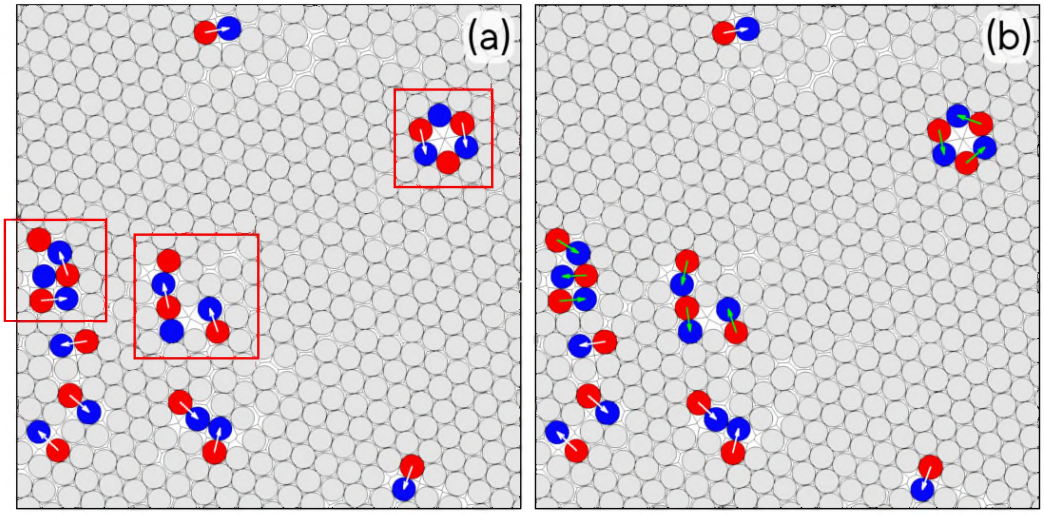

Figure 4.4: (a) Illustrative configuration with few point defects out of a large highly ordered snapshot. Red boxes highlight typical wrong assignments of the vectors ϵ_{ij} (see the text for the details). Once the tail of a vector is assigned to a 5–fold particle, no others arrows can start from the same point. Similarly vectors ending in a 7–fold particles. (b) Wrong assignments are fixed (green vectors) by means of the procedure described in the text. We select the right configuration out of a large number of possible ones, using the criteria of "maximum covering".

the number of particles in the nest-neighbors chain, which constitutes the defect, increases, we encounter cases where many different configurations of the vectors are allowed. See examples of such cases in Fig. 4.4 (a). The most reliable configuration for our purposes, among all the available ones, is the one which covers the most all the particles in the defect. Note that for arbitrarily complex defects' cores, it could be impossible to have one vector for each particle in the core. The "maximally covering" assignment of vectors corresponds to the one which maximises the number of vectors itself. However, for defects of very large number of particles, it is a huge numerical work to generate all the possible configurations of arrows due to the high complexity of the next-neighbors network.
Consider, as a reference for such complexity, the classical theories about *dimers coverings*, in which the degenericity on covering a given lattice with non-overlapping dimers has been estimated with great accuracy. Although our problem and the one of dimer coverings are not exactly equivalent, we can reasonably accept that the two have comparable amount of complexity. The number of allowed coverings for 2D triangular lattice is given for instance in [FMS02], and it is estimated to be of the order of 10^7 configurations for a lattice of about 3×10 sites with periodic boundary conditions.
We thus choose the final arrangement of vectors from a considerably large

number of possible ones. As a rule, we sample $n \times 10^3$ trial configuration, out of the all the possible ones, and we prove that, for reasonably small defects, this provides a correct basis for running the classification given in the list above (see Fig. 4.4 (b)).

4.2.2 Defects counting for AB disks

We perform a systematic analysis of the full spectrum of topological defects, introduced above, with the aim to further characterize the nature of the melting transition for a system of SP disks. The model used is the same AB disks model, presented in Section 3.1, with equations of motion given in Eq. (3.1). We will combine the results of this analysis, with all the information already established about the phase diagram of AB disks, published in [DLS+18] and illustrated with all the details in Chapter 3.
In particular, we will regularly refer to the phase diagram of Fig. 3.17. We remind that is has been determined mainly from the behavior of positional and bond-orientational correlation functions, according to the KTHNY theory. Orange regions have translational quasi-long-ranged order (QLRO) and true LR orientational order; within the blue region the system is hexatic, which means short-ranged positional and QLR orientational order; white region is the isotropic liquid phase, with no order. The dark region in the low-Pe regime is a liquid-hexatic co-existence region, related to the first-order liquid-hexatic transition, while the dark region above Pe $\sim$ 35 is the MIPS region. As already discussed in Chapter 3, liquid-hexatic and hexatic-solid phase transitions are found to overlap with the boundaries of the MIPS region, thus suggesting that the structure of the dense phase in motility-induced phase separation can change with increasing the activity. We will further investigate such possible scenario by means of the analysis of topological defects.

The first quantity we are interested in is the *defects ratio* for each different defect species, which is defined as the ratio between the number of particles involved in a given species, and the total number of particles in the system. Thus, *e.g.*, a vacancy constituted by five miscoordinated particles (as the one shown in Fig. 4.3 (d)) would give a contribution to the vacancy ratio of $5/N$, with N the total number of particles.

In order to produce reliable estimations of the defects ratio, we have performed MD simulations, using the methods described in Section 3.2, of systems of 262144 hard-disks, interacting through the Mie potential given in Eq. (3.4), in a simulation box with periodic boundary conditions. Differently from the cases shown in Chapter 3, we have used rectangu-

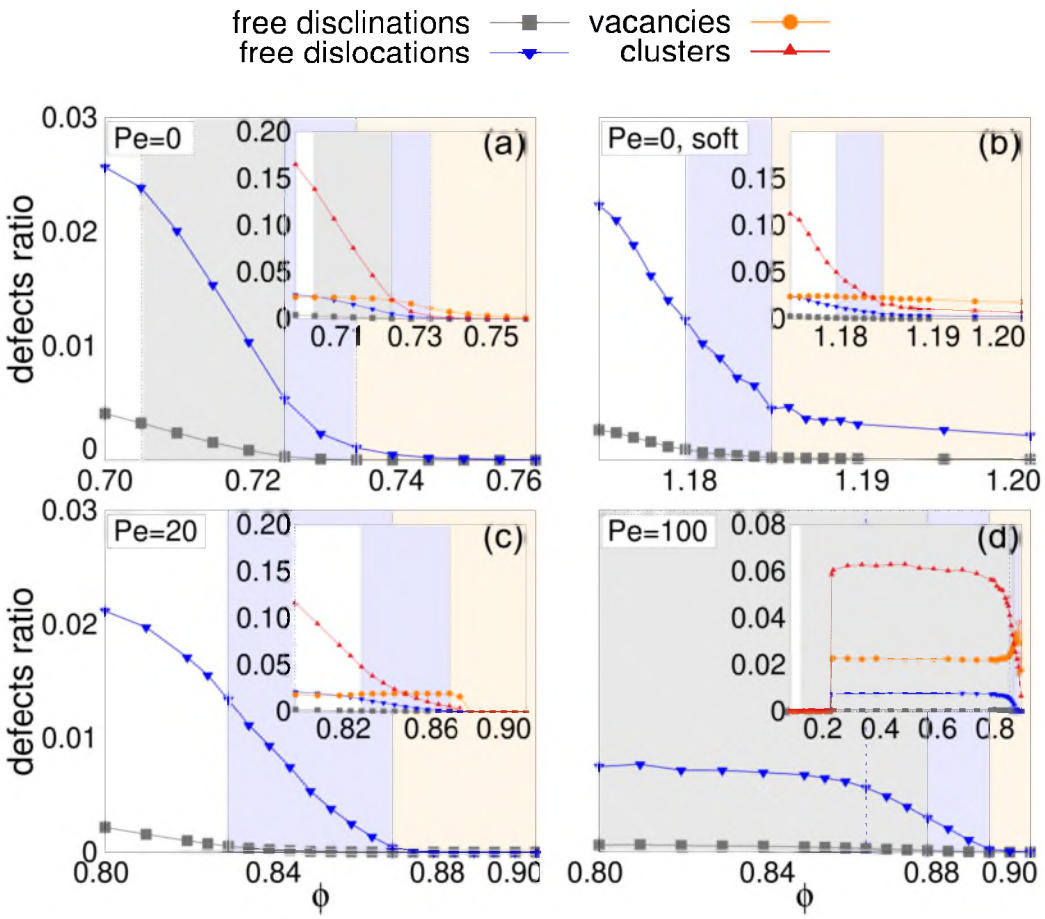

Figure 4.5: Normalized number of dislocations and disclinations as a function of ϕ for passive hard-disks (a), passive soft-disks (b), ABP at Pe = 20 (c) and Pe = 100 (d). All defects, including vacancies and clusters of defects, are shown in the insets. The solid, hexatic, phase-coexistence and liquid regions are shown in orange, blue, grey and white, respectively. The dashed blue line inside the MIPS region (d) indicates the ϕ above which local orientational correlations are scale-free.

lar simulation box of sizes L_x and L_y with ratio $L_x/L_y = 2/\sqrt{3}$, which is commensurate to a perfect triangular disks packing at every chosen global surface fraction. Such choice is required to have non-frustrated arrangements of hard disks, especially at density close the maximum packing, and to prevent thus the formation of topological defects due to geometrical frustration, that could hide the presence of thermally-excited ones.

We have used perfectly ordered initial conditions, with all the disks on a perfect triangular lattice of a given spacing, corresponding to the desired global surface fraction. Ordered configurations relax much faster than others towards stationarity in the cases of dense systems, which are the

ones on which we are mainly interested in. Moreover, there is a strong limit for the global density that can be reached with random packing procedures, which would prevent us to study the high-density region of the phase diagram. We adapted the time-step to enforce numerical stability, with gradually reducing the value of Δt in simulation time units (MDs)—see how we defined the units in Sec 3.2—for increasing Pe. For systems at Pe > 0 we have used a time-step $\Delta t = 0.005$, for Pe > 10 we used $\Delta t = 0.002$, while for Pe > 50 we used the smallest time-step $\Delta t = 0.001$.
Typical simulations took between 20×10^4 and 30×10^4 MDs. Longer runs of, say, $t_{run} \gtrsim 50 \times 10^4$, are required to ensure stationarity in the co-existence regions. As a rule, we let the system evolve in the stationary regime for 50×10^4 MDs. On average, each simulation lasting 100×10^4 MDs was runs on 48 processors for a total of ~ 96 hours for each cpu. We simulated 5 or at least 3 samples per parameter value.

Such considerable numerical effort is needed to reach reliable statistics over the small number of defects. We typically found $\sim 10^4$ defected cells out of N total per simulation in the hexatic phase, far from hexatic-liquid transition. Once classified in the different classes given above, we typically counted about 300 free dislocations, 10 free disclinations, 1000 vacancies (which on average include from 3 to 6 cells), and 100 clusters (of ~ 10 cells each).

The results of the counting are shown in Fig. 4.5. The main plots show free dislocations and free disclinations, across the solid-hexatic and hexatic-liquid transitions for passive hard-disks (in panel (a)) and active ones at Pe $= 20$ (panel (c)), and at Pe $= 100$ where the system exhibits MIPS. In the insets, together with dislocations and disclinations, also vacancies and clusters counting are shown.

As a first notable result, we observe that free disclinations and dislocations are absent in the solid phase (orange) of hard-disks systems. At the vicinity of the hexatic phase (blue), the number of free dislocations increases sharply, indicating that they break positional QLRO and mediate the solid-hexatic transition for all Pe, in a quite good accordance with the KTHNY theory. We find very similar results for all the values of activity explored, with Pe in the range (0,200).

It is worth saying that the observed behavior for free dislocations departs from a recent study reporting that the melting of the active solid phase is not driven by the proliferation of dislocations, as a KTHNY scenario would predict, opening the possibility of breaking orientational LRO in the absence of any defect [PD19]. Such mismatch between results about point defects for AB particles pushed us even more to deepen such analysis with a quantitative evaluation, as we will show from the next Section, of

the role of any possible kind of defects within melting.

As regards free disclinations, their density is very close to zero in the hexatic and detaches significantly from zero when the liquid appears, either as a pure phase, for soft passive disks and active hard disks at Pe = 20, or co-existing with the hexatic, as for passive hard disks in the first-order liquid-hexatic co-existence and at Pe = 100 with MIPS. These are really strong indications towards a KTHNY-like disclination-unbinding-mediated hexatic-liquid transition, regardless the transition is first-order or continuous.

The case at Pe = 100 needs to be clarified further, because in the MIPS coexistence region we only count defects belonging to the dense phase, excluding thus the gaseous component of the system, where defects counting would be meaningless. We identified particle clusters using the so-called *Density-based spatial clustering of applications with noise* (DBSCAN) algorithm [EKSX96] *. The parameters of the algorithm are chosen so as one particle is considered to belong to a cluster whenever it has at least 12 neighbors within a radius of $2.1\sigma_{\mathrm{d}}$ (that is slightly above the third shell radius of the triangular lattice).
The density of each kind of defect (inset of Fig. 4.5 (d)) remains almost unchanged below the point where orientational correlations change behavior from exponential to algebraic (blue dashed line, see Chapter 3) in the MIPS coexistence region and until the low density spinodal. This means the dense phase generated through MIPS is characterized by a given number of topological defects set by Pe.

Along with hard-disks, we also consider a system of passive soft disks with a pair interaction $U^{\mathrm{soft}}(r) = \varepsilon(\sigma/r)^6$, cutoff at $r_{\mathrm{cut}} = 2.6\sigma_d$. We use soft-disks as a benchmark passive case with different melting scenario. It has been shown indeed that for soft enough repulsion, hexatic-liquid melting turns into a continuous BKT-like transition [KK15] (see Section 3.4.1 for the details). As shown in Fig. 4.6, we first check this behavior explicitly for our soft potential, measuring translational and bond-orientational correlation functions, and the pressure. An almost perfect agreement emerges between our findings and the ones in [KK15], both about the location of the double-step transition, and the nature of hexatic-liquid melting. We indeed observe strictly increasing equation of state, as expected from a

*DBSCAN is a data clustering algorithm proposed by Martin Ester, Hans-Peter Kriegel, Jörg Sander and Xiaowei Xu in 1996. It is a density-based clustering non-parametric algorithm: given a set of points in some space, it groups together points that are closely packed together (points with many nearby neighbors), marking as outliers points that lie alone in low-density regions (whose nearest neighbors are too far away).

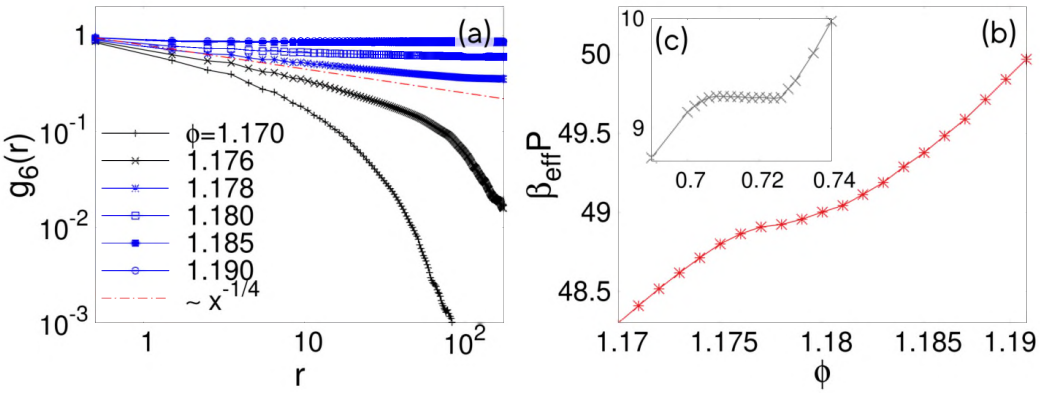

Figure 4.6: (a) Orientational correlation function for equilibrium soft disks. Consistently with the colour code used in Chapter 3 for hard disks, black curves correspond to parameters in the liquid phase, while blue curves are used for the hexatic. The red straight line is the critical power-law predicted by Halperin & Nelson for the liquid-hexatic BKT transition (see Chapter 2). (b) Equation of state in the region across the liquid-hexatic transition. (c) Equation of state for hard disks at equilibrium, as shown in Fig. 3.10.

second-order transition (see Fig. 4.6 (b)).
Concerning point defects' ratios, we find for soft disks a completely consistent picture with the scenario of a HN double-step transition. As shown in Fig. 4.5 (b), although free dislocation ratio is different from zero at all ϕ, its variation is considerably faster below the transition. Although the analysis of point defect for soft disks does not seem to bring any new insights about the understanding of the melting scenario for generic AB disks, the reason of having considered such additional system will be clearer later, as soon as we will discuss the role of extended defects. We aim indeed to compare the behavior of defect clusters, within equilibrium, between a first-order hexatic-solid transition (which is the case of hard disks) and a BKT one.

4.3 Grain-boundaries-mediated melting in 2D

Before proceeding further in the analysis of topological defects, and complementing the previous evidences from point defects with a detailed study of extended defects, we summarize in this Section the most important theoretical approaches to defects-mediate melting in 2D. Alongside KTHNY theory, many other hypothesis of melting based on different mechanisms of defects proliferation were developed. All such theories are grounded on the intuitive assumption the topological defects breaks solid periodicity, restoring orientational and translational symmetries.

One of the most noted of these theories was raised by Chui [Chu82,

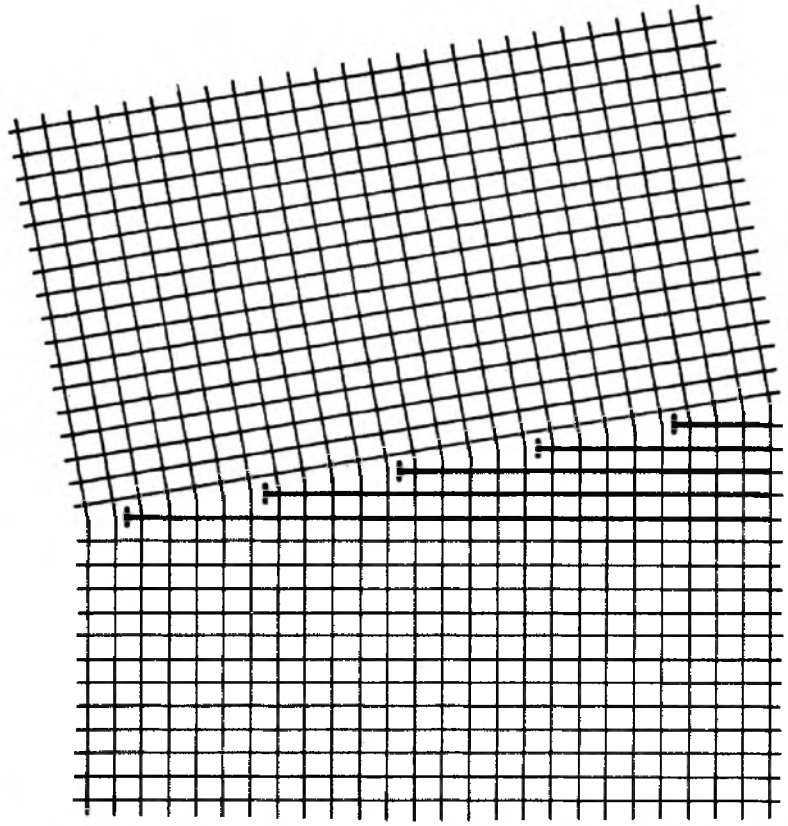

Figure 4.7: Small-angle grain boundary. The grain boundary can be seen to be made up of a line of dislocations. Figure adapted from [Str88].

Chu83]. It proposed, shortly after the dislocation and disclination mediated KTHNY theory, the possibility of grain-boundary-induced melting in which the two-step transition is preempted by a first-order transition involving a proliferation of grain boundaries. Grain boundaries are collective excitation of dislocations, as shown in Fig. 4.7, and have the effect of rotating one patch of crystal with respect to another. Although grain boundaries may be viewed as a string of dislocations, they are able to drive transition of a strongly different nature from the dislocation-mediated one. Infinite parallel grain boundaries interact indeed with an effective potential that is a short-ranged, differently from the long-ranged interaction between single dislocations.

Fisher, Halperin, and Morf [FHM79] had actually already considered the effects of small-angle grain boundaries on melting transition in a 2D electron solid. Small-angle grain boundaries are line defects of bonded

dislocations with equal Burgers vectors, perpendicular to the line itself. Taking into account thermally fluctuating straight grain boundaries, the authors demonstrated that they mediate a phase transition, with the critical point and the same nature of the Halperin-Nelson dislocation-unbinding-driven one. They thus concluded that no additional effects emerged by treating grain boundaries as extended defects, but only dislocations are relevant in the melting.

However, Chui performed a more accurate calculation of the grain boundaries free energy, assuming the following expansion in the grain boundary density n:

$$F = -An + Bn^2 + C/n + O(n^3)\,, \tag{4.1}$$

where the linear term in n accounts for isolated grain boundaries free energy and interactions between grain boundaries and bound dislocations, $C > 0$, while the second order term has negative negative coefficient ($B < 0$) and comes from grain boundaries crossing energy and the coupling with density changes.
Thanks to this low-density calculations, they demonstrated that dislocation unbinding is anticipated by grain boundaries proliferation mediated transition at a lower temperature. From geometrical consideration, they predicted that grain boundaries destroy at once both translational and orientational order, thus preventing the existence of the hexatic phase. Moreover, from the negative second order term, they infer that this single transition is a first-order transition, that can eventually become weakly first-order for high enough dislocation core energy. Effects of renormalization of the core energy and elastic constants were not included in the calculation.

Simulations of the disclination system [Str88], indicated a change from KTHNY melting to first-order melting below a core energy close to $\tilde{E}_c = 2.8 k_B T_m$, with T_m the HN transition temperature. These simulations gave support to Chui's prediction of the crossover core energy, but contradict his assertion that melting remains first order for higher core energies. According to these results, Chui's theory would correctly describes the situation for $E_c < \tilde{E}_c$, but the behavior becomes KTHNY-like for $E_c > \tilde{E}_c$, as the distance between dislocation pairs becomes large and Chui's low-density approximation breaks down.

Kleinert [Kle83] also developed a mean-field approach, finding a first-order transition, as the one predicted by Chui. The calculations were performed for a model that is based on the zero-temperature disclination interaction. Since dislocations can be composed of disclinations, this model

includes the possibility of both the dislocation- and disclination-unbinding transitions. The same model had been proposed earlier by Nelson [Nel82] in a dual form known as *Laplacian roughening model*. This model has been the subject of extensive Monte Carlo simulations (see [JK80, JH, SSC83, JT86, Str86]).

Point defects such as vacancies and interstitials may also play an important role in the melting process. Because of the relatively hard cores of most atomic interactions, vacancies usually have a much lower energy than interstitials. Joos & Duesbery [JD85] performed a zero-temperature calculation of defect energies in rare-gas systems. The low energy calculated for localized vacancies led them to conclude that melting transition might be driven by vacancies rather than by dislocation-unbinding.
Below a certain density, the energy of a vacancy becomes negative in these systems. The rare gases are described fairly well by a Lennard-Jones interaction potential. The competition between attractive and repulsive parts of the potential leads to the existence of a "preferred" lattice spacing. As the lattice is expanded beyond this spacing, eventually it is energetically favorable to break up the system and allow separation into islands of solid at a smaller lattice spacing and lakes of condensed vacancies. Thus vacancies may certainly be said to drive the transition, at low temperatures, from solid to solid-gas coexistence as a function of decreasing density. The Joos and Duesbery calculation of the lattice spacing at which this density-driven transition occurs is in good agreement with experimental rare-gas-on-graphite phase diagrams.

However, vacancies are an unlikely mechanism for the melting transition at higher densities and temperatures or in systems such as the $1/r^n$ potentials that do not have a "preferred" lattice spacing. They also cannot explain the purely temperature-driven melting from solid-gas to liquid-gas coexistence. Since vacancies do have a rather low energy, they exist in a non-negligible equilibrium concentration in the solid. However, since they are localized defects, vacancies do not disrupt the lattice structure at long distances. Only by aggregating into structures of the order of the system size they could affect the long-ranged order of the system and thus causing melting. Aggregates are favored since their energy is lower than that of an equivalent number of isolated vacancies. Such large aggregates are, however, no longer usefully viewed as vacancies. Indeed, as Joos & Duesbery pointed out, a string of vacancies that crosses the system is precisely an unbound dislocation pair.

Given this short overview on the most noted theories on defects-mediated melting in 2D, it is strongly evident that there is not a unified understanding about phase transitions in two spatial dimensions. Even

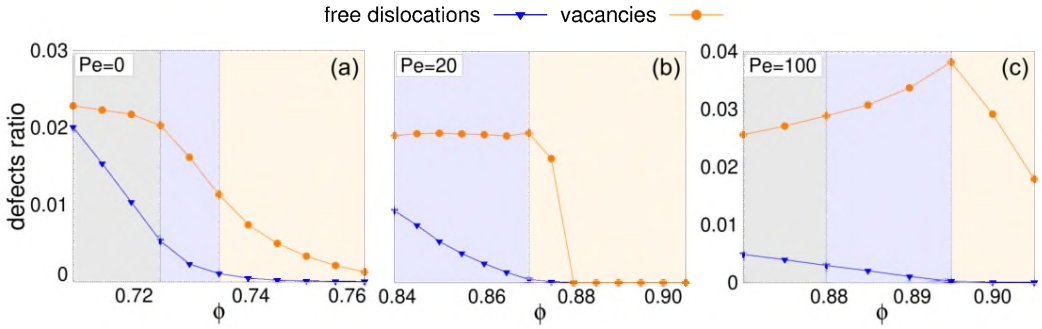

Figure 4.8: Free dislocation (blue lines) and vacancy (orange lines) ratios for Pe = 0, 20, 100 hard disks systems.

if the scenario introduced by Krauth *et al.* [BK11] seems to be quite reliable for hard disks in equilibrium and it is also supported by experiments [TAAD17], there is no guarantee that the same 'solution' can be extended outside the hard disks limit at equilibrium or for self-propelled particles. For this reason, as said, we will consider in the following whether different defects-mediated mechanisms, like the ones described in this Section, are much important for melting of a system of AB disks.

4.4 Clustering of defects for AB disks

Having shortly outlined the most relevant theories on defects-mediated melting, we now come back to the analysis of the ABP system. Within Section 4.2.2 we have widely discussed the behavior of point defects, such as dislocations and disclinations, with varying activity. However, as clearly indicated in the insets of Fig. 4.5, for all the cases considered, the ratio of miscoordinated particles involved in nearest-neighbors chains of non-zero total Burgers vector, namely the clusters in our counting, are largely present in the system. Cluster ratio actually overcomes the one of point defects of about one order of magnitude for a wide range of packing fraction, independently on the Péclet number. Likewise, vacancies are also excited in a considerable amount, of the same order of free disclinations. Therefore, besides having shown a substantial adherence of our model to the KTHNY scenario, we also want to further investigate the role of both vacancies and extended defects, which lie beyond the KTHNY theory, with respect to the phase transitions.

4.4.1 Vacancies

Starting from the vacancies, we show a detailed view in Fig. 4.8, with the same cases discussed before for hard disks. According to the description in [PL01] (see also Section 4.2.1), vacancies do not break positional QLRO and can thus be present in the solid phase. As shown in Fig. 4.8 (c), at high Pe (*e.g.* Pe = 100) the number of vacancies increases as we decrease ϕ in the solid regime and rapidly decays as we get into the hexatic, with a peak at the transition. Such decay is concomitant with an increase in the number of free dislocations, suggesting that vacancies give way to free dislocations, across solid-hexatic melting. Such behavior is still present, though less pronounced, at intermediate Pes (see Fig. 4.8 (b)). The case at Pe = 0 does not provide such clear message, even though vacancies increasing seems to have a smooth inflection point close to solid-hexatic transition.
Given that vacancies, as zero Burgers vectors assemblies, are completely equivalent to dislocation pairs, decreasing of them in favour of formation of free dislocations, is interpreted as another indication of dislocation-unbinding HN-like mechanism.

4.4.2 Defect clusters

As opposed to vacancies, clusters brake QLR translational order, and coherently, as shown in Fig. 4.5, they are absent in the solid phase. However, clusters dominate the distribution of defects in the hexatic phase, suggesting that topological excitation are collective rather than localized in this regime. Importantly, this also suggests that their proliferation might drive melting, instead of the unbinding of disclinations. As described in Section 4.3, clusters of defects in hard-disk systems have been associated to the formation of grain boundaries delimiting regions of different hexatic order [QGD14, KK15], which can drive an alternative first-order melting mechanism in 2D [Chu82, Chu83, Kle83]. However, the relationship between generic clusters of defects as counted here, and grain boundaries, is not clear yet.
Moreover, for passive soft- and active hard-disks at Pe = 20, there is no evidence for a first-order phase transition, and yet the density of clusters at the liquid-hexatic transition is very close to the passive hard-disk value ($\approx$ 0.05). This suggests that the proliferation of clusters might be generic and not responsible for the first-order character of the hexatic-liquid transition of passive hard disks.

According to standard definitions—see for example [Chu83]—grain

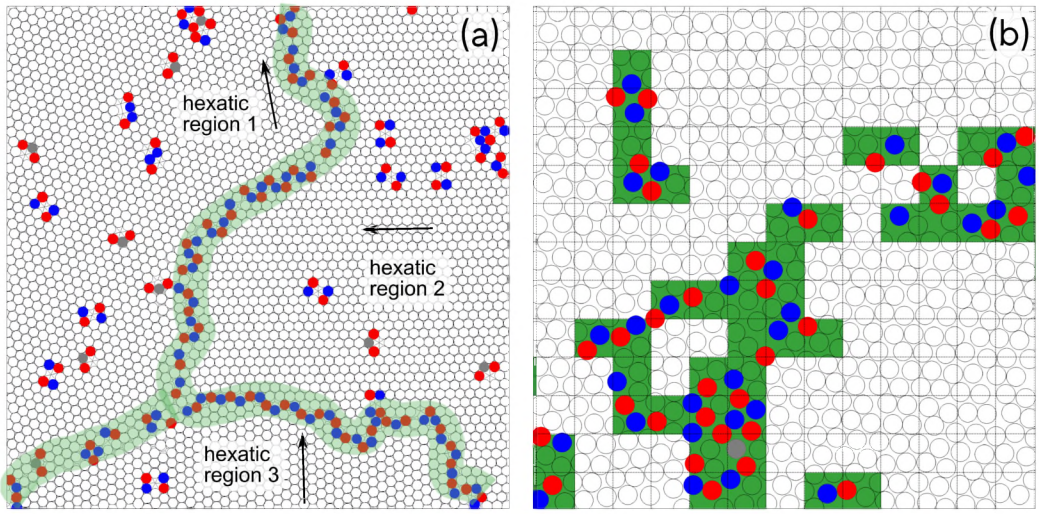

Figure 4.9: (a) Snapshot of a sub-box of linear size of $\sim 50\sigma_d$ out of a large-scale simulation at high activity. Colored particles are miscoordinated ones. See Fig. 4.4 for the color code. A detail of one grain boundary separating three hexatic regions is highlighted in green. (b) Coarse-graining procedure. A squared mesh is build over the simulation box (black dashed lines). One given site of the mesh is considered "occupied" if at least one defect particle has its center in it. Occupied cells are colored in green.

boundaries are constituted by a chain of free dislocations, with Burgers vectors pointing in the same direction, towards one of the two bulks delimited with the grain boundary itself. Fig. 4.9 (a) shows this typical topology of a grain boundary delimiting three hexatically ordered patches. Accordingly, within our picture, grain boundaries fall into the "cluster" species. In order to clarify whether grain boundaries or defect clusters formation is relevant for destroying QLR hexatic order, and thus whether it is connected to hexatic-liquid melting [SJCK+97, SJCK98, QWHC10, KK15, QGD14, DBMK15], we use the framework of percolation theory [SA18]. See Appendix C for a short overview of the most important features of percolation transition.

As shown in Fig. 4.9 (a), although the grain boundaries structure pretty good agrees with general definition given above in term of dislocations chains, defects chain along grain boundaries are not fully connected at the single cell scale. The microscopic gaps are filled via a coarse-graining procedure, routinely applied to study gelation (see for example [CDADG+04]). To be quantitative, we divide the simulation box into square cells and define a coarse-grained cluster as a set of connected cells with, at least, one defect. Two cells are connected if they share one side. In Fig. 4.9 (b) this coarse-graining procedure is sketched. The dotted lines separate

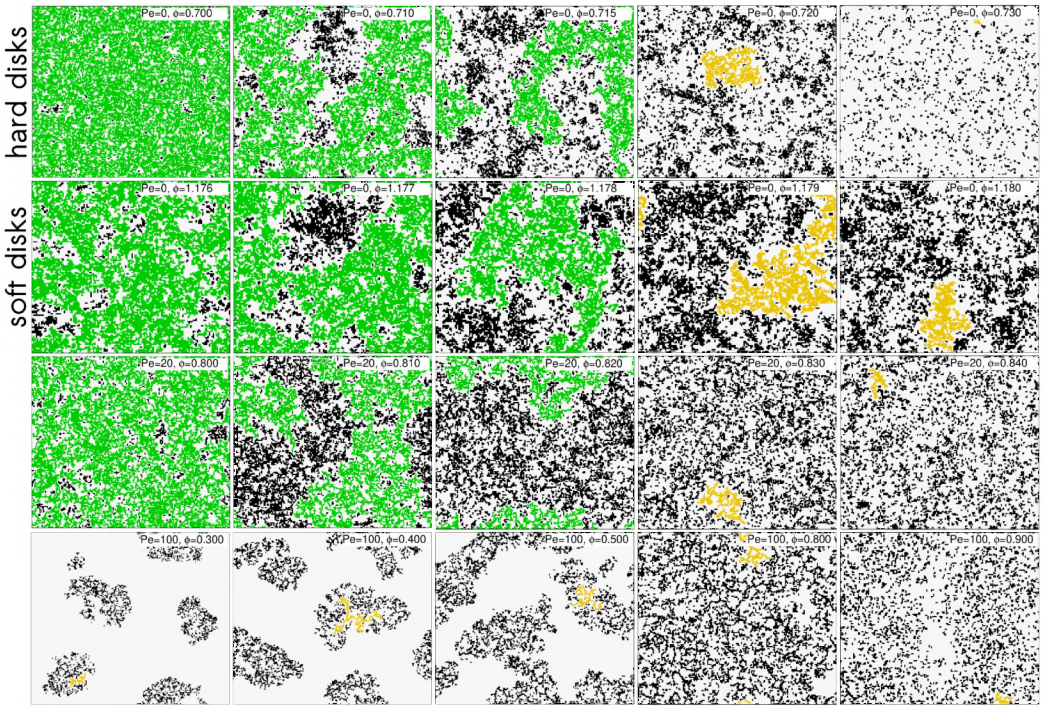

Figure 4.10: Representative snapshots of the systems for hard a soft passive disks, and hard disks at Pe = 20, 100, across the liquid-hexatic transition. The parameters Pe and ϕ are given in the keys. We remind, as a reference, that liquid-hexatic co-existence for passive hard disks is in the interval $\phi \in [0.705 : 0.725]$; melting transition is at $\phi_i \sim 1.178$ for passive soft disks, and $\phi_i \sim 0.830$ for Pe = 20 hard disks. At Pe = 100 we have MIPS in the interval [0.15 : 0.88].

space into $d_x \times d_y$ cells, where d_x and d_y are characterized by a length d_s, and guarantee the covering of the non-squared $L_x \times L_y$ simulation box with nearly squared cells, by choosing $d_{x,y} = L_{x,y}/\text{int}(L_{x,y}/d_s)$, where 'int' takes the integer part of the ratio $L_{x,y}/ds$.

In the following, we use $d_s = 3\sigma_d$ (see below for a discussion about the coarse-graining length), and we analyze the cluster size distribution $P(n)$ obtained by measuring the number of coarse-grained clusters made of n defected cells, excluding, whenever present, the percolating one. As a qualitative picture of the behavior of defect clusters, we report in Fig. 4.10 representative snapshots of the systems for the four cases considered so far, with coarse-grained clusters highlighted. We use black for finite-size clusters and yellow for the largest one, while green clusters are the ones which span all the system.

The percolation of coarse-grained clusters is qualitatively evidenced by the snapshots shown in Fig. 4.10. For equilibrium hard-disks in the solid

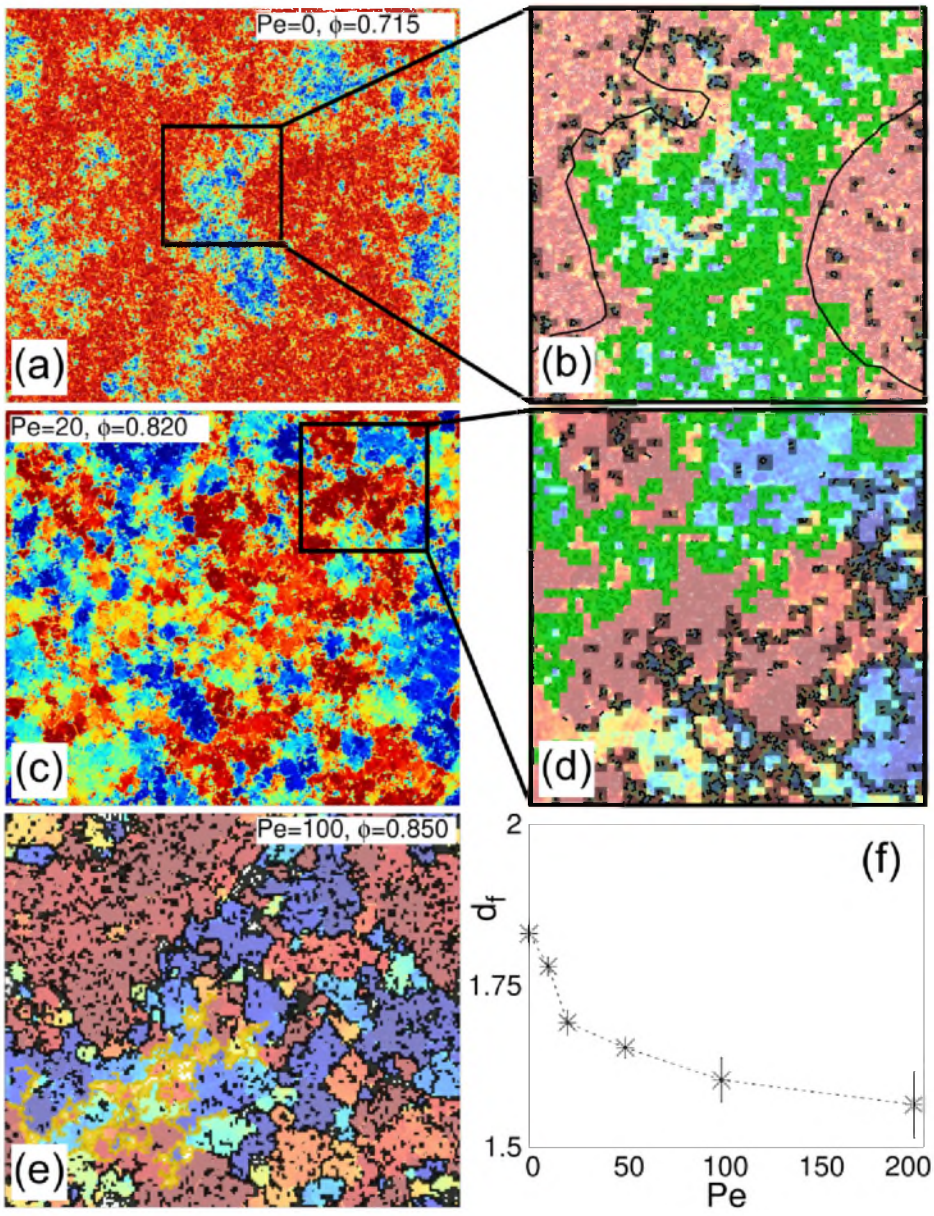

Figure 4.11: (a) Color map of ψ_6 (see Section 3.3 for the definition of the colors) within passive co-existence region. (b) Enlargement of (a) with the percolating defect coarse-graining cluster in green on top. The black line is a contour line for the local density, for $\phi = 0.715$, which indicates the co-existence of the regions of different densities. (c) and (d) show the same quantities for Pe = 20, for a density slightly below the percolation threshold. (e) Hexatic color map for Pe = 100 below the liquid-hexatic transition. Yellow points on top represent the large (finite) defect coarse-graining cluster. (f) The typical fractal dimension for the defect coarse-graining clusters with respect to the Péclet number.

phase, the largest cluster (in yellow) does not span the system. As we decrease ϕ, the size distribution broadens until a percolating cluster arises (in green), right in the middle of the liquid-hexatic co-existence region. The location of the percolating structure is correlated with the one of the liquid. This is shown by the map of the local hexatic order parameter, see Fig. 4.11 (a). They are also the regions of low local density, as inferred from the black contour line in Fig. 4.11 (b), which indicates the local density threshold of $\phi_{\text{loc}} = 0.715$. Thus, the emergence of a percolating cluster at Pe = 0 can be attributed to the percolation of the liquid domain.
For Pe = 20, there is no liquid-hexatic co-existence, and yet there is percolation close to the hexatic-liquid transition. In this case, coarse-grained clusters can be identified with grain-boundaries, as shown in Fig. 4.11 (c)-(d), and percolation with the emergence of a system-spanning network of them. At higher Pe, in the MIPS regime, we see large hexatic domains, leaving behind a network of grain-boundaries, that can become large but remains finite (see Fig. 4.11 (e)). We remind, however, that we ruled out the gaseous phase in the MIPS region, graphically replaced by the grey region in the fourth row of Fig. 4.10.
In the finite systems studied, at the hexatic-liquid transition, the statistics of the coarse-grained clusters is close to the one of clusters at critical percolation, irrespective of its discontinuous (for passive hard-disks) or continuous (for passive soft disks and ABP at Pe = 20) character. At Pe = 100, MIPS preempts the liquid-hexatic transition and thus the percolation-like behavior.

An essential aspect of critical percolation is the fractal morphology of the clusters. A way to analyze their geometry is to relate their size, n_C, to a length scale, *e.g.*, their radius of gyration $R_{g_C} = [\sum_{i\in C}(\mathbf{r}_i - \mathbf{r}_C)^2/n_C]^{\frac{1}{2}}$, where the sum runs over all cells in the cluster and $\mathbf{r}_C$ is the position of its center of mass, *via* the fractal dimension d_f, according to

$$n_C \sim {R_g}_C^{\,d_f} . \tag{4.2}$$

At criticality, the hyper-scaling relation $\tau = d/d_f + 1$ (d being the space dimensionality) relates d_f to the exponent τ of the size distribution, see Appendix C. The evolution of d_f with Pe, at the hexatic-liquid transition, is shown in Fig. 4.11 (f), suggesting that clusters are more ramified as the activity increases, in agreement with Fig. 4.10. Indeed, for higher Pe local crystalline order is enhanced leaving behind sharper grain boundaries and thus string-like clusters with smaller d_f.

In Fig. 4.12 we show $P(n)$ for (a) passive hard-disks, (b) soft-disks, (c) ABP at Pe = 20 and (d) Pe = 100, and varying ϕ across the different phase

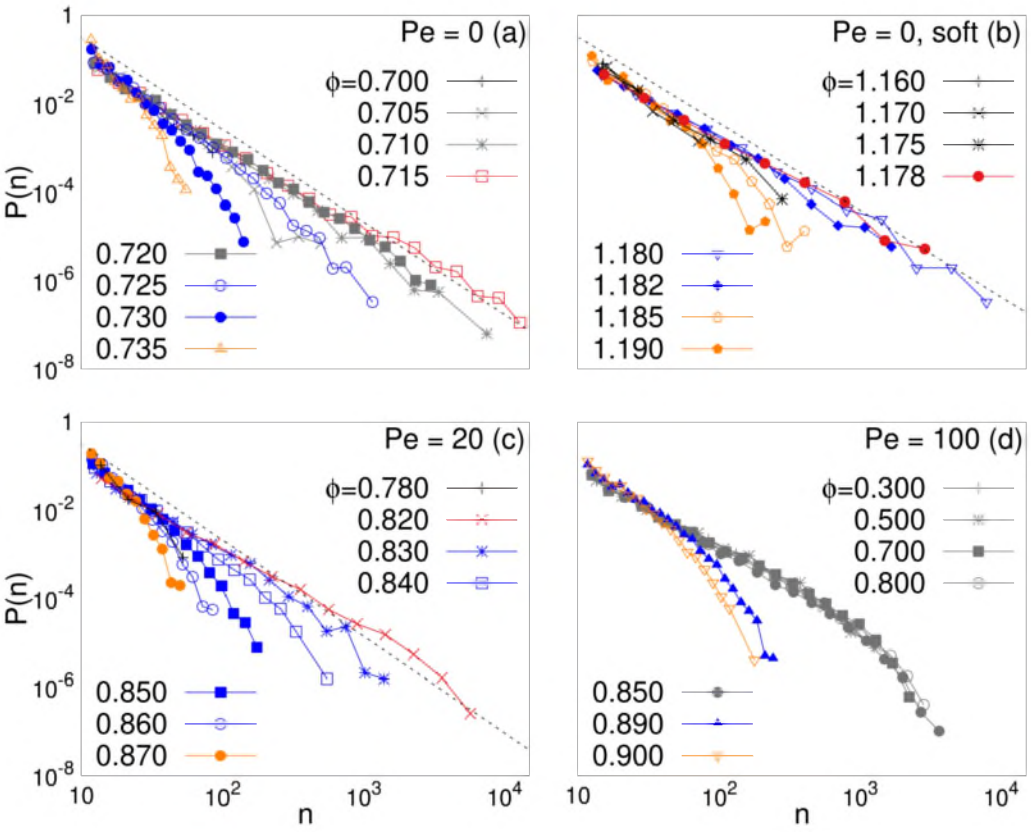

Figure 4.12: Cluster size distribution for (a) passive hard-disks, (b) soft-disks, (c) ABP at Pe = 20 and (d) Pe = 100 at different ϕ, given in the keys. We represent in red the curve we identify with percolation-like behavior. We show with dashed lines an algebraic decay $P(n) \propto n^{\tau}$. We use black for the liquid, blue for the hexatic, orange for the solid, and grey for co-existence.

transitions. Starting from the solid, the effect of decreasing ϕ is clear for all Pe, as the distribution broadens to include larger clusters. For passive disks, both hard and soft, and at Pe = 20, $P(n)$ becomes scale free (very) close to the value of ϕ above which orientational correlations become algebraic, see Chapter 3. The size distribution remains largely invariant within MIPS at fixed Pe = 100, similarly to what we saw in Fig. 4.5 (d). In Fig. 4.12 we also show $P(n) \sim n^{-\tau}$, with τ fixed from $\tau = 1 + d/d_f$, d_f being the extracted fractal dimension of the clusters. The measurement of d_f provides a consistent prediction for τ in $P(n)$.

We have to be extremely careful before claiming that there is a strict relation between a thermodynamic phase transition driven by the competition between interactions and fluctuations, such as melting, and a phenomenon of purely geometric nature, like percolation. In many spin

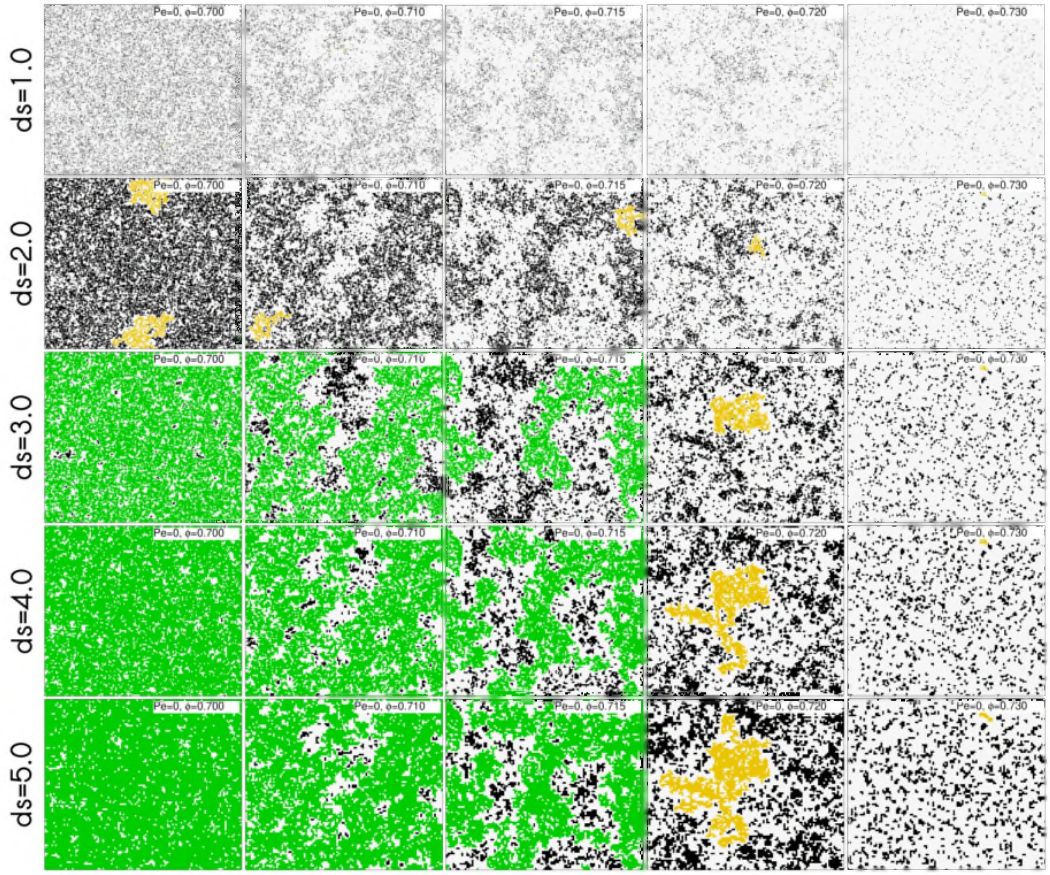

Figure 4.13: Effect of the coarse-graining scale on structure of the defect clusters. Snapshots with defects shown in black with the largest and non-percolating ones in yellow and the largest and percolating ones in green. The parameters Pe and ϕ are given in the keys and the value of the coarse-graining length is written vertically at the left of each row.

models, the properties of their second order thermal phase transitions can be rigorously described in terms of the critical percolation of suitably defined Fortuin-Kasteleyn (FK) clusters, that *are not* the obvious geometric ones one could *a priori* try to use [FK72, SA18]. Although the FK clusters should not be useful to describe a first order thermodynamic transition, in cases with very long correlation lengths such as the 2D Potts model with $Q \gtrsim 4$, one could easily see them percolate close to the transition in finite size samples. Our simulation results (on finite systems) provide clear evidences that active, passive, continuous and discontinuous hexatic-liquid transitions are accompanied by the percolation of defect clusters.

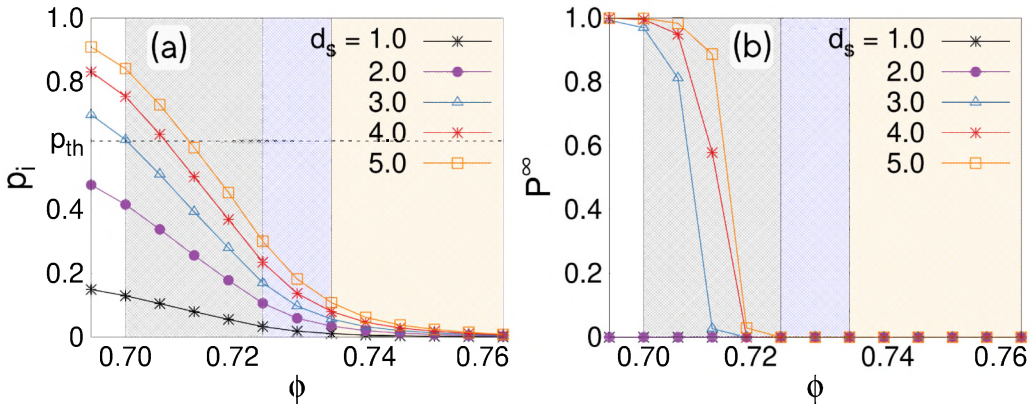

Figure 4.14: (a) Occupation probability (the probability of being occupied by a defect) for a given site as a function of ϕ at Pe = 0, for different choices of d_s, shown in the key, for hard disks. The horizontal dashed line is the percolation threshold for random site percolation in the cubic 2D lattice, shown as a reference. (b) The percolation probability of defect clusters as a function of ϕ for the same cases as in (a).

4.4.3 Comments on the coarse-graining procedure

We conclude this chapter with few comments about the reliability of the coarse-graining procedure used for cluster identification and analysis on percolation transition.

In Fig. 4.13 we investigate the effect of the coarse-graining length d_s used to construct the defect clusters, as explained before. We first observe that smaller coarse-graining length obviously lead to smaller clusters. Consequently, for $d_s \leqslant 2$ (in units of σ_d) we do not see percolation for this set of parameters. Nevertheless, we can identify a clear percolation threshold for ϕ in between 0.715 and 0.720 that is independent of d_s for $d_s \geqslant 3$, a relatively small value, that is very close to the particle size itself. The choice $d_s = 3$ is thus large enough to catch the correct morphology of extended defects and grain boundaries, and on the other hand it is small enough to prevent including isolated defects into large clusters.

In agreement with this qualitative analysis are the results shown in Fig. 4.14, about the so-called *percolation probability* P^∞, defined as the probability for a given site to belong to a percolating cluster. For standard percolation, it assumes zero value below the percolation transition, where no spanning clusters exists, and it rapidly increases to one at the critical point. Consistently with the snapshots in Fig. 4.13, we do not observe percolation for $d_s \leq 2$ ($P^\infty = 0$ everywhere), while for $d_s \geq 3$ the percolation threshold always falls in the coexistence region. We also show in Fig. 4.14 (a) the occupation probability. This standard quantity in perco-

lation theory corresponds in our problem to the probability for a cell in the coarse-graining mesh to be occupied with a defect. The theoretical percolation threshold for standard site percolation transition on a squared lattice is also shown. Percolation probability jumps to one, as soon as the occupation probability crosses p_{th}, confirming the accordance between our problem and a standard percolation picture .

Chapter 5

Elongated self-propelled particles

Natural and artificial active matter are rarely constituted by spherically symmetric elements. On the contrary, *anisotropic* objects are much more common. Examples of living realizations in which the constituents have anisotropic shapes include reconstituted layers of confluent epithelial cells [Par15] and biofilms formed by dense collections of rod-shaped bacteria [LBZ+14]. Artificial cases also exist and an example is given by shaken non-spherical grains [KSRS14].
Molecules have non-trivial shapes and the form of the elementary constituents have non trivial effects on the phase diagram and dynamic behavior. The crudest model for a diatomic molecule is a dumbbell made by identical beads attached to each other by an edge linking their centers. This is usually considered to be the simplest non-convex body. The liquid theory of ensembles of such molecules and their numerical investigation was the subject of intensive studies, some of them published in Refs. [TT85, Bou88, Woj92, GR92]. Certain experimental systems, such as monolayers of diatomic molecules absorbed on crystalline surfaces correspond, in an idealized representation, to a bidimensional dumbbell system [DSFT80]. One can easily imagine that dumbbell systems can jam more or less easily depending on the relation between the bond length and bead diameter, and the rigidity of the link, and these parameters have an effect on the melting/solidification mechanisms.
These are the main reasons that pushed us into the study of self-propelled dumbbell (SPD) system. With the same approach used for disks (see Chapter 3), we aim to clarify within this Chapter the most relevant aspects of this model, related to the dynamics of the molecules, motility-induced phase separation and the effects of alignment in the ordered phases. Our target involves a true novel perspective in the analysis of the active phases, because it consists in mapping the out-of-equilibrium phase transition

scenario onto the framework of 2D HN phase transitions, thus exploring the role of the hexatic phase into the phase diagram of SP dumbbells and, particularly, into the motility-induced phase separation. We will outline all the details of the numerical procedure used to determine the features of a full phase diagram for the dumbbells model, as widely treated in [CDGS17] and [PDC+18].

5.1 Active dumbbells: a minimal model of elongated SPPs

In this Section we present the model of SP dumbbells, we discuss the dynamical regimes of interest, which are related, as for the disks (see Chapter 3), with the stochastic equations of motion. We also provide some details about the numerical strategy used to solve the equations of motion.

5.1.1 Active Brownian equations of motion

Dumbbells are diatomic molecules, consisting of two circular beads of diameter σ_{d} and mass m_{d} bonded together by means of a stiff attractive interaction. We have been implemented two different choices for the bonds within our MD simulations: a rigid bond and a non linear elastic potential. We will describe both of these two methods later in the present Section for completeness. They both lead to very rigid molecules, with a quite fixed bead-to-bead distance.

The coupled stochastic equations for the evolution of a system of N dumbbells ($2N$ beads) are a natural extension of the ones for SP disks. In order to make a description for all the manifest interactions, we write the Brownian motion in the Ornstein-Uhlenbeck approximation, and we will move to the overdamped limit whether it is useful for the analysis.

Being $\mathbf{r}_i$ the position of the i-th bead, the equations of motion read

$$m_{\mathrm{d}}\ddot{\mathbf{r}}_i = -\gamma\dot{\mathbf{r}}_i + \mathbf{F}_{\mathrm{i,bond}} - \boldsymbol{\nabla}_i U + \mathbf{F}_{\mathrm{i,act}} + \boldsymbol{\eta}_i(t)\,, \tag{5.1}$$

where γ_{d} is the friction coefficient, U is the inter-particles potential and T is the temperature of the thermal bath, so that the Gaussian white random noise $\boldsymbol{\eta}_i(t)$ fulfills the fluctuation-dissipation theorem in the passive limit

$$\begin{aligned} \langle \eta_{i\alpha}(t)\rangle &= 0\,, \\ \langle \eta_{i\alpha}(t_1)\eta_{j\beta}(t_2)\rangle &= 2\gamma k_B T \delta_{ij}\delta_{\alpha\beta}\delta(t_1 - t_2)\,, \end{aligned} \tag{5.2}$$

with $\alpha, \beta = 1, 2$ labeling the two spatial coordinates. The total internal potential energy of the system is

$$U = \sum_{i=0}^{2N} \sum_{j=0; j\neq i}^{2N} U_{\text{Mie}}(|\mathbf{r}_i - \mathbf{r}_j|) \,, \tag{5.3}$$

with U_{Mie} [Mie03] the same purely repulsive potential used for the disks

$$U_{\text{Mie}}(r) = \left\{ 4\varepsilon \left[\left(\frac{\sigma}{r}\right)^{2n} - \left(\frac{\sigma}{r}\right)^{n} \right] + \varepsilon \right\} \theta(2^{1/n}\sigma - r) \,, \tag{5.4}$$

The exponent n is set to 32 for very hard beads, and the cutoff at the minimum $r_{\min} = 2^{1/n}\sigma$ ensures the potential derivative to be continuous in σ_d (see Fig. 3.1 in Chapter 3).

The force $\mathbf{F}_{\text{i,bond}}$ is the bond force between the two beads belonging to the same dumbbell. The direction of this force is along the center-to-center axis $\mathbf{n}_i$, which corresponds to the elongation direction of the whole molecule. The active force $\mathbf{F}_{\text{i,act}}$ has constant modulus F_{act} and the same direction $\mathbf{n}_i$. Its direction thus changes following the individual dumbbell's orientation. The self-propulsion breaks the head-to-tail symmetry of the dumbbells, and we choose, accordingly, that $\mathbf{n}_i$ points from the tail to the head. If we label with the index $(i + 1)$ bead paired to i, the equation for $\mathbf{r}_{i+1}$ would be

$$m_{\text{d}}\ddot{\mathbf{r}}_{i+1} = -\gamma\dot{\mathbf{r}}_{i+1} - \mathbf{F}_{\text{i,bond}} - \boldsymbol{\nabla}_{i+1}U + \mathbf{F}_{\text{i,act}} + \boldsymbol{\eta}_{i+1}(t) \tag{5.5}$$

being thus $2F_{\text{act}}$ the total active force on the single dumbbell.

5.1.2 Single dumbbell limit

In the limit of very dilute system, inter-particles interactions can be neglected and the Langevin dynamics can be treated analytically. We review here the key features of dumbbells in the very dilute regime, as derived for example in [SGL+14, CGS15], to identify important time scales and understand the dynamics of the interacting problem. Particularly, we will show how rotational diffusion for the single molecule emerges from the independence of the two noises acting on the beads.

As specified in the introduction to this Chapter, we are mainly interested in the viscous hydrodynamic regimes. Thus, from Eqs. (5.1), (5.5), we move to an overdamped Langevin description, which will considerably simplify the calculation. The single-dumbbell non-viscous case can be

handled analytically as well, with a similar approach but a more laborious calculation.

Taking the two overdamped equations for the two beads in a single dumbbell, we can extract the dynamics of the center of mass of the molecule $(\mathbf{r}_1 + \mathbf{r}_2)/2$, being $\mathbf{r}_1$ the head and $\mathbf{r}_2$ the tail. Within the center-of-mass reference frame all the mutual interactions, the repulsive pair-wise one and the bond force, cancel out

$$\gamma \dot{\mathbf{r}}_{\mathrm{CM}} = \mathbf{F}_{\mathrm{act}} + \boldsymbol{\xi} \tag{5.6}$$

where we introduce the new Gaussian white noise $\boldsymbol{\xi} = (\boldsymbol{\eta}_1 + \boldsymbol{\eta}_2)/2$ with momenta

$$\langle \boldsymbol{\xi} \rangle = 0 \; ; \quad \langle \boldsymbol{\xi}(t_1)\boldsymbol{\xi}(t_2) \rangle = \gamma k_B T \mathbf{1} \delta(t_1 - t_2) \; . \tag{5.7}$$

Note that the equation for the center of mass has the same form of the Langevin equation (3.1) that we prescribed in Chapter 3 for the dynamics of a single SP disk, besides the coupling with the thermal bath for the dumbbell involves both the two beads, resulting thus in a factor 1/2 in the strength of the noise. As for the disks, we directly access the diffusion coefficient $D_{0,\mathrm{CM}} = k_B T/(2\gamma)$ for the passive limit from the Green-Kubo relation of the mass transport.

To move on and compute the dynamics of the active dumbbells, we have to deal with rotation, which explicitly controls the direction of self-propulsion. Subtracting the equations for the head and tail we get the relative motion with $\mathbf{R} = \mathbf{r}_1 - \mathbf{r}_2$

$$\gamma \mathbf{R} = -2(F_{\mathrm{bond}} + F_{\mathrm{pair}})\mathbf{n} + \boldsymbol{\chi} \; , \tag{5.8}$$

which of course does not depend on activity. We have explicitly indicated the tail-to-head direction for the forces between the two beads, and we have defined another white Gaussian noise χ which satisfies

$$\langle \boldsymbol{\chi} \rangle = 0 \; ; \quad \langle \boldsymbol{\chi}(t_1)\boldsymbol{\chi}(t_2) \rangle = 4\gamma k_B T \mathbf{1} \delta(t_1 - t_2) \; . \tag{5.9}$$

If we denote with $\mathbf{n}_\perp$ the versor perpendicular to $\mathbf{n} = (\cos\theta, \sin\theta)$, it is easy to show that

$$\dot{\mathbf{R}} = \dot{R}\mathbf{n} + R\mathbf{n}_\perp \dot{\theta} \tag{5.10}$$

and that the noise $\boldsymbol{\chi}$ can be decomposed as

$$\boldsymbol{\chi} = \chi_\parallel \mathbf{n} + \chi_\perp \mathbf{n}_\perp \; , \tag{5.11}$$

with both $\chi_\parallel$ and $\chi_\perp$ two white Gaussian noises with zero mean and the same variance as χ.

Making use of such decomposition in (5.8), we obtain:

$$\begin{aligned} \gamma\dot{R} &= -2(F_{\text{bond}} + F_{\text{pair}}) + \chi_{\parallel} \, ; \\ \gamma R\dot{\theta} &= \chi_{\perp} \, . \end{aligned} \tag{5.12}$$

Assuming that, for very stiff bond interactions, the elongation R of the molecule can be fairly considered to be a constant equal to the bead's diameter σ_d, we get a pure diffusion equation for the orientation of the dumbbell:

$$\dot{\theta} = \sqrt{2D_\theta}\chi_{\perp} \, , \tag{5.13}$$

with diffusion coefficient

$$D_\theta = \frac{2k_BT}{\gamma\sigma_d^2} \, . \tag{5.14}$$

This result is quite relevant, because it shows how, oppositely to the model of SP disks of Chapter 3, rotational diffusion for dumbbells is built-in in the equations of motion for the two beads, and thus it is not needed to make assumptions with introducing it by hand. The elongated shape of the molecule is obviously the key ingredient of such behavior, which makes evident how non-spherical objects naturally fit models with self-propulsion.

Once the diffusive rotational motion has been reconstructed, we can use the calculation made for the dilute SP-disks model (see Section 3.1.1) to achieve the overdamped center of mass motion from Eq. (5.6):

$$\langle \Delta\mathbf{r}_{\text{CM}}(t)^2 \rangle = 4D_{0,\text{CM}}t + 2\left(\frac{F_{\text{act}}}{\gamma}\right)^2 \frac{1}{D_\theta}\left(t - \frac{1 - \mathrm{e}^{-D_\theta t}}{D_\theta}\right) , \tag{5.15}$$

which is a persistent random walk, where three separated regimes can be recognized. Beyond the inertial regime ($t \ll m/\gamma$) that is inherently discarded for our level of description, the characteristic time $\tau_P = 1/D_\theta$ of rotation separates a late-time diffusive regime, with diffusion coefficient

$$D = D_{0,\text{CM}} + \frac{1}{2D_\theta}\left(\frac{F_{\text{act}}}{\gamma}\right)^2 , \tag{5.16}$$

from an earlier one for $t \ll \tau_P$ where

$$\langle \Delta\mathbf{r}_{\text{CM}}(t)^2 \rangle = 4D_{0,\text{CM}}t + \left(\frac{F_{\text{act}}}{\gamma}\right)^2 t^2 \, . \tag{5.17}$$

Within this regime a second characteristic time $t^* = 4D_{0,\text{CM}}\gamma^2/F_{\text{act}}^2$ arises, from equalizing the two terms, between a diffusive regime before t^*, for $t_I \ll t \ll t^*$, and a ballistic one next, for $t^* \ll t \ll \tau_P$. See Fig. 5.1 for a sketch of the entire time-range considered, which includes, for clarity, also the early inertial motion.

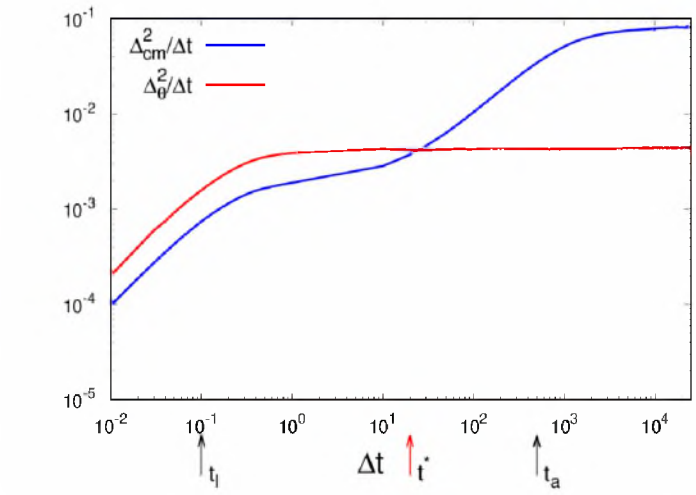

Figure 5.1: The single dumbbell center of mass mean-square displacement (MSD) divided by time delay, $\Delta^2_{\rm CM}/\Delta t$, as a function of Δt is shown with a blue solid line. The figure corresponds to $F_{\rm act} = 0.1$ and $T = 0.01$. The four regimes include the early inertial ballistic one, below t_I. The crossover times, indicated with arrows, are $t_I = 0.1$, $t^* = 20$ and $t_a = 500$ MDs, with time units defined in Section 5.1.3. Note that we use here the symbol τ_P, instead of t_a, for the persistence time. The angular MSD divided by time delay, $\Delta^2_{\theta}/\Delta t$, is also shown with a red solid line for a single molecule. It has only two time scales, separated by t_I. Inertial regime for angular MSD are shown here for completeness and it does not arise from our overdamped analysis (see the text for details).

5.1.3 Numerical approach for the finite-density problem

As soon as we add pair interactions between all the beads as in Eq. (5.1), an analytical approach is no longer available. We thus move to a numerical analysis with molecular dynamics for dealing with the finite density problem.

We performed a large number of simulations at fixed global surface fraction

$$\phi = \frac{N\pi\sigma_{\rm d}^2}{2L^2}\,, \tag{5.18}$$

and the Péclet number

$$\mathrm{Pe} = \frac{2F_{\rm act}\sigma_{\rm d}}{k_B T}\,. \tag{5.19}$$

exploring a wide portion of the (Pe,ϕ) plane.

As for the disks, the Péclet number can be interpreted as the ratio between the work done by the active force when translating the dumbbell by its characteristic size, $2\sigma_{\rm d}F_{\rm act}$, over the thermal energy scale $k_B T$.
In order to take under control the inertia, an active Reynolds number Re

$\mathrm{Re}^{\mathrm{act}} = m_{\mathrm{d}} F_{\mathrm{act}}/(\gamma^2 \sigma_{\mathrm{d}})$ can be defined in analogy with the hydrodynamic one (see Section 3.2). It is the ratio between the active force transport $F_{\mathrm{act}}/(\gamma\sigma_{\mathrm{d}})$ and the viscous transport term estimated as γ/m_{d}.

We provide, as a reference, the typical magnitude of these parameters, in units of σ_d, m and ε. Since we set $k_B T = 0.05$ and $\gamma = 10$, and we span self-propulsion strengths between 0 and 5, we thus have the Péclet number in the range $[0-200]$ and $\mathrm{Re}^{\mathrm{act}}$ in the range $[0-0.05]$, which is both compatible with the choice corresponding to the modelling of bacterial colonies, and with the assumptions made in the previous subsection. In fact, such global values correspond to a ratio τ_P/τ_I between the persistence time and the inertial time of $\sim 10^3$. The same choice of the parameters does not allow instead to observe separate t^* and τ_I because their ratio is typically of order 1. We thus observe only the initial ballistic active regime and the late diffusive one.

The same numerical algorithm described for the disk model in Section 3.2 is used for integrating the full passive dynamics for dumbbells with the software LAMMPS. However, as underlined in the previous Subsection, self-propulsion direction for dumbbells does not evolve separately from the single beads, but it diffuses along the main axis of each molecule. This direction is determined step-by-step by the implementation of the bond interaction between pairs of monomers.

We apply two different types of bonds, with quite indistinguishable results for numerical integration. The first comes from the finitely extensible non-linear elastic (FENE) potential

$$U_{\mathrm{FENE}}(r) = -\frac{1}{2} k r_0^2 \log\left[1 - (r/r_0)^2\right], \tag{5.20}$$

which mimic a hookeian interaction with elastic constant k, but it grows to infinity as $r - r_0^-$, preventing thus the dumbbells from stretching more than r_0. This simply avoids the breaking of the molecules during their evolution. The values $k = 30$ and $r_0 = 1.5$ are chosen in the respective units.

The FENE bond can be easily added to the inter-particle potential between each pair of beads, and is then integrated together with the repulsive potential. It establishes a new time-scale in the model, for the fluctuations in time of the dumbbells' elongation

$$\tau_{\mathrm{osc}} = 2\pi\sqrt{m/k}\,, \tag{5.21}$$

which is of order of unity. This other time scale forces us to choose a small enough integration timestep $\Delta t \ll \tau_{\mathrm{osc}}$, for preventing the bond energy to

diverge during one integration step. We accordingly choose $\Delta t \sim 10^{-2}$. Note that this timestep is still one order longer the inertial characteristic time τ_I, in agreement with our assumption for all the inertial effects to be negligible.

We also adopted, in place of the FENE, explicit constraints to the motion of the beads. This constraint, implemented with the RATTLE scheme [And83], leads to rigid molecules with a distance of σ_d between each head-tail couple. Although no new time scales arise with this method, we use the same timestep size $\Delta t \sim 10^{-2}$ to keep the integration stable with respect to the whole potential energy.

A typical run involves $\sim 10^5$ molecules and lasts for more than 10^7 integration timesteps, which corresponds to a time 10^5 in the time units considered. It is a long enough time to have stationary measurements for all the quantities of interest. We use different initial conditions, such as ordered, disordered, equilibrated without activity, in order to estimate the typical correlation times involved in the dynamics of the system. Some of the data sample from different type of initial configurations are given in Fig. 5.4 in the next Section, to ensure stationarity after quenching the system from different points in the phase space.

5.2 MIPS for dumbbells and properties of the dense phase

In this Section we review some of the most relevant features of aggregation in a system of SP dumbbells, which involve pattern formation in polar order and velocity field. These aspects are not observed for SP isotropic particles and they are directly related to the elongation along the self-propulsion direction.

Several works already demonstrated that MIPS, as an ubiquitous phenomenon of active systems, is also present for the model of SP dumbbells [GLS14, SGMO14, GMST15]. Also in a suspension of dumbbells, as for the more simple case of disks, high enough activity and density can trigger a density instability, which leads to strong phase segregation, with formation of large clusters, long-living in a homogeneous gaseous phase.

As already shown for instance in [SGMO14], MIPS is actually favored for SP dumbbells, with respect to disks. In Fig 5.2 a comparison between the two cases is shown, which undoubtedly leads to think that both elongation and non-convex shape of dumbbells are responsible for favoring MIPS.

Another important distinction between isotropic and elongated SP par-

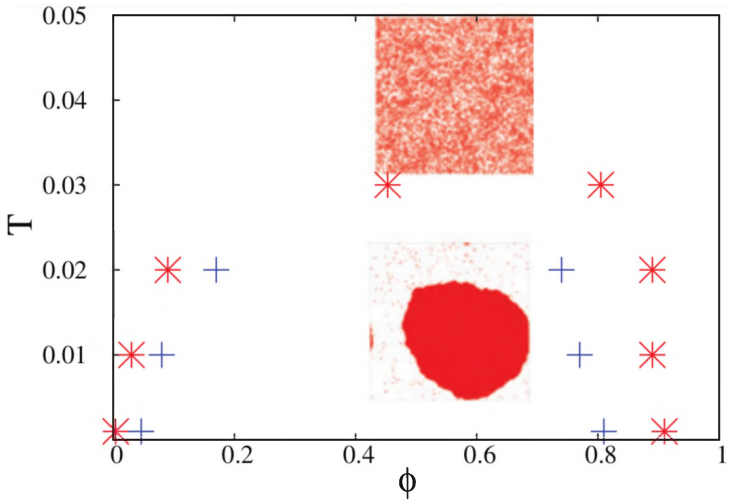

Figure 5.2: Phase diagram for the active dumbbell suspension (stars), in the density-temperature plane, together with snapshots of the system in the uniform (top) and phase separated (bottom) regimes. The temperature $T = 0.03$ in the given units limiting from above the phase boundary corresponds to the Péclet number $\mathrm{Pe} = 33$. The corresponding phase diagram for active spherical particles is denoted by pluses; this was found by simulating spheres with $F_{\mathrm{act}} = \gamma = 1$. Figure adapted from [SGMO14].

ticles arises from previous studies. The rotation of clusters of dumbbells around their center of mass, sustained by activity, is observed, for instance in [SGMO14]. As seen for the disks, for high enough activity, motility-driven aggregates are quite perfectly packed and the same happens for dumbbells. This point will be more clear in the next Section, but one readily accepts that our rigid dimers could be arranged with all the beads on a perfect triangular lattice. However, in a such ordered arrangement, while for the disks the self-propulsion direction is still allowed to freely diffuse over the angular coordinate, orientational degrees of freedom are frozen for the dumbbells. This provides a non-zero quenched global torque for clusters of dumbbells.

We further studied this feature, first observing the behavior of the polar field and the velocity, and then considering relations between pattern formations and macroscopic rotation of clusters. The results of such observations will serve as preparatory elements in the next Section, where we will complete our analysis, considering the hexatic order and Halperin-Nelson phase transition scenario, in the same way we have been done for the disks (see Chapter 3). Hexatic order will reveal even stronger differences between disks an dumbbells and will allow to capture the true phase diagram of this molecular model.

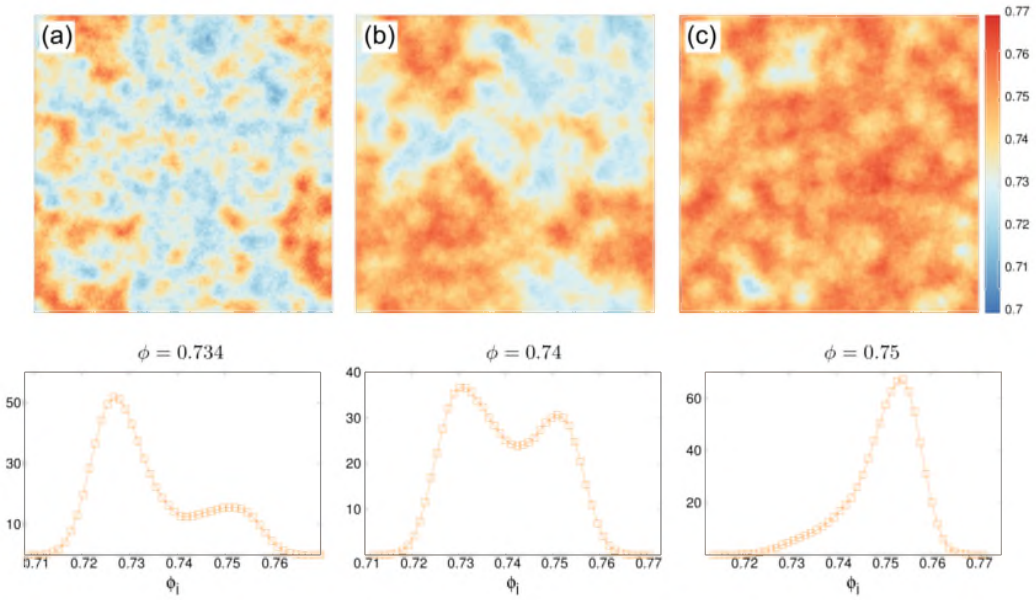

Figure 5.3: Stationary state of the passive system in the co-existence region of the phase diagram. Global packing fraction is given in the key. In the first row a color map of the local density is shown for the system (a) slightly above the lower binodal, (b) in the middle of the co-existence region and (c) slightly below the upper binodal. The probability density function of the local density is shown in the second row for the same cases.

5.2.1 Continuity of the co-existence region with activity

Among all the properties of MIPS introduced above, our analysis shows that, interestingly, phase separation for dumbbells is a robust phenomenon against activity. As shown in [CDGS17], we have been observed that passive dumbbell system exhibits phase co-existence between a low-density liquid and a high-density hexatic. This scenario agrees with a first-order liquid-hexatic transition of the same character of the one found for passive disks by Krauth *et al.* (see Chapters 2 and 3). We will focus on the ordering features of the two coexisting phase in the next Section, while we deal here only with co-existence.

As shown in Fig. 5.3, measures of the local density reveal phase co-existence for Pe= 0 in the global surface fraction range $\phi \in [0.730 - 0.756]$. Local density is computed using the method described in Chapter 3, taking as single-particle density the ratio between the area occupied by one single bead and its corresponding Voronoi cell, and than coarse-graining over a length of order $10\sigma_d$. Local density pdfs are thus extracted from local density sampling, averaging over different realization of the dynamics. Averages are also taken over steady-states of the system resulting from

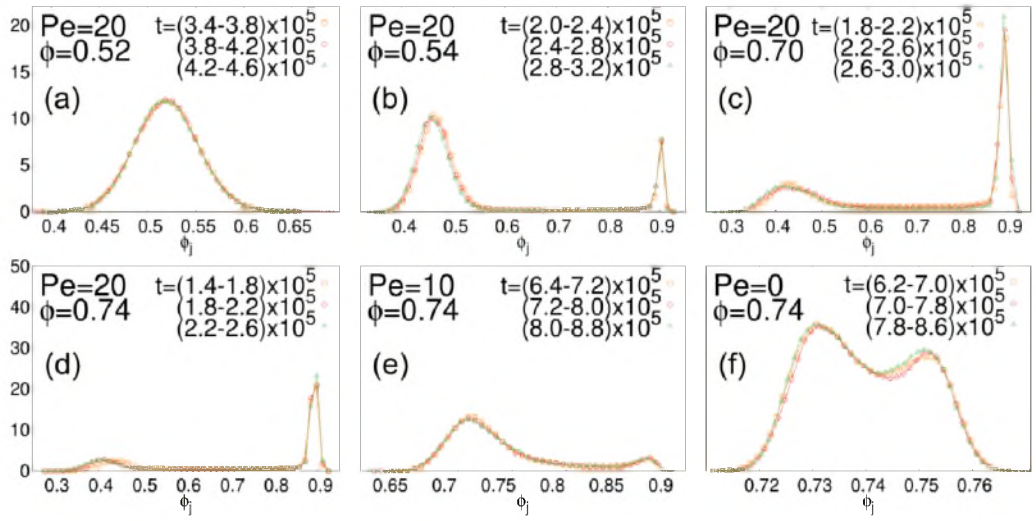

Figure 5.4: Distributions of local densities at $\phi = 0.52$ (a), 0.54 (b), 0.7 (c) and fixed Pe = 20 (first row, random initial configurations), and Pe = 20 (d), 10 (e), 0 (f) and $\phi = 0.74$ (second row, starting from equilibrium configurations of the passive system). The various curves correspond to data sampled over different time intervals given in the keys, to show stationarity.

different starting conditions. In particular we ensured that the same density pdf is obtained both starting from globally ordered and completely disordered systems.

Taking the system in the passive co-existence region and perturbing it by turning on a small amount of activity, we observed that, surprisingly, phase co-existence is maintained. After having explored this behavior for a big number of points in the Pe> 0 region close to the passive co-existence in the (ϕ – Pe) parameters' space, we concluded even very small values of activity are able to enhance phase co-existence with respect to the passive scenario.

As shown in Fig. 5.4, increasing further activity, a finite range of global surface fraction where the system is separated exists. We are able to determine the binodal for co-existence region by computing local density pdfs, and observing that, as for the standard equilibrium phase co-existence, the mean values of the two density peaks belonging to the two phases do not change with varying the global density at fixed activity.
By means of such information, we are able to conclude that equilibrium co-existence region not only is retained for arbitrary activity, but also merges continuously with the MIPS region observed in older works (see Section 5.2). Increasing Pe from 0 to large values where MIPS dominates as a pure activity-drive phenomenon, inside the connected co-existence

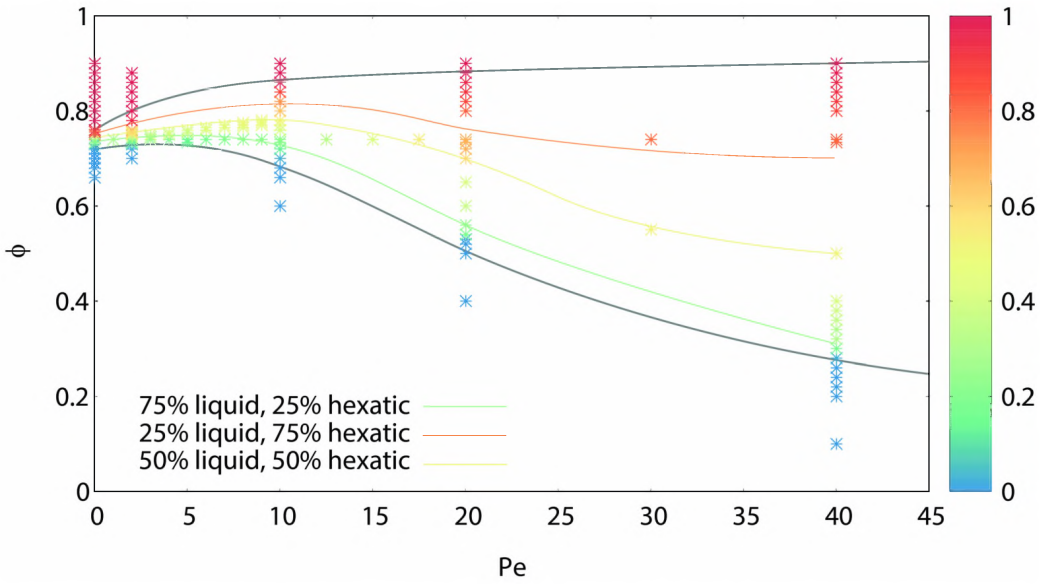

Figure 5.5: Co-existence in the (ϕ−Pe) space for the dumbbells model. Black solid lines indicate the lower and upper boundaries of the co-existence region. Below the lower line the system is in the liquid phase, while above the upper one it is hexatically ordered. See the text for the details. The points represent all the cases considered for simulations, colored proportional to the fraction of the dense phase, according to the color scale shown on the right.

region the distance between the two peaks of local density pdfs increases, meaning that activity enhances segregation with continuity. We remind that for SP disks activity acts in a very different way, first killing the passive liquid-hexatic co-existence region and then, beyond a critical point around Pe$\sim$ 35, driving MIPS (see Chapter 3).

Along with the location of the co-existence boundaries, we have been traced lines in the (Pe − ϕ) plane with constant area fraction of the two phases. See three of these lines in Fig. 5.5. We evaluated the amount of surface occupied by one of the two co-existing phases by first measuring the coarse-graining local density, then settling a density threshold in the way between the two peaks in the pdfs and finally dividing the particles between the two phases and extracting the whole area fraction that they cover. The three lines shown in the Figure will be useful in the next analysis about the features of the dense phase, for comparing cases at different Pes excluding the role of the global density.

5.2.2 Shape-induced polar order

In order to investigate the alignment of head-tail dumbbell orientations inside the clusters, which is absent in the passive case but expected to depend on the strength of the active force, we compute the *local polarization field* $\mathcal{P}$ and we evaluate its probability distributions. For each dumbbell inside the dense ordered phase we considered a unit vector $\mathbf{p}_i$ in the tail-to-head direction. We then average such measure over a squared grid with spacing of the order of few σ_d, obtaining a coarse-grained polarization field. We find quantitatively similar results for coarse-graining lengths ranging from $5\sigma_d$ to $20\sigma_d$, that are small enough spacing with respect to the system size and large enough to allow sampling over many single-dumbbell measures. To visualize the local values of $\mathcal{P}$, we evaluated its modulus and we colored each zone according to its magnitude.

We follow the evolution of the probability distributions of the local polarization modulus in the dense phase with varying activity and choosing global densities along the curves of constant area fraction 50%-50% (Fig. 5.6-(a)) and 25%-75% (Fig. 5.6-(b)) of the dense and the gaseous phase.

For low Pe values (Pe= $0, 10$) the pdfs show a single peak at small values of the local polarization modulus, revealing the absence of any polar order. This is also evident from the coarse-grained polarization fields of the clusters, that look completely disordered regardless of being inside or at the border of clusters and dominated by low-polarization values with sporadic negligible ordered parts.

As the activity increases (Pe$\geq$ 20) the probability distributions exhibit a two peak structure showing that activity tends to induce an effective polar interaction between dumbbells, reflected in the emergence of large ordered patterns in the clusters polarization field. While along the 50%-50% lines the coarse-grained polarization field remains typically with no polar order (white regions) in the central part of the clusters and ordered on the border, along the 25-75% line and Pe$\geq$ 40, if the activity is strong enough, the peak corresponding to random orientation tends to disappear. In these cases, the disordered region at the center of each cluster is reduced to a small white spot, otherwise stated, a defect for the polarization field. A deeper look into the local polarization field, see Fig. 5.6-(c), reveals the emergence at Pe= 40 of an aster structure with a charge equal to $q = 1$. At larger activity (Pe= $100, 200$), the aster evolves into a spiralling pattern. Notice that this spiralling pattern is associated to an increased angle between the defect and the local polarization field.

To clarify the reason for the appearance of the aster pattern with a defect at the cluster's center we can trace back the evolution of one of

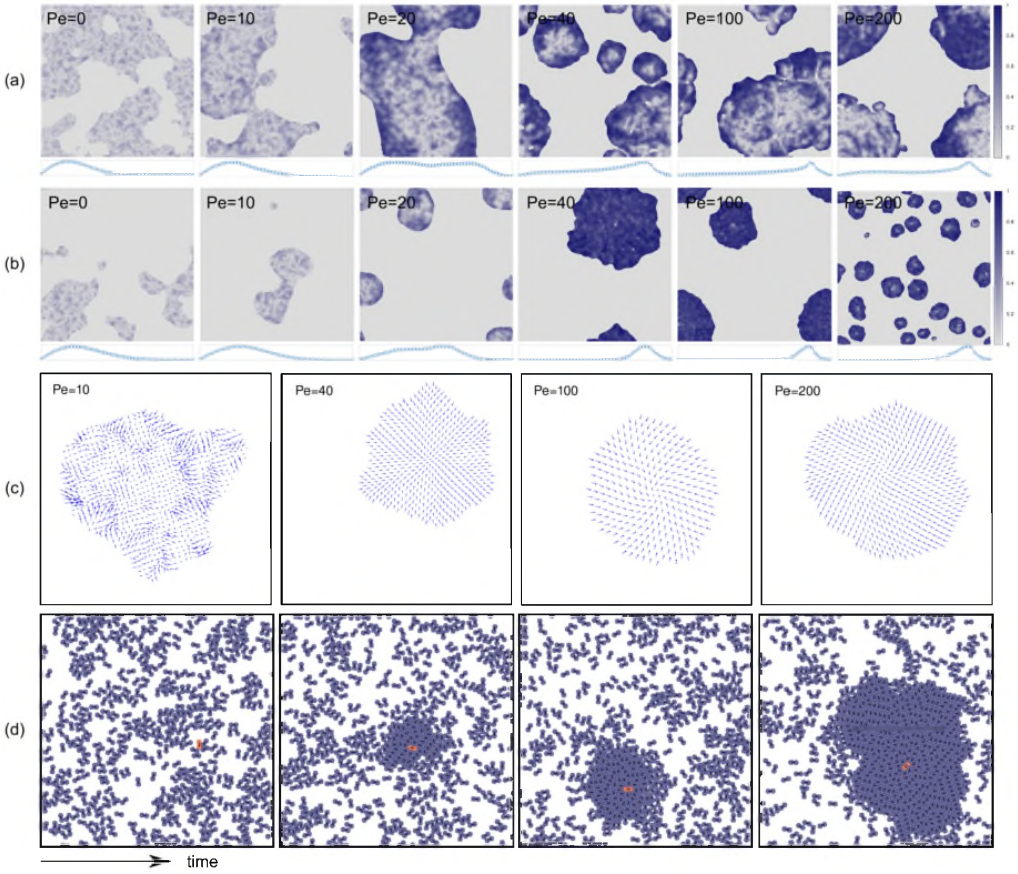

Figure 5.6: (a) Map of the local polarization modulus $|\mathcal{P}|$ (above) and pdfs of the local polarization modulus (below), both smoothed over regions with radius $R = 5\sigma_d$ at different Pe number ranging from Pe = 0 to Pe = 200 (see the keys) along the curve with 50%-50% proportion of ordered and liquid regions (yellow curve in Fig. 5.5). (b) The same for values of the parameters along the curve with 25%-75% of dense and lose components, respectively (green curve in Fig. 5.5). (c) Local polarization field $\mathcal{P}$ at Pe = 10, 40, 100, 200 in the 25%-75% line. Increasing Pe, the clusters exhibit a spiralling pattern with an increasing angle between $\mathcal{P}$ and the vector pointing toward the cluster centres. See text for the details. (d) Snapshots taken from a single run at four different times, $t = 66000, 67000, 72000, 78000$ (in time units), from left to right. They show how the cluster is formed around the 'central' dumbbell coloured in red that triggers aggregation. The parameters are Pe = 40 and $\phi = 0.310$.

the dumbbells that is located near the defect, at Pe= 40. In this way we can go back to the event that triggered the MIPS in the first place. In Fig. 5.6-(d) a series of snapshots of the formation of the cluster are shown, with the traced dumbbell colored in orange. The cluster formation process starts with multiple head-to-head dumbbells collisions (thus without polar order). After the initial nucleation, other dumbbells start to segregate on

the cluster, with a pathway that is necessarily on average directed towards the cluster's center. Larger activities allow the initial colliding direction to remain fixed after segregation. This allows the polar field to be ordered in an aster (or spiral) pattern, and not disordered as observed at the lower value Pe= 10.

5.2.3 Macroscopic effects of polar alignment. Enstrophy and cluster rotation

We already mentioned in the introduction to this Section, that because of an understandable quenching of rotation, clusters of active dumbbells perform rigid rotation around their center of mass. Since we have been established that clusters are present for all values of activity for our system, we wanted to explore cluster rotation along the entire phase separation region, from Pe= 0 to very strong self-propulsion.

For such analysis we have been evaluated the velocity field by first averaging over a typical time (t = 1 in the given units) the instantaneous velocity of each bead relative to the center of mass of the full system and then coarse-graining these values over square plaquettes with side R. We used different values of R depending on the typical cluster size. In particular, it must be larger than the particle's size and smaller than the typical size of the aggregated phase. We found appropriate lengths in the range $[10-20\sigma_d]$ (all the results shown here have been obtained with $10\sigma_d$).

After having computed the velocity, we have been evaluated a suitable quantity called *enstrophy*, useful to describe vorticity. The enstrophy is defined as

$$\epsilon = \frac{1}{2}\sum_j |\boldsymbol{\omega}(\boldsymbol{r}_j)|^2 \,, \tag{5.22}$$

where $\boldsymbol{r}_j$ locates the grid points for the coarse-grained velocity and $\boldsymbol{\omega} = \boldsymbol{\nabla}\times\boldsymbol{v}_j$ is the vorticity vector, with $\boldsymbol{v}_j$ the coarse-grained velocity field. While the kinetic energy gives a measure of the strength of flow in the system, the enstrophy is a measure of the presence of vortices in the velocity field and it can be used to understand whether clusters rotate driven by activity.

In Fig. 5.7 we show the pdfs of the enstrophy, evaluated over several independent and stationary configurations. The panels display the results for systems at different Pe numbers, Pe= 20, 100, 200, along the 50%-50% curve in the phase diagram. The inserts are maps of the velocity field and show its typical behavior. The probability of finding a non-zero value of the enstrophy decreases smoothly for low Pe number with an exponential tail (not distinguishable in the plot), with the snapshots of the velocity

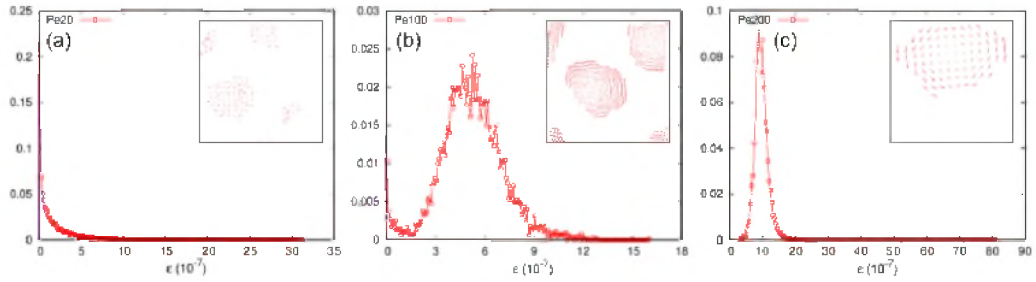

Figure 5.7: Main plots: the enstrophy pdfs at Pe = 20, 100, 200 along the 50%-50% curve. Inserts: coarse-grained velocity field in four representative instantaneous configurations at the same parameters. The peaks appearing in the pdfs at Pe = 100, 200, are associated to clusters undertaking a rotational motion.

field at Pe= 20, 40 (not shown) suggesting a lack of coherent rotation. It can be checked that the exponential decay at Pe= 20, 40 is very close to the one at Pe= 0, meaning the enstrophy values are purely associated to the thermal noise. Since we do not expect any relevant vortical behavior in the passive case, the noise level can be approximately estimated by measuring the enstrophy distribution at Pe= 0. Moreover, as noticed in the previous Subsection, for low values of the Pe number the coarse-grained polarization field looks completely disordered, while at Pe= 40 the dumbbells tend to point along the radial direction towards the center of the cluster without exhibiting a spiralling pattern. In both cases these features seem to prevent a coherent rotation. At higher Pe (see the cases at Pe= 100, 200), the probability distribution function of the enstrophy develops a multi-peak structure depending on the number and size of the clusters on scales clearly distinguishable from the noise contributions. We interpret this behavior as a clear evidence of the onset of cluster rotation. For intermediate values of the activity such as Pe= 70, we can also observe cases of a coherent, even if less evident, rotation.

In Ref. [SGMO14] the authors presented a minimal mean-field framework within which it is possible to understand the physics of these rotating aggregates. It is based on the assumptions that rotating clusters are very dense objects with negligible density fluctuations, and that cluster rotation is a rigid motion. Both of these two points are already clear from our analysis.
A macroscopic momentum balance in the Stokes regime reads

$$0 = -\nabla P + \mathbf{f}^{\mathrm{act}} - \tilde{\gamma}\boldsymbol{v}\,; \quad \nabla \cdot \boldsymbol{v} = 0\,, \tag{5.23}$$

with P the pressure field, $\mathbf{f}^{\mathrm{act}}$ and $\tilde{\gamma}\boldsymbol{v}$ the active force and the viscous force per unit area, respectively. Since active force is proportional to the

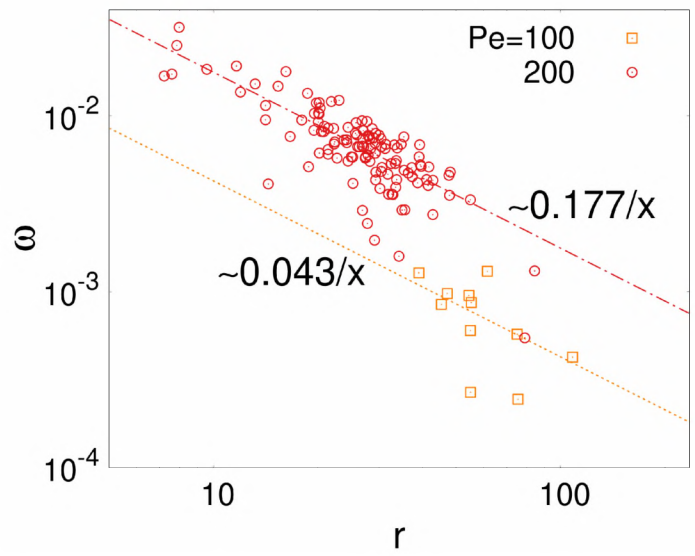

Figure 5.8: Log-log scatter plot of the angular velocity ω of the clusters versus their radius r, at Pe= 100, 200 along the 25%-75% curve. A fit of the function a/r for each Pe is shown as an inclined line, with $a = 0.043, 0.177$ for Pe= 100, 200, respectively.

polarization vector $\boldsymbol{\mathcal{P}}$ and stress tensor is non zero inside clusters, this equation also accounts for the different direction between $\boldsymbol{\mathcal{P}}$ and $\mathbf{v}$ in the dense regions, that we also observe in our case for high enough Pe, having the polarization a spiralling pattern and the velocity a vortex-like one. In the liquid phase pressure becomes negligible, leading to parallel $\boldsymbol{\mathcal{P}}$ and $\mathbf{v}$.

From Eq. (5.23) one can also argue a scaling law for the angular velocity with the average radius R of the cluster. Given the rigidity of the cluster which means that $\mathbf{v} = \omega r \mathbf{e}_\theta$ (being $\mathbf{e}_\theta$ the unit vector along the azymuthal direction), Eq. (5.23) leads to $\omega = f_{\parallel}^{\text{act}}/(\tilde{\gamma}R)$, with $f_{\parallel}^{\text{act}}$ the projection of self-propulsion force per unit area along the direction of the velocity.

Together with the $1/R$ scaling, in the same context it was found that the order of magnitude of the angular velocity is around 10^{-4}. If one accepts the simplifying assumption that the clusters perform a uniform motion, the enstrophy is the angular velocity squared and, in this approximation, its order of magnitude is compatible with the data shown in Fig. 5.7.

In order to measure the mean angular velocity of the rotating clusters and the orientations of the dumbbells inside each cluster, it is necessary to distinguish between the particles belonging to a cluster, characterized by high-density, and the free particles moving in low density regions. To perform this task, we used a density-based clustering algorithm, DBSCAN (Density-Based Spatial Clustering of Application with Noise) [EKSX96],

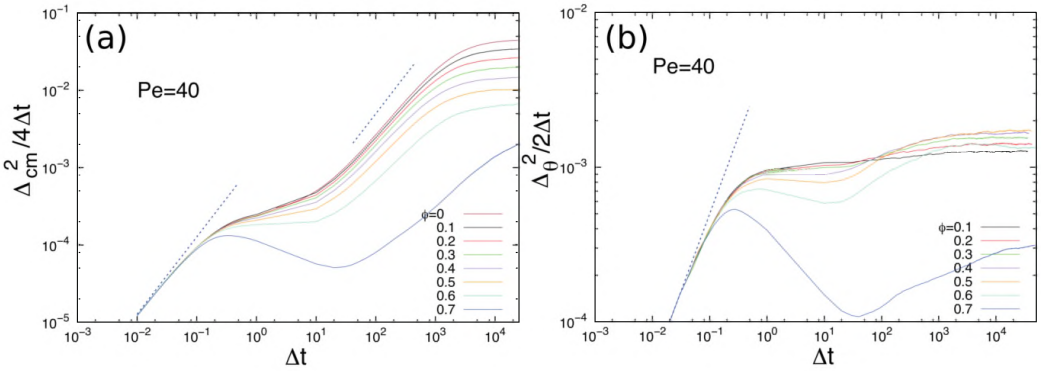

Figure 5.9: (a) The overall dumbbell centre of mass mean-square displacement $\Delta^2_{\rm cm}$ as a function of Δt, for various densities given in the key. See the text for a discussion. (b) Same for the angular mean-square displacement Δ^2_θ as a function of Δt.

that gathers points closely packed together and that marks as noise points lying in low-density regions. We associate a particle to a cluster when it has at least 10 nearby particles within a circle of radius $2\sigma_d$ around its center, and in this way we are able to locate all the cluster aggregates (and the particles contained in each of them).
Once the clusters are identified, we first associate a radius to them, by calculating the radius of a disk with the same moment of inertia. Then we calculate the angular moment with respect to the cluster's center of mass. In this way, we easily get an estimate of the angular speed of the rotating clusters around their center of mass. In Fig. 5.8 we show the results obtained at Pe= 100, 200 along the 25%-75% curve, which quite well agree with the $1/R$ scaling.

5.2.4 Mean-square displacements

The positional mean-square displacement of the center of mass of the single dumbbell of Eq. (5.15) generalizes to

$$\Delta^2_{\rm cm}(\Delta t) = \frac{1}{N}\sum_{i=1}^{N}\langle(\boldsymbol{r}_{{\rm cm}_i}(t+\Delta t) - \boldsymbol{r}_{{\rm cm}_i}(t))^2\rangle \tag{5.24}$$

and the rotational one to

$$\Delta^2_\theta(\Delta t) = \frac{1}{N}\sum_{i=1}^{N}\langle(\theta_i(t+\Delta t) - \theta_i(t))^2\rangle \tag{5.25}$$

in a system with N dumbbells. These global measurements can lead to confusing or even misleading results in heterogeneous cases with phase

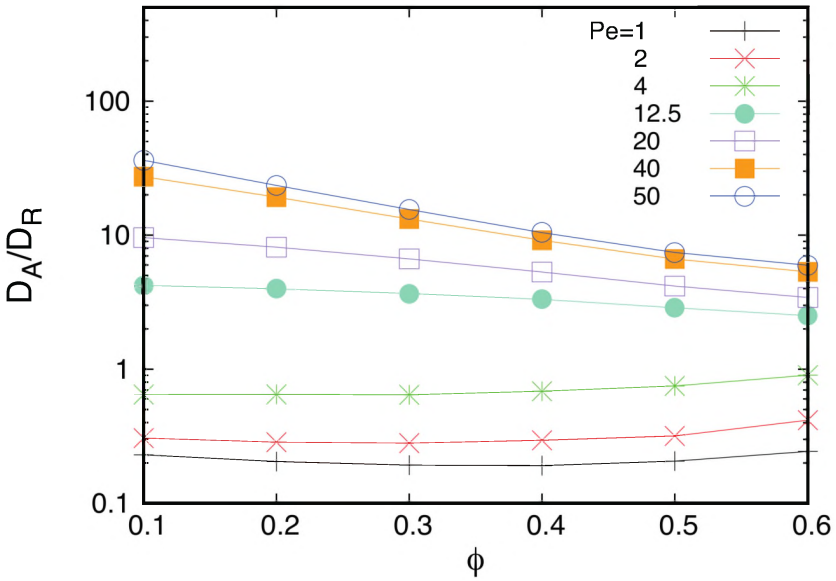

Figure 5.10: The ratio between the translational and the rotational diffusion constants as a function of packing fraction for various values of the Péclet number given in the key.

co-existence. When this arises, a distinction between particles in the dense and liquid phases may be necessary to understand the behavior of these quantities and, more generally, of the system as a whole. This can be done, for example, by following the pdf of the displacement along a chosen direction, say x, at a certain time-lag Δt:

$$p(\Delta x_{\rm cm}, \Delta t) = \frac{1}{N}\sum_{i=1}^{N} \delta(\Delta x_{\rm cm} - \Delta x_{{\rm cm}_i}(\Delta t)) \,, \tag{5.26}$$

$$p(\Delta_\theta, \Delta t) = \frac{1}{N}\sum_{i=1}^{N} \delta(\Delta_\theta - \Delta_{\theta i}(\Delta t)) \,, \tag{5.27}$$

for a single run, and their average over many repetitions of the dynamics under the same conditions.

The finite density effects on the dynamics, for relatively low Pe values, that is to say, mostly in the liquid phase, were evaluated in [SGMO14, SGL$^+$14]. The four dynamic regimes in the center of mass MSD of a single dumbbell, described in Sec. 5.1.2, are preserved for sufficiently low densities. The translational diffusion constant D_A in the ultimate diffusive regime (see Eq. (5.15)) and rotational diffusion constant, D_θ, once normalized by the thermal energy scale k_BT, depend only on ϕ and Pe. D_A diminishes with increasing density while, for sufficiently high Pe, D_θ first increases and next decreases with ϕ. Both are enhanced by Pe and

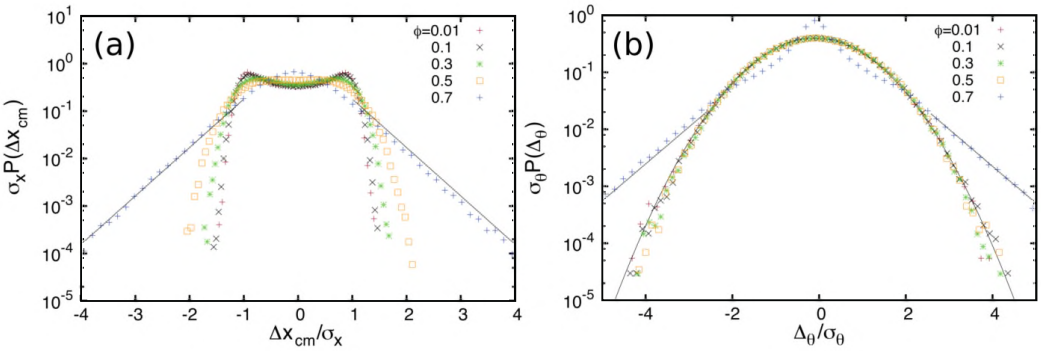

Figure 5.11: (a) The pdf of the centre of mass displacement along the horizontal axis at a fixed $\Delta t = \tau_P/2$ for which the total centre of mass displacement is non-monotonic, see Fig. 5.9 (a). Pe = 40 and densities given in the key. σ_x is the dispersion of this pdf. (b) The pdf of the angular displacement for the same case as in (a). σ_θ is the dispersion of this pdf.

the functional dependence on this parameter is more involved than just quadratic. However, at sufficiently large packing fraction the density effects are stronger and a qualitative change in the properties of the MSDs are found, as can be seen in Figs. 5.9 (a) and (b).

The liquid like behavior, with the four regimes recalled in Sec. 5.1.2, is progressively modified by the increasing density. For the globally denser system, $\phi = 0.7$, an anomaly in the first diffusive and second ballistic regimes in the center of mass MSD is clear, see Fig. 5.9 (a). The rotational properties are modified even more, with the rotational MSD being strongly affected already at $\phi \simeq 0.35$ and the rotational diffusion constant D_θ being enhanced by density beyond this value of ϕ.

Another view on the global motion of the system is given by the comparison between the center of mass diffusion constant and the rotational diffusion constant, both measured in the last time-delay regime. This is shown in Fig. 5.10 in the form of the ϕ dependence of the ratio D_A/D_θ for different Pe numbers, ranging from Pe = 1 to Pe = 50. At large Pe, say Pe$\leq$ 50, the ratio weakly decreases with ϕ while at small Pe the trend is the opposite. If we consider the typical values of translational and rotational diffusion coefficients for non-tumbling bacterial colonies [EWG15, VLN$^+$11], the experimental ratio D_A/D_R appears slightly higher than our results.

The qualitative change in the global dynamics is a consequence of the co-existence of dumbbells that move very differently in the sample. This is confirmed by the analysis of the probability distributions of the individual dumbbell center of mass and angular displacements displayed in Fig. 5.11 (a) and (b). These figures, constructed for a fixed value of time

delay $\Delta t = \tau_P/2$ (the intermediate ballistic regime in the single molecule limit), present in fact wide tails at high density $\phi = 0.7$, strongly deviating from the Gaussian behavior.

5.3 Liquid-hexatic transition and phase diagram

Once we have presented a general view of phase separation of SP dumbbells over the (ϕ – Pe) space, we now move to ask whether co-existence is related to an underlying phase transition. In the same way we have been done for the disks in Section 3.5, we use here all the concepts of KTHNY theory of melting in 2D for studying liquid-hexatic and hexatic-solid-transition for both passive and active dumbbell system. This was actually the central purpose of [CDGS17], and we are going to review here some of the main results that we found there and that we explored further in [PDC+18].

5.3.1 Phase diagram

Therefore, following initial studies in, *e.g.*, [GLS14, SGMO14, VLN+11] that focused on the boundary enclosing MIPS at high Pe, in [CDGS17] we presented the full phase diagram of the active dumbbell model, that is shown if Fig. 5.12.

Here we show how, as found in Subsection 5.2.1, co-existence between a dense and a dilute phase extends all the way to Pe= 0, with no "critical" ending point at a non-zero Pe, in a scenario different from what has been stated in the literature so far. The dilute phase has no order and behaves as an active liquid or gas while the dense phase has orientational order and it is therefore an active hexatic phase. These results, as for the disks, made contact with the recent advances in the understanding of two-dimensional melting of passive disk systems in interaction: namely, the first order kind of the transition between liquid and hexatic phases and the ensuing co-existence between the two [WMB95, BKW09, BK11, EAG+13, KK15].

We explain in the next Subsection how we obtained this phase diagram using all the observables described in Section 3.3. Notice that since the disks forming the dumbbells are not completely hard, some overlap between them is possible and values of ϕ that are slightly larger than the close packing limit can be accessed in the simulation (recall that the close packing fraction of disks in two dimensions is achieved by a perfect triangular lattice and it amounts to $\phi_{cp} \approx 0.91$).

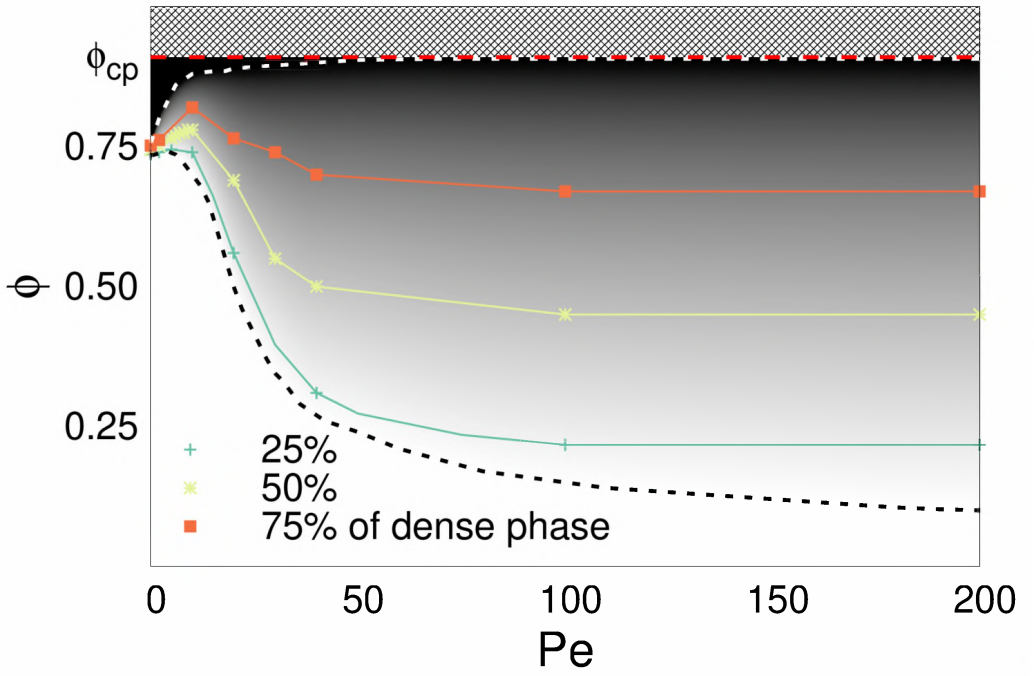

Figure 5.12: Phase diagram of the active dumbbell system. The grey scale represents the amount of dense ordered phase in the system. The dotted curves are the location of the lower (in black) and upper (in white) limits of coexistence. In the black region above the white dotted line the system is in a single ordered phase. The solid colored line-points indicate curves on which there is a constant proportion of areas covered by the dense and dilute phases in the co-existence region (see the key). The horizontal red dotted line at $\phi_{cp} = 0.91$ refers the close packing limit of hard disks.

5.3.2 Hexatic and positional order

The specific problem we have been faced to build the phase diagram was to determine the nature of the co-existing phase with varying the activity. We start with the passive system, where, as stated in Sec. 5.2.1, there a finite range of surface fraction ($\phi \in [0.730 - 0.756]$) with co-existence between two phase of different density, and then we move to Pe> 0. From bimodal shape of local density pdfs we know the co-existing densities of these two phases. We computed then the hexatic and positional correlation functions, in the way that we described in Chapter 3, using as items the single beads instead of the whole molecules. Indeed, as stated above, the beads are the ones which arrange on a triangular lattice in the limit of highly order configuration.

The orientational and positional correlation functions are shown in Figs. 5.13, 5.14 and 5.15, side-by-side, for three activities Pe$= 0, 2, 10$, and

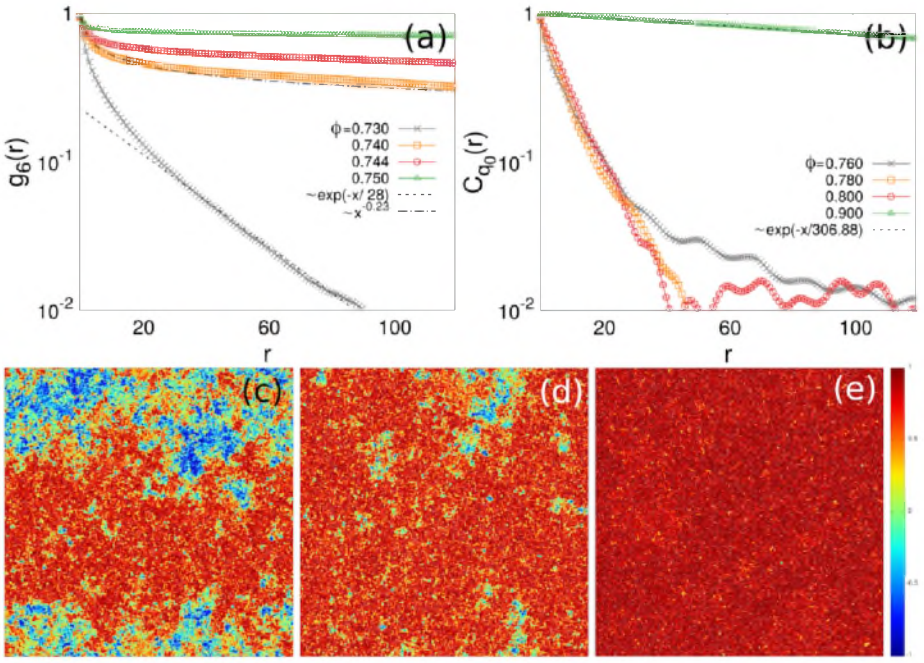

Figure 5.13: Orientational correlation functions (a) and positional correlation functions (b), as defined respectively in Sec. 3.3 for Pe= 0 and different values of the packing fraction indicated in the keys, in log-lin scale. The highest density with an exponential decay and the lowest density with power-law decay are fitted with a dotted and a dashed line, respectively. For (b) the latter is absent. Above, three snapshots representing local hexatic parameter through the methods described in text, for Pe= 0 and ϕ = 0.740 (c), 0.750 (d), 0.800 (e).

various packing fractions indicated in the keys. Below these plots, typical configurations in the stationary regime of various representative pairs (Pe, ϕ) are displayed, in order to better understand the behavior of the correlations. All correlation functions are plotted on a log-lin scale, in order to clearly identify transitions between exponential and power-law decays. Moreover, the highest density with exponential decay and the lowest density with power-law decay (if present) are fitted with a dotted and a dashed lines, respectively.

For all the values of the activity, Pe= 0, 2, 10, the orientational correlation function changes from an exponential decay at low ϕ to an algebraic one at high ϕ. We interpret this change as being due to the fact that the density parameter is moving across the coexistence region, so that the region above coexistence is characterized by quasi-long-ranged orientational order. This same behavior was found in the first order liquid-hexatic transition of passive spherical particles [KK15]. It allows us to claim that, both in

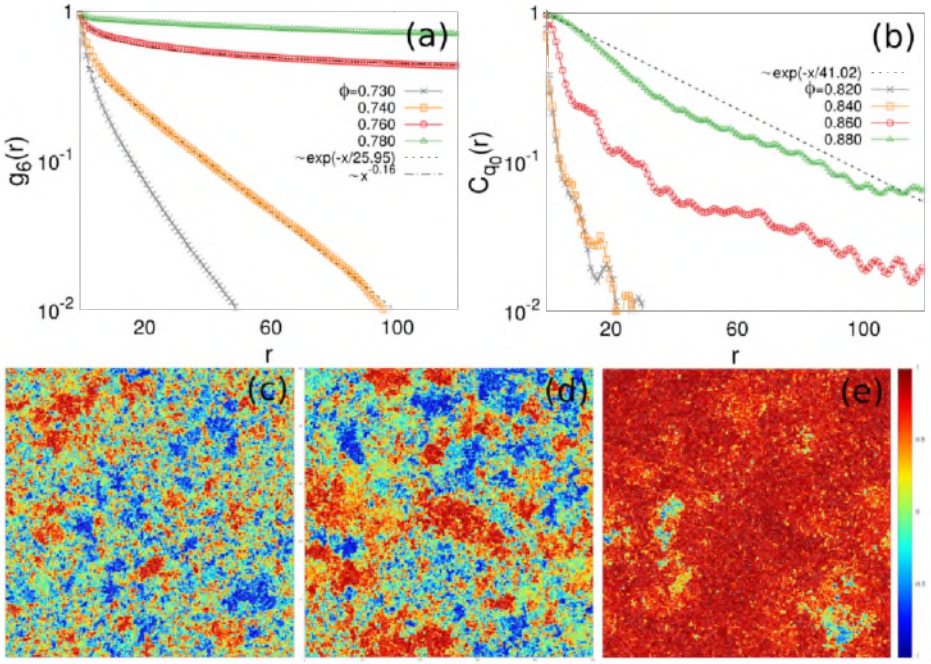

Figure 5.14: Orientational correlation functions (a) and positional correlation functions (b) for Pe= 2, in log-lin scale and with exponential and power-law fits provided. Below, typical snapshots for Pe= 2 and ϕ = 0.730 (c), 0.740 (d), 0.800 (e).

equilibrium and for all positive values of the activity, co-existence between a disordered phase and a hexatically ordered one, depicted with the grey gradient in the phase diagram of Fig. 5.12.

On the other hand, positional correlation functions never exhibit algebraic decay, except in the close-packing limit (see, for example, the curve at Pe= 0 and ϕ = 0.900 in Fig. 5.13-(b), which can be still fitted by an exponential). Since monomers are constrained to be attached in pairs, they cannot arrange on a triangular lattice at any $\phi < \phi_{cp}$, forcing the positional correlations of the monomers to decay exponentially.

See for example in Fig. 5.13-(b) than even at ϕ = 0.800 the positional order is short-ranged, although the system is already orientationally ordered as shown by the snapshot in Fig. 5.13-(e).

With positive activity we can also observe some mixed cases, *e.g.* the curve at Pe= 2, ϕ = 0.880 in Fig. 5.14-(b), with an initial algebraic decay and an exponential tail, since activity is able to drive the system to form very close-packed ordered domains together with disordered regions among them (see the snapshot in Fig. 5.14-(e)). Increasing activity further, the upper limit of the coexistence is pushed towards higher values of the

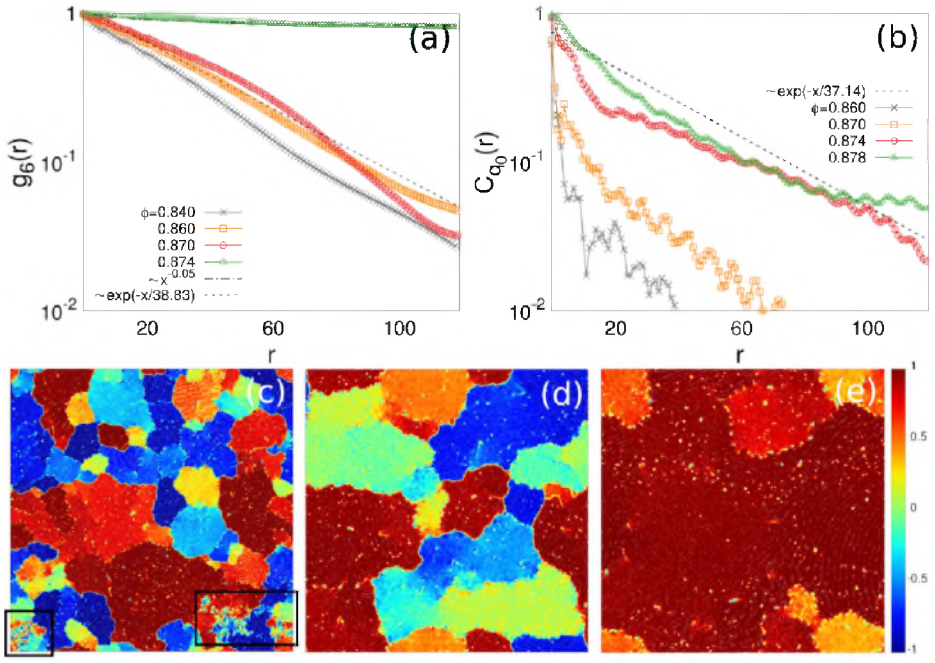

Figure 5.15: Orientational correlation functions (a) and positional correlation functions (b) for Pe= 10, in log-lin scale and with exponential and power-law fits provided. Below, snapshots for Pe= 10 and ϕ = 0.860 (c), 0.872 (d), 0.874 (e). In the snapshot (c) the two disordered regions are highlighted by the two black squares.

packing fraction. This makes the analysis of the phase above coexistence much more demanding, because of the slowing down of the relaxation time. Snapshots in Fig. 5.15-(c,d) are one below (note the small disordered hole at ϕ = 0.860) and one above the co-existence limit and they are both in a metastable polycrystalline state explaining why both the orientational order and the positional one decay within the system size. The exact nature of the transition between the hexatic and solid phases for the dumbbell system and its location in the phase diagram are still open questions. We aim to go deeper into them in our future works.

5.3.3 Structure factor

We complement our analysis of order for passive and active dumbbell with showing the static structure factor calculated from the positions of the beads as

$$S(\mathbf{k}) = \frac{1}{2N}\langle \sum_{i=1}^{2N}\sum_{j=1}^{2N} e^{i\mathbf{k}\cdot(\mathbf{r}_i-\mathbf{r}_j)}\rangle \,, \tag{5.28}$$

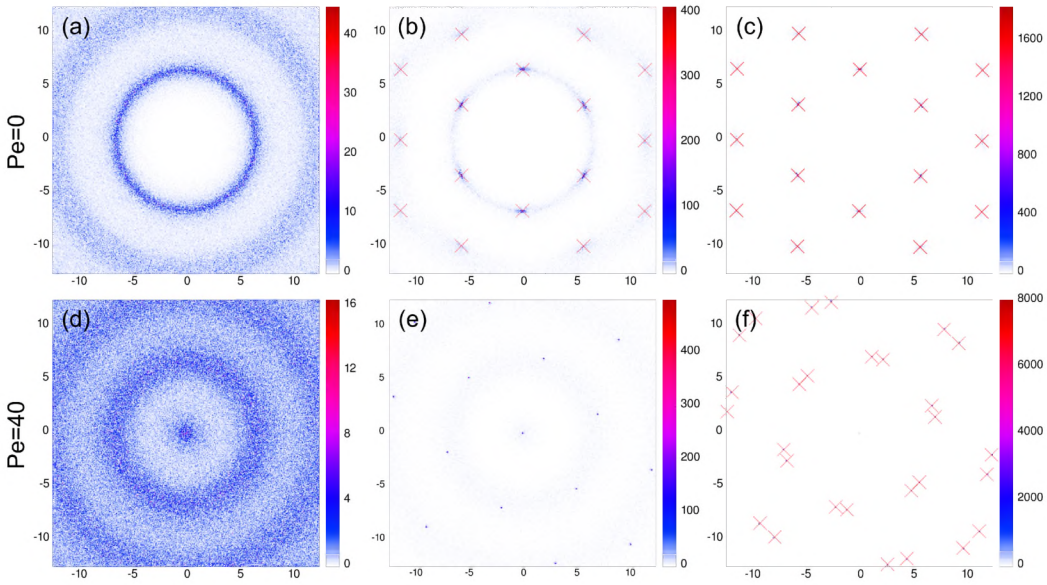

Figure 5.16: The structure factor in stationary states of the dumbbell system for Pe= 0 in the first row and Pe= 40 in the second row. The densities are (a) $\phi = 0.72$ in the liquid phase, (b) $\phi = 0.74$ in the co-existence region and (c) $\phi = 0.76$ in the hexatic phase, (d) $\phi = 0.26$ (active liquid), (e) $\phi = 0.28$ (active co-existence) and (e) $\phi = 0.34$ (active hexatic). The crosses in the last panels of each row are located at the positions of the Bragg peaks (see the text for an explanation).

where average is over different configuration in the same steady state. Fig. 5.16 the structure factor is shown in units of $1/\sigma_d$ for three cases without activity in the first row for different values of global density and three cases at Pe= 40 in the second row. For both the two rows the three cases are computed from the system in the liquid phase, in the co-existence region, and in the hexatic phase. We clearly see from the figure that liquid is a isotropic phase, while hexatic show six-fold periodicity. In the structure factor in the co-existence both the two behavior overlap, giving confirmation of co-existence between isotropic liquid and hexatic.

In the hexatic case, for both Pe= 0 and 40, predicted positions of the six peaks are shown, as computed from the base vector system in the reciprocal space

$$\mathbf{k}_1 = \frac{4\pi}{a\sqrt{3}}\left(\sqrt{3}/2, -1/2\right), \qquad \mathbf{k}_2 = \frac{4\pi}{a\sqrt{3}}\left(0, 1\right), \tag{5.29}$$

where a is the spacing in the real lattice that is related to the surface fraction of the ordered phase as

$$a = \left(\frac{\pi}{2\sqrt{3}\phi}\right)^{1/2} \sigma_{\mathrm{d}} \, . \tag{5.30}$$

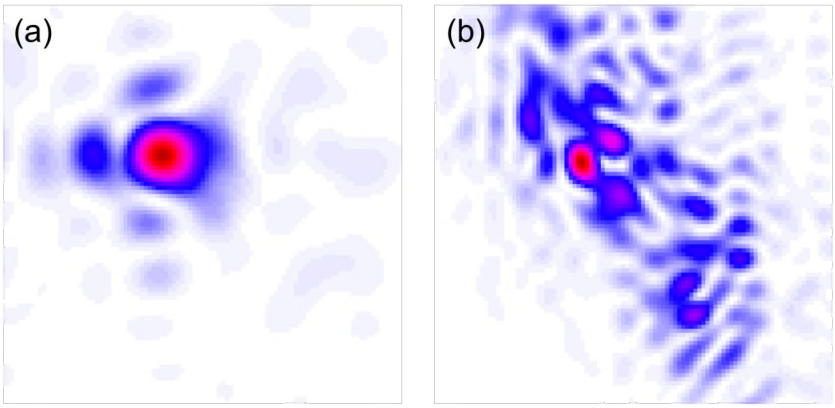

Figure 5.17: Detail of one of the six peaks in the static structure factor for (a) disks and (b) dumbbells at equilibrium. For the disks the system is the solid phase (see Chapter 3), while for dumbbells we chose a high value of surface fraction, deep in the hexatic phase, close to the maximum-packing limit.

In the same figure is also shown an enlargement of the structure of the peaks used, as described before, for calculating the translational correlation function. While for the disks this peaks has a regular symmetric structure, as the power-law singularity expected in a 2D solid [HN78], for the dumbbells it is much more broadened. Clearly, the structure of the six peaks representing the triangular order for the beads merges with the internal structure of the molecules, strongly indicating the absence of quasi-long-range positional order.

Appendix A

Gradient expansion for kinetic coarse-grained model of RT particles

We demonstrate here the result in Eq. (1.15). A standard way to analyze equation (1.14) is to consider the so-called hydrodynamic limit in which suitable moments of the distribution functions change smootly in space and in time. A gradient expansion of equation (1.14) can be performed in such limit and a hierarchy of equations, one for each order of the derivative, results. According to such expansion, the distribution functions can be written as

$$f = f^{(0)} + f^{(1)} + f^{(2)} + \dots , \tag{A.1}$$

where $f^{(n)}$ is a $\sim O(D^n)$ contribution, where D denotes derivatives over space or time. In the hydrodynamic limit, every successive derivative applied to f is assumed to make it much smaller, that is:

$$O(D^n) \ll O(D^{n-1}) \ll \dots \ll O(D^1) \ll O(D^0) \equiv \mathbf{I} , \tag{A.2}$$

hence

$$f^{(n)} \ll f^{(n-1)} \ll \dots \ll f^{(1)} \ll f^{(0)} . \tag{A.3}$$

The details of the calculus can be found in [GMST15]. The zero-order equation reads

$$f^{(0)} = \frac{\rho}{\Omega_d} , \tag{A.4}$$

where ρ is the density of swimmers at $\mathbf{r}$ and is simply given by the integral in (1.14), Ω_d is the d-dimensional solid angles. Thus, to the leading order, we immediately get that no term other than $f^{(0)}$ contributes to the coarse-grained hydrodynamic density ρ.

Including first- and second-order derivatives in the gradient expansion, and taking the integral over the directions, is straight using (A.4) to obtain

$$\partial_t \rho + \frac{1}{\Omega_d} \int \mathrm{d}^{d-1}\mathbf{u}\, \partial_i (v u_i \rho) - \frac{\tau}{\Omega_d} \int \mathrm{d}^{d-1}\mathbf{u}\, \partial_t \partial_i (v u_i \rho) - \frac{\tau}{\Omega_d} \int \mathrm{d}^{d-1}\mathbf{u}\, \partial_i (v u_i \partial_j (v u_j \rho)) = 0 \,. \tag{A.5}$$

Because, for symmetry reasons, the second and the third integral in above expression are zero, from the relation

$$\frac{\int \mathrm{d}^{d-1}\mathbf{u}\, u_i u_j}{\Omega_d} = \frac{\delta_{ij}}{d} \,, \tag{A.6}$$

one finally obtains

$$\partial_t \rho = \frac{\tau}{d} \boldsymbol{\nabla} \cdot \left[v \boldsymbol{\nabla} (\rho v) \right] . \tag{A.7}$$

Appendix B

Orientational long-range order in 2D flocking

Let's consider a large number of people on a flat plane, with no references in the space (no preferred directions), who are able to see their neighbors up to a short distance around them, like they are in the fog. Let's now imagine to ask these people to do their best to point all in the same direction, with the only reference of their nearest neighbors. The Mermin-Wagner theorem, as stated in Section 1.2, ensures that, regardless their ability of pointing in the same direction with respect to their neighbors, they do not manage to align. Enough far apart people would point in completely different directions.

The result of this imaginary experiment would change much if one asks to the same people to *walk* in the same direction. They would certainly be able to do that with a rather good precision. Two widely separated people (who do not see each other) will move about the same direction.

A quite simple "dynamical", though much insightful, argument is used in [Ton18] to explain such apparent violation of the Mermin-Wagner theorem. Obviously, the reason why walkers can overcome the limitation of the theorem is that they are out-of-thermal equilibrium. While pointers can easily associated to an equilibrium system of aligning objects (think for instance to a system of magnetic spins) where errors in the alignment play the role of the temperature, self-sustained motion, like for active systems described in Section 1.1, is a inherent non-equilibrium character. Even though it is easy to recognize that the key ingredient for violating the Mermin-Wagner theorem is the movement, we are interested here in outlining a quantitative argument which accounts for such violation.

Starting with non-moving pointers, it is a rather good approximation to

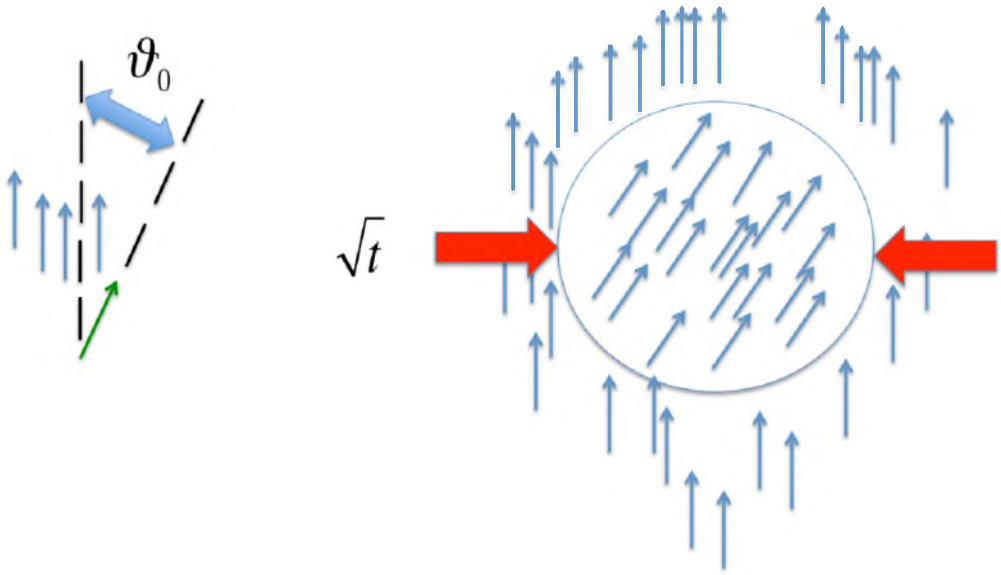

Figure B.1: Evolution of a single error in the pointers problem. The original error θ_0 gets shared evenly after a time $\sqrt{t}$ among all of the pointers within a distance $\propto t$ of the original pointer, and then it diffuses over the system. Figure adapted from [Ton18]

assume that pointing process follows the Vicsek-like protocol (see Eq. (1.1))

$$\theta_i(t+1) = \langle \theta_j(t) \rangle_n + \eta_i \,, \tag{B.1}$$

with $\langle\rangle_n$ an average over the nearest neighbors and η_i Gaussian white noises of zero mean and variance Δ.
It is fundamental for the following argument to note that this updating rule leads to a noisy diffusion equation for θ_i. We can easily show this for a square lattice of pointers. In 2D, Eq. (B.1) reads

$$\begin{aligned} &\theta(x_i, y_i, t+1) - \theta(x_i, y_i, t) = \\ &\frac{1}{4}\Big[\theta(x_i + a, y_i, t) + \theta(x_i - a, y_i, t) + \theta(x_i, y_i + a, t) + \theta(x_i, y_i - a, t)\Big] \\ &- \theta(x_i, y_i, t) + \eta_i(t) \,, \end{aligned} \tag{B.2}$$

with a the lattice spacing, which is nothing but the discrete version of the equation

$$\partial_t \theta = D\nabla^2\theta + \eta \,, \tag{B.3}$$

with a given diffusion constant D.

From the diffusive behavior of θ we can first readily deduce the conservation law

$$\frac{\mathrm{d}}{\mathrm{d}t}\int_V \mathrm{d}^d\mathbf{r}\theta(\mathbf{r},t) = D\int_{\partial V} \mathrm{d}\mathbf{S}\cdot\boldsymbol{\nabla}\theta(\mathbf{r},t) \,. \tag{B.4}$$

Then, we can infer that an initial fluctuation $\theta(\mathbf{r}, t = 0)$ spreads in the time t of a range $w(t) \propto r \propto \sqrt{t}$, as schematically shown in Fig. B.1.
From conservation law and diffusive spreading we can estimate the decaying of fluctuations. An initial localized fluctuation θ_0 (see Fig. B.1) spreads over a range $r(t) \propto \sqrt{t}$ and it gets shared among $N(t) \propto [r(t)]^d \propto t^{d/2}$ pointers. This means that averaged fluctuations for each pointer scale as $\theta(t) \propto \theta_0/t^{d/2}$. The total number $N(t)$ of pointers in the spreading area at the time t have made a total number of errors (due to the noise) of the order $N(t)t$.
Since the noises are independent, we can easily compute the average fluctuations as

$$\sqrt{\langle\theta^2\rangle} \propto \frac{\sqrt{N(t)t}}{N(t)} \propto r^{1-d/2} , \tag{B.5}$$

which diverges for $d < 2$ as r goes to infinity. It can be shown with a slightly more accurate proof, that it diverges logarithmically ($\sqrt{\langle\theta^2\rangle} \propto \sqrt{\ln(r)}$) for $d = 2$. Such result coincides with the Mermin-Wagner theorem for pointers, according to which fluctuations destroy the long-range order for systems in less that three dimensions.

Let's try to apply the same argument for the moving pointers, which we will call "flockers" from now on. We have to understand how the fluctuations spread through the flock, while it moves with an average non-zero velocity v_0. We call a "blob" the group of flockers whose velocities at time t are correlated with the velocity of one reference flocker at time $t = 0$. The velocity of the blob perpendicular to the mean direction of the flock is $\delta\mathbf{v}_\perp \sim v_0\theta$ for small θ, which is the deviation of the mean direction of the blob with respect to the one of the flock. Thus the blob wanders laterally relative to the flock of an amplitude

$$\delta x_\perp \sim \sqrt{\langle v_\perp^2\rangle}\, t \sim v_0 \sqrt{\langle\theta^2\rangle}\, t \propto t^{3/2-d/4} . \tag{B.6}$$

On the other hand, fluctuations along the direction of the flock are of the order $v_0[1 - \cos(\theta)] \sim \theta^2$, thus much smaller than the lateral ones. Comparing lateral fluctuations with the width of the blob calculated above for the non-moving pointers, we obtain

$$\frac{\delta x_\perp}{w(t)} \propto \frac{t^{3/2-d/4}}{t^{1/2}} \propto t^{1-d/4} , \tag{B.7}$$

which diverges for $d < 4$. This means that for low enough dimension of the space, the hypothesis of isotropic diffusion for the fluctuation does not apply for flockers.

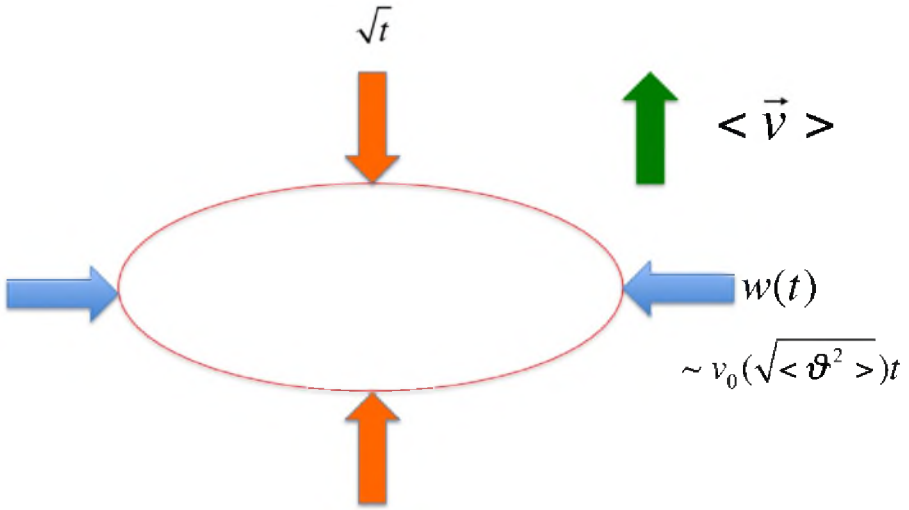

Figure B.2: Correct picture of the evolving blob. It still grows diffusively in the direction of the mean flock velocity (vertical in this figure), but grows laterally at a rate dominated by convection, rather than diffusion. Figure adapted from [Ton18]

Actually, the shape of the blob becomes anisotropic for flockers in $d < 4$, as sketched in Fig. B.2. Proceeding as for the passive pointers, we note that the number of flockers making errors within a time t is $N(t) \propto [w(t)]^{d-1}\sqrt{t}$. Since the flockers make one error per time unit, the total number of errors inside the blob after a delay t is $N(t)t$, and thus the root mean square fluctuations of θ is

$$\sqrt{\langle\theta^2\rangle} \sim \frac{\sqrt{N(t)t}}{N(t)} \propto t^{1/4} w^{(1-d)/2} . \tag{B.8}$$

From our previous estimation of the lateral spreading $w(t)$ in (B.6) we can compute

$$w(t) \propto t^{\frac{5}{2(d+1)}} , \tag{B.9}$$

and thus

$$\sqrt{\langle\theta^2\rangle} \propto w^{\frac{3-2d}{5}} . \tag{B.10}$$

Since, for $d = 2$, fluctuations spread with the blob lateral size with a negative exponent, we conclude that the flock is able to sustain long-range orientational order.
Note that, interestingly, the exponents found with this (not rigorous) argument are the same obtain from a much more rigorous renormalization group procedure for the hydrodynamic model (see [TT95, TT98]).

Appendix C

A short overview on percolation transition

Percolation phenomena are historically related to filtering problems in nature, such as filtering of fluid through porous materials. This old problem has been recasted from long time into a simple theoretical model, and largely studied as a paradigmatic phenomenon in statistical physics. For an extended treatment of percolation theory see for instance [SA18].

Quantities of interest in a percolation problem

To introduce the general problem of percolation, we consider an arbitrary periodic lattice in d spatial dimensions, with the related network of nearest neighbors both for lattice sites and bonds. Thinking for instance to a square lattice in two dimensions, two dual networks can be recognized: the one of the squared cells with four neighbors each, and the one of the bonds with four links for each node. Thus, for a given lattice, two different percolation problems can be posed, namely a so-called *site percolation* and a *bond percolation*.
Within this summary we deal only with site percolation. It is defined by assigning an *occupation probability* p, which is the probability for each cell to be "occupied", begin thus $(1 - p)$ the probability for a given cell to be empty. For completeness, the dual problem of bond percolation is equivalently posed with attributing a probability p to each bond to be open.
A *cluster* is defined as a set of neighboring occupied sites. Percolation transition settles with increasing the occupation probability, as soon as one cluster that span the whole (infinite) system appears. The transition value p_{th} of the occupation probability is called *percolation threshold*. See in

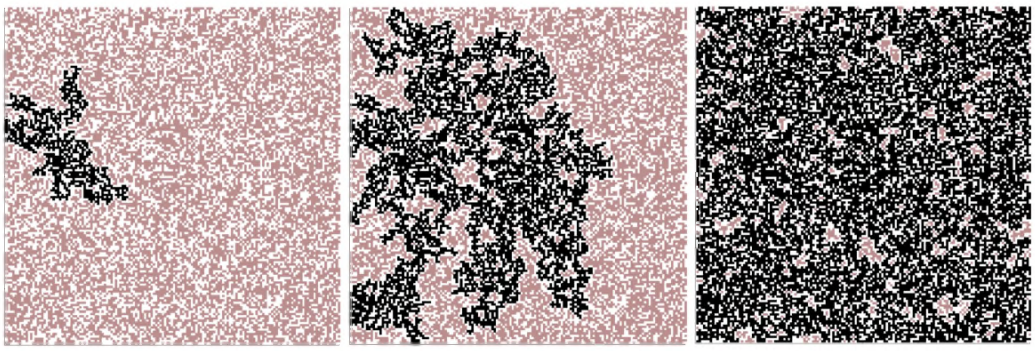

Figure C.1: Percolation in 2d square lattices with system size $L \times L = 150 \times 150$. Occupation probability $p = 0.55, 0.59, 0.65$, respectively. Notice, that the largest cluster percolates through the lattice from top to bottom in this example when $p \geqslant 0.59$.

Fig. C.1 a typical example of a percolation transition for a square lattice in 2D.

Understandably, percolation theory deals mainly with quantities related to the statistics of the clusters, aiming to study the behavior of such connected objects and to infer their critical behavior. We define here some of the most relevant of the quantities involved.

The most important quantity is the cluster number $n_s(p)$, which denotes the number of s-clusters per lattice site. The average number of clusters of size s in a hypercubic lattice of linear size L is $L^d n_s(p)$, d being the dimensionality of the lattice.

Below the percolation threshold the cluster number has a cutoff size s_ξ. Such characteristic cluster size must diverge as $p \to p_{\text{th}}$ to account for the appearance of an infinite cluster at the percolation threshold. It is reasonably to assume, both from general theory of critical phenomena and from analytical treatment of percolation on a 1D lattice and on a Bethe lattice, that s_ξ diverges as a power law. Thus a first critical exponent can be defined as follows:

$$s_\xi \propto |p_{\text{th}} - p|^{-\frac{1}{\sigma}} \qquad \text{for } p \to p_{\text{th}}^- \,. \tag{C.1}$$

If one site is occupied, it belongs to one of the clusters (given that even an isolated occupied site belongs to a 'cluster' of size one). The probability that the cluster to which an occupied site belongs contains s site is

$$w_s = \frac{s\, n_s(p)}{\sum_{s=1}^{\infty} s\, n_s(p)} = \frac{s\, n_s(p)}{p} \,. \tag{C.2}$$

Hence, the average size $S(p)$ of the cluster is given by

$$S(p) = \sum_{s=1}^{\infty} s\, w_s = \sum_{s=1}^{\infty} \frac{s^2\, n_s(p)}{\sum_{s=1}^{\infty} s\, n_s(p)} \,. \tag{C.3}$$

Also for the average cluster size we assume the power law divergence at the percolation threshold

$$S(p) \propto |p_{\text{th}} - p|^{-\gamma} \qquad \text{for } p \to p_{\text{th}}^{-} \,. \tag{C.4}$$

The so-called *strength* of the infinite cluster $P(p)$ is defined as the probability that an arbitrary site belongs to the infinite cluster. It is equal to zero below the percolation threshold, because there are not infinite clusters, and it grows to one across the transition. We assume that this quantity goes to zero as a power law, thus defining another critical exponent as follows:

$$P(p) \propto (p - p_{\text{th}})^{\beta} \qquad \text{for } p \to p_{\text{th}}^{+} \,. \tag{C.5}$$

Scaling assumption for cluster numbers

To understand the critical behavior of percolation transition, that is to compute the values of the critical exponent defined above, a knowledge of the cluster number $n_s(p)$ is needed. Despite the large amount of studies on percolation, such knowledge is still no available in general. As already mentioned in the previous Section, we are only able to compute analytically the cluster number only for some special cases: the 1D lattice and the Bethe lattice (see [SA18]). Making use of the results in these two simple cases, a scaling ansatz can be formulated for the general form of $n_s(p)$ on an arbitrary lattice in $d > 1$.
A good scaling ansatz that encodes all the features we have outlined so far for occupation probability close to the critical points is the following:

$$n_s(p) = q_0 s^{-\tau} f[q_1(p - p_{\text{th}})s^{\sigma}] \qquad \text{for } s \gg 1 \text{ and } p \to p_{\text{th}} \,, \tag{C.6}$$

where q_0, q_1 and p_{th} are non-universal parameters, τ and σ are universal critical exponents, and f is a universal scaling function. Note, however, that the form of the scaling function f is not predicted by the scaling ansatz and has to be determined from numerical experiments. Moreover, both f and the critical exponents depend on the dimensionality.

Besides τ and σ which govern the scaling behavior of the cluster numbers, we have defined two more critical exponents in the previous Section,

i.e. γ and β. As for standard critical behaviors, the critical exponents are not independent numbers, but they are related through some scaling relations. In order to derive the scaling relation for γ, we can make use of the known cluster number for the Bethe lattice (which still has to recovered as a special case from the general form (C.6))

$$n_s(p) \propto s^{-\tau} \exp\left(-\frac{s}{s_\xi}\right) . \tag{C.7}$$

From this result we can compute the average cluster size

$$\begin{aligned} S(p) &\propto \sum_{s=1}^{\infty} s^2 n_s(p) \\ &\propto \sum_{s=1}^{\infty} s^{2-\tau} \exp\left(-\frac{s}{s_\xi}\right) \\ &\simeq \int_1^{\infty} s^{2-\tau} \exp\left(-\frac{s}{s_\xi}\right) \mathrm{d}s \\ &= s_\xi^{3-\tau} \Gamma(3-\tau) , \end{aligned} \tag{C.8}$$

with Γ the Gamma function [AoSS48]. Thus, since $\Gamma(3-\tau)$ is just a coefficient, from (C.1) and (C.4) we obtain

$$\gamma = \frac{3-\tau}{\sigma} . \tag{C.9}$$

For the second scaling relation we have to compute the percolation probability $P(p)$. Since one occupied site either belongs to an infinite cluster or to a finite one, we for all p, below or above the percolation threshold, that

$$\begin{aligned} -P(p) &= \sum_{s=1}^{\infty} s\, n_s(p) - p \\ &= \sum_{s=1}^{\infty} s\, n_s(p) - p_{\mathrm{th}} + (p_{\mathrm{th}} - p) \\ &= \sum_{s=1}^{\infty} \left[s\, n_s(p) - s\, n_s(p_{\mathrm{th}}) + \mathrm{O}(p - p_{\mathrm{th}}) \right] \\ &\simeq \int_1^{\infty} q_0 s^{1-\tau} \Big(f[q_1 (p - p_{\mathrm{th}}) s^\sigma] - f[0] \Big) \mathrm{d}s , \end{aligned} \tag{C.10}$$

where the general scaling ansatz has been used. After some algebra we obtain

$$\begin{aligned} P(p) &= -q_0(q_1|p-p_{\rm th}|)^{\frac{\tau-2}{\sigma}} \int |z|^{\frac{2-\tau}{\sigma}-1}\Big[f(z)-f(0)\Big]\frac{1}{\sigma}\mathrm{d}z \\ &= -q_0(q_1|p-p_{\rm th}|)^{\frac{\tau-2}{\sigma}} \begin{cases} \text{const.}(\neq 0) & \text{for } p > p_{\rm th} \\ 0 & \text{for } p < p_{\rm th} \end{cases} \end{aligned} \tag{C.11}$$

Thus, from (C.5)

$$\beta = \frac{\tau-2}{\sigma} \,. \tag{C.12}$$

Cluster structure

To conclude our summary on percolation, we now turn to deal with the geometry of the clusters. The most relevant quantity for this purpose is the radius of gyration R_g of a give s-cluster, defined as

$$R_g = \left[\frac{1}{s}\sum_{i=1}^{s}|\mathbf{r}_i - \mathbf{r}_{\rm CM}|^2\right]^{1/2} , \tag{C.13}$$

with $\mathbf{r}_{\rm CM}$ the position of the center of mass of the cluster.
We also define the correlation function (or *pair connectivity*) $g(\mathbf{r})$ as the probability that a site a distance $\mathbf{r}$ apart from an occupied site belongs to the same cluster. We note that this correlation function satisfy the identity

$$\sum_r g(\mathbf{r}) = S(p) \,, \tag{C.14}$$

since the sum is the average number of sites to which an occupied site is connected.
From the pair correlation function we can define a correlation length

$$\xi^2 = \frac{\sum_{\mathbf{r}} r^2 g(\mathbf{r})}{\sum_{\mathbf{r}} g(\mathbf{r})} = \frac{\sum_s 2R_g^2 s^2 n_s(p)}{\sum_s s^2 n_s(p)} \,, \tag{C.15}$$

which represents the average distance between two sites belonging to the same cluster. It is thus expected to diverge at the percolation threshold as

$$\xi \propto |p-p_{\rm th}|^{-\nu} \qquad \text{for} p \to p_{\rm th}^- \,. \tag{C.16}$$

From many experiments on percolation, we know that percolating clusters at the critical point are fractal objects. Therefore, is $M(L)$ denotes the

mass of the percolating cluster within linear distance L, its fractal dimension D is defined from the relation

$$M(L) \propto L^D \,, \tag{C.17}$$

which allows us to assume that $R_g \propto s^{1/D}$, close to the critical point.
From the definition (C.15) and from the other scaling relations, we obtain for the percolating clusters

$$\xi^2 \propto \frac{\sum_s 2s^{2+2/D} n_s(p)}{\sum_s s^2 n_s(p)} \propto |p - p_{\text{th}}|^{-2\nu} \,. \tag{C.18}$$

This allows as to find the last scaling relation

$$D = \frac{1}{\nu\sigma}. \tag{C.19}$$

Useful numbers

We finally give in this Section a summary table for the values of the percolation threshold p_{th} for different lattices (Fig. C.2) and the values of the critical exponents for different spatial dimensions (Fig. C.3).

Lattice	# nn	Site percolation	Bond percolation
1d	2	**1**	**1**
2d Honeycomb	3	0.6962	$1 - 2\sin(\pi/18) \approx 0.65271$
2d Square	4	**0.592746**	**1/2**
2d Triangular	6	**1/2**	$2\sin(\pi/18) \approx 0.34729$
3d Diamond	4	0.43	0.388
3d Simple cubic	6	0.3116	0.2488
3d BCC	8	0.246	0.1803
3d FCC	12	0.198	0.119
Bethe lattice	z	**1/(z-1)**	**1/(z-1)**

Figure C.2: The percolation threshold for the site percolation problem is given in column 3 for various lattices in various dimensions. Column 2 lists the number of nearest-neighbours (nn), also known as the coordination number. Note that, within a given dimension, the percolation threshold decrease with increasing number of nearest-neighbours.

Exponent	**1d**	**2d**	3d	4d	5d	6d	**Bethe**
α	1	$-2/3$	-0.62	-0.72	-0.86	-1	-1
β	**0**	5/36	0.41	0.64	0.84	1	**1**
γ	**1**	43/18	1.80	1.44	1.18	1	**1**
ν	**1**	**4/3**	0.88	0.68	0.57	1/2	**1/2**
σ	**1**	36/91	0.45	0.48	0.49	1/2	**1/2**
τ	**2**	**187/91**	2.18	2.31	2.41	5/2	**5/2**
$D(p = p_c)$	**1**	**91/48**	2.53	3.06	3.54	4	**4**

Figure C.3: The critical exponents for the percolation theory problems in dimensions $d = 1, 2, 3, 4, 5, 6$ and in the Bethe lattice.

Bibliography

[AM76] N. W. Ashcroft and N. D. Mermin. ***Solid State Physics***. 1976.

[And83] H. C. Andersen. **RATTLE: A "Velocity" Version of the SHAKE Algorithm for Molecular Dynamics Calculations**. *Journal of Computational Physics*, 52:24, 1983.

[AoSS48] M. Abramowitz, United States. National Bureau of Standards, and I.A. Stegun. ***Handbook of Mathematical Functions with Formulas, Graphs, and Mathematical Tables***. U.S. Government Printing Office, 1948.

[ASR02] R. Aditi Simha and S. Ramaswamy. **Hydrodynamic Fluctuations and Instabilities in Ordered Suspensions of Self-Propelled Particles**. *Phys. Rev. Lett.*, 89:058101, Jul 2002.

[AW62] B. J. Alder and T. E. Wainwright. **Phase Transition in Elastic Disks**. *Phys. Rev.*, 127:359–361, Jul 1962.

[BDLL+16] Clemens Bechinger, Roberto Di Leonardo, Hartmut Löwen, Charles Reichhardt, Giorgio Volpe, and Giovanni Volpe. **Active particles in complex and crowded environments**. *Rev. Mod. Phys.*, 88:045006, Nov 2016.

[Ber71] V. L. Berezinskii. **Destruction of long-range order in one-dimensional and two-dimensional systems having a countinuous symmetry group I. Classical systems**. *Soviet Physics JETP*, 32(3):493–500, 1971. Russian original - Zh. Eksp. Teor. Fiz., 59 907-20 (1970).

[Ber72] V. L. Berezinskii. **Destruction of long-range order in one-dimensional and two-dimensional systems having a countinuous symmetry group I. Quantum systems**. *Soviet*

Physics JETP, 34(3):610–616, 1972. Russian original - Zh. Eksp. Teor. Fiz., 61 1144-1156 (1971).

[Ber11] E. Bernard. *PhD Thesis:* ***Algorithms and applications of the Monte Carlo method: Two-dimensional melting and perfect sampling***. 2011.

[BK11] E. P. Bernard and W. Krauth. **Two-Step Melting in Two Dimensions: First-Order Liquid-Hexatic Transition**. *Phys. Rev. Lett.*, 107:155704, Oct 2011.

[BKW09] Etienne P. Bernard, Werner Krauth, and David B. Wilson. **Event-chain Monte Carlo algorithms for hard-sphere systems**. *Phys. Rev. E*, 80:056704, Nov 2009.

[BLS13] Julian Bialké, Hartmut Löwen, and Thomas Speck. **Microscopic theory for the phase separation of self-propelled repulsive disks**. *EPL (Europhysics Letters)*, 103(3):30008, Aug 2013.

[Bou88] T. Boublik. **Equation of state of planar hard dumbbells**. *Molecular Physics*, 63:685, 1988.

[Bra94] A.J. Bray. **Theory of phase-ordering kinetics**. *Advances in Physics*, 43(3):357–459, 1994.

[BSL12] Julian Bialké, Thomas Speck, and Hartmut Löwen. **Crystallization in a Dense Suspension of Self-Propelled Particles**. *Phys. Rev. Lett.*, 108:168301, Apr 2012.

[Cat12] Michael E Cates. **Diffusive transport without detailed balance in motile bacteria: does microbiology need statistical physics?** *Rep. Prog. Phys.*, 75(4):042601, 2012.

[CC95] P. M. Chaikin and Lubensky T. C. ***Principles of condensed matter physics***. 1995.

[CDADG+04] Antonio Coniglio, Lucilla De Arcangelis, E Del Gado, A Fierro, and N Sator. **Percolation, gelation and dynamical behaviour in colloids**. *J. Phys.: Cond. Matt.*, 16(42):S4831, 2004.

[CDGS17] L. F. Cugliandolo, P. Digregorio, G. Gonnella, and A. Suma. **Phase co-existence in bidimensional passive and active dumbbell systems**. *Phys. Rev. Lett.*, 119:119, 2017.

[CGS15] L. F. Cugliandolo, G. Gonnella, and A. Suma. **Rotational and translational diffusion in an interacting active dumbbell system**. *Phys. Rev. E*, 91:062124, Jun 2015.

[Chu82] ST Chui. **Grain-boundary theory of melting in two dimensions**. *Phys. Rev. Lett.*, 48(14):933, 1982.

[Chu83] ST Chui. **Grain-boundary theory of melting in two dimensions**. *Phys. Rev. B*, 28(1):178, 1983.

[CT13] M. E. Cates and J. Tailleur. **When are active Brownian particles and run-and-tumble particles equivalent? Consequences for motility-induced phase separation**. *EPL (Europhysics Letters)*, 101(2):20010, Jan 2013.

[CT15] Michael E. Cates and Julien Tailleur. **Motility-Induced Phase Separation**. *Annual Review of Condensed Matter Physics*, 6(1):219–244, 2015.

[DBMK15] Sven Deutschländer, Charlotte Boitard, Georg Maret, and Peter Keim. **Grain-boundary-induced melting in quenched polycrystalline monolayers**. *Phys. Rev. E*, 92(6):060302, 2015.

[DLS+18] P. Digregorio, D. Levis, A. Suma, L. F. Cugliandolo, G. Gonnella, and I. Pagonabarraga. **Full Phase Diagram of Active Brownian Disks: From Melting to Motility-Induced Phase Separation**. *Phys. Rev. Lett.*, 121:098003, Aug 2018.

[DSFT80] R. D. Diehl, C. G. Shaw, S. C. Fain, and M. F. Toney. **Low-Energy Electron Diffraction Results for Physisorbed Nitrogen on Graphite**. In S. K. Sinha, editor, *Ordering in Two Dimensions*. North-Holland, New York, 1980.

[EAG+13] M. Engel, J. A. Anderson, S. C. Glotzer, M. Isobe, E. P. Bernard, and W. Krauth. **Hard-disk equation of state: First-order liquid-hexatic transition in two dimensions with three simulation methods**. *Phys. Rev. E*, 87:042134, 2013.

[EKSX96] M. Ester, H. P. Kriegel, J. Sander, and X. Xu. **A Density-Based Algorithm for Discovering Clusters in Large Spatial Databases with Noise**. In *Proceedings of the Second International Conference on Knowledge Discovery and Data Mining (KDD-96), Portland, Oregon, USA*, pages 226–231, 1996.

[EWG15] J Elgeti, RG Winkler, and G Gompper. **Physics of Microswimmers - Single Particle Motion and Collective Behavior**. *Rep. Prog. Phys.*, 78:056601, 2015. arXiv:1412.2692.

[FHM79] Daniel S Fisher, BI Halperin, and R Morf. **Defects in the two-dimensional electron solid and implications for melting**. *Phys. Rev. B*, 20(11):4692, 1979.

[FK72] Cornelius Marius Fortuin and Piet W Kasteleyn. **On the random-cluster model: I. Introduction and relation to other models**. *Physica*, 57(4):536–564, 1972.

[FM12] Y. Fily and M. C. Marchetti. **Athermal Phase Separation of Self-Propelled Particles with No Alignment**. *Phys. Rev. Lett.*, 108:235702, Jun 2012.

[FMS02] P. Fendley, R. Moessner, and S. L. Sondhi. **Classical dimers on the triangular lattice**. *Phys. Rev. B*, 66:214513, Dec 2002.

[Fri64] J. Friedel. ***Dislocations***. Pergamon Press, 1964.

[GLS14] G. Gonnella, A. Lamura, and A. Suma. **Phase segregation in a system of active dumbbells**. *International Journal of Modern Physics C*, 25(12):1441004, 2014.

[GMST15] G. Gonnella, D. Marenduzzo, A. Suma, and A. Tiribocchi. **Motility-induced phase separation and coarsening in active matter**. *Comptes Rendus Physique*, 16(3):316–331, 2015.

[GR92] C. W. Goulding and M. Rigby. **Shape effects in 2-dimensional hard molecule fluids**. *Molecular Physics*, 75:623, 1992.

[HN78] B. I. Halperin and David R. Nelson. **Theory of Two-Dimensional Melting**. *Phys. Rev. Lett.*, 41:121–124, Jul 1978. Erratum Phys. Rev. Lett. 41, 519 (1978).

[HRRS04] Yashodhan Hatwalne, Sriram Ramaswamy, Madan Rao, and R. Aditi Simha. **Rheology of Active-Particle Suspensions**. *Phys. Rev. Lett.*, 92:118101, Mar 2004.

[IK50] J. H. Irving and J. G. Kirkwood. **The Statistical Mechanical Theory of Transport Processes. IV. The Equations of Hydrodynamics**. *The Journal of Chemical Physics*, 18(6):817–829, 1950.

[JD85] B. Joos and M. S. Duesbery. **Dislocation Energies in Rare-Gas Monolayers on Graphite**. *Phys. Rev. Lett.*, 55:1997–2000, Nov 1985.

[JH] W. Janke and Kleinert H. **First Order in 2D Disclination Melting**, journal = Phys. Lett. A, volume = 105, pages = 134–138, year = 1984.

[JK80] W. Janke and H. Kleinert. **Superflow in ^{3}He-B in the Presence of Magnetic Fields at all Temperatures**. *Phys. Letters A*, 78:363, 1980.

[JT86] W. Janke and D. Toussaint. **Laplacian roughening on a triangular lattice**. *Phys. Lett. A*, 116:387–391, 1986.

[Kap13] Raymond Kapral. **Perspective: Nanomotors without moving parts that propel themselves in solution**. *The Journal of Chemical Physics*, 138(2):020901, 2013.

[KK15] S. C. Kapfer and W. Krauth. **Two-Dimensional Melting: From Liquid-Hexatic Coexistence to Continuous Transitions**. *Phys. Rev. Lett.*, 114:035702, Jan 2015.

[Kle83] H Kleinert. **Disclinations and first order transitions in 2D melting**. *Physics Letters A*, 95(7):381–384, 1983.

[KMvG07] P. Keim, G. Maret, and H. H. von Grünberg. **Frank's constant in the hexatic phase**. *Phys. Rev. E*, 75:031402, Mar 2007.

[Kos74] J. M. Kosterlitz. **The critical properties of the two-dimensional xy model**. *Journal of Physics C: Solid State Physics*, 7(6):1046–1060, mar 1974.

[KR06] J. Kolafa and M. Rottner. **Simulation-based equation of state of the hard disk fluid and prediction of higher-order virial coefficients**. *Molecular Physics*, 104(22):3435, 2006.

[KSRS14] N. Kumar, H. Soni, S. Ramaswamy, and A. K. Sood. **Flocking at a distance in active granular matter**. *Nat. Commun.*, 5:4688, 2014.

[KT73] J. M. Kosterlitz and D. J. Thouless. **Ordering, metastability and phase transitions in two-dimensional systems**. *Journal of Physics C: Solid State Physics*, 6(7):1181–283, 1973.

[lam] Large-scale atomic and molecular massively parallel simulator. URL: `http://lammps.sandia.gov/`.

[Lan37a] L. D. Landau. **On the theory of phase transitions I**. *Phys. Z. Sowjet*, 11:26, 1937.

[Lan37b] L. D. Landau. **On the theory of phase transitions II**. *Phys. Z. Sowjet*, 11:545, 1937.

[LBZ+14] G. Lambert, A. Bergmann, Q. Zhang, D. Bortz, and R. Austin. **Physics of biofilms: the initial stages of biofilm formation and dynamics**. *New J. Phys.*, 16:045005, 2014.

[LCP17] D. Levis, J. Codina, and I. Pagonabarraga. **Active Brownian equation of state: metastability and phase coexistence**. *Soft Matter*, 13:8113–8119, 2017.

[LLKP86] L. D. Landau, E. M. Lifshitz, A. M. Kosevich, and L. P. Pitaevskii. ***Course of Theoretical Physics. Vol.7 - Theory of Elasticity***. 1986.

[LMC08] Davide Loi, Stefano Mossa, and Leticia F. Cugliandolo. **Effective temperature of active matter**. *Phys. Rev. E*, 77:051111, May 2008.

[LMC11a] Davide Loi, Stefano Mossa, and L. F. Cugliandolo. **Effective temperature of active complex matter**. *Soft Matter*, 7:3726–3729, 2011.

[LMC11b] Davide Loi, Stefano Mossa, and Leticia F. Cugliandolo. **Non-conservative forces and effective temperatures in active polymers**. *Soft Matter*, 7:10193–10209, 2011.

[Mer68] N. D. Mermin. **Crystalline Order in Two Dimensions**. *Phys. Rev.*, 176:250–254, Dec 1968. Errata Phys. Rev. B 20, 4762 (1979); Phys. Rev. B 74, 149902 (2006).

[Mie03] G. Mie. **Zur kinetischen Theorie der einatomigen Körper**. *Annalen der Physik*, 11:657, 1903.

[MJR+13] M C Marchetti, J-F Joanny, S Ramaswamy, T B Liverpool, J Prost, M Rao, and R A Simha. **Hydrodynamics of soft active matter**. *Rev. Mod. Phys.*, 85(3):1143, 2013.

[MM15] G. De Magistris and D. Marenduzzo. **An introduction to the physics of active matter**. *Physica A: Statistical Mechanics and its Applications*, 418:65 – 77, 2015. Proceedings of the 13th International Summer School on Fundamental Problems in Statistical Physics.

[MP17] Jeffrey L. Moran and Jonathan D. Posner. **Phoretic Self-Propulsion**. *Annual Review of Fluid Mechanics*, 49(1):511–540, 2017.

[MR96] A. H. Marcus and S. A. Rice. **Observations of First-Order Liquid-to-Hexatic and Hexatic-to-Solid Phase Transitions in a Confined Colloid Suspension**. *Phys. Rev. Lett.*, 77:2577–2580, Sep 1996.

[MR97] A. H. Marcus and S. A. Rice. **Phase transitions in a confined quasi-two-dimensional colloid suspension**. *Phys. Rev. E*, 55:637–656, Jan 1997.

[MVW87] C. A. Murray and D. H. Van Winkle. **Experimental observation of two-stage melting in a classical two-dimensional screened Coulomb system**. *Phys. Rev. Lett.*, 58:1200–1203, Mar 1987.

[MW65] J. E. Mayer and Wm. W. Wood. **Interfacial tension effects in finite, periodic, two-dimensional systems**. *The Journal of Chemical Physics*, 42(12):4268–4274, 1965.

[MW66] N. D. Mermin and H. Wagner. **Absence of Ferromagnetism or Antiferromagnetism in One- or Two-Dimensional Isotropic Heisenberg Models**. *Phys. Rev. Lett.*, 17:1133–1136, Nov 1966.

[Nab67] F. R. N. Nabarro. ***Theory of Crystal Dislocations***. Clarendon Press, 1967.

[Nel78] David R. Nelson. **Study of melting in two dimensions**. *Phys. Rev. B*, 18:2318–2338, Sep 1978.

[Nel82] David R. Nelson. **Laplacian roughening models and two-dimensional melting**. *Phys. Rev. B*, 26:269–283, Jul 1982.

[NH79] David R. Nelson and B. I. Halperin. **Dislocation-mediated melting in two dimensions**. *Phys. Rev. B*, 19:2457–2484, Mar 1979.

[Par15] J. A. Park *et al.* **Unjamming and cell shape in the asthmatic airway epithelium**. *Nat. Mater.*, 14:1040, 2015.

[PD19] Siddharth Paliwal and Marjolein Dijkstra. **The role of topological defects in the two-stage melting and elastic behaviour of active Brownian particles**. *arXiv:1907.04767*, 2019.

[PDC+18] Petrelli, Isabella, Digregorio, Pasquale, Cugliandolo, Leticia F., Gonnella, Giuseppe, and Suma, Antonio. **Active dumbbells: Dynamics and morphology in the coexisting region**. *Eur. Phys. J. E*, 41(10):128, 2018.

[Pei] R. E. Peierls. **Bemerkungen über umwandlungstemperaturen**. *Helv. Phys. Acta*.

[Pet17] I. Petrelli. *Master thesis:* ***"Equazione di stato e coesistenza di fase in sistemi di particelle passive e autopropulse con interazione di volume escluso"***. 2017.

[PL01] Alexandros Pertsinidis and XS Ling. **Equilibrium configurations and energetics of point defects in two-dimensional colloidal crystals**. *Phys. Rev. Lett.*, 87(9):098303, 2001.

[PP18] Amir Masoud Pourrahimi and Martin Pumera. **Multifunctional and self-propelled spherical Janus nano/micromotors: recent advances**. *Nanoscale*, 10:16398–16415, 2018.

[QGD14] Weikai Qi, Anjan P Gantapara, and Marjolein Dijkstra. **Two-stage melting induced by dislocations and grain boundaries in monolayers of hard spheres**. *Soft Matter*, 10(30):5449–5457, 2014.

[QWHC10] Wei-Kai Qi, Ziren Wang, Yilong Han, and Yong Chen. **Melting in two-dimensional Yukawa systems: A Brownian dynamics simulation**. *J. Chem. Phys.*, 133(23):234508, 2010.

[Ram10] Sriram Ramaswamy. **The Mechanics and Statistics of Active Matter**. *Annual Review of Condensed Matter Physics*, 1(1):323–345, 2010.

[RBH13] Gabriel S. Redner, Aparna Baskaran, and Michael F. Hagan. **Reentrant phase behavior in active colloids with attraction**. *Phys. Rev. E*, 88:012305, Jul 2013.

[Red01] Sidney Redner. ***A Guide to First-Passage Processes***. Cambridge University Press, 2001. doi:10.1017/CBO9780511606014.

[RHB13] Gabriel S. Redner, Michael F. Hagan, and Aparna Baskaran. **Structure and Dynamics of a Phase-Separating Active Colloidal Fluid**. *Phys. Rev. Lett.*, 110:055701, Jan 2013.

[SA18] Dietrich Stauffer and Ammon Aharony. ***Introduction to percolation theory***. Taylor & Francis, 2018.

[Sch93] M. J. Schnitzer. **Theory of continuum random walks and application to chemotaxis**. *Phys. Rev. E*, 48:2553–2568, Oct 1993.

[SGL+14] A. Suma, G. Gonnella, G. Laghezza, A. Lamura, A. Mossa, and L. F. Cugliandolo. **Dynamics of a homogeneous active dumbbell system**. *Phys. Rev. E*, 90:052130, Nov 2014.

[SGMO14] A. Suma, G. Gonnella, D. Marenduzzo, and E. Orlandini. **Motility-induced phase separation in an active dumbbell fluid**. *EPL (Europhysics Letters)*, 108(5):56004, 2014.

[Sim03] R. Aditi Simha. *PhD Thesis*. Indian Institute of Science, 2003.

[SJCK+97] Frank L Somer Jr, GS Canright, Theodore Kaplan, Kun Chen, and Mark Mostoller. **Inherent structures and two-stage melting in two dimensions**. *Phys. Rev. Lett.*, 79(18):3431, 1997.

[SJCK98] Frank L Somer Jr, GS Canright, and Theodore Kaplan. **Defect-unbinding transitions and inherent structures in two dimensions**. *Phys. Rev. E*, 58(5):5748, 1998.

[SK66] H. E. Stanley and T. A. Kaplan. **Possibility of a Phase Transition for the Two-Dimensional Heisenberg Model**. *Phys. Rev. Lett.*, 17:913–915, Oct 1966.

[Spe19] Thomas Speck. **Thermodynamic approach to the self-diffusiophoresis of colloidal Janus particles**. *Phys. Rev. E*, 99:060602, Jun 2019.

[SR02] R.Aditi Simha and Sriram Ramaswamy. **Statistical hydrodynamics of ordered suspensions of self-propelled particles: waves, giant number fluctuations and instabilities**.

Physica A: Statistical Mechanics and its Applications, 306:262 – 269, 2002.

[SS78] T. Schneider and E. Stoll. **Molecular-dynamics study of a three-dimensional one-component model for distortive phase transitions**. *Phys. Rev. B*, 17:1302–1322, Feb 1978.

[SSC83] Katherine J. Strandburg, Sara A. Solla, and G. V. Chester. **Monte Carlo studies of a Laplacian roughening model for two-dimensional melting**. *Phys. Rev. B*, 28:2717–2731, Sep 1983.

[SSC+18a] Alexandre P Solon, Joakim Stenhammar, Michael E Cates, Yariv Kafri, and Julien Tailleur. **Generalized thermodynamics of motility-induced phase separation: phase equilibria, Laplace pressure, and change of ensembles**. *New Journal of Physics*, 20(7):075001, jul 2018.

[SSC+18b] Alexandre P. Solon, Joakim Stenhammar, Michael E. Cates, Yariv Kafri, and Julien Tailleur. **Generalized thermodynamics of phase equilibria in scalar active matter**. *Phys. Rev. E*, 97:020602, 2018.

[SSW+15] Alexandre P. Solon, Joakim Stenhammar, Raphael Wittkowski, Mehran Kardar, Yariv Kafri, Michael E. Cates, and Julien Tailleur. **Pressure and Phase Equilibria in Interacting Active Brownian Spheres**. *Phys. Rev. Lett.*, 114:198301, 2015.

[Str86] Katherine J. Strandburg. **Crossover from a hexatic phase to a single first-order transition in a Laplacian-roughening model for two-dimensional melting**. *Phys. Rev. B*, 34:3536–3539, Sep 1986.

[Str88] Katherine J Strandburg. **Two-dimensional melting**. *Rev. Mod. Phys.*, 60(1):161, 1988.

[SWW+19] M. Reza Shaebani, Adam Wysocki, R. G. Winkler, G. Gompper, and H. Rieger. **Computational models for active matter**. *arXiv:1910.02528*, 2019.

[TAA+18] Alice L. Thorneywork, Joshua L. Abbott, Dirk G. A. L. Aarts, Peter Keim, and Dullens Roel P. A. **Bond-orientational order and Frank's constant in two-dimensional colloidal**

hard spheres. *J. Phys. Condens. Matter*, 30(10):104003, Mar 2018.

[TAAD17] Alice L. Thorneywork, Joshua L. Abbott, Dirk G. A. L. Aarts, and Roel P. A. Dullens. **Two-Dimensional Melting of Colloidal Hard Spheres**. *Phys. Rev. Lett.*, 118:158001, Apr 2017.

[TAMO89] Y. Tang, A. J. Armstrong, R. C. Mockler, and W. J. O'Sullivan. **Free-expansion melting of a colloidal monolayer**. *Phys. Rev. Lett.*, 62:2401–2404, May 1989.

[TC08] J. Tailleur and M. E. Cates. **Statistical Mechanics of Interacting Run-and-Tumble Bacteria**. *Phys. Rev. Lett.*, 100:218103, May 2008.

[Ton18] Jonh Toner. **Why walking is easier than pointing: Hydrodynamics of dryactive matter**. *arXiv:1812.00310*, 2018.

[TT85] J. Talbot and D. J. Tildesley. **The planar dumbbell fluid**. *The Journal of Chemical Physics*, 83:6419, 1985.

[TT95] J. Toner and Y. Tu. **Long-Range Order in a Two-Dimensional Dynamical XY Model: How Birds Fly Together**. *Phys. Rev. Lett.*, 75:4326–4329, Dec 1995.

[TT98] J. Toner and Y. Tu. **Flocks, herds, and schools: A quantitative theory of flocking**. *Phys. Rev. E*, 58:4828–4858, Oct 1998.

[TYB14] S. C. Takatori, W. Yan, and J. F. Brady. **Swim Pressure: Stress Generation in Active Matter**. *Phys. Rev. Lett.*, 113:028103, Jul 2014.

[VCBJ+95] T. Vicsek, A. Czirók, E. Ben-Jacob, I. Cohen, and O. Shochet. **Novel Type of Phase Transition in a System of Self-Driven Particles**. *Phys. Rev. Lett.*, 75:1226–1229, Aug 1995.

[vGKM14] Hans-Hennig von Grünberg, Peter Keim, and Georg Maret. ***Phase Transitions in Two-Dimensional Colloidal Systems***, chapter 2, pages 41–86. John Wiley & Sons, Ltd, 2014.

[vGKZM04] H. H. von Grünberg, P. Keim, K. Zahn, and G. Maret. **Elastic Behavior of a Two-Dimensional Crystal Near Melting**. *Phys. Rev. Lett.*, 93:255703, Dec 2004.

[VLN+11] Chantal Valeriani, Martin Li, John Novosel, Jochen Arlt, and Davide Marenduzzo. **Colloids in a bacterial bath: simulations and experiments**. *Soft Matter*, 7(11):5228, 2011.

[WL00] Xiao-Lun Wu and Albert Libchaber. **Particle Diffusion in a Quasi-Two-Dimensional Bacterial Bath**. *Phys. Rev. Lett.*, 84:3017, Mar 2000.

[WMB95] H. Weber, D. Marx, and K. Binder. **Melting transition in two dimensions: A finite-size scaling analysis of bond-orientational order in hard disks**. *Phys. Rev. B*, 51:14636–14651, May 1995.

[WMY92] R. G. Winkler, H. Morawitz, and D. Y. Yoon. **Novel molecular dynamics simulations at constant pressure**. *Molecular Physics*, 75(3):669–688, 1992.

[Woj92] K. W. Wojciechowski. **Mote Carlo simulations of highly anisotropic 2-dimensional hard dumbbell-shaped molecules - nonperiodic phase between fluid and dense solid**. *Phys. Rev. B*, 46:26, 1992.

[WTS+] R. Wittkowski, A. Tiribocchi, J. Stenhammar, R.J. Allen, D. Marenduzzo, and M.E. Cates. **Scalar ϕ^4 field theory for active-particle phase separation**, journal = Nat Commun, volume = 5, pages = 4351, year = 2014.

[WWG15] Roland G. Winkler, Adam Wysocki, and Gerhard Gompper. **Virial pressure in systems of spherical active Brownian particles**. *Soft Matter*, 11:6680–6691, 2015.

[You79] A. P. Young. **Melting and the vector Coulomb gas in two dimensions**. *Phys. Rev. B*, 19:1855–1866, Feb 1979.

[ZLM99] K. Zahn, R. Lenke, and G. Maret. **Two-Stage Melting of Paramagnetic Colloidal Crystals in Two Dimensions**. *Phys. Rev. Lett.*, 82:2721–2724, Mar 1999.

[ZM00] K. Zahn and G. Maret. **Dynamic Criteria for Melting in Two Dimensions**. *Phys. Rev. Lett.*, 85:3656–3659, Oct 2000.

[ZMAM97] K. Zahn, J. M. Méndez-Alcaraz, and G. Maret. **Hydrodynamic Interactions May Enhance the Self-Diffusion of Colloidal Particles**. *Phys. Rev. Lett.*, 79:175–178, Jul 1997.

Publications

Attached below are the titlepages of the publications of our group during my PhD, to make the reader aware of their content.

- L. F. Cugliandolo, PD, G. Gonnella, and A. Suma. **Phase co-existence in bidimensional passive and active dumbbell systems**. Phys. Rev. Lett.,119:119, (2017).
- G. Negro, L.N. Carenza, PD, G. Gonnella, A. Lamura. **Morphology and flow patterns in highly asymmetric active emulsions**. Physica A: Statistical Mechanics and its Applications, 503, (2018).
- PD, D. Levis, A. Suma, L.F. Cugliandolo, G. Gonnella, I. Pagonabarraga. **Full Phase Diagram of Active Brownian Disks: From Melting to Motility-Induced Phase Separation**. Phys. Rev. Lett., 121, (2018).
- I. Petrelli, PD, L.F. Cugliandolo, G. Gonnella, A. Suma. **Active dumbbells: Dynamics and morphology in the coexisting region**. Eur. Phys. J. E, 41(10):128, (2018).
- PD, D. Levis, A. Suma, L. F. Cugliandolo, G. Gonnella, I. Pagonabarraga. **2D melting and motility induced phase separation in Active Brownian Hard Disks and Dumbbells**. Journal of Physics: Conference Series 1163 (2019).
- G. Negro, L.N. Carenza, PD, G. Gonnella, A. Lamura. **In silico characterization of asymmetric active polar emulsions**. AIP Conference Proceedings, 2071, 1 (2019).
- PD, D. Levis, L.F. Cugliandolo, G. Gonnella, I. Pagonabarraga. **Clustering of topological defects in two-dimensional melting of active and passive disks**. arXiv:1911.06366 (2019).

Phase Coexistence in Two-Dimensional Passive and Active Dumbbell Systems

Leticia F. Cugliandolo,[1,2,*] Pasquale Digregorio,[3] Giuseppe Gonnella,[3] and Antonio Suma[4]
[1]Sorbonne Universités, Université Pierre et Marie Curie–Paris VI,
Laboratoire de Physique Théorique et Hautes Énergies, 4 Place Jussieu, 75252 Paris Cedex 05, France
[2]Kavli Institute for Theoretical Physics, University of California at Santa Barbara, Santa Barbara, California 93106, USA
[3]Dipartimento di Fisica, Università degli Studi di Bari and INFN, Sezione di Bari, via Amendola 173, Bari I-70126, Italy
[4]SISSA–Scuola Internazionale Superiore di Studi Avanzati, Via Bonomea 265, 34136 Trieste, Italy
(Received 28 November 2016; revised manuscript received 13 June 2017; published 29 December 2017)

We demonstrate that there is a macroscopic coexistence between regions with hexatic order and regions in the liquid or gas phase over a finite interval of packing fractions in active dumbbell systems with repulsive power-law interactions in two dimensions. In the passive limit, this interval remains finite, similar to what has been found in two-dimensional systems of hard and soft disks. We did not find discontinuous behavior upon increasing activity from the passive limit.

DOI: 10.1103/PhysRevLett.119.268002

Interest in the behavior of 2D (and also 3D) macroscopic systems under continuous and homogeneous input of energy has been boosted by their connection with active matter [1–8]. This new type of matter can be realized in various ways. Systems of self-propelled particles constitute an important subclass, with natural examples such as suspensions of bacteria [9–11] and artificial ones made of Janus [12–14] or asymmetric granular [15] particles. In all these cases, the constituents consume internal or environmental energy and use it to displace. Very rich collective motion arises under these out of equilibrium conditions, and liquid, solid and segregated phases are observed [16–21]. In particular, in active Brownian particle systems, segregation, also called motility induced phase separation (MIPS), was claimed to occur only above a large critical threshold of the activity [19,22–25].

Besides, the behavior of passive disks is a classic theme of study in soft condensed matter. Recently, Bernard and Krauth argued that 2D melting of hard and soft repulsive disks occurs in two steps, with a continuous Berezinskii-Kosterlitz-Thouless transition between the solid and hexatic phases and a first-order transition between the hexatic and liquid phases, when density or packing fraction are decreased at constant temperature [26]. The hexatic phase has no positional order but quasi-long-range orientational order, while the solid phase has quasi-long-range positional and proper long-range orientational order. Liquid and quasi-long-range orientationally ordered zones coexist close to the liquid phase, within a narrow interval of packing fractions.

In this Letter, we study the phase diagram of a two-dimensional model of active purely repulsive dumbbells and show that it does not comply with the MIPS scenario. We prove that the phase separation found at high values of the activity continuously links, in the passive limit, to a finite coexistence region as the one predicted by Bernard and Krauth for 2D melting of hard and soft repulsive disks [26]. There is no nonvanishing critical value of activity needed for segregation in this system, making the popular MIPS scenario at least not general.

The reason for choosing a dumbbell model is that many natural swimmers have an elongated shape, and a hard dimer is the simplest approximation of such anisotropy [27–29]. This geometry favors aggregation at intermediate densities and sufficiently strong activation [23,30–35]. In this limit, the evolution of an initial homogeneous phase occurs by nucleation and growth of clusters [31] and the system phase separates. At the other extreme, for sufficiently low densities and not so strong activity, particles form only very small clusters that do not coalesce [32,36,37]. The results in this Letter complement these two extreme limits. In the absence of activity, we confirm the

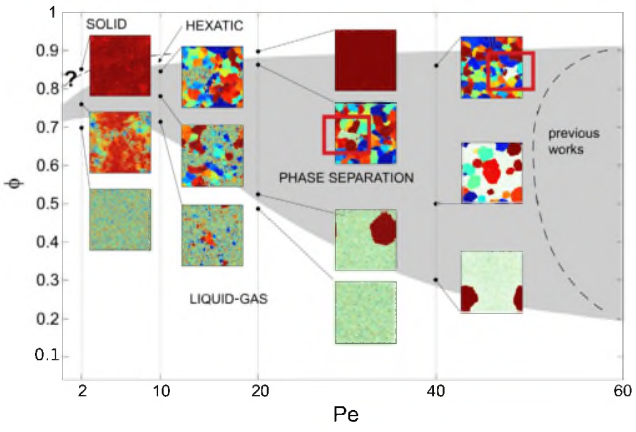

FIG. 1. The phase diagram and some representative local hexatic parameter maps. Note the red rectangular contours in the boxes at Pe = 20 and Pe = 40 that surround the disordered regions. The way in which the phase boundaries are determined is explained in the text and more details are given in the Supplemental Material [40].

Physica A 503 (2018) 464–475

Contents lists available at ScienceDirect

Physica A

journal homepage: www.elsevier.com/locate/physa

Morphology and flow patterns in highly asymmetric active emulsions

G. Negro [a,*], L.N. Carenza [a], P. Digregorio [a], G. Gonnella [a], A. Lamura [b]

[a] Dipartimento di Fisica, Università degli studi di Bari and INFN, Sezione di Bari, Via Amendola 173, 70126 Bari, Italy
[b] Istituto Applicazioni Calcolo, CNR, Via Amendola 122/D, 70126 Bari, Italy

HIGHLIGHTS

- The morphology and the dynamics of an emulsion made of a polar active gel and an isotropic passive fluid is studied.
- We focus on the case of a highly off-symmetric ratio between the active and passive components.
- In absence of activity the stationary state is characterized by an hexaticaly ordered array of droplets.
- Small amount of activity favors the elimination of defects in the array of droplets.
- Rising activity new and interesting morphologies arises depending on whether the system is contractile or extensile.

ARTICLE INFO

Article history:
Received 4 November 2017
Received in revised form 16 February 2018
Available online 9 March 2018

ABSTRACT

We investigate numerically, by a hybrid lattice Boltzmann method, the morphology and the dynamics of an emulsion made of a polar active gel, contractile or extensile, and an isotropic passive fluid. We focus on the case of a highly off-symmetric ratio between the active and passive components. In absence of any activity we observe an hexatic-ordered droplets phase, with some defects in the layout. We study how the morphology of the system is affected by activity both in the contractile and extensile case. In the extensile case a small amount of activity favors the elimination of defects in the array of droplets, while at higher activities, first aster-like rotating droplets appear, and then a disordered pattern occurs. In the contractile case, at sufficiently high values of activity, elongated structures are formed. Energy and enstrophy behavior mark the transitions between the different regimes.

1. Introduction

The capability of different systems of using energy taken from their environment to go out of thermal equilibrium, gives rise to a wealth of behaviors [1]. They range from swarming, self-assembly, spontaneous flows to other collective properties [2–5]. This boosted a deep interest in addressing their study in order to look for possible new physics, explore common features between different systems, and develop new strategies in designing synthetic devices and materials with smart properties.

Self-propelled objects represent a remarkable example of active matter. Starting from the seminal model of Vicsek [6] for swarms, it was later realized that common features can be traced in several systems at different scales promoting the introduction of statistical models able to describe such behaviors [7–10]. Another example of active matter, sharing

* Corresponding author.
E-mail addresses: giuseppe.negro@ba.infn.it (G. Negro), l.carenza@studenti.uniba.it (L.N. Carenza), pasquale.digregorio@ba.infn.it (P. Digregorio), g.gonnella@ba.infn.it (G. Gonnella), a.lamura@ba.iac.cnr.it (A. Lamura).

https://doi.org/10.1016/j.physa.2018.03.011
0378-4371/

Editors' Suggestion

Full Phase Diagram of Active Brownian Disks: From Melting to Motility-Induced Phase Separation

Pasquale Digregorio,[1] Demian Levis,[2,3,*] Antonio Suma,[4,5] Leticia F. Cugliandolo,[6] Giuseppe Gonnella,[1] and Ignacio Pagonabarraga[2,3]

[1]*Dipartimento di Fisica, Università degli Studi di Bari and INFN, Sezione di Bari, via Amendola 173, Bari, I-70126, Italy*
[2]*CECAM Centre Européeen de Calcul Atomique et Moléculaire, Ecole Polytechnique Fédérale de Lausanne, Batochimie, Avenue Forel 2, 1015 Lausanne, Switzerland*
[3]*UBICS University of Barcelona Institute of Complex Systems, Martí i Franquès 1, E08028 Barcelona, Spain*
[4]*SISSA—Scuola Internazionale Superiore di Studi Avanzati, Via Bonomea 265, 34136 Trieste, Italy*
[5]*Institute for Computational Molecular Science, Temple University, Philadelphia, Pennsylvania 19122, USA*
[6]*Sorbonne Université, Laboratoire de Physique Théorique et Hautes Energies, CNRS UMR 7589, 4 Place Jussieu, 75252 Paris Cedex 05, France*

(Received 25 May 2018; published 31 August 2018)

We establish the complete phase diagram of self-propelled hard disks in two spatial dimensions from the analysis of the equation of state and the statistics of local order parameters. The equilibrium melting scenario is maintained at small activities, with coexistence between active liquid and hexatic order, followed by a proper hexatic phase, and a further transition to an active solid. As activity increases, the emergence of hexatic and solid order is shifted towards higher densities. Above a critical activity and for a certain range of packing fractions, the system undergoes motility-induced phase separation and demixes into low and high density phases; the latter can be either disordered (liquid) or ordered (hexatic or solid) depending on the activity.

DOI: 10.1103/PhysRevLett.121.098003

Active materials are out-of-equilibrium systems in which the dynamics of their elements break detailed balance [1]. Examples can be found in living systems, e.g., the collective motion of large animal groups [2,3], bacteria swarming [4], and the formation of traveling fronts of actin filaments [5], as well as in synthetic ones, like self-propelled grains [6] or self-catalytic colloidal suspensions [7]. Despite such diversity, the emergence of activity-induced collective behavior is captured by minimal models that yield accurate descriptions and shed light on their universal character. A key example is the active Brownian particles (ABP) model, which considers spherical self-propelled particles with only excluded volume interactions [8–13]. A hallmark of active particle systems is that at high enough density and activity, self-propulsion triggers a motility-induced phase separation (MIPS) into a low-density gas in coexistence with a high-density drop [10–17], resembling the equilibrium liquid-gas transition but in the absence of cohesive forces and without a thermodynamic support [18,19].

Although active particles can in principle move in three dimensions (3D), in most experimental set-ups they are confined to two dimensions (2D). Most studies of 2D ABP focused on MIPS, and they have therefore been largely restricted to intermediate densities [10–19]. In contrast, their solidification, or melting, has received little attention [20–22], and the connection between the high Pe behavior and the equilibrium physics as $\mathrm{Pe} \to 0$ has been, surprisingly, disregarded. In particular, the fate of 2D melting (with its intermediate hexatic phase) under active forces, has been investigated for dumbbell systems [23], where MIPS is continuously connected to the passive liquid-hexatic coexistence. This result shed new light on the very nature of MIPS, and it showed the importance of exploring the full phase diagram at high densities. In this Letter, we address this issue in the paradigmatic ABP model.

Melting in 2D is a fundamental problem that has remained elusive despite decades of intensive research [24,25]. The transition was initially claimed to be first order [26] and later argued to follow a different scenario, with an intermediate hexatic phase, separated by continuous transitions mediated by the unbinding of defects [27–29]. More recently, numerical simulations [30–32], followed by experiments on colloidal monolayers [33], clarified the picture. They indicate that melting of passive hard disks takes place in two steps: as the packing fraction is increased, a first-order transition between the liquid and hexatic phases occurs, followed by a continuous Berezinskii-Kosterlitz-Thouless (BKT) transition between the hexatic and the solid. The hexatic phase exhibits quasi-long-range orientational order and short-range positional one, while the solid phase has quasi-long-range positional and long-range orientational order. Liquid and hexatic phases coexist close to the liquid phase, within a narrow interval of packing fractions.

Eur. Phys. J. E (2018) 41: 128
DOI 10.1140/epje/i2018-11739-y

THE EUROPEAN PHYSICAL JOURNAL E

Regular Article

Active dumbbells: Dynamics and morphology in the coexisting region*

Isabella Petrelli[1], Pasquale Digregorio[1], Leticia F. Cugliandolo[2], Giuseppe Gonnella[1], and Antonio Suma[3,4,a]

[1] Dipartimento di Fisica, Università degli Studi di Bari and INFN, Sezione di Bari, via Amendola 173, Bari, I-70126, Italy
[2] Sorbonne Université, Laboratoire de Physique Théorique et Hautes Energies, CNRS UMR 7589, 4 Place Jussieu, 75252 Paris Cedex 05, France
[3] SISSA - Scuola Internazionale Superiore di Studi Avanzati, Via Bonomea 265, 34136 Trieste, Italy
[4] Institute for Computational Molecular Science, College of Science and Technology, Temple University, Philadelphia, PA 19122, USA

Received 30 April 2018 and Received in final form 13 September 2018
Published online: 25 October 2018

Abstract. With the help of molecular dynamics simulations we study an ensemble of active dumbbells in purely repulsive interaction. We derive the phase diagram in the density-activity plane and we characterise the various phases with liquid, hexatic and solid character. The analysis of the structural and dynamical properties, such as enstrophy, mean-square displacement, polarisation, and correlation functions, shows the continuous character of liquid and hexatic phases in the coexisting region when the activity is increased starting from the passive limit.

1 Introduction

We open this article with a description of a number of noticeable facts of active, but also passive, matter that have motivated our studies of an ensemble of self-propelled dumbbells in purely repulsive interaction confined to move in a two-dimensional space.

1.1 Non-equilibrium dynamics under local bulk energy injection

Active materials are many-body systems composed of self-driven units that convert stored or ambient free energy into systematic movement. They are, typically, living systems, and the size of their elements ranges over many scales, from microorganisms or cells to birds or fish. Artificial realisations, sometimes easier to control in experiments, have also been designed and include self-propelled colloids [1–4], nanorods [5], droplets [6,7] and active gels made by cytoskeleton extracts in the presence of molecular motors [8,9] as well as vibrated mechanical walkers [10–13].

From the point of view of physics, active materials are novel and very interesting objects of study. They are maintained out of equilibrium by the continuous injection of energy at a microscopic scale within the samples. The microscopic dynamics explicitly break detailed balance and, in consequence, no equilibrium theorem can be used as a guideline to understand the macroscopic behaviour. Nevertheless, since the consumed energy is partly dissipated into the medium, different non-equilibrium steady states establish and they are still amenable to be studied with physics tools. Phase transitions between such steady states are possible even in low-dimensional cases. The full characterisation of the dynamic phase diagram and the various phases is one of the issues that attracts physicists' attention.

1.2 Density, form, and dimensionality

The dynamics of systems as seemingly unrelated as flocks of birds, swarms of bacteria and vibrated rods share many features in common and, up to a certain extent, they can be treated within the common theoretical framework of active fluids or suspensions [14–24]. Different approaches aimed at a coarse-grained description based on general symmetry arguments are available but fluctuations and phase transitions have been especially analysed in the context of agent-based models. Although many papers study

* Contribution to the Topical Issue "Flowing Matter, Problems and Applications", edited by Federico Toschi, Ignacio Pagonabarraga Mora, Nuno Araujo, Marcello Sega.

[a] e-mail: antonio.suma@gmail.com

IOP Conf. Series: Journal of Physics: Conf. Series 1163 (2019) 012073 doi:10.1088/1742-6596/1163/1/012073

2D melting and motility induced phase separation in Active Brownian Hard Disks and Dumbbells

Pasquale Digregorio[1], Demian Levis[2,3], Antonio Suma[4,5], Leticia F. Cugliandolo[6], Giuseppe Gonnella[1], Ignacio Pagonabarraga[2,3]

[1] Dipartimento di Fisica, Università degli Studi di Bari and INFN, Sezione di Bari, via Amendola 173, Bari, I-70126, Italy
[2] CECAM Centre Européeen de Calcul Atomique et Moléculaire, Ecole Polytechnique Fédérale de Lausanne, Batochimie, Avenue Forel 2, 1015 Lausanne, Switzerland
[2] UBICS University of Barcelona Institute of Complex Systems, Martí i Franquès 1, E08028 Barcelona, Spain
[4] SISSA - Scuola Internazionale Superiore di Studi Avanzati, Via Bonomea 265, 34136 Trieste, Italy
[5] Institute for Computational Molecular Science, Temple University, Philadelphia, PA 19122, USA
[6] Sorbonne Université, Laboratoire de Physique Théorique et Hautes Energies, CNRS UMR 7589, 4 Place Jussieu, 75252 Paris Cedex 05, France

Abstract. Recently, we characterized the complete phase transition diagram in the ϕ-Pe parameter space for two models of active brownian particles in two dimensions. These models are composed of hard disks and dumbbells, respectively, the former being isotropic and the latter anisotropic. Here, we want to outline all the most significant features of these two paradigmatic models and compare them.
Remarkably, the phase diagrams of the two models are affected differently by the introduction of activity. Disks present a two-stage melting scenario from Pe=0 to about Pe=3, with a first order phase transition between liquid and hexatic and a Berezinskii-Kosterlitz-Thouless transition between hexatic and solid. At higher activities, the three phases are still observed, but the transition between liquid and hexatic becomes a BKT transitions without a distinguishable coexistence region. Dumbbells, instead, present a macroscopic coexistence between hexatically ordered regions and disordered ones, over a finite interval of packing fractions, for all activities, included Pe=0, without any observable discontinuity in the behavior upon increasing Pe.

1. Introduction

Active materials evolve out of thermal equilibrium because their constituents are able to extract energy from the environment and inject it into the system, breaking detail balance [1]. Among others, Active Brownian Particles (ABP) model constitutes a standard paradigmatic model to study the impact of activity on soft matter [2, 3, 4]. For many of the active systems cited above, self-propulsion is able to trigger a motility-induced phase separation (MIPS) between a low-density gas-like phase and dense stable aggregates [5], reminiscent of the equilibrium liquid-gas transition but in the absence of cohesive forces and without a thermodynamic framework to support it [6, 7].

It is worth saying that the most intriguing phenomena induced by activity, as well as the most promising experimental applications, concern systems confined in 2D layers. Being interested

In Silico Characterization of Asymmetric Active Polar Emulsions

G. Negro[1,a)], L.N. Carenza[1,b)], P. Digregorio[1,c)], G. Gonnella[1,d)] and A. Lamura[2,e)]

[1]*Dipartimento di Fisica, Università degli studi di Bari and INFN, Sezione di Bari, Via Amendola 173, 70126 Bari, Italy.*
[2]*Istituto Applicazioni Calcolo, CNR, Via Amendola 122/D, 70126 Bari, Italy.*

[a)]Corresponding author: giuseppe.settimio.negro@gmail.com
[b)]livio.carenza@uniba.it
[c)]pasquale.digregorio@ba.infn.it
[d)]g.gonnella@ba.infn.it
[e)]a.lamura@iba.ac.cnr.it

Abstract. In this paper an in silico study of the behavior of an active polar emulsion is reported, focusing on the case of a highly off-symmetric ratio between the polar (active) and passive components, both for the extensile and contractile case. In absence of activity the system is characterized by an hexatic-ordered droplets phase. We find that small extensile activity is able to enhance the hexatic order in the array of droplets with respect to the passive case, while increasing activity aster-like rotating droplets appear. In contractile systems activity creates shear flows and elongated structures are formed.

INTRODUCTION

Active matter is a class of materials whose constituents are able to consume energy to move or to exercise stresses locally [1]. Research in this field has been mainly focused on single-component active systems and to a lesser extent on the behavior of solutions of active and passive components. Binary fluids with an active component have been considered in [2, 3] and very recently [4] a model has been introduced, where emulsification of the active component is favored by the presence of surfactant added to the mixture. This model generalizes the active gel theory to describe the behavior of a mixture of isotropic passive and polar active fluids, and, by numerical simulations, it was shown that activity strongly affects the behavior of the mixture, leading to a variety of morphologies whose formation strongly depends on the intensity and the kind of active doping. Indeed, polar active fluids are said to be either extensile (*e.g.* bacterial colonies and microtubules bundles) or contractile (*e.g.* actine and myosin filaments) according to the nature of the stress exerted by the active component on its neighborhood. Introducing a parameter that represents the strength of the active stress acting in the system (see Section MODEL AND METHODS), intensity of active doping can be tuned. This corresponds experimentally to keeping under control the amount of ATP in active gels of bundled microtubles [5] or the amount of oxygen available, the concentration of ingredients, or the temperature in bacterial suspensions.

In this work we complement previous analysis by considering a highly off-symmetric mixture with a $10 : 90$ ratio between the active and passive components, both for extensile and contractile systems. In this case the equilibrium state of the system is characterized by an ordered array of droplets of the minority phase positioned at the vertices of a triangular lattice. We will show that, in spite of the strong unbalance between the two components, activity greatly affects the morphology of the system, leading to the development of a wide range of patterns both for the concentration and the velocity field. A small amount of extensile activity favors the elimination of defects in the system, as shown by measuring the number of defects in Voronoi tessellation. Increasing activity, isolated droplets tend to merge forming big rotating droplets with an aster-like shape. In the contractile case activity promotes the rupture of the hexagonal phase and the appearance of a matrix of the active component in the passive flowing background, differently from what happens in the symmetric case[4].

TIM 18 Physics Conference
AIP Conf. Proc. 2071, 020012-1–020012-8; https://doi.org/10.1063/1.5090059
Published by AIP Publishing. 978-0-7354-1799-1/$30.00

Clustering of topological defects in two-dimensional melting of active and passive disks

Pasquale Digregorio,[1] Demian Levis,[2,3] Leticia F. Cugliandolo,[4,5] Giuseppe Gonnella,[1] and Ignacio Pagonabarraga[2,3]

[1] *Dipartimento di Fisica, Università degli Studi di Bari and INFN, Sezione di Bari, via Amendola 173, Bari, I-70126, Italy*
[2] *CECAM Centre Européen de Calcul Atomique et Moléculaire, Ecole Polytechnique Fédérale de Lausanne, Batochimie, Avenue Forel 2, 1015 Lausanne, Switzerland*
[3] *UBICS University of Barcelona Institute of Complex Systems, Martí i Franquès 1, E08028 Barcelona, Spain*
[4] *Sorbonne Université, Laboratoire de Physique Théorique et Hautes Energies, CNRS UMR 7589, 4 Place Jussieu, 75252 Paris Cedex 05, France*
[5] *Institut Universitaire de France, 1 rue Descartes, 75005 Paris France*

(Dated: November 18, 2019)

We provide a quantitative analysis of all kinds of topological defects present in 2D passive and active repulsive disk systems. We show that the passage from the solid to the hexatic is driven by the unbinding of dislocations. Instead, although we see dissociation of disclinations as soon as the liquid phase appears, extended clusters of defects largely dominate below the solid-hexatic critical line. The latter percolate at the hexatic-liquid transition in continuous cases or within the coexistence region in discontinuous ones, and their form gets more ramified for increasing activity.

In two-dimensions (2D), thermal fluctuations often prevent the emergence of long-range order (LRO), as illustrated by the absence of spontaneous magnetization in 2D Heisenberg magnets [1] and positional order in 2D particle systems [2]. However, different kinds of phase transitions driven by topological defects can still occur: for example, in 2D planar magnets, the binding-unbinding of vortices mediate the so-called Berezenskii-Kosterlitz-Thouless (BKT) transition between a paramagnet and a low temperature critical phase with quasi-long-range magnetic order (QLRO) [3, 4].

The nature of the melting transition in 2D crystals is far more involved and controversial [5, 6], partly due to the fact that particle systems might have two types of order, translational and orientational, and thus two kinds of topological defects, dislocations and disclinations. The most standard picture of 2D melting in spherically symmetric particle systems follows the work of Kosterlitz-Thouless-Halperin-Nelson-Young (KTHNY) [7, 8], according to which the transition from the solid (with positional QLRO and orientational LRO) to the isotropic liquid occurs in two-steps, separated by an intermediate hexatic phase characterized by orientational QLRO. These solid-hexatic and hexatic-liquid transitions are of BKT type, driven by the unbinding of dislocations and disclinations, respectively. While evidence for the KTHNY scenario has been given in some experiments [9] and simulations [10–13], alternative mechanisms have also been proposed [5, 6] and, in particular, one in which the continuous two-step scenario is preempted by a single solid-liquid first-order transition driven by the aggregation of defects into grain-boundary-like structures [14–16]. Recent simulations [17–19] and experiments [20] have shown that the melting of equilibrium (passive) repulsive disks shares aspects of both scenarios: a BKT solid-hexatic transition but a first-order hexatic-liquid one, if the interaction potential is stiff enough. It has thus been suggested that the disclination-unbinding mechanism should be preempted by a first-order transition involving the proliferation of clusters of defects, forming a percolating network in the liquid regime [12, 18, 19]. However, neither a quantitative analysis of such clusters nor the derivation of a theory for the stability of the hexatic phase against grain-boundaries have been conducted. Moreover, and surprisingly enough, no clear experimental evidence and very little numerical one [19] for dislocation unbinding at the solid-hexatic transition exists.

Besides the issues that still remain unclear for systems of passive particles, the classical problem of 2D phase transitions is experiencing a resurge of interest in the context of active matter systems. These are collections of self-propelled particles which pump energy from their environment and convert it into motion in the presence of dissipation, but in a way that breaks detailed balance [21–23]. The question now is how these non-equilibrium 'active' fluctuations affect the phase behavior of 2D particle systems [24–28] and the role played by topological defects. It has recently been shown that self-propelled hard-disks follow the two-step melting scenario of their passive counterparts at small activities, up to a threshold above which hexatic-liquid coexistence, characteristic of the first-order nature of the transition, disappears [26, 28]. Both the hexatic-liquid and solid-hexatic transitions are shifted to higher densities as the degree of activity is increased and, at sufficiently high activities, these transitions overlap with a coexistence region purely triggered by self-propulsion, the so-called Motility-Induced Phase-Separation (MIPS) [29]. Although topological defects are known to be crucial in understanding 2D equilibrium phase transitions, little attention has been paid to their study in self-propelled systems [25, 28] and thus the very nature of the phase transitions is still to be understood.

In this Letter we systematically study the full spectrum